# Analysis by “reverse engineering” methods of ultra-table piezoelectric resonators and noise modelling.

Alok Pokharel

**THESE DE DOCTORAT DE L'ETABLISSEMENT**
**UNIVERSITE BOURGOGNE FRANCHE-COMTE**

**PREPAREE A L'UNIVERSITE DE FRANCHE-COMTE**

Ecole doctorale n°37

ED SPIM

Doctorat de Sciences pour l'Ingénieur

Par

M. POKHAREL Alok

# Analyse par des méthodes de "reverse engineering" de résonateurs piézoélectriques hautes performances et modélisation du bruit.

# Analysis by "reverse engineering" methods of ultra-table piezoelectric resonators and noise modelling.

Thèse présentée et soutenue à Besançon, le 10 Septembre 2020.

Composition du Jury :

| | | |
|---|---|---|
| M. PRIGENT Michel | Professeur des Universités, XLIM, IUT du Limousin, Limoge, | Président |
| M. CILIBERTO Sergio | Directeur de Recherche, CNRS, ENS Lyon, | Rapporteur |
| M. LLOPIS Olivier | Directeur de Recherche, CNRS, LAAS, Toulouse, | Rapporteur |
| M. DEVEL Michel | Professeur des Universités, FEMTO-ST, ENSMM, Besançon, | Examinateur |
| M. VOROBYEV Nicolas | Ingénieur CNES, Toulouse, | Examinateur |
| M. IMBAUD Joël | Maître de Conférences, FEMTO-ST, ENSMM, Besançon, | Codirecteur de thèse |
| M. STHAL Fabrice | Professeur des Universités, FEMTO-ST, ENSMM, Besançon, | Directeur de thèse |

*Dédicace*

*À mes Parents.*

*À mon frère.*

*À Elina.*

# ACKNOWLEDGEMENTS

It is a privilege and honour to receive the constant support of all the members of FEMTO-ST and ENSMM throughout the period of my thesis to achieve this dream of my life. I will always remain grateful and indebted for their valuable support through the course of this dissertation.

This thesis work would not have been possible without the financial support of "Région Bourgogne Franche-Comté" and the LABEX Cluster of Excellence FIRST- TF (ANR-10-LABX-48-01) for supporting this thesis work in their program "Investissement d'Avenir" operated by French National Research Agency (ANR). I would like to thank CNES for providing resonators for my thesis work and to the project supported by ANR ASTRID titled ECLATEMPS (Etude de Cristaux de LGT pour Applications Temps-Fréquence) (ANR-12-ASTR-0030-01) for providing LGT resonators. I am also thankful to FEMTO-ST department of Time and Frequency and ENSMM and to l'École Doctorale SPIM for all the follow-ups and support during the 4 years period.

I would like to express my humble gratitude to my thesis advisor Professor Fabrice Sthal for his guidance and patience towards me throughout the period of this thesis. His motivation, encouragement, being up-to-date and a sense of "proving by doing" role was an unimaginable base to help me focus on my work. Similarly, I feel grateful to thank my co-advisor Associate Professor Joël Imbaud whose perspective I admire in starting to do a work little by little as commendable throughout the journey of my thesis. Together with this, I am very much thankful to Joël for some of the experimental part of my thesis.

I thank Professor Michel Devel for his high-level expertise in helping me understand the theoretical part of my thesis. His ideas were a boon to find a solution for modelling phase noise from a statistical perspective and along with this my gratitude for accepting to report on this thesis. Also, I would like to thank Professor Célestin C. Kokonendji from Laboratoire de Mathématiques de Besançon, for his presentations in understanding stable distributions.

I would like to thank the jury members Sergio Ciliberto, Directeur de Recherche in CNRS, Laboratoire de Physique de l'ENS Lyon and Olivier Llopis, Directeur de Recherche in CNRS-LAAS, Toulouse.

I would like to thank Michel Prigent, Professeur des Universités from XLIM, IUT du Limousin, Limoge and Nicolas Vorobyev, Ingénieur at CNES from Toulouse to examine this work.

I equally thank Serge Galliou (ex-director) and Yann Kersalé (current director) of FEMTO-ST, department of Time and Frequency for allowing me to work in the lab during my thesis period.

I thank Sarah and Fabienne at FEMTO-ST, department of Time and frequency for their sincere administrative help. Not to forget Clara Lahu from HR department, ENSMM and Alika Rossetti from UBFC SPIM for their administrative and scholarly help during my thesis.

I would also thank David Vernier for his active help in providing me electronic equipment for LabView tutorials and Phillippe Abbé for all the technical help in the lab regarding electronics and mechanics.

I would also like to thank my cool colleagues Etienne and Jérémy, with whom I had a chance to have a humorous time and not a single working day was there where we did not pass out jokes or made fun of something. I am thankful for an exciting unplanned trip with Guillaume, Sabina, and Giacomo to Colmar and Abondance, it was really an awesome moment. I thank Alexandre (an office mate and a friend with a big sound...Ha!Ha!Ha!), together we had an amazing trip to Orlando, Miami, and Tampa. I also thank Anthony my colleague during the end year of my thesis, Rémy a cool sportive friend and Melvin, Gregoire, François, Stefania, Gauthier, Kevin, Falzon with whom I passed memorable times of my life. I also thank the newcomers Arthur, Tung, Isha, Merieme and Shambo with whom I had a wonderful time.

I would also like to thank my family members for providing me all the emotional support during the period of my thesis.

# TABLE OF CONTENTS

# GENERAL OVERVIEW

The continued research on quartz crystals has led to the optimization of piezoelectric resonators used in devices in the time and frequency domain. Their applications were initially limited to military devices, but they can now be found in many different electronic devices available for the public.

A crystal resonator is specified to operate at a given (resonance) frequency, within a given temperature range for best results, and under severe conditions of vibrations over a long period. The equations of motion of quartz representative volume elements, incorporating piezoelectric effects, allow us to find resonance frequencies and their corresponding modes of vibrations as a function of orientation of the resonator axes with respect to the crystallographic axes. The BAW (Bulk Acoustic Wave) quartz crystal resonators used for this thesis can operate at three different modes of vibration i.e. extension-compression mode *A*, fast shear mode *B* and slow shear mode *C*. The inversion point temperature of this kind of resonator with an SC (Stress Compensated) cut vibrating at 3$^{rd}$ overtone mode-*C* is around 80-85° C. For this kind of resonator, the quality factor is in order of two and half millions at 5 MHz resonant frequency.

Applications of this kind of resonators are quite common in metrological systems (atomic clocks in GNSS satellite positioning devices) for a frequency range between 0.8 MHz and 200 MHz. The best BAW resonators can have a short-term relative stability in time of about $10^{-14}$ at room temperature, so that they are termed as “ultra-stable”. Researches are still going on to try to improve that stability value or prove that it is an intrinsic material limit and find all the factors affecting it. We know that the short-term stability of an oscillators built from a resonator is dependent on the quality factor (loaded) of the resonator which itself depends on the quality of the material, but also that it is not the only driving factor. The fundamental origin of this stability limit is still unknown, but we can study limiting factors through their impact on the random fluctuations in frequency and phase of the resonator output signal (frequency noise or phase noise). This kind of work has been carried out, for years, in the Time and Frequency department at FEMTO-ST (and its LPMO and LCEP ancestors), notably through the development of a state of the art comparison technique to measure the noise in resonators from BAW resonators (5 MHz - 5 GHz). In this PhD thesis, we mainly concentrated on the study of the low frequency part of the Power spectral density of phase noise which is roughly inversely proportional to the inverse of the frequency shift with respect to the resonance frequency used (commonly known as “1/*f* noise” or “flicker noise” in the quartz crystal resonator community).

Following previous works in FEMTO-ST in collaboration with CNES and several other European partners, a large quantity of very high performance 5 MHz ultra-stable SC-cut quartz crystal resonators were provided for reverse engineering during this thesis work. Here, “reverse engineering” should be understood like “going back to the cause of the problem by dismantling the resonators and characterizing their parts”. Along with this, resonators fabricated from other piezoelectric materials

such as LGT (Langatate) have also been used. Hence, comparative investigations were carried out to study the influence of the type of material and crystallographic defects, on $1/f$ phase noise in acoustic resonators.

**Thesis organisation:**

The work carried out in this thesis has been organised into five chapters as:

- Chapter 1 begins with a brief description of quartz as a piezoelectric material, equivalent electrical circuit of quartz, governing equations in quartz, a short background on the quartz resonators used for this thesis and their possible use in metrological devices. Then, detailed information regarding the different kinds of noise in resonators are given, with equations that are used in all the succeeding chapters.

- Chapter 2 focuses on the technical part of this thesis. It introduces a unique phase noise measurement technic used for acoustic quartz resonators in FEMTO-ST. This chapter includes all the necessary details required for setting up and using the phase noise measurement bench. Similarly, it also details the alternative phase noise measurement technic used for low motional resistance resonators i.e. LGT resonators. Finally, the chapter concludes with results of some phase noise measurements using these classical and alternative phase noise measuring technics.

- Chapter 3 deals with the study of propagation of acoustic waves in a plano-convex shaped quartz crystal resonator. The work starts with the definition of an infinite piezoelectric plate as a theoretical basis to introduce the concept of energy trapping in a quartz resonator. The chapter further gives core details of modelling of a plano-convex resonator with electrodes using Stevens and Tiersten's model and implements all the tensor equations necessary for the design as derived in Chapter one. Similarly, the frequencies of overtones and anharmonic modes of the 5 MHz SC-cut plano-convex resonators along with the frequency-temperature effects occurring in them are determined. Then, we discuss results of phase noise measurement in plano-convex quartz resonators at two different temperatures i.e. 353K and 4K. The classification of our resonators according to their short-term stability values (good, average, or bad) and their Q-factors is then discussed. Finally, we validate the Stevens and Tiersten's model using the Finite Element Method as implemented in COMSOL – Multiphysics, for most of the visible modes of vibration for mode-*C*.

- Chapter 4 presents result of statistical tests that we performed on series of 101 phase noise measurements at 353K on the same resonator pairs. More precisely, after providing some background information on some peculiar statistical distributions of probability known as stable distributions and Mittag-Leffler distributions, we briefly review the main ideas of several papers that use them for the modelling of some physical processes that happen during relaxation

of a short perturbation imposed to the system, using statistical thermodynamics. We then give account of tests of intermittency as a possible physical origin of 1/*f* noise in our resonator, using Mittag-Leffler distribution and conclude with discussing the fits of the distribution of the 101 relative PSD of noise averaged over the frequency interval in which the 1/*f* modelisation is appropriate.

- In Chapter 5, we describe the analysis performed on dismantled good and bad resonators as part of a "reverse engineering" program which is a crucial work for this thesis. Photographs of the internal part have been taken by a high definition camera from different angles. This allowed us to see the defects visible to the naked eye on the mounting, on the electrodes and on the crystal itself. Further, to see the intrinsic crystal defects i.e. dislocations and inclusions, X-rays diffraction and laser scattering have been used, respectively.

# Chapter 1 Introduction

From more than half a century, resonators have been serving in time and frequency applications as the popular and simpler piezo-electronic device. The piezo-electronic device consists of piezoelectric material for e.g. Quartz, Langatate ($La_3Ga_{5.5}Ta_{0.5}O_{14}$), Gallium orthophosphate ($GaPO_4$) etc., dimensioned, oriented according to their crystallographic axes, and equipped with a pair of conducting electrodes. Vice versa, these electrodes excite the resonator into mechanical vibration because of piezoelectric effect. The result is that, a resonator behaves like a R-L-C circuit composed of a resistor, inductor, and capacitor. This leads the vibrational energy to be minimum except when the frequency of the driving field is in the periphery of one of the normal modes of vibration "energy trapping" and resonance occurs.

As the fact of today, different piezoelectric materials are on investigation for resonator characteristics, but for many years, quartz resonators had been preferred in satisfying needs for precise frequency control and selection. Compared to other piezoelectric resonators, like, those made from ceramics and single-crystal materials, quartz resonators have unique combination of properties. The materials properties of quartz are both extremely stable and highly repeatable from one specimen to another. Likewise, the acoustic loss of the quartz resonator is particularly low, leading directly to one of the key properties of resonators i.e. high Quality (Q) factor. Its intrinsic Q is around $2.7 \cdot 10^6$ at 5 MHz. Therefore, this low loss factor and frequency stability of resonators make quartz the most sought-after material in designing and manufacturing ultra-stable high frequency resonators.

## 1.1 The world of Quartz Crystal

Materials used for acoustics are usually characterised by the elastic linearity, high quality factor i.e. Q, zero temperature coefficients (ZTCs) of frequency, and more precisely by the presence of piezoelectricity. Piezoelectricity has many benefits like, mechanism of efficient transduction between mechanical motion and electrical variables. Similarly, the compensation of stress and temperature transient, evolved from non-linearities is possible with quartz, making available high stability bulk acoustic wave (BAW) resonators and the Surface Acoustic Waves (SAW) resonators, which provides conveniently accessible time axes for signal processing operations like convolution [1]. Whereas, from the application point of view, for several oscillator applications, the piezoelectric coupling $k$ need not to be large. The reason is that, the operating point of an oscillator confines to the resonator inductive region where a small coupling resembles a narrow inductive range, and high oscillator stability.

Modern-day applications in acoustics include devices like, wireless transceivers for voice, data, internets, Wireless Local Area Networking (WLAN) including WLAN robot, timing and security applications, Code Division Multiple Access (CDMA) filters, non-volatile memories, and micro-electromechanical (MEMS)/ micro-optomechanical (MOMS) devices. Some of the SAW applications are analog signal processing (convolvers, duplexers, delay lines, and filters), for the mobile

telecommunications, multimedia, and Industrial-Scientific-Medical (ISM) bands, wireless passive identification tags, sensors, transponders, and microbalances. BAW applications include resonators in precision clock oscillators, front-end GPS filters for cell phones, thin-films, solidly mounted resonators (SMRs), and stacked crystal filters (SCFs) formed as SMRs, for integration with microwave heterojunction bipolar transistors (HBTs).

### 1.1.1 Why do we need quartz

The answer, quartz is the only known material that possess the following combination of properties [1]:

- Piezoelectric (as the whole world knows!).
- Zero temperature coefficient cuts.
- Stress/thermal transient compensated cuts.
- High acoustic Q and naturally low loss.
- Capable of withstanding 35,000-50,000 g shocks.
- Very stable.
- Capable of integrating with micro and nano-electronic components.
- Easy to process, hard but not brittle, under normal conditions, low solubility in everything except fluoride etchants.
- Abundance in nature: it is easy to grow in large quantities, at low cost, and with high purity and perfections. Data from 2015 A.D shows that, fabricated crystal makes up to 3,769 tonnes per year and is second only to silicon.

### 1.1.2 History of innovation of quartz that led to its usage

History of innovation of quartz summarises below [1]:

**1800-1900s**- Piezoelectric effects discovered by Brothers Pierre and Jacques Curie; first hydrothermal growth of quartz in Lab was possible.

**1910- 1920s**- First quartz crystal oscillator and first quartz crystal-controlled clock was developed.

**1930-1940s**- Temperature compensated BAW AT/BT cuts developed.

**1950- 1960s**- Quartz bars were commercially viable; theory of vibration of anisotropic plates were proposed.

**1960-1970s**- "Energy trapping" theory came in to play to reduce unwanted modes; surface acoustic wave (SAW) cuts; temperature compensated ST was developed; stress compensated (SC) compound cut developed; BVA resonators were fabricated; cryo-pumps were proposed.

**1980-1990s**- Stress-compensated BAW compound cut (SBTC) developed; thin-film resonators realized; solidly mounted resonators fabricated.

### 1.1.3 Quartz used in resonators

Quartz has always been a most common material used for fabricating resonators. In the beginning, natural quartz has a long history of use to fabricate resonators, but later, because of high purity, low production costs and easy handling, synthetic crystals took over the market for resonator fabrication. However, today, the use of natural quartz has been limited for the fabrication of pressure transducers in deep wells.

We can use any object made of elastic material, possibly as a crystal because all the materials have natural resonant frequency of vibrations. Just take an example of material like steel, which is very elastic and has a high speed of sound. In fact, in mechanical filters, people used steels before quartz. Today, a properly cut and mounted quartz can distort in the electric field supplied by the electrodes on the crystal. Hence, when the field removed, the quartz generates the electric field and returns to the previous shape. Nevertheless, the advantage of using the material quartz is the presence of its elastic constants where its size changes in a way to maintain the frequency dependence on temperature to be very low. However, the temperature specific characteristics depends on the mode of vibration and the angle of quartz cut. This is advantageous because the resonant frequency of the plate depends on its size and does not change much. Some of the popular modes of vibrations are in Figure 1.1.

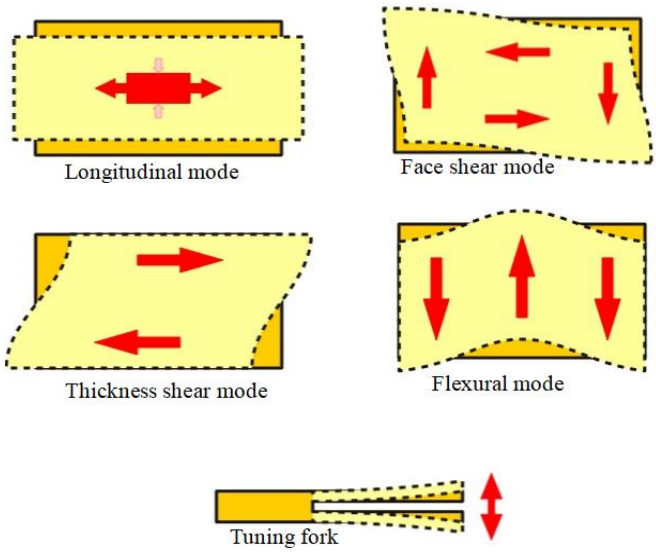


*Figure 1.1: Different modes of vibration used in resonator fabrication [2].*

The benefit of using different modes of vibration is that, the fabrication of different sized resonators and oscillators been made possible as can be seen in Figure 1.2 and Figure 1.3 respectively. However, to be specific, we do not intend to establish all the historical advancement of quartz resonators and oscillator except for few already mentioned above; rather, the purpose of showing different kinds of resonators and oscillators in Figure 1.2 and Figure 1.3 is to picturize how the technology has made the adaptation of quartz crystals to the small electronic devices.

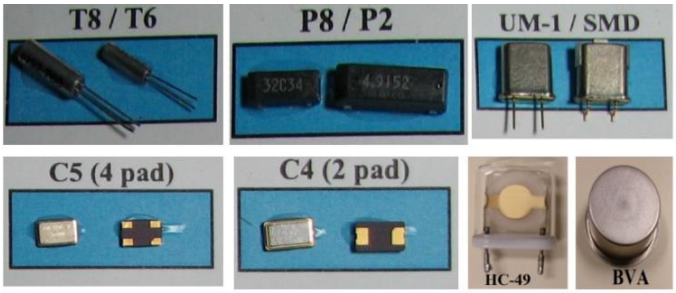


*Figure 1.2: Different kinds of fabricated resonators [2].*

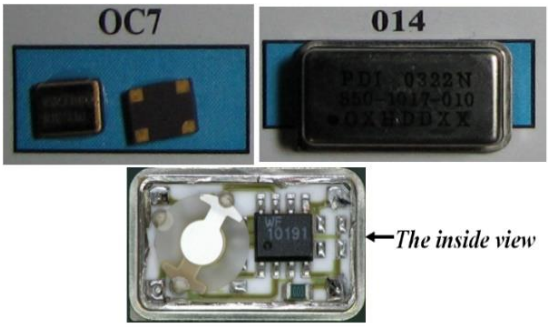


*Figure 1.3: Small-sized oscillator fabricated using quartz crystal [2].*

Major real-life usages of quartz are given in Table 1.1 [1]:

| Aerospace | Research/metrology | Industry | Consumer | Automotive |
|---|---|---|---|---|
| Communications | Atomic clocks | Telecom | Watches/clocks | Engine control |
| Navigation | Instruments | Aviation | Cell phones | Trip computer |
| Radar | Astronomy | Disk drives | Radio/Hi-Fi | GPS |
| Sensors | Space tracking | Modems | Colour TV | |
| Guidance | Celestial investigation | Computers | Pacemakers | |
| Warfare | | Digital systems | VCR/Video camera | |

*Table 1.1: Table of quartz uses in different domains.*

## 1.2 BAW resonator

### 1.2.1 Equivalent circuit of a resonator

The circuit in Figure 1.4 is an electrical equivalent circuit for a quartz crystal resonator where $C_0$ is the parasitic capacitance that accounts for all the stray capacitive effects in the circuit. The motional parameters $C_1, R_1 \; and \; L_1$ are the capacitance, resistance, and inductance respectively in series. When this circuit extends as, $C_n, R_n, and \; L_n$ , each series arm accounts for one resonance and represents the overtones or harmonics of that resonant frequency as shown in Figure 1.5.

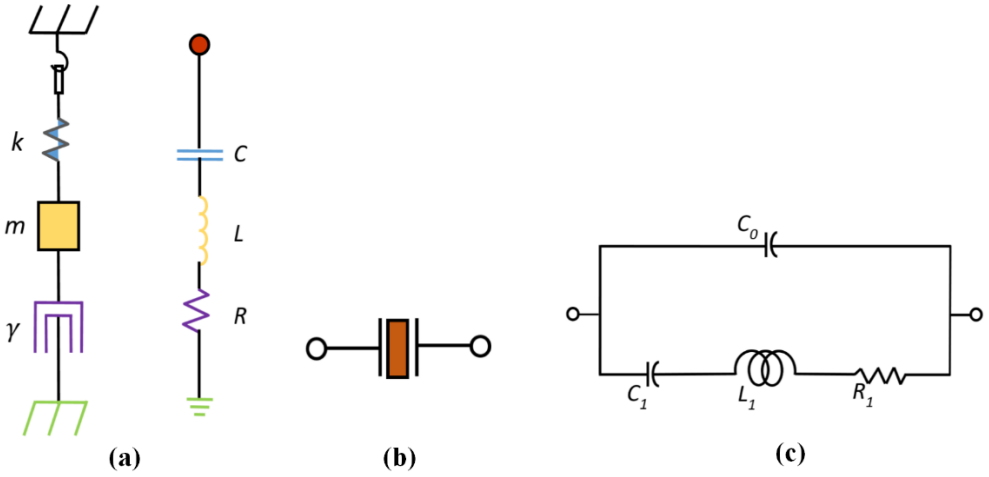


*Figure 1.4: a. Mechanical-Electrical equivalent, b. Crystal unit symbol, c. Electrical [3] equivalent circuit.*

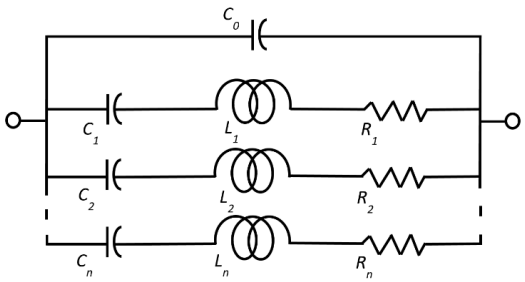


*Figure 1.5: Extended equivalent circuit with overtones.*

Further, the extended circuit resembles three families of motion namely Mode-*A*- longitudinal mode, Mode-*B*- fast shear mode and Mode-*C*- slow shear mode, as in Figure 1.6., for an anisotropic material.

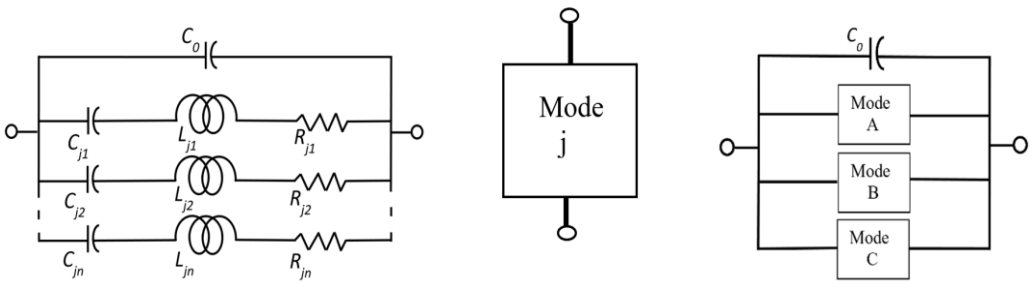


*Figure 1.6: Equivalent circuit resembling three families of motion.*

As a first approach, we assume that no external forces act on our resonator system except the damping. The governing differential equation derived from Newton's second law of motion for 'free and damped' vibration will be:

$$mu'' + \gamma u' + ku = 0 \qquad (1.1)$$

Where, $m$ is the mass, $u$ is the displacement of the mass from an equilibrium position, $\gamma$ is the viscous damping coefficients and $k$ is the spring constant and are all positive. Upon solving for the roots of the characteristic equation above, we get:

$$r_{1,2} = \frac{-\gamma \pm \sqrt{\gamma^2 - 4mk}}{2m} \tag{1.2}$$

Moreover, the three possible cases are **critical damping** $\gamma = 2\sqrt{mk} = \gamma_{CR}$, **over damping** $\gamma > 2\sqrt{mk}$ and **under damping** $\gamma < 2\sqrt{mk}$. Then equation (1.1) will be:

$$mu^{"} + 2\zeta\omega_0 u' + \omega_0^2 u = 0 \tag{1.3}$$

Where, $\omega_0 = \sqrt{\frac{k}{m}}$ is the natural frequency of resonance i.e. the resonant frequency, $\zeta = \frac{\gamma}{\gamma_{CR}}$ is the damping ratio and $\gamma_{CR} = 2\sqrt{mk}$ is the critical damping ratio. For the under-damping case where $\zeta < 1$, the roots of the characteristic equation will be complex of the form $r_{1,2} = \lambda \pm \mu i$. For the underdamped case, given the equation of harmonic vibration by $u = Ae^{j\Omega t}$, the frequency $\Omega$ will be a complex pair, one of them being:

$$\Omega = \omega_0\sqrt{1-\zeta^2} + i\omega_0\,\zeta \text{ Or } \Omega = \omega_{Re} + i\omega_{im} \tag{1.4}$$

Where $\omega_{Re}$ and $\omega_{im}$ are the real and imaginary part of the frequencies.

The damping of the displacement $u$ measures as:

$$\delta = \frac{2\pi\zeta}{\sqrt{1-\zeta^2}} = \frac{2\pi\omega_{im}}{\omega_{Re}} \tag{1.5}$$

Which clearly helps us to calculate the Quality factor $Q$ as the inverse of the damping, given by:

$$Q = \frac{1}{\delta} = \frac{\omega_{Re}}{2\pi\omega_{im}} \tag{1.6}$$

Where $\delta = 2\pi\zeta$ from equation (1.5) and (1.6), and $Q$ can be written as:

$$Q = \frac{1}{2\zeta} \text{ Or } Q = \frac{\sqrt{km}}{\gamma} \tag{1.7}$$

The equation clears the concept that $Q$ depends on the viscous damping coefficient $\gamma$.

For designing the piezoelectric resonators and oscillators, it is necessary to relate the quality factor $Q$ to the equivalent electrical parameters as shown in Figure 1.4. For simplicity, let us consider a simple series R-L-C circuit [4] in Figure 1.7, than the resonance means to be a condition, when the net total reactance becomes zero and the resonant frequency $f_r$ is that frequency at which the resonance occurs, a clear picture in Figure 1.8.

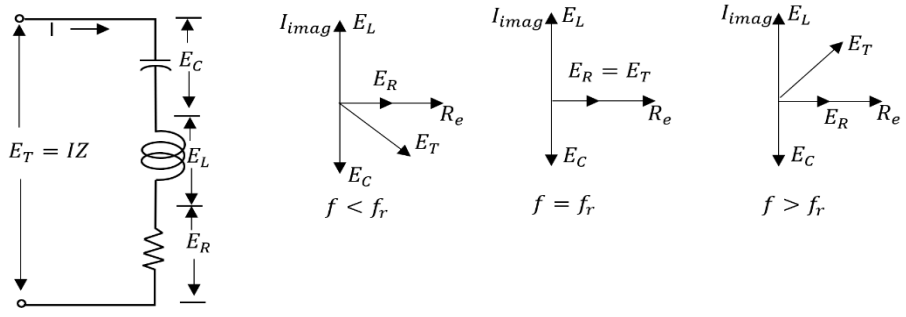


*Figure 1.7: Series RLC circuit diagram.*

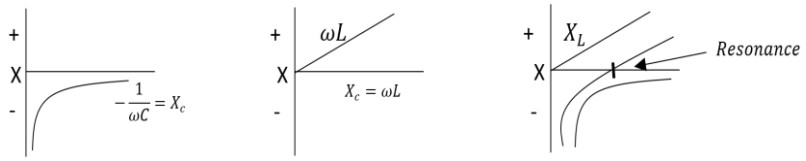


*Figure 1.8: Phasor diagram for RLC circuit.*

When the reactance of the inductor is equal to reactance of the capacitor, the sum of the voltage drop across the inductor and capacitor is zero. The total voltage, which is the phasor sum of the individual drops, is then a minimum for a given current and equals to the drop due to the resistance. If the frequency increases above the resonance, the total reactance will increase so that for a given current the voltage will be greater. Likewise, if the frequency decreases below the resonance, the total reactance and voltage will increase again. Hence, the total impedance of the series circuit can be determined by:

$$Z = R + j\left(\omega L - \frac{1}{\omega C}\right) \tag{1.8}$$

It follows that $|Z|$ is minimum when:

$$\omega L = \frac{1}{\omega C} \tag{1.9}$$

Alternatively, the resonant frequency is:

$$f_r = \frac{1}{2\pi\sqrt{LC}} \tag{1.10}$$

At this frequency the reactive term, which is the only one and varied with frequency, disappears. And for resonance:

$$Z_r = R \tag{1.11}$$

At lower frequencies $\frac{1}{\omega C} > \omega L$, and the total reactance is capacitive, while at higher frequency higher than resonance $> \frac{1}{\omega C}$ . Therefore, the frequency at which the curve crosses the abscissa is the point of resonance.

Let us now build the relationship with the quality factor $Q$ as mentioned in the beginning with the circuit components in Figure 1.4. The universal definition of $Q$ is:

$$Q = 2\pi \frac{Max.energy\ stored}{Energy\ dissipated} \tag{1.12}$$

In terms of the circuit components, it realises as:

$$Q = \frac{I^2 X_L}{I^2 R} = \frac{X_L}{R} = \frac{X_C}{R} \tag{1.13}$$

For the circuit components R-L-C is:

$$Q = \frac{\omega L}{R} = \frac{1}{\omega C R} \tag{1.14}$$

Also, be written as:

$$Q = \frac{\omega}{BW} \tag{1.15}$$

Where, $\omega = \omega_r$ is series resonant frequency. Now we have the resonant frequency, bandwidth $(BW)$ and $Q$ related together the further relationship can be established with the quality factor of the electrical equivalent to the mechanical equivalent from the relation below from equations (1.13), (1.14) and (1.15) as:

$$Q = \frac{1}{\omega RC} = \frac{\sqrt{L}}{R\sqrt{C}} = \frac{\sqrt{\frac{L}{C}}}{R} \tag{1.16}$$

Now we can relate $Q$ by the formula compared with equation (1.7) where the resistance $R$ is equivalent to the viscous damping $\gamma$, inductance $L$ equivalent to the mass $m$ and capacitance $C$ equivalent $\frac{1}{k}$. However, in Figure 1.4, the circuit has a shunt capacitor $C_0$, and this causes the series resonant frequency $\omega_r = \omega_0$ to shift and so do the $Q$. As a result of this, a parallel resonant frequency $\omega_{pr}$ comes into play. Nevertheless, already mentioned before, we consider that the presence of all stray capacitances internal to the enclosure of the resonator into capacitor are included in $C_0$.Thus, the relation below gives the two resonant frequencies in series and parallel:

$$\omega_0^2 = \frac{1}{L_j C_j}, \omega_{pr}^2 = \frac{1}{L_j \frac{C_j C_0}{C_j + C_0}} \tag{1.17}$$

Where, $j$ is the different modes of acoustic vibration. This now presents the need to introduce a fix capacitor in series $C_t$, which helps the resonator always maintain a fix value of frequency of resonance. The modified expression with loaded capacitor than becomes [5]:

$$\frac{\omega_0 - \omega_{pr}}{\omega_0} = \frac{C_j}{2(C_0 + C_t)} \tag{1.18}$$

### 1.2.2 Realisation of Q factor in BAW resonators

The Q-factor obtained above with dissipation is an expression for a damped system represented in the form of motional parameters $R$, $L$ and $C$. When we come to implement this concept in real-life, a resonator consists of a mounted substrate, there is a leakage of energy into the substrate through the mounting support, and inevitably, they are due to electrodes damping and air damping. Nevertheless, for the resonator packed in a vacuum, the significant loss is because of an interaction between vibrations of the resonator with the mounted substrate. Understood as, the Q-factor of the quartz crystal resonator diminishes because of losses from the mounting arrangements, atmospheric effects, and electrodes. This phenomenon will be clear in equation (1.19).

Similarly, the different dissipative mechanisms that occur within the resonator as briefly mentioned before needs a consideration during the modelling stage for an acoustic resonator. However,

being specific about these losses i.e. usually inverse of Q-factor (as $1/Q$), in quartz crystal resonators, we can represent it as a summation of the dissipative mechanism as:

$$\frac{1}{Q} = \frac{1}{Q_{thermoelastic}} + \frac{1}{Q_{phonons-phonons}} + \cdots + \frac{1}{Q_{scattering}} + \frac{1}{Q_{holders}} + \frac{1}{Q_{TLS}} + \cdots \quad (1.19)$$

In the summation above particularly, there are two types of energy losses i.e. *intrinsic losses* in the material and *engineering losses*. The intrinsic losses in equation (1.19) includes the $\frac{1}{Q_{phonons-phonons}}$ terms related to interactions between thermal and acoustic phonons and $\frac{1}{Q_{thermoelastic}}$ is related to thermal gradients generated by the acoustic wave itself. These thermoelastic losses occur at lower frequencies to higher frequencies up to MHz. The engineering losses includes $\frac{1}{Q_{holders}}$ terms and includes those constraints induced because of mechanical activities of the resonator. Similarly, $\frac{1}{Q_{scattering}}$ is the diffraction losses relative to the surface condition of the material, and $\frac{1}{Q_{TLS}}$ where, *TLS* stands for *Two Level System* relates to an absorption because of the presence of pre-existing impurities and possible material defects. To minimize these engineering losses, an appropriate design and optimized manufacturing is necessary, where the high-quality quartz crystals used from a natural seed where the impurities can be collected on the edges of the quartz bar through an intense electric field through a sweeping process.

### 1.2.3 Relationship between Q-factor and temperature

The Q-factor expressed as in equation (1.12), and practically as equation (1.14), where the Q-factor and bandwidth has the inverse relation, the direct analysis of the system losses is possible to predict. To establish a relationship further to acoustics, an acoustic wave propagating in a solid, i.e. the coefficient of absorption of any sound wave $\alpha(\omega)$ characterising the variation of the amplitude of the wave with the propagation distance or the ratio of average dissipated energy to the incident energy is:

$$\alpha(\omega) = \frac{1}{2}\frac{Average\ dissipated\ energy}{Energy\ flow\ of\ the\ incident\ wave} \quad (1.20)$$

From Landau et al. [6], we have the relation, which connects this coefficient of absorption to Q-factor as:

$$Q = \frac{\omega}{2\alpha(\omega)V_\alpha} \quad (1.21)$$

Where, $V_\alpha$ is a group velocity of the wave.

The equations (1.20) and (1.21) mentions how the coefficient of absorption and relationship between quality factors in quartz crystal resonator exists. The dissipative mechanism in equation (1.19) shows the existence of temperature dependence. *El Habti et al.* [7] have shown the experimental variation of Q as a function of temperature from ambient temperature up to cryogenic temperatures. There are lots of predictions based on this Q-factor and temperature graph in [7], but for our work, we

concentrate on the interaction of the acoustic waves or acoustic phonons with thermal waves or thermal phonons at higher temperatures. There are the two propositions based on these interactions i.e. *Akhiezer's* proposition $\omega \cdot \tau \ll 1$ and *Landau-Rumer's* proposition $\omega \cdot \tau \gg 1$, where $\omega$ is the frequency and $\tau$ is the lifetime of the thermal phonons. For our work, we stick with the *Akhiezer's* proposition, which seems to explain the relationship between the Q-factor and temperature from 20 K to 300 K, which is also the near working temperature for our BAW quartz crystal resonator.

**Akhiezer's proposition:**

The validity of his model is based on when $\omega \cdot \tau \ll 1$, where the average lifetime of the thermal phonon between two successive phonon interactions i.e. acoustic and thermal phonons and is very small compared to the period of oscillation. For the temperature range of 20 K - 300 K, the absorption coefficient [7], is given by:

$$\alpha(\omega) \propto Tf^2 \tag{1.22}$$

To establish a clearer idea of the relationship, we insert equation (1.21) in (1.22) which gives:

$$Q \cdot f \propto \frac{2\pi^2}{TV_\alpha} \tag{1.23}$$

These relationships show that the product of Q-factor and frequency of resonance remains a constant. On the other hand, the independence of Q-factor and frequency can also be seen in Chapter 3 on Table 3.3 and Table 3.4 for different modes of vibrations where we have different frequencies of resonance and Q-factors. For a SC-cut quartz crystal resonator excited in mode-*C* we have at 5 MHz as:

$$Q \cdot f = 2.7 \cdot 10^6 \times 5 \cdot 10^6 = 1.35 \cdot 10^{13} \tag{1.24}$$

The independence of relationship between the Q-factor and frequency of resonance reveals in a different perspective in Chapters ahead where we have the experimental graphs showing the plot between the frequency fluctuation (Phase noise in our case) and the Q-factor. Similarly, the maximum limiting case for the intrinsic absorption exists at, $\omega \cdot \tau = 1$, where the intrinsic losses relates to $\omega_\tau$ by:

$$\frac{1}{Q} \propto \frac{\omega \cdot \tau}{1 + \omega^2\tau^2} \tag{1.25}$$

Where, $\tau = \tau_0 \exp\left(\frac{E_A}{k_B T}\right)$, with $\tau_0$ is the relaxation constant and $E_A$ is the activation energy, $k_B$ is the Boltzmann constant, and $T$ is the temperature.

### 1.2.4 Governing tensor equations of continuum mechanics for a piezoelectric material

The properties of piezoelectric materials are defined by elastic, dielectric and piezoelectric tensor components. Because of the inherent asymmetrical nature of piezoelectric materials and the fact that we want to predict different response directions, a tensor-based description of the properties of these

materials is unavoidable. Generally, these components are by far not constant; they depend on temperature, applied mechanical stress and electric field strength. Furthermore, they are amplitude dependent and become non-linear or even non-reversible when the applied signal stress or signal field amplitude exceeds a characteristic limit of the material.

It is a fact that we must deal with the directionality of the response of piezoelectric materials and consequently with tensors, which complicate engineering to some extent, however; on the other hand, it offers a great design potential for engineers in the development of piezoelectric devices.

We use Voigt notation for indices of all possible piezoelectric tensors (an example in Table 1.2), where we consider the propagation of plane wave through a piezoelectric material in any direction $\vec{n}(n_1, n_2, n_3)$ in the orthonormal form $(x_1, x_2, x_2)$ [8].

| *ij* or *kl* | 11 | 22 | 33 | 23 or 32 | 31 or 13 | 12 or 21 |
|---|---|---|---|---|---|---|
| *p* or *q* | 1 | 2 | 3 | 4 | 5 | 6 |

*Table 1.2: Voigt notation for representation of indices.*

For a purely mechanical problem in any solid, the equation of dynamics using the Einstein's convention for the summation of the repeated indices is:

$$\rho \frac{\partial^2 u_i}{\partial t^2} = \frac{\partial T_{ij}}{\partial x_j} \tag{1.26}$$

Where, $\rho$ is the mass density, $u_i$ is the elastic displacement, $T_{ij}$ is the stress tensor, $x_j$ is the component of vectors $(x_1, x_2, x_3)$ [9][10].

From Hooke's law, we have the expression of $T_{ij}$ as:

$$T_{ij} = c_{ijkl} \frac{\partial u_l}{\partial x_k} \tag{1.27}$$

Where $c_{ijkl} = c_{ijlk}$ is the elastic stiffness tensor and the equation of motion (1.26) expresses as:

$$\rho \frac{\partial^2 u_i}{\partial t^2} = c_{ijkl} \frac{\partial^2 u_l}{\partial x_j \partial x_k} \tag{1.28}$$

Hence, the solution of the wave equation is a sinusoidal progressive plane wave, given by:

$$u_i = u_i^0 e^{-j\omega\left(\frac{n_j x_j}{v}\right)} e^{j\omega t} \tag{1.29}$$

Where, $\frac{n_j x_j}{v}$ is the propagative term, $u_i^0$ is the amplitude of the wave, $n_j$ is the component of the unit vector, $v$ is the wave speed and $\omega$ is the pulsation. Therefore, for a purely electrical problem, from Maxwell's equation of the electric field we have:

$$E_i = -\frac{\partial \Phi}{\partial x_i} \tag{1.30}$$

Where, Φ is a scalar potential in the electric field whose solution is an exponential:

$$\Phi = \Phi_0 e^{-j\omega\left(\frac{n_j x_j}{v}\right)} e^{j\omega t} \tag{1.31}$$

The potential applied creates an electrical induction given by the Poisson equation:

$$\frac{\partial D_j}{\partial x_j} = \rho_e \tag{1.32}$$

Where, $\rho_e$ is a charge density.

In case of any conductor, the equation of conservation of electric charges is:

$$\frac{\partial J_i}{\partial x_i} + \frac{\partial \rho_e}{\partial t} = 0 \tag{1.33}$$

Where, $J_i$ is a current density.

The piezoelectricity comprises the definition of both the electrical and mechanical expressions. Now to be clearer about the propagation of electrical and mechanical waves in the quartz or any piezoelectric material we need to establish a complete description, which is possible by coupling the contributions of the equations above. From the Gibbs free energy equation (details on [1]), we have:

$$\Delta S_\alpha = \alpha_\alpha^E \Delta \boldsymbol{T} + s_{\alpha\beta}^E \Delta T_\beta + d_{i\alpha} \Delta E_i \tag{1.34}$$

$$\Delta D_i = p_i^T \Delta \boldsymbol{T} + d_{i\alpha} \Delta T_\alpha + \varepsilon_{ik}^T \Delta E_k \tag{1.35}$$

Where, $\boldsymbol{T}$ is bold for temperature and the non-bold with indices represents stress tensor component, $i, k$ = 1, 2, 3 and $\alpha, \beta$ = 1, 2….,6 (Voigt's notation), $\alpha_\alpha^E$ are the thermal expansion coefficients, $s_{\alpha\beta}^E$ the elastic compliances at constant electric field, $d_{i\alpha}$ the piezoelectric constants, $p_i^T$ the pyroelectric coefficients, and $\varepsilon_{ik}^T$ the permittivities at constant stress. In isothermal form, there are four sets of equations called the piezoelectric equations or piezoelectric constitutive equations with tensors to fourth ranks as [8]:

$$\begin{Bmatrix} T_{ij} = c_{ijkl}^D S_{kl} - h_{kij} D_k \\ E_i = -h_{ikl} S_{kl} + \beta_{ik}^S D_k \end{Bmatrix} \tag{1.36}$$

$$\begin{Bmatrix} S_{ij} = s_{ijkl}^D T_{kl} + g_{kij} D_k \\ E_i = -g_{ikl} T_{kl} + \beta_{ik}^T D_k \end{Bmatrix} \tag{1.37}$$

$$\begin{Bmatrix} T_{ij} = c_{ijkl}^E S_{kl} - e_{kij} E_k \\ D_i = e_{ikl} S_{kl} + \varepsilon_{ik}^S E_k \end{Bmatrix} \tag{1.38}$$

$$\begin{Bmatrix} S_{ij} = s_{ijkl}^E T_{kl} + d_{kij} E_k \\ D_i = d_{ikl} T_{kl} + \varepsilon_{ik}^T E_k \end{Bmatrix} \tag{1.39}$$

Where, $T_{ij}$ as stress tensor, $c_{ijkl}^{D}$ elastic constants tensor with constant electrical induction, $h_{kij}$ piezoelectric constant tensor in $V/m$, $S_{kl}$ deformations tensor, $\beta_{ik}^{S}$ impermeability tensor at constant strain, $s_{ijkl}^{D}$ flexibility constants tensor at constant induced potential, $g_{kij}$ piezoelectric constant tensor in $Vm/N$, $\beta_{ik}^{T}$ impermeability tensor at constant stress, $c_{ijkl}^{E}$ elastic constant tensor at constant electric field, $\varepsilon_{ik}^{S}$ a dielectric permittivity constant tensor with constant deformation, $s_{ijkl}^{E}$ flexibility constant tensor at constant electric field, $\varepsilon_{ik}^{T}$ a dielectric permittivity constant tensor with constant constraints. These piezoelectric constitutive equations represent a form of matrixes using Voigt's notation as in Table 1.2. There are piezoelectric stress constant, $h$ constant (not specifically named), strain constant and voltage constant i.e. $e_{ij}$, $h_{ij}$, $d_{ij}$ and $g_{ij}$ respectively. We represent them as:

$$e_{ip} = d_{iq}c_{qp}^{E} \tag{1.40}$$

$$h_{ip} = g_{iq}c_{qp}^{D} \tag{1.41}$$

$$d_{ip} = g_{kp}\varepsilon_{ik}^{T} \tag{1.42}$$

$$g_{ip} = d_{kp}\beta_{ik}^{T} \tag{1.43}$$

Where, the indices $p \to \alpha$ and $q \to \beta$ have the definition in Table 1.2.

We consider one pair of tensor equation (1.38) from the four sets of tensor equations. This pair of equation lacks the viscoelastic loss term $\eta_{ijkl}$. Hence, we rewrite the equation of tensor including the viscoelastic term as:

$$T_{ij} = c_{ijkl}^{E}u_{k,l} - e_{kij}E_k + \eta_{ijkl}\dot{u}_{k,l} \tag{1.44}$$

Here, the deformation tensor replaces by the expression $u_{k,l}$.

The equations represents in Christoffel's form [8] i.e. for $\frac{\partial u_i}{\partial x_j} \equiv u_{i,j}$ which represents the partial derivative of $u_i$ w.r.t $x_j$. Therefore, from equations (1.26), (1.32) and (1.38), represents the tensor equations as:

$$\begin{Bmatrix} T_{ij,j} = c_{ijkl}^{E}u_{k,jl} + e_{kij}\Phi_{,kj} + \eta_{ijkl}\dot{u}_{k,l} = \rho\ddot{u}_i \\ D_{j,j} = e_{jkl}u_{k,jl} - \varepsilon_{ik}^{S}\Phi_{,kj} \end{Bmatrix} \tag{1.45}$$

**Akhiezer regime:**

In Akheiser regime [11], the wave equation bases on Hooke's law, from equation (1.26) and (1.28), we have:

$$\rho\frac{\partial^2 u_i}{\partial t^2} = c_{ijkl}\frac{\partial^2 u_l}{\partial x_j \partial x_k} + \eta_{ijkl}\frac{\partial^3 u_l}{\partial x_j \partial x_k \partial t} \tag{1.46}$$

Where, $c_{ijkl}$ is the constant for relaxed and un-relaxed elastic stiffness, $\eta_{ijkl}$ is effective viscosity. We now examine any symmetrical solid, that is to say an isotropic solid whose description requires a

viscosity coefficient specific to compression $\chi$ and specific to shear stress $\eta$, where the Lamé parameters for an isotropic solid $\lambda = c_{11} - 2c_{44}$ and $\mu = c_{44}$ makes the expression for a tensor equation for an isotropic solid as:

$$T_{ij} = (c_{11} - 2c_{44})\delta_{ij}S + \chi\delta_{ij}\frac{\partial S}{\partial t} + 2c_{44}S_{ij} + 2\eta\frac{\partial S_{ij}}{\partial t} \tag{1.47}$$

The expression deduces in the form with reference to equation (1.46) we have:

$$\begin{aligned}\frac{\partial T_{ij}}{\partial x_j} = (c_{11} - 2c_{44})\frac{\partial S}{\partial t} + \chi\frac{\partial^2 S}{\partial x_i \partial t} + c_{44}\left(\frac{\partial^2 u_i}{\partial x_j^2} + \frac{\partial^2 u_j}{\partial x_i \partial x_j}\right) \\ + \eta\left(\frac{\partial^3 u_i}{\partial x_j^2 \partial t} + \frac{\partial^3 u_j}{\partial x_i \partial x_j \partial t}\right)\end{aligned} \tag{1.48}$$

Where, we have, $S = \frac{\partial u_j}{\partial x_j}$

$$\rho\frac{\partial^2 u_i}{\partial t^2} = (c_{11} - c_{44})\frac{\partial S}{\partial x_i} + c_{44}\frac{\partial^2 u_i}{\partial x_j^2} + (\chi + \eta)\frac{\partial^2 S}{\partial x_i \partial t} + \eta\frac{\partial^3 u_i}{\partial x_j^2 \partial t} \tag{1.49}$$

The equation in the simplified form is if we consider only the longitudinal plane wave $x_1 (i = j = 1)$:

$$\rho\frac{\partial^2 u_1}{\partial t^2} = c_{11}\frac{\partial^2 u_1}{\partial x_1^2} + (\chi + 2\eta)\frac{\partial^3 u_1}{\partial x_1^2 \partial t} \tag{1.50}$$

Considering the plane wave solution as $u_1 = u_1' e^{-\alpha_L x_1} e^{i\omega\left(t - \frac{x_1}{V_L}\right)}$ we have, for longitudinal wave, for $\omega\tau \ll 1$:

$$V_L = \sqrt{\frac{C_{11}}{\rho}} \text{ and } \tau = \frac{\chi + 2\eta}{c_{11}} = \frac{\chi + 2\eta}{\rho V_L^2} \tag{1.51}$$

$$\alpha_L = \frac{\omega^2\tau}{2V_L} = \frac{\omega^2(\chi + 2\eta)}{2\rho V_L^3} = 2\pi^2\frac{\chi + 2\eta}{\rho V_L^3}f^2 \tag{1.52}$$

Where, $V_L$ is the speed of the longitudinal wave and $\alpha_L$ is the attenuation of the longitudinal wave. The equation of propagation (1.49) for transverse wave polarises at $x_2 (i = 2)$ and propagates along $x_1 (j = 1)$, is of the form $(\partial/\partial x_2 = 0)$, and $u_2 = u_1' e^{-\alpha_T x_1} e^{i\omega(t - x_1/V_T)}$ is the plane wave solution, and we have, the speed of the transverse wave $V_T$ as:

$$V_T = \sqrt{\frac{C_{44}}{\rho}} \ , \qquad \tau = \frac{\eta}{\rho V_T^2} \ , \qquad \alpha_T = 2\pi^2\frac{\eta}{\rho V_T^3}f^2 \tag{1.53}$$

Where, $V_T$ is the speed of the transverse wave and $\alpha_T$ is the attenuation of the transverse wave. The expression $\alpha_T$ alone intervenes the shear coefficient. This attenuation coefficient in a path of a wavelength is inversely proportional to the quality factor:

$$\alpha_T\lambda \cong \pi\omega\tau = \frac{\pi}{Q} \tag{1.54}$$

## 1.3 Background of BAW resonators in FEMTO-ST

In order to characterize high performance, ultra-stable 5 MHz BAW SC-cut quartz crystal resonator for space applications the institute FEMTO-ST (Franche-comté Electronique Mécanique Thermique et Optique- Science et Technologie) and CNES (Centre Nationale d'Etudes Spatiales), launched the research work with the initiative of better understanding the intrinsic origin of $1/f$ flicker noise in quartz crystal resonators [12]. They promulgated this initiative by fabricating several resonators from the same mother quartz crystal, as shown in Figure 1.9 below, in partnership with many European manufacturers. From the fabricated resonators, we measured the motional parameters and the unloaded Q-factor of the resonators at C-mode of vibration. On an average, the Q-factors are 2.5 million at an inversion point temperature around 80°C for a good number of resonators. All these resonators imply the use of the proven Tiersten plano-convex model for fabrication. Similarly, for realizing the resonator, regarding the dimension of this mother block, it is 220 mm in Y-axis, 110 mm in X-axis and 36 mm Z-axis. The red-marks on the mother block shows the Y-cut sliced parts used for evaluating the dislocations using X-rays method. In large, it was possible to fabricate around 100 and plus resonators in total from this mother block , where an example of few cut plates can be seen in Figure 1.10 along with an example of fabricated quartz resonator.

*Figure 1.9: Mother quartz crystal.*

Likewise, we have tabled the results in Chapter 3 for resonant frequencies of the fabricated resonators regarding various harmonic and anharmonic modes with the comparison of experimental resonant frequencies with those resonant frequencies obtained from Tiersten's formula to expand the idea of differences observed between practical and experimental aspects of resonators.

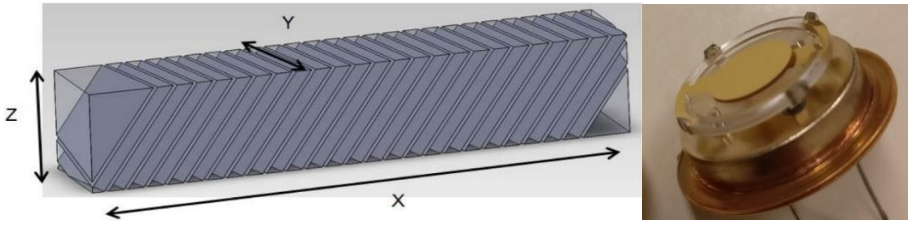


*Figure 1.10: Left: SC-cut quartz pieces (blanks) before processing.*
*Right: Example of a processed blank mounted resonator.*

## 1.4 Basics in Metrology

Stability and Frequency control of any time and frequency device like resonator at high frequency application is a necessity to compete with the modern world of technology. With the advancement in technical world, particularly, the world of electronics, the noise of the components affects an electronic system it constitutes. The noise affects all the elements of measurement chain and disturbs the precision. For e.g. let us consider a clock signal $x(t)$ with a highly pure sinusoidal signal. Ideally, we have [13]:

$$x(t) = x_0 \cos(2\pi f_0 t) \tag{1.55}$$

We will have:

$$x(t) = x_0[1 + \alpha(t)] \cos[2\pi f_0 t + \varphi(t)] \tag{1.56}$$

where, $x_0$ is the amplitude of the peak voltage, $f_0$ is the carrier frequency, $\alpha(t)$ is the deviation in amplitude from its nominal value, $\varphi(t)$ represents the deviation of the phase from its nominal value. If we plot the phase with the function of time, we will have:

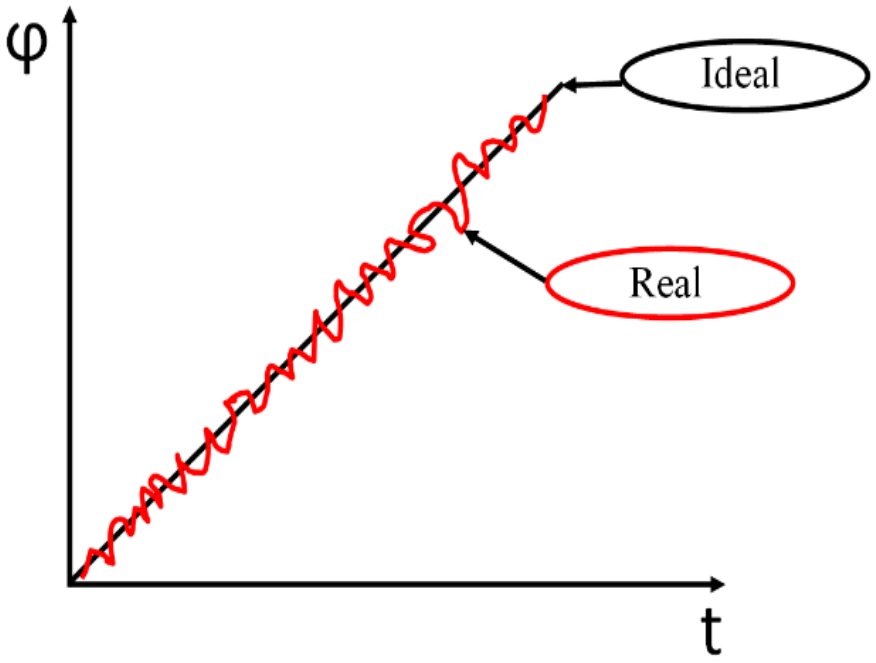


*Figure 1.11: Phase vs time graph for ideal and real phases of the pure sinusoidal signal.*

We can see in Figure 1.11 as from the equation (1.56) the value of instantaneous frequency $\omega_0 = 2\pi f_0 t$ is given by $\left(\omega_0 + \frac{d\varphi(t)}{dt}\right)$ where $\varphi(t)$ changes the phase as a function of time from its nominal value. When we see the spectrum of an ideal and real signal, we have in Figure 1.12,

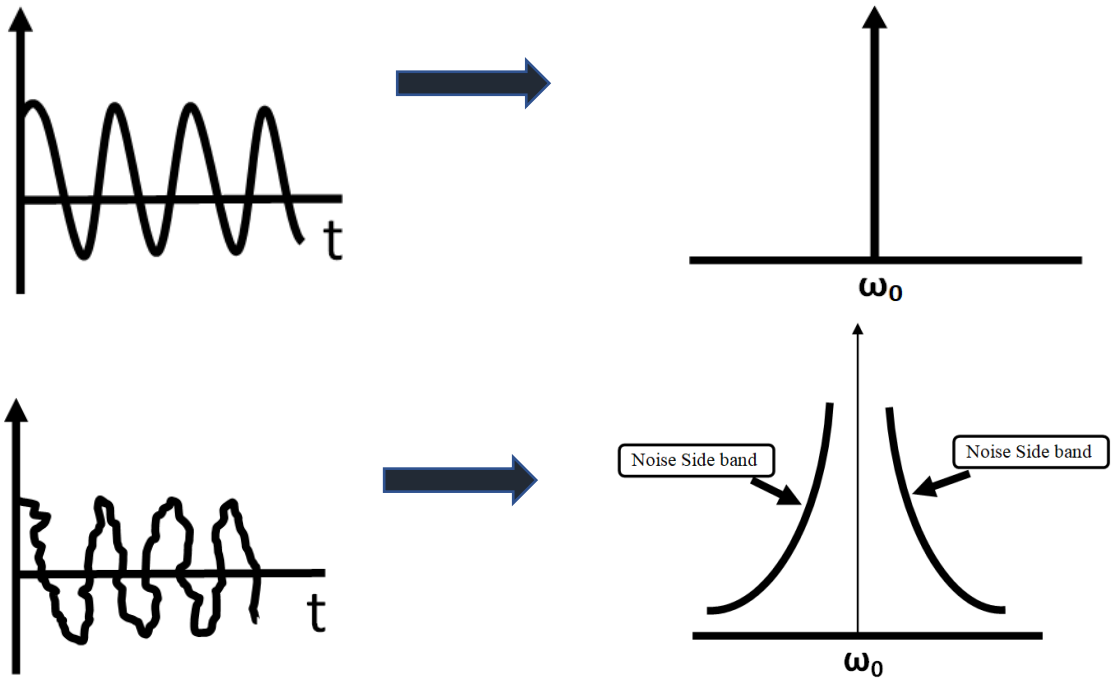


*Figure 1.12: Up: From left to right, time and frequency domain ideal signal*
*Down: From left to right, time, and frequency domain real noisy signal.*

As we can see in Figure 1.12 (Up), instead of having a delta function at $\omega_0$ which corresponds to $x_0 \cos(\omega_0 t)$, we have additional spurs on the either sides, corresponding to the modulation terms $\varphi(t)$. In a strictly significant way $\varphi(t)$ is sinusoidal. Therefore, because of noise (Phase noise), you have carrier plus noise side bands (spurs) in Figure 1.12 (down) instead of having a pure carrier signal.

***Noise side bands*:** In radio communications, a side band is a band of frequencies higher than or lower than the carrier frequency $\omega_0$ containing power because of modulation process. The sidebands contain all the Fourier components of the modulated signal except the carrier. In a conventional transmission, the carrier and both side bands are present. The transmission where only one side band transmits, terms as SSB (Single Side Band). Since, the bands are mirror images which side band is used is the matter of convention. In SSB, the carrier is suppressed significantly reducing the power without affecting the information in the sideband.

Likewise, when we see these things in time domain, the ideal signal propagates and let us say is sinusoid, and then we may have the representation of the effect of noise like in Figure 1.13. Hence, as far as the noise is concerned it is going to change the zero crossings of an ideal sinusoid. These noises resemble frequency fluctuations, which corresponds to the fluctuations of period, and almost all the frequency measurements are the measurements of the phase or period fluctuations. For e.g. most of the frequency, counters detect the zero crossing of the sinusoidal voltage, which is the point at which the voltage is most sensitive to phase fluctuation as shown in Figure 1.13. However, the sad part is that there is always a fluctuation in the system that causes the zero crossing to shift.

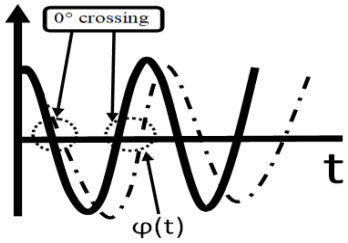


*Figure 1.13: Schema of zero degree crossing for ideal sinusoid as an effect of $\varphi(t)$.*

**Effects of phase noise (fluctuations) in radio communications:**

1. *Reciprocal mixing:*

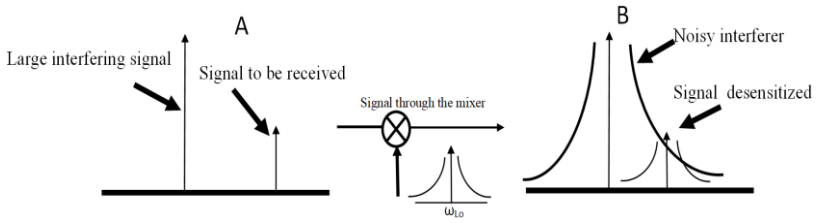


*Figure 1.14: Signal transmit and receiving affected by noise.*

Reciprocal mixing is the form of noise that occurs within receivers as a result of the phase noise which appears on signals. The phase noise spreads out on either side of the signal and causes disturbance to the main signal. As in Figure 1.14 if the interferer in the vicinity is large, enough as A and the phase noise side bands are large enough, this could naturally desensitize the receiver as in B.

2. *Transmitter affecting the receiver sensitivity:*

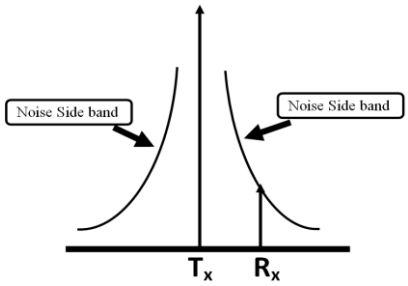


*Figure 1.15: Effect on Transmitter because of noise.*

In Figure 1.15, $T_x$ and $R_x$ are the carriers of transmitter and receivers, respectively. In reference to the figure, let us suppose that we have a strong transmitter signal, where, a receiver band is close to it. Then, for a full duplex system (we receive and transmit at the same time) if the phase noise of the transmitter is very large it will affect the receiver sensitivity. However, it need not to be the transmitter in the same system, for e.g. we can just assume someone is trying to make a phone call next to you, he/she could have very powerful $T_x$, it can be something nearby affecting the receiver as shown in Figure 1.15. Nevertheless, there are many possible effects of phase noise and further discussion is not the objective of this thesis. Therefore, our focus will be more on discussing the measurement strategy of frequency fluctuations.

## 1.5 Statistical method of generalizing frequency fluctuations

The random nature of the instabilities or fluctuations forces a need for the deviation (Phase) to represent through a spectral density plot. The term spectral density [14] describes the power distribution (mean square deviation) as a continuous function, expressed in units of energy within a given bandwidth. We will try to represent it more mathematically and build a physical meaning to our system.

### 1.5.1 Power Spectral Density (PSD)

We suppose $X(t)$ from equation (1.56) to be a random process, where we establish a truncated realisation of $X(t)$ as:

$$X_T(t,\lambda_i) = \begin{cases} X(t,\lambda_i), & |t| \leq \frac{T}{2} \\ 0, & otherwise \end{cases} \tag{1.57}$$

Where, $\lambda_i$ is the $i^{th}$ realisation of the random signal $X_T$. Now, we will try to establish the bigger picture of this mathematical approach based on Figure 1.11 and Figure 1.12.

In the Figure 1.16 B, C and D the short form F.T stands for Fourier transform. Now, from Figure 1.16, we consider a single small frequency band from the Fourier spectrum and take an average of all of these. Because of this, we end up with one frequency domain representation, which is going to be an expected value of the average. Hence, we can define the power spectral density in the form as:

$$S_x(f) = PSD_x(f) = \lim_{T\to\infty}\left\{\frac{1}{T}|X_T(t,\lambda)|^2\right\} \tag{1.58}$$

This is the general expression for power spectral density mathematically. On the other hand, to be more precise for application in noise, Wiener-Khintchine theorem evaluates the Fourier transform of the autocorrelation function $\Gamma_{XX}(\tau)$ to define the noise spectral density as:

$$S_X(f) = TF[\Gamma_{XX}(\tau)] = \int_{-\infty}^{+\infty} \Gamma_{XX}(\tau).\exp(-j2\pi f\tau)\, d\tau \tag{1.59}$$

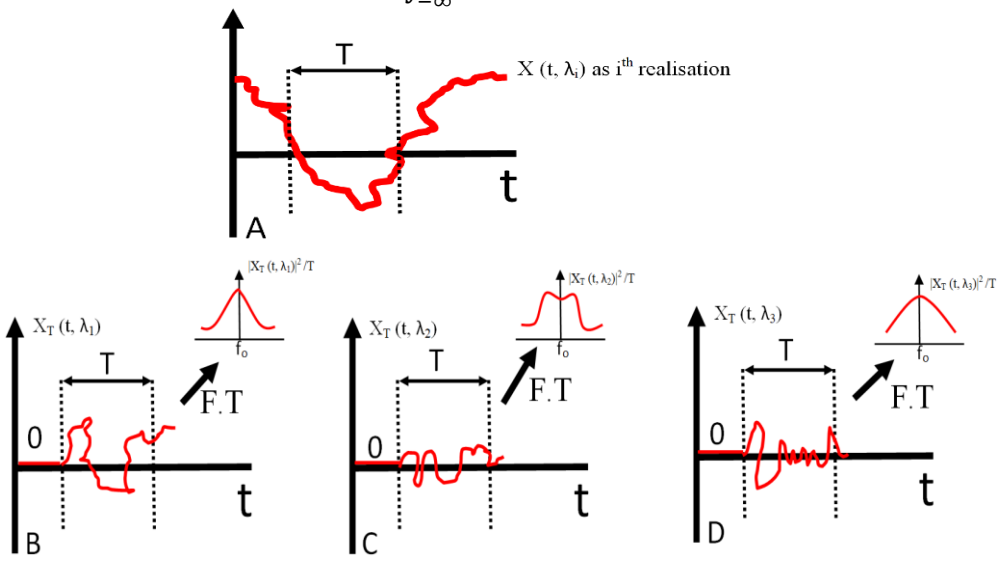


*Figure 1.16: Different realisation of the random signal.*

It is a need for us to link this spectral density to the time and frequency domain, which makes possible using Parseval's theorem. Parseval's theorem shows that the normalised power of a signal in one domain is the same for the other domain. Hence, the total power is obtained by the summation of the contributions of different harmonics and independent of the domain (either time or frequency) given as:

$$P = \lim_{T\infty} \frac{1}{T} \int_{-T/2}^{+T/2} x^2(t)dt = \int_{-\infty}^{+\infty} S_\varphi(f)df \tag{1.60}$$

Where, $S_\varphi(f)$ is a power spectral density representing the power distribution in the frequency domain. The PSD provides information of the power distribution and the temporal variations of the signal in the frequency domain i.e. if the power is concentrated in the low frequencies it shows slow variations and conversely at high frequencies, high variations. Therefore, by the help of the PSD of frequency fluctuation formulas it is easier to determine the proper functioning of the resonator, identify it and troubleshoot future errors in fabrications. Serially, we will now establish below a base for fluctuation measurements in Bulk Acoustic Wave (BAW) quartz crystal resonator.

**Single side band phase noise measurement:**

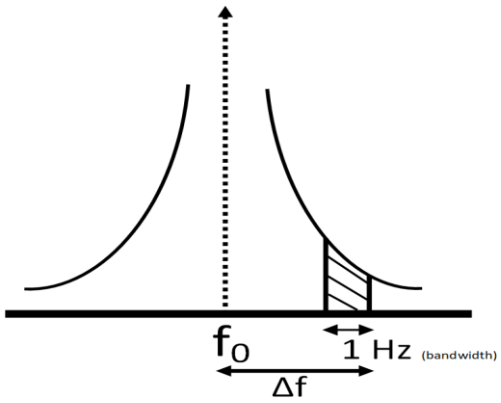


*Figure 1.17: Spectrum representing the noise and offset frequency.*

Let us consider the nominal frequency to be $f_0$, $\varphi(t)$ is going to create noise on side bands. We are going to define the noise in single side bands as the ratio of the power spectral density at an offset frequency $\Delta f$ as in Figure 1.17 i.e. the noise power in 1 Hz bandwidth at an offset between $\Delta f$ and $f_0$. Now, taking the ratio of that noise power to the power at $f_0$ which is the carrier power, represented as whole below:

$$\mathscr{L}(\Delta f) = 10\log_{10}\left[\frac{P_{1\,Hz}(f_0+\Delta f)}{P_s(carrier)}\right] \tag{1.61}$$

This is the definition of the single side band power and its unit is $dBcHz^{-1}$ (decibel below carrier per hertz). There are systems that measure phase noise in different bandwidths other than 1 Hz. To understand the importance of the phase noise of a system, its impact needs an evaluation on an offset frequency band. This offset is nothing but a distance in frequency from the carrier frequency. If the noise of a signal is constant as a function of the frequency on the offset band, then the noise level scales

by adding $10\log_{10}(\Delta f)$ to the level measured in the band of Hz. For example, if the noise level shown in a bandwidth of 1 kHz, then the noise level means to be about 30 dB higher than bandwidth of 1 Hz. (*This concept of phase noise measurement is obsolete and no longer an IEEE definition for phase noise measurement the new concept is detailed below in section (1.6)).*

**Amplitude noise**

It has a negligible influence for the noise in resonators. The noise in the amplitude always remains in the amplitude of the signal and does not affect the phase of the carrier signal. On some circumstances, the amplitude noise and the phase noise are added for e.g. the white additive noise has both amplitude and phase noise added. These kinds of white noise decompose and separate as amplitude and phase noise at a gap of -3dB from the main white noise level. These days it has been possible to diminish the amplitude noise technically, like, an oscillator today comes being amplitude stabilized.

### 1.5.2 Different kinds of intrinsic noises in the electronic system

We have already mentioned phase noise with the most significant ones to our resonator system; likewise, it is equally necessary to have a knowledge in the intrinsic noise that is prevalent in an electronic system. The kind of intrinsic noise we are working within our thesis is the $1/f$ flicker noise. Particularly, intrinsic noises can be categorised as reducible kinds and non-reducible kinds. For example, thermal noise and shot noise are the kinds of non-reducible noises and generation-recombination and $1/f$ flicker noise are the kinds of reducible noise.

**Thermal noise**

This noise has a resistive origin. It also has the bigger picture in electronic transformers namely "Copper or ohmic losses". This form of noise, also referred to as Johnson Nyquist Noise [15], [16] arises because of thermal agitation of the charge carriers-typically electrons in a conductor. As the temperature, and hence the agitation of the charge carriers increases so does the level of noise. This noise is the major form of noise experienced in the low noise amplifiers and the like. To reduce it, very high-performance amplifiers, for e.g. those used for radio astronomy, etc., have been operated at very low temperatures.

Thermal noise occurs regardless of the applied voltage where the charge carriers vibrate because of the temperature. It appears in the electronic circuit regardless of the quality of the component used. The noise level is dependent upon the temperature and the value of the resistance. Therefore, the only way to reduce the thermal noise content is to reduce the temperature of operation or reduce the value of the resistors in the circuit. Other forms of noise might also be present; therefore, the choice of the resistor type may play a part in determining the overall noise level, as the different types of the noise will add together. In addition to this, thermal noise is only generated by the real part of an impedance i.e. resistance, the imaginary part does not generate noise.

Generally, thermal noise is effectively a white noise and extends over a wide power spectrum. The noise power is proportional to the bandwidth. It is therefore possible to define a generalised Power Spectral Density (PSD), $S_V(f)$, of the voltage noise $V_n$ within a given bandwidth $\Delta f$:

$$S_V(f) = \frac{\overline{V_n^2}}{\Delta f} = 4k_B TR \tag{1.62}$$

Where $k_B$ is the Boltzmann constant i.e. $1.38 \cdot 10^{-23} J.K^{-1}$ and $R$ is the resistance in ohms. In the same way the PSD of the current noise $I_n$ is:

$$S_I(f) = \frac{\overline{I_n^2}}{\Delta f} = \frac{4k_B T}{R} \tag{1.63}$$

Therefore, by the help of these formulas we can predict the amount of voltage and current noise of any electric circuit with resistance.

**Shot noise**

It is a kind of white noise whose spectral density is because of random fluctuations of the DC electric current that has an origin from the flow of discrete charges. This noise is less significant in comparison to other intrinsic noises like Johnson-Nyquist noise and Flicker noise. In the contrary, shot noise is independent of temperature and frequency, in contrast to Johnson-Nyquist noise, which is proportional to temperature. For e.g. if N is the number of charge carriers passed during an interval of time $\Delta t$:

$$\bar{N} = \frac{I}{q} \cdot \Delta t \tag{1.64}$$

Where, $I$ is an average current, $q = 1.6 \cdot 10^{-19} C$ is the charge in Coulomb. Therefore, the shot noise has an expression of PSD of current noise as [15] [16]:

$$S(I_n) = \frac{\overline{I_n^2}}{\Delta f} = 2qI \tag{1.65}$$

**Generation and recombination noise**

The name itself resembles the carrier generation and carrier recombination, the process by which the mobile charge carriers (electrons and holes) creates and eliminates. This noise relates to the fluctuations in the number of charge carriers due to non-deterministic generation and recombination of electron-hole pairs. The crystalline defects of any semiconductor material in its bandgap are the possible origin for this kind of noise. This kind of noise generates a random signal whose amplitude is inversely proportional to the semiconductor volume. The PSD of generation and recombination noise is:

$$S(f) = \frac{4 \cdot \tau \cdot \overline{\delta N^2}}{1 + \omega^2 \cdot \tau^2} \tag{1.66}$$

Where, $\omega$ is the pulsation of the signal, $\overline{\delta N^2}$ is the variance of fluctuation, $\tau$ is the carrier lifetime of either majority or minority carrier of the semiconductor material.

**$1/f$ Flicker noise**

It is a kind of electronic noise with the PSD being proportional the inverse of frequency as $1/f$. Widely known as "Flicker" it is sometimes referred to as pink noise or just $1/f$ noise. In 1925, J.B Johnson published his research of voltage drop fluctuations in vacuum tubes [17]. Following the inconsistency in results by Schottky, Johnson proposed a theory for small shot-effect (today called shot noise), for low frequencies. Later, Schottky explained the work regarding Johnson's findings on physical meaning for the surface of cathodes. Hence, Johnson than compared the voltage fluctuation to the irregularity in the brightness of light- known as flicker and he named it Flicker effect, modern day called as Flicker noise or $1/f$ noise. It is omnipresent in almost all electronic devices. Usually in electronic devices, it shows up as a low-frequency phenomenon, since higher frequencies are taken over by white noises from other sources. The PSD of the $1/f$ noise is:

$$S(f) = \frac{K \cdot I^{\beta}}{f^{\alpha}} \tag{1.67}$$

Where, *K* is the factor dependent on the environment in which the current in the device propagates. Hence, we will not be discussing more about flicker noise in this chapter because in chapters ahead we have a whole information explaining the origin and scientific contribution in the research of flicker noise in electronic and non-electronic domain from various researchers around the world.

## 1.6 Fluctuations measuring basics in Time domain and Frequency domain

### 1.6.1 Time domain characteristics

Characterisation in time domain is the measure of stability of the fluctuations of frequency and phase as a function of time [18]. The frequency measurements repeat several times i.e. $t_p$ to $t_{p+1}$ for the sampling frequencies from $\bar{y}_p$ and $\bar{y}_{p+1}$. The Allan variance gives as:

$$\sigma_y^2(\tau) = \frac{1}{2}\langle\left(\bar{y}_{p+1} - \bar{y}_p\right)^2\rangle \tag{1.68}$$

Where, $\left(\bar{y}_{p+1} - \bar{y}_p\right)$ is the differences between pairs of successive measurement of, $\bar{y}_p = \frac{f_p - f_0}{f_0}$ is the relative frequency fluctuations for $p$ samples and $\langle\ \ \rangle$ denotes the time average of an infinite number of $\left(\bar{y}_{p+1} - \bar{y}_p\right)^2$.

### 1.6.2 Frequency domain characteristics

The measure of frequency instability is the spectral density of fractional frequency fluctuations, $S_y(f)$, given by:

$$S_y(f) = y_{rms}^2(f).\frac{1}{BW} \tag{1.69}$$

Where, $y_{rms}(f)$ is the rms fractional frequency deviation as a function of Fourier frequency, *BW* is the width of the frequency band in Hz and the units of $S_y(f)$ are $Hz^{-1}$.

The measure of phase instability can be characterised by the power spectral density of phase fluctuation, $S_\varphi(f)$ given by:

$$S_\varphi(f) = \varphi^2(f)\frac{1}{BW} \tag{1.70}$$

The unit of $S_\varphi(f)$ are $rad^2Hz^{-1}$.

The spectral densities $S_y(f)$ and $S_\varphi(f)$ are one sided since the Fourier frequency $f$ ranges from 0 to $\infty$ and includes fluctuations from both the upper and lower sidebands of the carrier. Moreover, in fact from the autocorrelation function, the spectral density of noise is a real and even function. $S_\varphi(f)$ is the quantity used in metrological application; however, $\mathscr{L}(f)$ is much popular in use, pronounced as "$el\ of\ f$" and defined classically as:

$$\mathscr{L}(f) = \tfrac{1}{2}S_\varphi(f) \tag{1.71}$$

In decibels:

$$\mathscr{L}(f) = S_\varphi(f) - 3\ dB \tag{1.72}$$

The unit of $\mathscr{L}(f)$ is $dBcHz^{-1}$ which stands for "decibel below carrier" per hertz.

Similarly, the exact definition by IEEE would be the ratio of power in one sideband, to the phase modulation by noise in 1 Hz bandwidth to the total signal power (carrier and sidebands) as:

$$\mathscr{L}(f) = \frac{power\ density\ in\ one\ phase\ noise\ modulation\ sideband,per\ Hz}{total\ signal\ power} \tag{1.73}$$

This definition is obsolete and not in use these days for various ambiguous issues for a number of reasons [13].

The frequency fluctuations $S_y(f)$ represents in phase fluctuations $S_\varphi(f)$ in terms of $S_x(f)$ which is the PSD of $x(t)$ as:

$$S_x(f) = x^2(f)\ \frac{1}{BW} \tag{1.74}$$

Where, we have:

$$S_x(f) = \frac{1}{4\pi^2 f_0^2}S_\varphi(f) \tag{1.75}$$

$$S_y(f) = \frac{f^2}{f_0^2}S_\varphi(f) \tag{1.76}$$

From the experimental measurements and theories, regarding the power spectrum fluctuation and distribution in resonators, the fluctuations of spectrum have a power law nature an example of which can be seen in Figure 1.18 and represents as:

$$S_y(f) = \sum_{i=-1}^{+2} h_i \cdot f^i \tag{1.77}$$

And we have:

$$S_{\varphi}(f) = \sum_{j=0}^{-3} b_j \cdot f^j \tag{1.78}$$

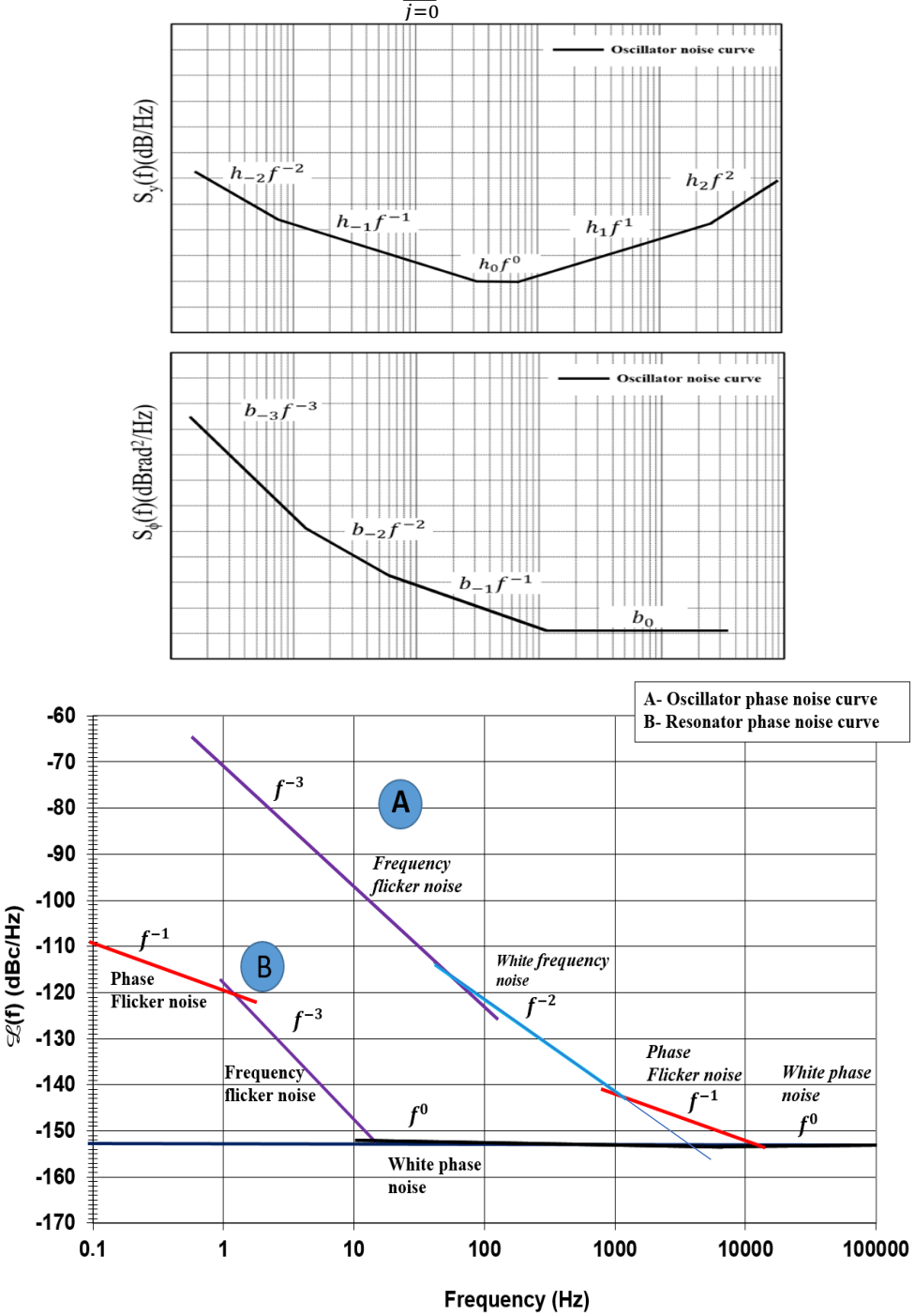


*Figure 1.18: The power laws for noise in oscillator and resonator.*

### 1.6.2.1 Frequency flicker noise

These are the kind of noise characterised by the PSD of phase noise proportional to the inverse of the frequency and originates from the flicker noise process which modulates the frequency of the oscillator.

Below is the brief in Table 1.3 and details on the kind of noise as we have shown in the Figure 1.18:

| Noise type | $S_\varphi(f)$ | $S_y(f) \leftrightarrow S_\varphi(f)$ |
|---|---|---|
| Frequency Flicker | $b_{-3}f^{-3}$ | $h_{-3}f^{-3} = \frac{b_{-3}}{f_0^2}f^{-2}$ |
| White frequency noise | $b_{-2}f^{-2}$ | $h_{-2}f^{-2} = \frac{b_{-2}}{f_0^2}f^{-1}$ |
| Phase flicker noise | $b_{-1}f^{-1}$ | $h_{-1}f^{-1} = \frac{b_{-1}}{f_0^2}f^{0}$ |
| White phase noise | $b_0 f^0$ | $h_0 f^0 = \frac{b_0}{f_0^2}f^2$ |

*Table 1.3: Classical noise slope.*

#### *1.6.2.2 White frequency noise*

This noise has the origin to the thermal fluctuations of a resonator, to white noise in the oscillator loop, or to the white noise of the signal at the VCO (Voltage Controlled Oscillator) input [13] of the oscillator. The phase noise associated to white frequency noise is proportional to the slope.

#### *1.6.2.3 Phase flicker noise*

The resonator or the other unknown sources may generate this kind of noise whose PSD is proportional to $1/f$, which modulates the phase of the microwave signal.

#### *1.6.2.4 White phase noise*

This is the thermal noise floor of the noise measurement bench. These are the common form of noise seen because of electron hole recombination in semi-conductor materials. The white phase noise present generates a random signal with amplitude and is inversely proportional to the volume of the semi-conductor material.

## 1.7 Leeson's effect for Phase noise in resonator

From Leeson's theory [13] [19], the frequency fluctuations of oscillator links to the phase fluctuations $\Delta\theta$ and the amplifier of the oscillation loop. Hence, any fluctuations in phase will result in the relative frequency fluctuation in the oscillator output as given by the relation:

$$\frac{\Delta f}{f_0} = \frac{\Delta\theta}{2Q} \tag{1.79}$$

A resonator acts as the low pass filter, because of this reason the cut-off frequency is termed as the Leeson frequency $F_L$. In this model, the noise only modulates the phase inside the bandwidth of the resonator, which is as:

$$BW = \frac{f_0}{2Q_L} = F_L \tag{1.80}$$

Where, $f_0$ is the resonant frequency of the resonator and $Q_L$ is the loaded quality factor obtained from the transfer function of the resonator. In resonator, there is a series of process involved in finding the Leeson frequency point, which later gives the value of the loaded quality factor. First, we spot the $\pm 1^\circ$

phase spot from the transfer function. Usually, the transfer function data consists of Amplitude and Phase as a function of frequency. Once the value of phase gets the right spot relative to frequency, we take the ratio of the $\pm 1^{\circ}$ phase with its respective value of frequency. This allows us to have a value of degree of phase deviation per Hz. Hence, the inverse of this deviation per Hz in radian gives us the exact lesson frequency value in Hz and as from the formula for the given bandwidth $BW$ and resonant frequency $f_0$, we will have the loaded quality factor $Q_L$.

The PSD of the phase fluctuation at the output of the oscillator is:

$$S_{\varphi}(f) = \frac{1}{f^2} S_{\Delta f} = \left(\frac{f_0}{2Q_L}\right)^2 \frac{1}{f^2} S_{\Delta\theta}(f) \tag{1.81}$$

The above equation is valid if, $f < F_L = \frac{f_0}{2Q_L}$

The rapid phase variations $\Delta\theta$ i.e. higher Fourier frequencies is filtered by the resonator itself. The illustration of these phenomena has a representation in the Figure 1.19. Hence, the rapid fluctuations pass through the amplifier and are present at its output without returning to its input. We have than:

$$S_{\varphi}(f) = S_{\Delta\theta}(f) \tag{1.82}$$

Where the above equation is valid if, $f > F_L = \frac{f_0}{2Q_L}$

The PSD of the phase fluctuations also termed as the Leeson's formula modifies from the equations above as:

$$S_{\varphi}(f) = S_{\Delta\theta}(f) \cdot \left[1 + \left(\frac{f_0}{2Q_L}\right)^2 \cdot \frac{1}{f^2}\right] = S_{\Delta\theta}(f) \cdot \left[1 + \frac{F_L^2}{f^2}\right] \tag{1.83}$$

Where we have $F_L = \frac{f_0}{2Q_L}$ as the Leeson frequency.

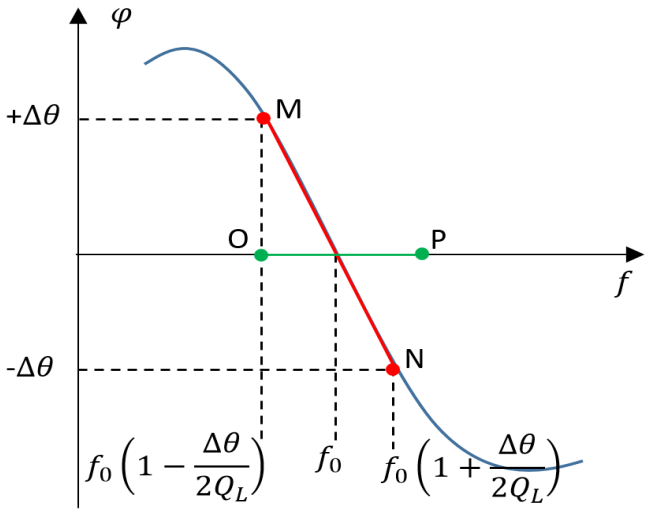


*Figure 1.19: Phase versus Frequency curve of the resonator.*
*$f < F_L$ Follows path MN and $f > F_L$ Follows path OP.*

At the output of a buffer amplifier, the power spectral density of phase fluctuations of the signal becomes:

$$S_{\Delta\theta}(f) = \left(1 + \frac{f_c}{f}\right) \frac{FTk_B}{P_{IN}} \tag{1.84}$$

Where $F$ is the noise factor of the amplifier, $k_B$ is the Boltzmann constant, $P_{IN}$ the carrier power at the input of the amplifier, $f_c$ is called the phase noise corner frequency and is dependent on the amplifier and the carrier power at the input. The Figure 1.20 shows the variations of $S_\varphi(f)$ as a function of $f_c$ and $f_L$. Part 1 and Part 2 resemble the nature of phase noise of the resonator due to Leeson effect. The corner frequency $f_c$ filters by the resonator because of its high loaded quality factor, which later influences the Leeson frequency to cause the filtering effect.

We can now express the slope of the PSD of relative frequency fluctuations, $S_y(f) = \frac{f^2}{f_0^2} \cdot S_\varphi(f)$ and the superposition of the slope of these fluctuations at base Fourier frequencies has fluctuating nature and we deduce at 1 Hz bandwidth as:

$$S_y(1\ Hz) = \frac{1}{f_0^2} \cdot S_\varphi(1\ Hz) \tag{1.85}$$

From equations (1.80)

$$S_\varphi(1\ Hz) = \frac{f_0^2}{4Q_L^2} \cdot S_{\Delta\theta}(1\ Hz) \tag{1.86}$$

The Allan variance given as:

$$\sigma_y^2(1s) = 2 \cdot \ln(2) \cdot S_y(1\ Hz) \tag{1.87}$$

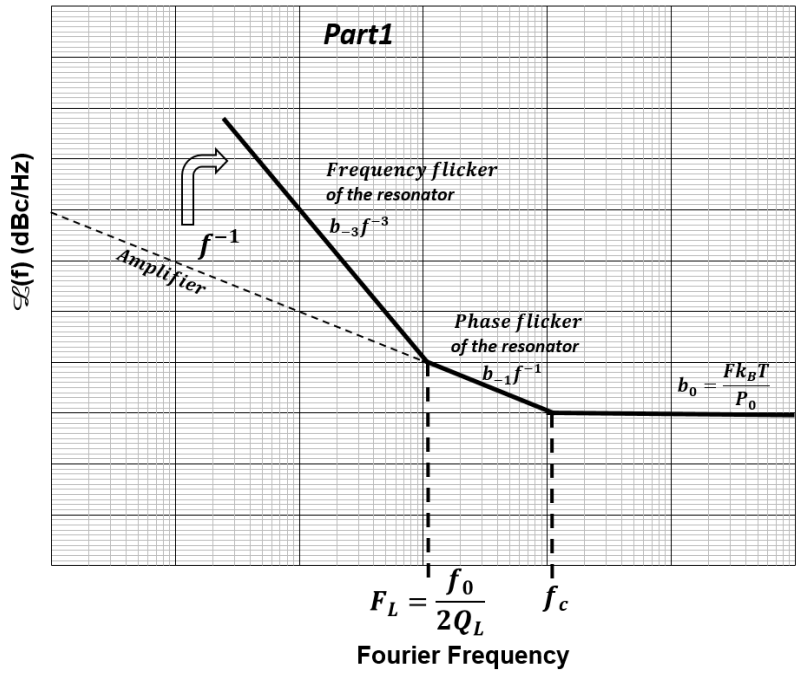

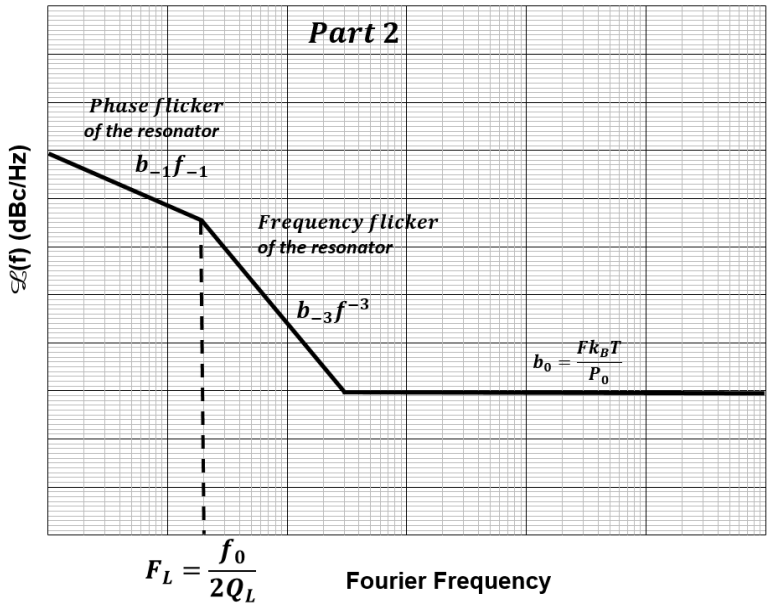


*Figure 1.20: Lesson effect on the phase noise curve of the resonator.*

Now the term limiting the performance of the oscillator because of $1/f$ nature of fluctuations from the resonator simplifies as:

$$\sigma_y(1s) = \sqrt{2 \cdot \ln(2) \cdot \frac{1}{4Q_L^2} \cdot S_{\Delta\theta}(1\ Hz)} \tag{1.88}$$

Therefore, the above result allows us to establish a relationship between the phase fluctuations i.e. phase noise, frequency fluctuations and the loaded quality factor of the resonator. Leeson's model allows us to understand the influence of loaded quality factor and effect on the level of phase noise from the resonator. The next part of our work will be to measure this phase noise from the resonator following the IEEE standards.

## 1.8 Summary

In this chapter, starting from the use of resonator in metrology, problems of fluctuations and kinds, governing equations of continuum mechanics for piezoelectric materials, basic principle of resonator operation, mechanical equivalent circuit, and electrical equivalent circuit was realised. The need for resonator as an electrical device, the use of quartz as the piezoelectric device and the possible problems of phase noise on resonator was the heart of the work.

# Chapter 2 Noise measurement technic

Noise is a huge constraint-causing disturbance in the normal operation of any electronic system. With the advancement in technology, there is a need for a higher efficiency with the cost of fabricating any electronic device using less and less amount of power. For e.g. in instrumentation, noise disrupts the precision of the measurement chain. The disruptions seem like the frequency fluctuations, which can further limit the rate of data transmission to other or within any interfacing system. Therefore, for metrological applications, for a time and frequency device like clock, there is a need for a high purity in spectral density of any signal because its performance bases on the level of noise in phase.

The chapter details on the technical aspects of measuring $1/f$ phase noise in BAW resonators. We have tried to provide almost all the details gradually, on measuring phase noise using the well-known carrier suppression technic. Similarly, the chapter details with the improvement of phase noise measurement technic or as to say a possible update to measuring phase noise technic on different kinds of resonators i.e. Langatate resonator (LGT). Therefore, in this chapter we will be specific to the work regarding measurement of $1/f$ phase noise in quartz crystal resonators and Langatate crystal resonators.

## 2.1 Phase noise measurement using Carrier Suppression Technic

This is a well-known noise measurement technic in Time and Frequency domain popularly termed as “The carrier suppression technic” in Figure 2.1. It is a passive noise measurement system used on piezoelectric resonators for more than 10 years. The carrier suppression technic characterizes the inherent phase stability of any ultra-stable resonators. This method, also known as the interferometric method [20]-[23], is a differential method that offers one of the highest sensitivities for the measurement of noise on a pair of Devices Under Test (DUT). Similarly, the resonator is placed in a loop with an amplifier to create an oscillator, the contribution of the noise of an amplifier is potentially greater than the noise of the resonator. Therefore, it is difficult in the case of ultra-stable devices to distinguish whether the noise contribution is from the resonator or from the associated amplifier. Thus, a differential measurement between two almost similar resonators makes it possible to eliminate the noise contribution of the excitation source.

In the carrier suppression technic, we perform a subtraction of the outputs of two signals from the resonators (combination 180° out of phase). While combining signals from both DUTs, the resonant frequency of both the DUTs are matched by the help of the series capacitor inside the oven and the impedance matching circuits balances the Q-factor of the DUTs. Later, the phase is adjusted by the offset adjusters present on the bench. This process allows the signal to combine and amplify without adding the noise from the amplifier, thus highlighting the noise of the DUT. A FFT (Fast Fourier Transform) analyser performs the basic frequency band detection by mixing this signal with the source of the bench. In all cases, the correlated noise upstream of the bench (including that of the source) largely eliminates. The entire amplification chain thus makes it possible to bring the noise levels of the

DUTs above the limits of the measuring devices. Hence, the measurement floors are thus of the order of $-160\ dBcHz^{-1}$ at 1 Hz of the carrier. Nevertheless, the resonators must be impedance-conditioned (to obtain a loaded quality factor of the order of 60% of the unloaded quality factor) and must be temperature controlled to limit the frequency-temperature effect.

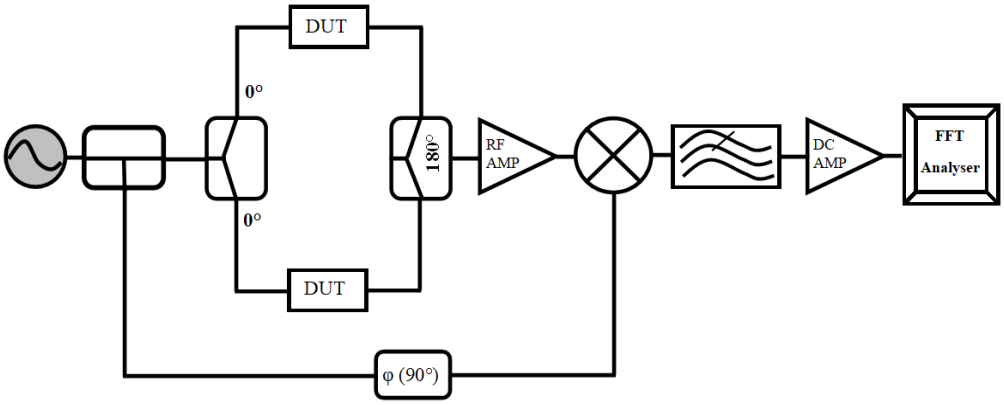


*Figure 2.1: Phase noise measurement bench using carrier suppression technic.*

During my thesis, I used the noise measurement technic mentioned above as a principal setup to measure phase noise of SC-cut Bulk Acoustic Wave (BAW) quartz crystal resonators and on resonators manufactured with Langatate crystals (LGT). For the latter phase noise measurement application, I have developed an input and output matching system for these resonators having low impedance (<10 ohms). This matching circuit consists of transformers, in an impedance matching circuit that allowed us to measure the phase noise under enough loaded quality factor conditions which was not the case using the traditional impedance matching circuit.

## 2.2 Phase Noise Measurement Technic in BAW resonators

The main objective of the noise measurement bench for quartz crystal resonators is to measure the stability of the resonator [5]. Several stages are necessary for performing this kind of measurement. It is important to realize all these stages to obtain the most precise results. For these measures, it is imperative to minimize the changes in temperature as well as the vibrations on the ground; these parameters have a direct influence on the results for the characterization of resonators. Hence, we perform phase noise measurement once we realize the inversion point temperature and motional parameters.

### 2.2.1 Measurement of the Inversion Point Temperature and Motional Parameters

This is the first step of characterization of the resonators before connecting to phase noise measurement bench. It is imperative to follow the same protocol for each device to do noise measurement. These two steps i.e. inversion point temperature and motional parameters are complementary; they are realized one after the other.

### 2.2.2 Identification of Resonator Pins

Each resonator manufacturers have their own pin configuration. Therefore, it is necessary to exactly spot where the resonance pins are. For this, we start by using the impedance-analyzing mode of Agilent 4395A [24] , and the fixture Agilent 16092A test kit [25] and impedance test kit 43961A. To realize the impedance for the resonance, firstly we must connect the impedance kit 43961A to the analyzer in Figure 2.2 as:

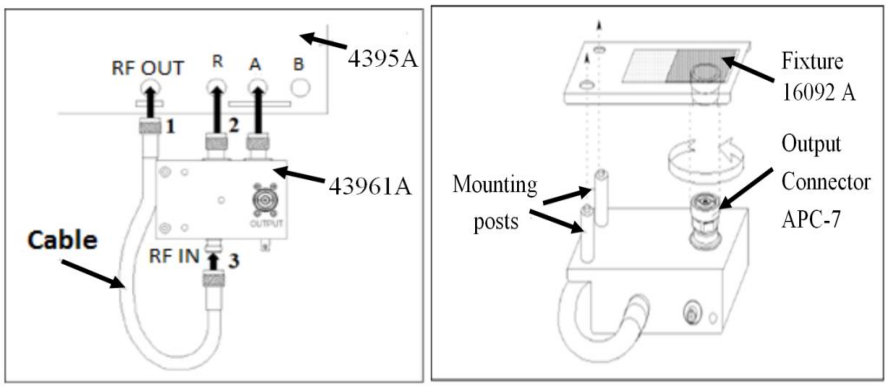


*Figure 2.2: Connecting the impedance test kit and Fixture 16092 A.*

- Connect the cable to the RF OUT port of the analyzer.
- Connect two connectors of the 4395A to the R and A ports of the 43961A.
- Connect the other connector of the cable to the RF IN port of the 43961A.

Then, connecting the test fixture 16092A to the impedance test kit 43961A:

- Turn the **APC-7** connector of the impedance test kit OUTPUT port.
- Set the mounting posts of the test station into the twin-locating hole at the corner of the test fixture.
- Connect the connector on the underside of the test fixture to the OUTPUT port of impedance kit.

When the impedance kit and the fixture connects to the analyser, it is necessary to place the resonator on the plate using the clamps placed on it**.** Only two pins allow obtaining the resonance, there are only two possibilities shown below in Figure 2.3 as:

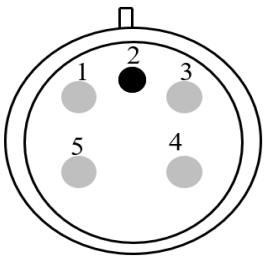


*Figure 2.3: Bottom view of the resonator.*

The pins where we can find the resonance are pair 1 and 4 or 3 and 5. To verify the resonance, mounting the pin pair with the fixture 16092A is necessary as in Figure 2.4.

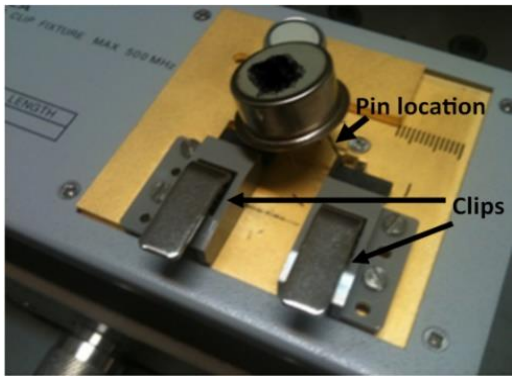


*Figure 2.4: Resonator mounted on fixtures.*

### 2.2.3 Internal and external structure of the oven and components used

As in Figure 2.5 Bottom center in A, one should insert the resonator on the top central part of the oven. Then the test electronic plate in B along with the resonator, as seen in C. Finally, the resonator with electronic plate is required to weld on the oven points as shown in D.

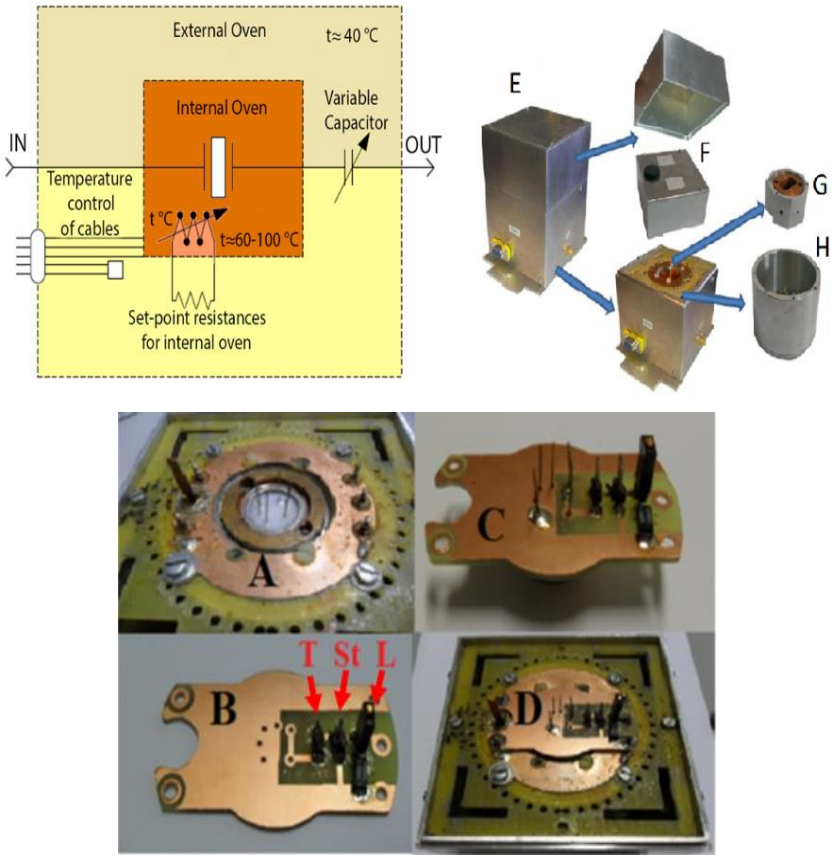


*Figure 2.5: Left Top: Temperature distribution in the thermostat, Top Right: E- full oven, F- access for resonator tuning, G- internal oven cap, H-external oven. Bottom center: Resonator impedance measuring mode: A: Location of resonator in oven, B: Test electronic plate (T-Transmission, St- Short circuit, L- 50Ω loaded), C: Resonator mounted in PCB, D: Resonator with test PCB welded in oven.*

The oven implies automatic digital heating system. In automatic method, we have used the thermostat that represents a system with two ovens: internal and external as in Figure 2.5. The internal

oven maintains the constant temperature near the resonator and external oven suppresses the effect of temperature from the external environment.


*Figure 2.6: Temperature Control Box.*

The temperature control box in Figure 2.6 was fabricated by a master's student during his internship in FEMTO-ST, Time & Frequency Dept., in ENSMM. The principle of this digital control box bases on a variation of voltage. The reference voltage of the internal oven controller changes to have a variable set point temperature. In practice, the box has a circuit with a DAC (Digital to Analog Converter) that can drive the internal oven digitally using an I2C port.

### 2.2.4 The value calibration of the thermostat

The minimum pitch measured was 0.017°C (which corresponds to a change in the 1-bit DAC value). Moreover, the range of variation of the temperature of the inner furnace is 60 to 100° C, which corresponds to DAC values of 1485-4095. Therefore, the simple equation relating the temperature of the oven and the value of DAC is given by **T = 0.017*DAC value + 34.766**.

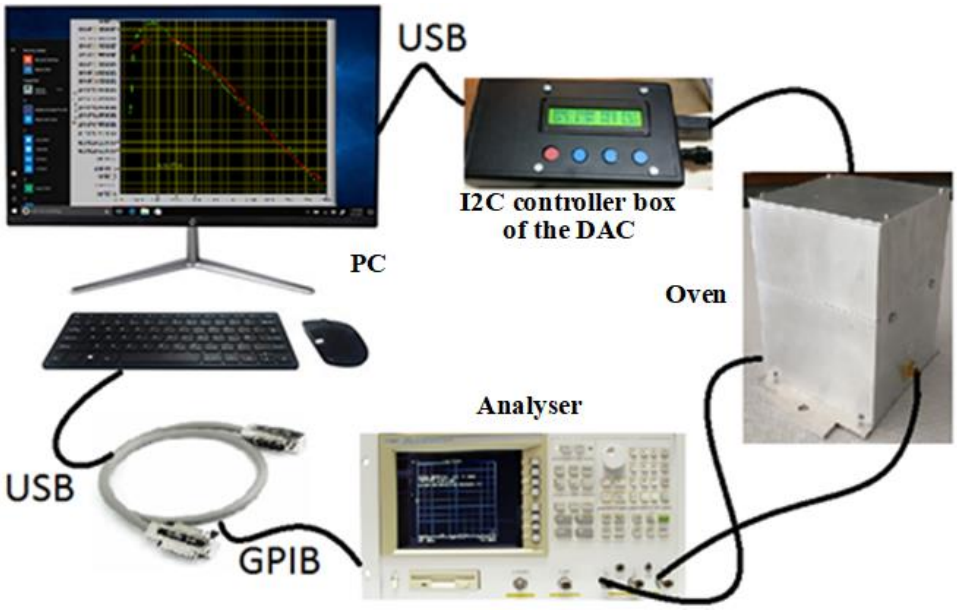


*Figure 2.7: The functional diagram of determination of point of inversion.*

The determination of inversion point temperature begins by putting the resonator in the thermostat as mentioned before. The control box is used to set the initial temperature set point and it needs to wait for the thermostat to stabilize. There is no hard and fast rule, but we leave the resonator in thermostat for at least 2 hours after the control box reaches the set point temperature to be sure that

the steady state is reached. The software LabVIEW helps to determine the turnover point temperature for our system. Examples of turnover temperature graph for SC-cut quartz resonator are in sections ahead. Once this step is complete, we then adjust the analyzer to the impedance measurement mode and calibrate the analyser with three circuit states i.e. OPEN (0 S), SHORT (0 Ω) and LOAD (50 Ω) which can be viewed in Figure 2.5 B as T, St and L respectively. Once the calibration performed, the oven connects to the analyser and the motional parameters are measured.

The next step is measuring phase noise once we know the inversion point temperature and motional parameters for the resonators. We use the well-known carrier suppression technic for measuring phase noise in resonators. The measurement of phase noise allows measuring the short-term stability of the resonators. This measurement carries out in a non-disruptive environment (without shocks, vibration, and temperature variation).

## 2.3 Preparation of resonator for phase noise measurements

Unlike the impedance measurement PCB, the transfer function PCB has resistances for impedance matching network, series, and parallel capacitances for adjusting the resonant frequencies. The circuit on left in Figure 2.8 have three equivalent sections i.e. $Req1$, $Req2$ and $Req3$. All these three equivalent sections contribute for balancing the equivalent input and output impedance of the transfer function circuit following the maximum power transfer law.

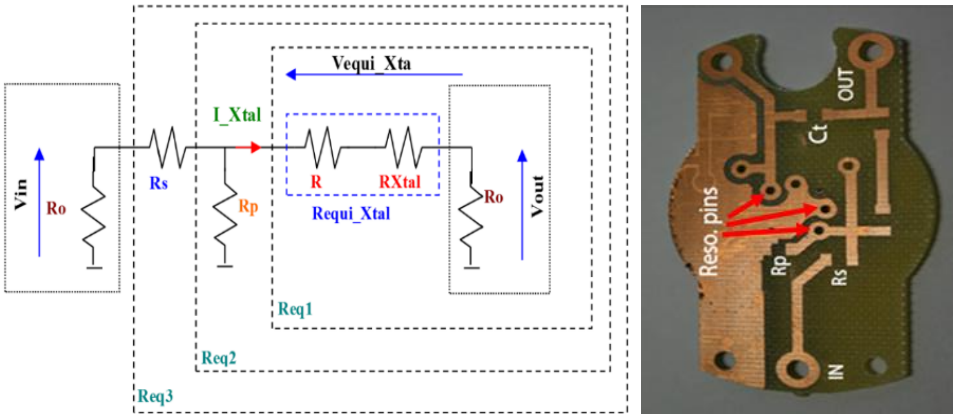


*Figure 2.8: Left: Circuit diagram of impedance matching unit of the transfer function PCB, Right: Transfer function PCB.*

Similarly, we use the motional parameters obtained previously for the calculation of $C_t$ (details in Chapter 1 equation (1.18). However, the selection of the values of resistance in series $R_s$ and parallel $R_p$ is very crucial to regulate the power dissipation and loaded quality factor $Q_L$ in the resonator (equation (2.1)). Resistances $R_s$ and $R_p$ respectively, are chosen around $20\,\Omega$ and $30\,\Omega$. For these values of resistances and for a 5 MHz SC-cut quartz resonator, the excitation power of the resonator is around $65\,\mu W$, the resonator induced loss is about 15 dB and the loaded quality factor $Q_L$ is around 1.35 million, an example in Table 2.1.

| Resonator mounted properties | |
|---|---|
| $R_s$ | 20.50 Ω |
| $R_p$ | 34.80 Ω |
| $R_{xtal}$ | 75 Ω |
| $R_{equi\_Xtal}(R_{xtal} + parasitic)$ | 112.23 Ω |
| $I_{xtal}$ | 0.76 mA |
| $Q_{unloaded}$ | 2225000 |
| $P_{equi\_Xtal\_\mu W}$ | 65.31 µW |
| $Reso_{induced\_loss}$ | 15 dB |
| $Q_L$ | 1350000 |
| $R_0$ | 50 Ω |

*Table 2.1: Features of resonator for performing noise measurements.*

The loaded Quality factor $Q_L$ as a function of $R_s$ and $R_p$ given by:

$$Q_L = Q_{unloaded} \times \left( \frac{R_{equi\_Xtal}}{R_{equi\_Xtal} + R_0 + \left( (R_s + R_0) \times \left( \frac{R_p}{R_s + R_p + R_0} \right) \right)} \right) \quad (2.1)$$

Once the PCB assembles in the oven with the resonator, we measure the transfer function of the resonator. The Figure 2.9 shows the transfer function graph of the 5 MHz SC-cut quartz crystal resonator.

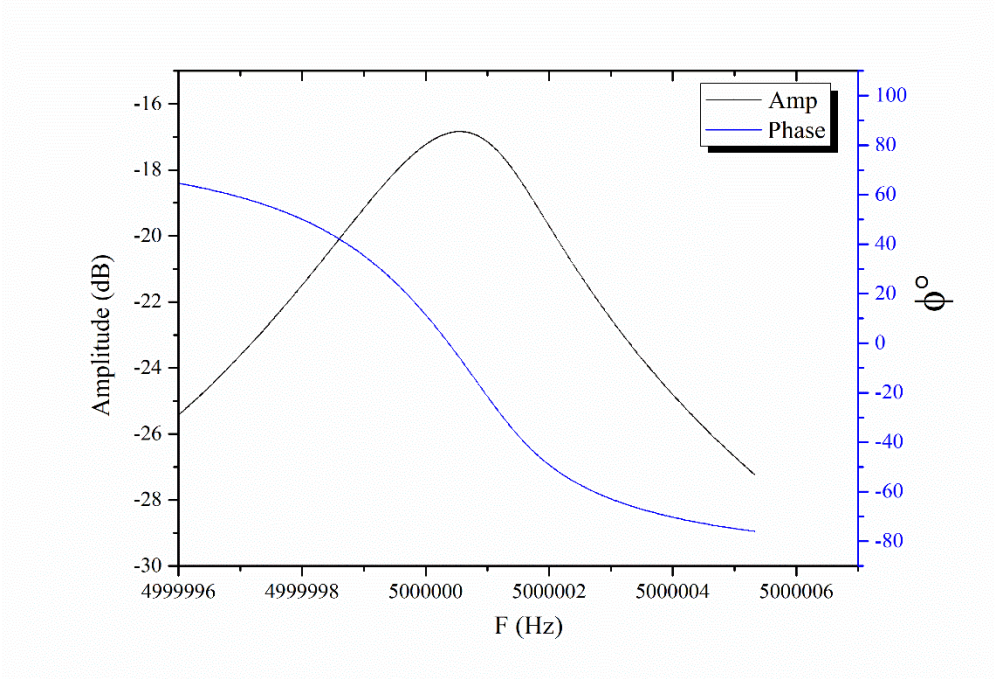


*Figure 2.9: Transfer function of the resonator on Spectrum Analyser.*

### 2.3.1 Phase noise measurement bench using carrier suppression technic

The phase noise measurement using carrier suppression technic in Figure 2.10 involves series of phase noise measurements of components that contribute to the noise floor before measuring the phase noise of the resonators.

***The phase noise floor:*** The noise measurement floor allows determining the white noise of the measurement bench. We do this by using resistances. The noise floor measurement determines the limit of the lowest level of noise that is possible to measure by the bench. This helps to determine the exact level of phase noise from the measuring device. The measurement bench is divided into two parts i.e. interferometric part and synchronous detector part.The first step of the measuring bench consists of measuring the noise of FFT analyser HP 3561A in Figure 2.11.We measure the PSD (Power Spectral Density) of voltage fluctuation which we later realise to phase fluctuation.

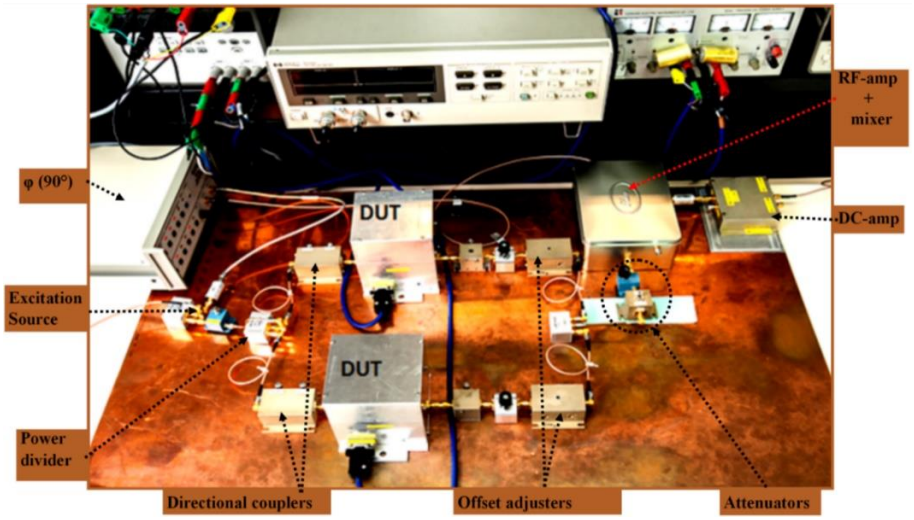


*Figure 2.10: Setup for Carrier suppression bench.*

*Figure 2.11: Hewlett-Packard 3561A Dynamic Signal Analyzer.*

The process starts with connecting a 50 Ω resistor to the input of the FFT analyser. The power spectral desity of the voltage fluctutation $S_v(f)$ at 1 kHz is -155 $dBV^2Hz^{-1}$. This is the minimum level of detection by FFT HP 3561A. The second step consists by connecting a DC amplifier that will raise the noise from DUT above the maximum limit of FFT analyser.The resitance 50 Ω is connected to the DC amplifier through LPF (Low Pass Filter). The spectrum at the output has the form:

$$[S_v(f)]_{FFT+DC} = G_{DC} \cdot [S_v(f)]_{DC} + [S_v(f)]_{FFT} \quad (2.2)$$

The PSD of voltage fluctuation at the input of DC amplifier is:

$$[S_v(1\ kHz)] = -176\ dBV^2/Hz \quad (2.3)$$

The DC amplifier gain $G_{DC}$ = +49 dB pulls the noise to -127 $dBV^2/Hz$ which is above the FFT analyzer limit. The next step is followed by connecting a mixer to the input of LPF. This combination leads to the formation of synchronous detector and the noise floor can be expressed as:

$$[S_v(f)]_{Floor} = G_0 \cdot [S_v(f)]_{mixer} + G_0 \cdot [S_v(f)]_{DC} + [S_v(f)]_{FFT} \quad (2.4)$$

$[S_v(f)]_{mixer}$, $[S_v(f)]_{DC}$, $[S_v(f)]_{FFT}$ represents PSD of voltage fluctuation of mixer, DC amplifier and FFT analyser as a function of resistance of 50 Ω connected at the input of the synchronous detector. Therefore, DC amplifier plays the vital role of bringing the noise from the device to a level superior than the FFT analyser floor where we have the expression below:

$$G_0 \cdot [S_v(f)]_{mixer} > G_0 \cdot [S_v(f)]_{DC} > [S_v(f)]_{FFT} \quad (2.5)$$

The next crucial step comes to the characterisation of the RF amplifier which is a connecting bridge between the interferometric part with the synchronous detector part. It's considered as an ideal amplifier with very low level of noise connected to the bench. We follow the same method as before for measuring the noise dissipated from the RF amplifier. To the input of RF amplifier, we connect a 50 Ω resistance. The thermal noise is represented by $b_e = Fk_BTB$ where $F$ is the thermal noise factor of a RF device, $k_B$ is the Boltzman constant which is $1.38 \cdot 10^{-23} J \cdot K^{-1}$, $T$ is the room temperature 294 K and $B$ is the pass-band of the device. The PSD of thermal noise at 1 Hz bandwidth is $Fk_BT$. Hence, this noise when amplified, the noise spectrum at the output of the amplifier and at the input to the synchronous detector gets multiplied by the gain of the amplifier. The next step now continues with connecting the interferometric bench with the synchronous detector.

### 2.3.2 Calibration of the carrier suppression technic

After connecting the synchronous detector with the interferometric bench we have to calibrate the final setup, as a whole "Carrier Suppression" bench. The interferometric part consisting of DUT's (Device Under Test) are connected to the synchronous detector as shown in Figure 2.12. We follow the standard IEEE norm for phase noise as $\mathscr{L}(f)$ in $dBcHz^{-1}$. The first step starts with defining the phase gain $K_\varphi$ of the bench. One of the arms with a DUT of the noise bench is injected with a side band where the frequency $f_s$ and the power $P_s$ is already known. This side band is the frequency injected at a difference of 0.4 Hz from the source frequency. The side band is equivalent to the phase modulation of the effective value given by:

$$\varphi_{rms} = \sqrt{\frac{P_s}{2P_0}} \quad (2.6)$$

Where $P_0$ is the power from the signal pump. This effective value induces a voltage at the output of the mixer $V_0 = \sqrt{K_\varphi} \cdot \varphi_{rms}$ ,where for known $P_0$, $P_s$ we have $V_0^2 = K_\varphi \frac{P_s}{2P_0}$ expressed in dB as:

$$\left[S_{V_0{}^2}(f)\right]_{dBVrms^2} = \left[K_\varphi\right]_{dBVrms^2/dBrad^2} + [P_s - P_0]_{dBm} - 3\ dB \quad (2.7)$$

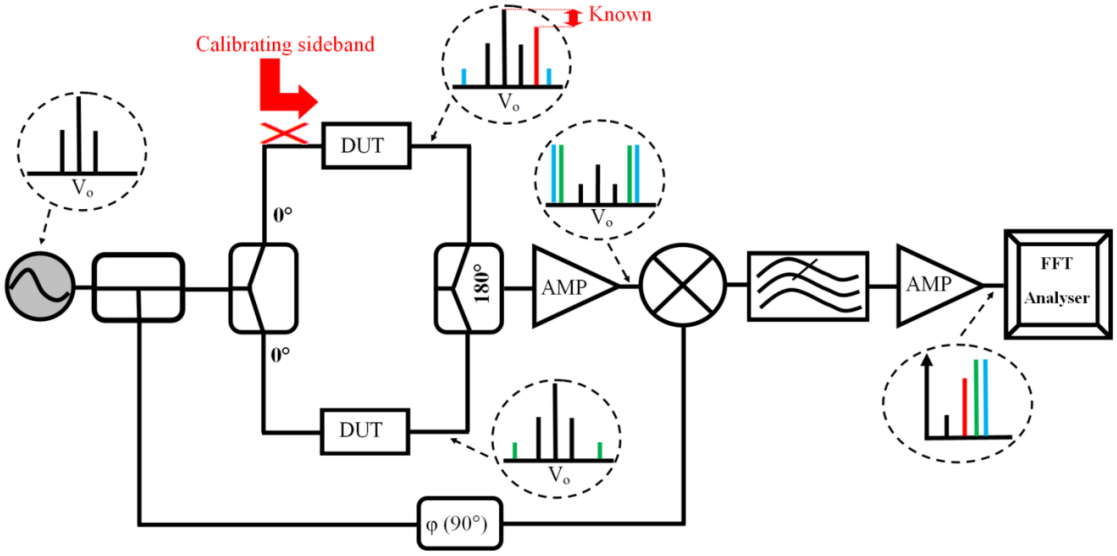


*Figure 2.12: Phase noise measurement bench with carrier suppression technic.*

The coefficient $K_\varphi$ in dB is determined by measuring the difference in level of carrier and side bands and measuring the contribution of sidebands in the spectrum $[S_{V_s{}^2}(f)]_{dBVrms^2}$.The expression in equation (2.7) modifes to:

$$[K_\varphi]_{dBVrms^2/dBrad^2} = [S_{V_s{}^2}(f)]_{dBVrms^2} - [P_s - P_0]_{dBm} + 3\ dB \qquad (2.8)$$

Also by definition:

$$K_\varphi = \frac{S_V(f)}{S_\varphi(f)} \qquad (2.9)$$

Then we have from equations (2.8) and (2.9) above:

$$[S_\varphi(f)]_{dBrad^2/Hz} = [S_V(f)]_{dBVrms^2/Hz} - [K_\varphi]_{dBVrms^2/dBrad^2} \qquad (2.10)$$

Therefore the expression for $\mathcal{L}(f)$ considering all the equations above we have:

$$\mathrm{L}\ (f)dBc/Hz\ = [S_V(f)]_{dBVrms^2/Hz} - [S_{V_s{}^2}(f)]_{dBVrms^2} + [P_s - P_0]_{dBm} - 6\ dB \qquad (2.11)$$

### 2.3.3 Example of phase noise measurement on Quartz resonators

The Figure 2.13 above shows a typical example of phase noise measured in 5 MHz quartz crystal resonator. It is excited at third overtones i.e. mode-C300 as the fundamental mode of operation. This result represents the phase noise of a resonator having a power dissipation of around 65 $\mu$W for the value of around 75 Ω as the intrinsic resistance of the quartz resonator. The loaded quality factor $Q_L$ was around 1.5 million which was approximately 64% of the unloaded quality factor of any BAW quartz resonator. The noise floor in Figure 2.13 is -155 $dBV^2Hz^{-1}$ at 1 kHz for a driving power of 35.5 $\mu$W.

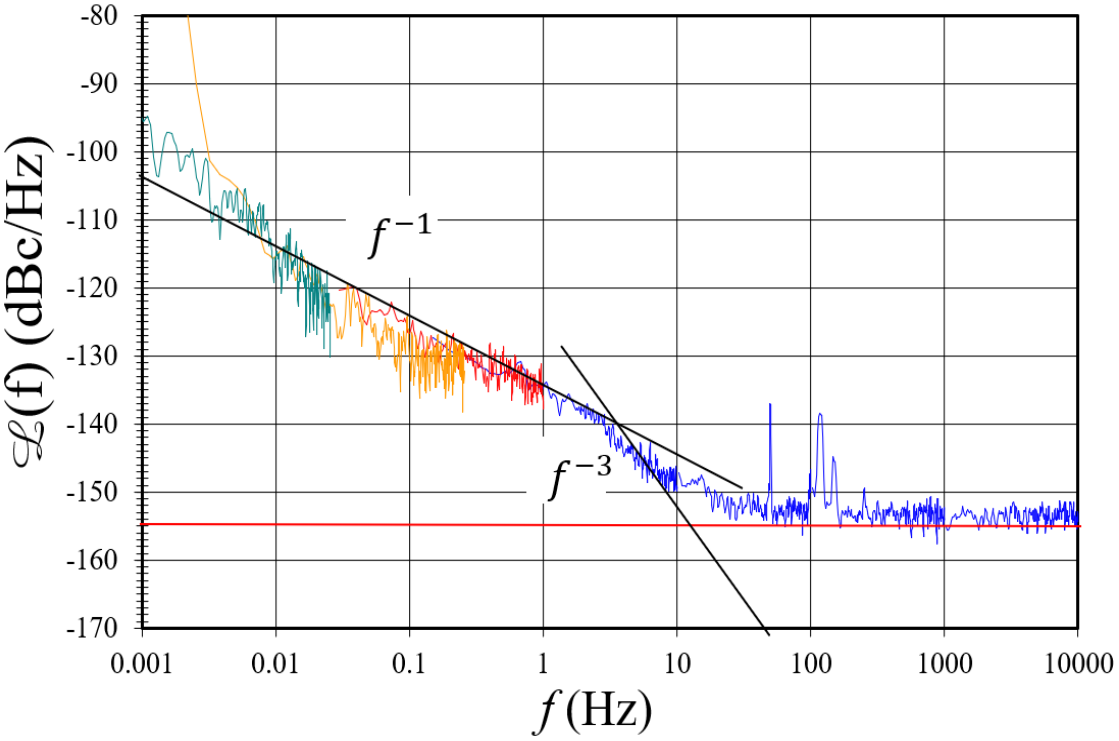


*Figure 2.13: Phase noise measurement plot of 5 MHz quartz crystal resonator.*

## 2.4 Improved phase noise measurement technic on Langatate resonators

This part covers the research and experiment on the phase noise measurement of Langatate (LGT) resonators using carrier suppression technic with special impedance adaptation setup. The topics are classed as follows; - the development and growth of LGT and characterisation below 250 °C and, - the study of phase noise on Langatate crystal resonators.

### 2.4.1 Development, growth of LGT and characterisation below 250 °C

Calcium Gallium Germanium (CGG) crystals ($Ca_3Ga_2Ge_4O_{14}$,) were first discovered and synthesized in early 1980's in Russian Federation [26]-[34]. Early analysis included analysing crystal structure and optical properties [26], [32]-[34] and electromechanical properties including temperature-compensated orientations at room temperature and low acoustic loss [30], [34]. After 1991, massive research on LGS (Langasite $La_3Ga_5SiO_{14}$) for acoustic wave applications showed that it has the potential to be an alternative for quartz in BAW (Bulk Acoustic Wave) and SAW (Surface Acoustic Wave) because of its higher coupling and absence of phase transition up to 1470 °C, and phase velocity relatively being lower than in quartz [35]-[36]. Particularly, LGT's (Langatate $La_3Ga_{5.5}Ta_{0.5}O_{14}$) growth and atomic structures are considerably appropriate for acoustic wave applications by 1997 [37]. The following year, demonstration of two independent sets of ambient temperature LGT elastic, piezoelectric, and dielectric constants were done [38]-[39]. Further, LGT was proved to have zero-temperature-coefficient BAW orientation around ambient temperature [38], LGT resonators fabricated had better Q-f products than LGS, and further studies on LGT Q-factor were soon published in number of articles [40]-[56].

LGT is grown from a melt by Czochralski method, where the starting seed of crystal is slowly rotated and pulled from the molten components of LGT to come together to form mass on the seed of crystal [37] [40]-[41], [46]-[47]. Growth from Czochralski method requires careful observation regarding, melting temperature, composition and rate of rotation during the process to reduce the crystal defects [37][40]-[41], [47]. Langatate crystals also grow using floating zone method and the vertical Bridgman method [48]-[49]. However, studies on LGT and LGS uniformity [50]-[51] found that LGT had very low defect density and better uniformity over LGS. At ambient temperature, extraction of LGT's, elastic, piezoelectric and dielectric constants is done by BAW plate resonance, plus echo, and Resonant Ultra-sound Spectroscopy (RUS) techniques [52]-[60]. The reported temperature range for the use of LGT has been seen from -50 °C to 145 °C or less but the early data sets of LGT constants have not been sufficiently accurate to identify temperature compensated orientations [59], [61]-[62].

### 2.4.2 Study of phase noise of Langatate crystal resonators

The demand for electronic systems and sensors working at high temperature (>200 °C) presents a need for research of materials capable of operating at high temperatures [64]-[65]. Few examples of high temperature applications are in the automotive, aerospace, power generation, nuclear, metal and ceramic part manufacturing, and industrial process control industries [65][66]-[69]. These kinds of applications involve intense environments that involve temperature above 500 °C to 1600 °C regarding few applications on high pressure, corrosion and vibration [70]-[72]. In the time and frequency domain, acoustic-electronic devices such as Bulk Acoustic Wave (BAW), Surface Acoustic Wave (SAW) and Film Bulk Acoustic Resonator (FBAR), resonators are used as portable sensors, filters and other small and reliable frequency control devices [73]-[79]. These acoustic-electronic devices fabricated with materials like quartz, lithium niobate, lithium tantalate, and lead zirconate titanate (PZT), because of problems like phase transitions, material degradation, or acoustic propagation losses above 500° C is not capable functioning at high temperature conditions. Thanks to new piezoelectric crystals like the langasite family of crystals and gallium orthophosphate ($GaPO_4$) it is now possible to operate at high temperature thus they are being investigated for high temperature applications [80]-[83]. Uniquely, the langasite family of crystals (langasite, LGS, $La_3Ga_5SiO_{14}$; langanite, LGN, $La_3Ga_{5.5}Nb_{0.5}O_{14}$; langatate, LGT, $La_3Ga_{5.5}Ta_{0.5}O_{14}$), as a whole called LGX retain piezoelectricity up to 1470 °C, with higher piezoelectric coupling than quartz, and better acoustic wave temperature-compensated orientation around ambient temperature [83], [84]-[86]. LGT among LGX crystals has higher piezoelectric coupling and lower acoustic losses and is easier to grow with less twinning defects than LGN [89]-[93].

The acoustic-electronic devices require the acoustic wave properties to be characterised in the target temperature range. To follow with this strategy, twelve years ago, FEMTO-ST [94] fabricated the first 10 MHz ultra-stable LGT oscillator whose fractional frequency stability and the phase noise almost similar to quartz oscillators i.e. $10^{-13}$ and $-110\ dBcHz^{-1}$ at 1 Hz Fourier frequency. However, the disadvantageous behaviour in frequency-temperature characteristics in comparison to quartz crystal

resonators still exists. In this work, high quality LGT resonator pairs at 10 MHz have been measured on an advanced phase noise measurement system setup in collaboration with Centre National d'Etudes Spatiales (CNES). The noise measurement system is equipped with carrier suppression technic and allows a passive characterization of the resonator pair in Fourier frequencies. Because of low intrinsic impedance, lower than 10 Ω, special adaptation was necessary using transformers to maximize the loaded Q-factor in the measurement system. The simulation of an impedance bridge was done in Pspice software using an advance optimization process. The resonators are named *a*, *b* and *c* and had been characterized in terms of impedance, turnover temperature, amplitude-frequency effect, and phase noise. Therefore, for this work here, we report the resulting short-term stability of the resonators measured on their metrological vibrating *C*-mode at 10 MHz.

### 2.4.3 LGT resonator parameters

The fabricated LGT resonators are in Y-1° cut to achieve a turnover temperature point near 80°C. The applied power to measure the motional parameters is around 60 µW. Figure 2.14 shows the amplitude and phase of impedance about the resonant frequencies of the resonators *a*, *b*, and c.

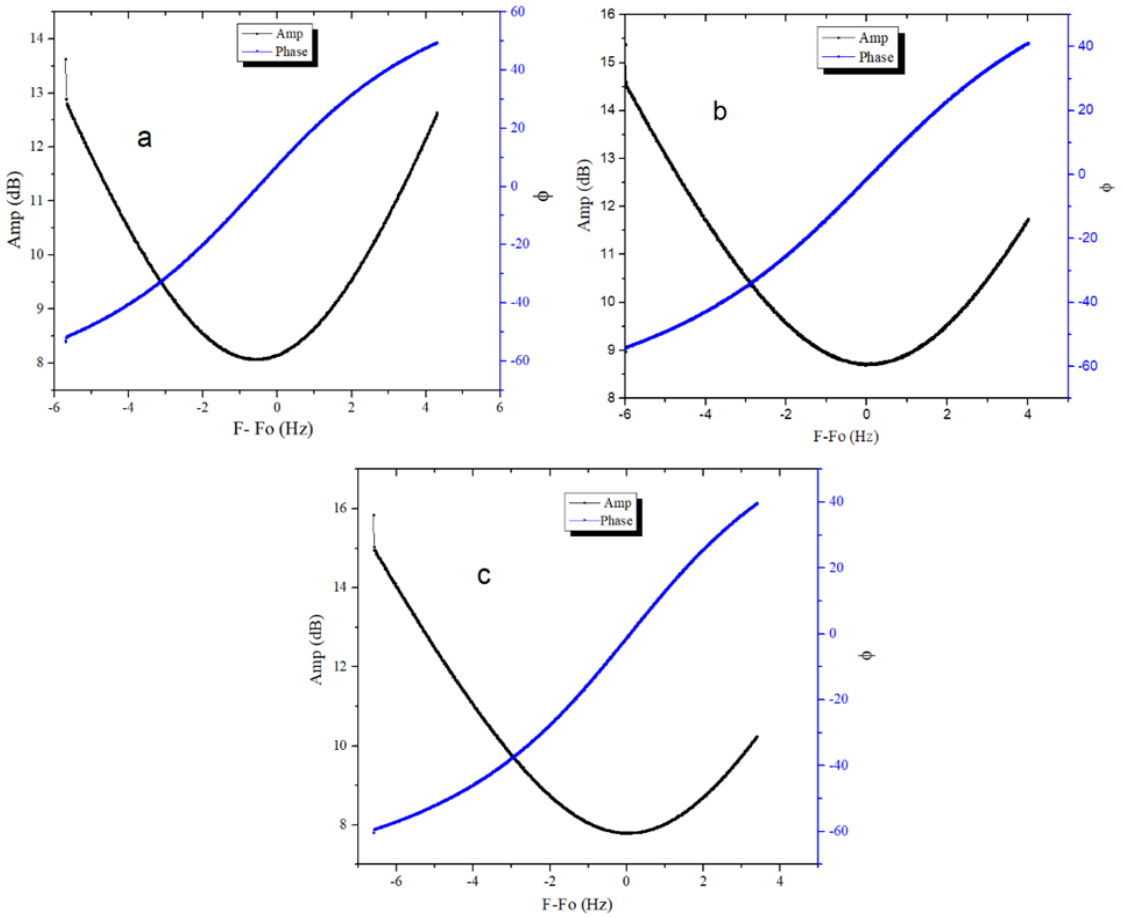


*Figure 2.14: Amplitude and phase of the resonators a, b and c, at approximately 60-µW excitation power respectively.*

Table 2.2 enlists the experimental values of the resonant frequencies at the turnover temperatures, the turnover temperatures PI, the motional parameters *R* and *L* and *C*.

| **Resonators** | $f_{res}$**-10 MHz Hz** | **PI (°C)** | β (ppb/°$C^2$) | R (Ω) | L (mH) | $C_0$ (pF) | Q ($10^6$) |
|---|---|---|---|---|---|---|---|
| *a* | 44.8 | 85.3 | -67.7 | 8.1 | 153 | 17.3 | 1.19 |
| *b* | 34.4 | 83.7 | -59.4 | 8.7 | 150 | 17.0 | 1.08 |
| *c* | 29.4 | 83.6 | -72.6 | 7.8 | 158 | 17.2 | 1.27 |

*Table 2.2: Experimental values of motional parameters, turnover temperature (PI), and Q-factor.*

The thermal nature behaves as a parabolic curve as seen on Figure 2.15 given by:

$$\frac{\partial f}{f_0} = \frac{f_{T_r} - f_{T_0}}{f_{T_0}} = \beta \cdot (T_r - T_0) \tag{2.1}$$

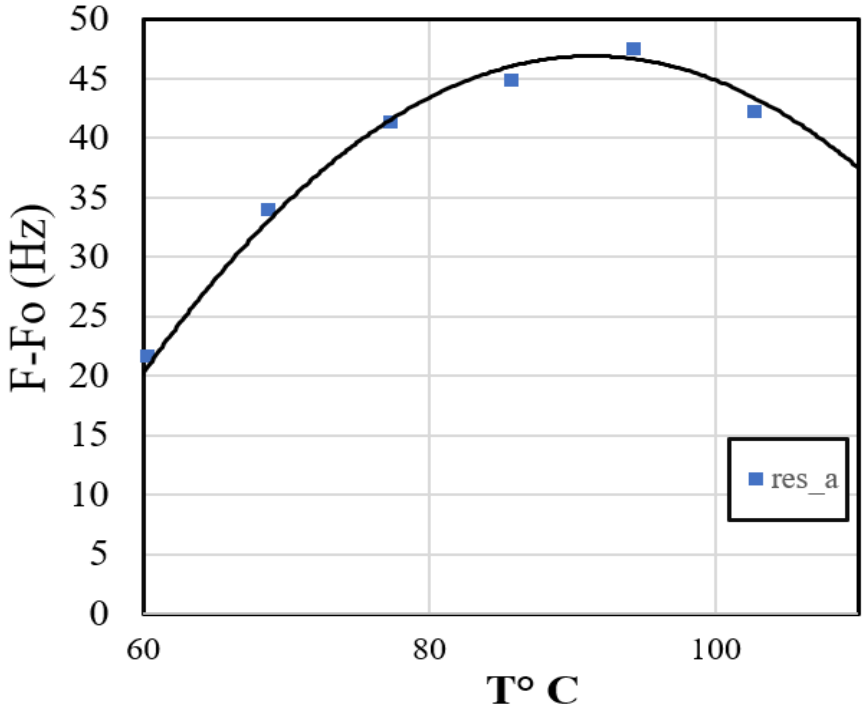


*Figure 2.15: Frequency-temperature curve of a LGT resonator.*

Where, $T_0$ is the turnover temperature $f_{T_r}$ is the value of frequency obtained at temperature $T_r$ and $\beta$ is the parabolic constant whose value depends on the resonator cut. The turnover temperatures for all the three resonators are to be same around 84°C on average. The value of $\beta$ deviated with almost the same magnitude. Unlike discussions in [95], there are no high range of frequency fluctuations in these LGT resonators that we have but the parabolic nature of the turnover temperature curve raises a question for the existence of high temperature sensitivity effect still prevailing in LGT resonators. The $\beta$ values are around six times more sensitive than that of SC-cut quartz resonators. The varied excitation power on resonators from few tens $\mu W$ to few mW as shown in Figure 2.16 has no significant observations except for the shift in amplitude and phase. The relative frequency variations are around $-3.2 \cdot 10^{-10}/W$ for LGT resonators in [96].

### 2.4.4 Phase noise measurement with special adaptation circuit

The use of popular noise measurement technic "carrier suppression" allowed us to measure phase noise on 10 MHz LGT crystal resonators. The carrier suppression bench has the equivalent flicker noise floor in terms of Allan deviation up to $8 \cdot 10^{-15}$ in terms of stability. All the components of the bench are optimized to operate at 10 MHz frequency. As mentioned at the beginning of this chapter, the bench comprises of three vital sections namely; the excitation source, Device under test (DUT) and the output FFT analyzer. Being the double arm bench, the input power from the excitation source is splitted in such a way so as to deliver equal amount of power on both the arms of the bench. Each arm is equipped with a tunning capacitor and an attenuator to adjust the frequency shift and loaded quality factor $Q_L$ . The signals from both the arms are 180° shifted to be sure of the complete suppression of the carrier. The two signals are then combined and amplified by a RF amplifier and then fed to the mixer. Now that the influence of the carrier source is highly reduced, the only remaining fluctuations in the output signal would be the noise from the DUT. Finally, after mixing in the baseband and amplifying, the output signal is fed to the FFT analyzer to observe the power spectral density of phase fluctuations. All the components of the bench have been matched at 50 Ω. Classically, the LGT resonators are matched to 50 Ω using a half π-bridge as used for quartz crystal resonators a schema shown in Figure 2.17. Using the classical circuit, the loaded quality factor $Q_L$ was around 100 k, which was far less than the 60% of the unloaded quality factor $Q$. There was a real need to update the impedance matching circuit in order to improve $Q_L$ for being able to measure the phase noise from the LGT resonators.

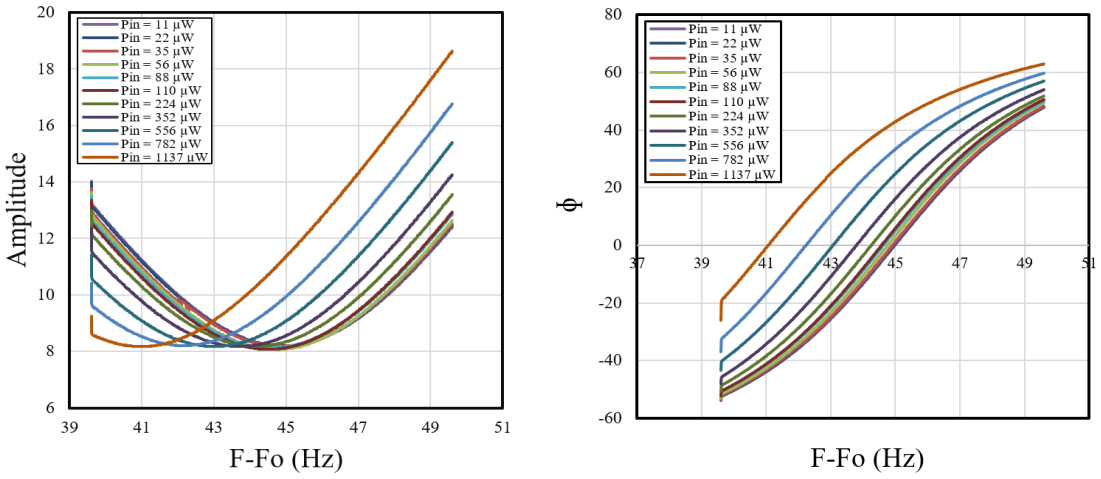


*Figure 2.16: Typical (left): Amplitude- Frequency and (right): Phase- Frequency curve of LGT resonator for different excitation powers.*

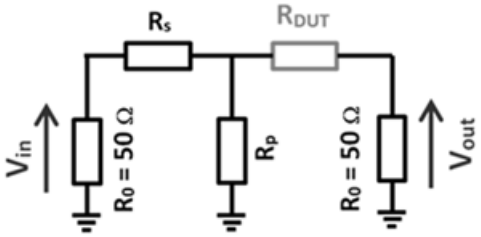


*Figure 2.17: Classical half-π impedance matching circuit (50 Ω).*

### 2.4.5 Pspice introduction, modelling, and simulation

PSpice: SPICE stands for (Simulation Program for Integrated Circuits Emphasis) is a general-purpose Analog circuit simulator used to verify circuit designs and to predict circuit behaviour. Pspice is a PC version of SPICE. PSpice has standard components (such as NAND, NOR, IC's, Flip-flops, Digital gates, Transformers, resonators, OP-amps etc.) in Analog and Digital libraries, which makes it useful tool for a wide range of Analog and Digital applications. PSpice is a copyright product of the OrCAD Corp., USA and we are using OrCAD Cadence which is version 17.2-2016.

We used transformer as an impedance matching circuit, which allowed us to improve our loaded quality factor $Q_L$ of the resonator. The Figure 2.18 below shows the special impedance matching circuit designed in PSpice. The circuit is the extension of the classical impedance matching circuit comprising of series resistance $R_s$ parallel resistance $R_p$ frequency and adjusting capacitor $C_t$. The circuit so extended has an equal input and output impedance around $50\ \Omega$.

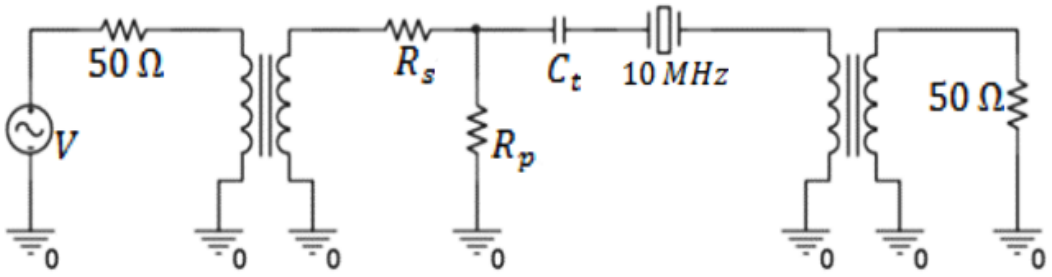


*Figure 2.18: Impedance matching circuit using transformers (50 Ω).*

Surface mount RF transformer for impedance matching:

**Mini-circuits RF Transformers**

RF transformers are widely used in low-power electronic circuits for impedance matching to achieve maximum power transfer. Essentially, an RF transformer consists of two windings linked by a mutual magnetic field. When one winding, the primary has an AC voltage applied to it, a varying flux is developed; the amplitude of the flux is dependent on the applied voltage and number of turns in the winding. Mutual flux linked to the secondary winding induces a voltage whose amplitude depends on the number of turns in the secondary winding. By designing the number of turns in the primary and secondary winding, any desired step-up or step-down voltage ratio can be realised.

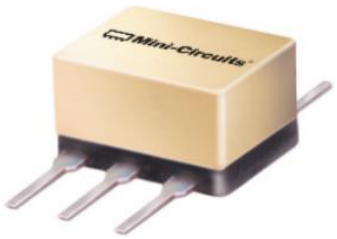


*Figure 2.19: T1-16 case style-W38 Mini- circuits RF transformer.*

The kind of transformer used in our circuit design is a RF transformer from Mini-circuits in Figure 2.19. This transformer has an operating frequency of 0.3 to 120 MHz between -20 °C to 85 °C. The RF power rating is quarter watts which is more than enough for our operating range and we consider lossless transformers used for our experiments. The relationship between impedance and the primary and secondary winding of the transformer as seen on Figure 2.20 can be calculated using the relationship below followed by the installation in the impedance matching circuit and finally in oven:

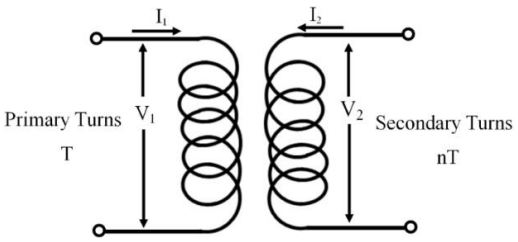


$$V_2 = nV_1 \qquad (2.2)$$
$$I_2 = I_1/n$$

$$Z_2 = \frac{V_2}{I_2} = \frac{nV_1}{I_1/n} = n^2\frac{V_1}{I_1} = n^2 Z_1$$

Therefore, $Z_2 = n^2 Z_1$

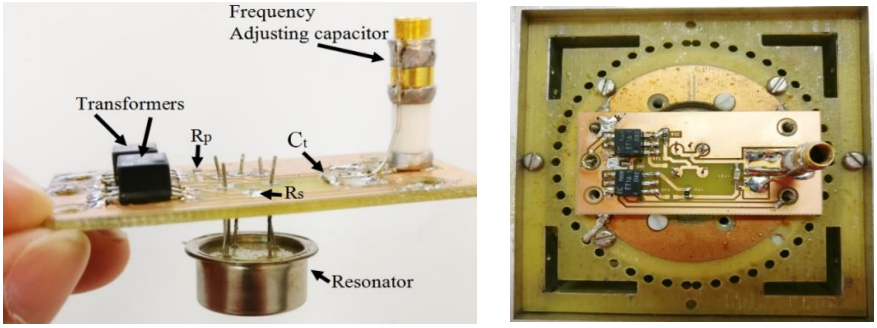


*Figure 2.20: Top: Internal structure of a transformer on primary and secondary sides. Bottom left: Side view of the experimentally installed impedance matching circuit, Bottom Right: Top view of circuit installed on oven.*

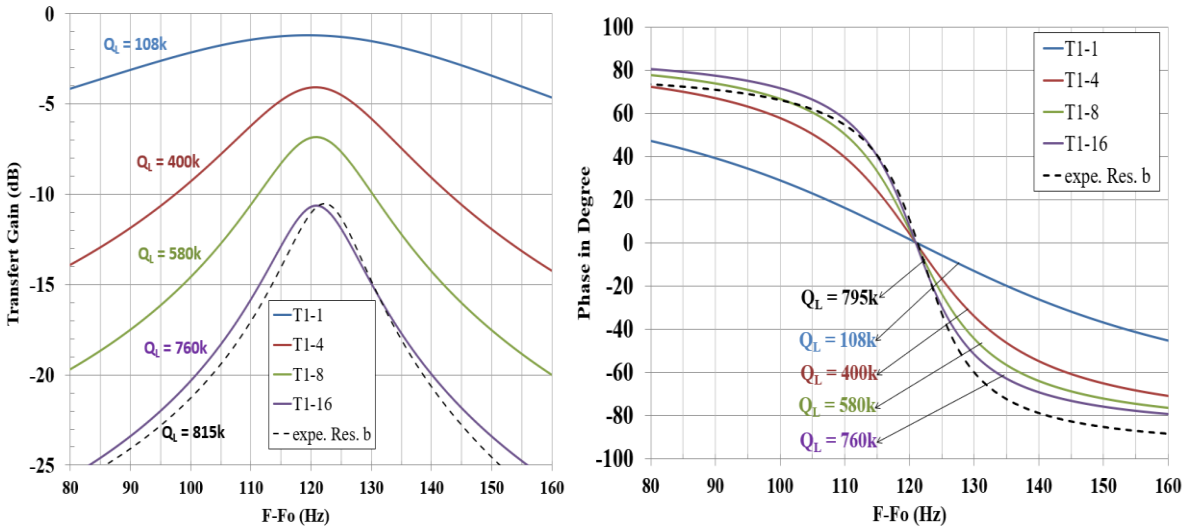


*Figure 2.21: Amplitude and phase of the transfer function simulated with some transformer ratios compared to experimental results.*

Figure 2.21 clearly shows the simulation results of the Q-factor after the installation of the transformers. As we can see from the graph that with using the impedance transformation ratio 1:1 to 1:8 the loaded Q-factor $Q_L$ was almost like 60% below the unloaded Q-factor i.e. around 1.2 million at 10 MHz. Hence, by using 1:16 impedance transformation ratio we arrived having around 60% of the loaded quality factor but the experimental result was better than the simulation i.e. we succeeded in attaining almost 68% of the unloaded Q-factor by installing the matching circuit using transformers with impedance transformation ratio 1:16. The simulation and experimental results showed a good match to measure the phase noise on 10 MHz LGT resonator.

## 2.5 Phase noise measurement results of LGT resonators

### 2.5.1 Measurement of noise floor

The measurement of noise floor of the system is at 10.000121 MHz as shown in Figure 2.22, which corresponds to the tuned frequency of the resonators. Noise floor measurement launches by replacing the DUT's (Device Under Test) generally by a pair of resistors, with an equivalent resistor on both the arms of the noise measurement bench. The result of the measurement in Figure 2.22 assures that there were no visible effects caused on the measurement bench because of using transformers. The spurs seen on the phase noise graph above 100 Hz is because of mixing between the synthesizer reference at 10 MHz and its output signal at 10.000121 MHz and a spur at 121 Hz generates. The spurs seen at 50, 100, and 150…Hz are the spurs from the power supply, which feeds in the oven, and with resonator being inside, produced other spurs. To understand this, we can say that the mixing between the frequencies at 100 Hz and 121 Hz leads to 21 Hz spur.

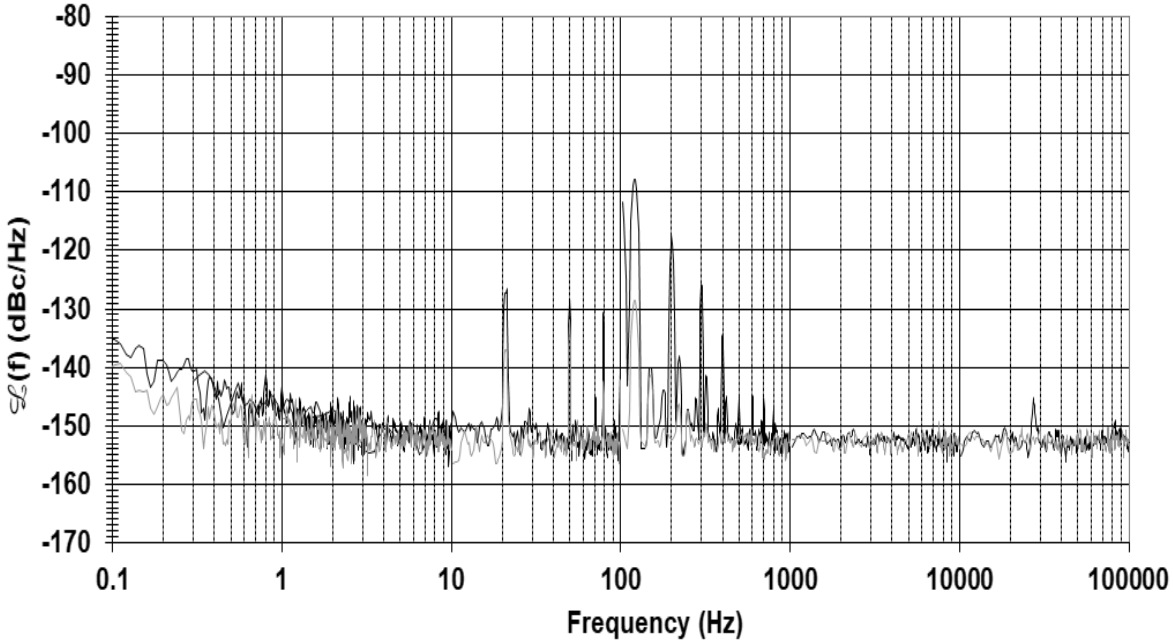


*Figure 2.22: Phase noise of the floor with oven turned on (dark) and off (light). Source frequency is 10.000121 MHz.*

### 2.5.2 Measurement of phase noise in LGT resonators

The phase noise in LGT resonators are measured in pairs and for this case it is the pair of resonators $a$ and $b$. The graph is the one-sided power spectral density of phase fluctuations versus the Fourier frequency shown in Figure 2.23 below. The offset frequency in phase noise graph shows up to 100 kHz. The power dissipation by the resonators were around 120 $\mu$W. The single sided power spectral density of phase fluctuations $\mathscr{L}(f)$ at 1 Hz bandwidth is around $-128\ dBcHz^{-1}$. At 1 kHz of offset frequency for the pair of resonators, the noise floor level was around $-156\ dBcHz^{-1}$. The calculation of short-term stability $\sigma_{y\_floor}$ was in the same way as done for the quartz crystal resonators and found to be $3 \cdot 10^{-13}$. We achieved this result using the transformers with T1-16 impedance ratio, which as result optimized the loaded quality factor $Q_L$. The optimisation of the loaded quality factor reveals itself by the value of PSD as in Figure 2.23 and its asymptotic approach to determine Leeson frequency $F_L$. The approach used to determine the Leeson frequency was performed by the same process as for the quartz crystal resonators as mentioned in the chapter 1 of this thesis work. Table 2.3 sums up the measured phase noise of the resonators and the flicker floor of the short-term stability obtained from the measurements of $\mathscr{L}$ (1 Hz) computed from the Leeson frequency $F_L$ [97].

| Resonator pairs | ***a-b*** | ***a-c*** | ***b-c*** |
|---|---|---|---|
| $F_L(Hz)$ | 6.3 | 5.7 | 6.3 |
| $\mathscr{L}$ (1 Hz) (dBc/Hz) | $-128$ | $-127$ | $-129$ |
| $\sigma_{y\_floor}$ | $2.99 \cdot 10^{-13}$ | $3.04 \cdot 10^{-13}$ | $2.66 \cdot 10^{-13}$ |

*Table 2.3: Y-cut LGT crystal resonator features in terms of noise measurement.*

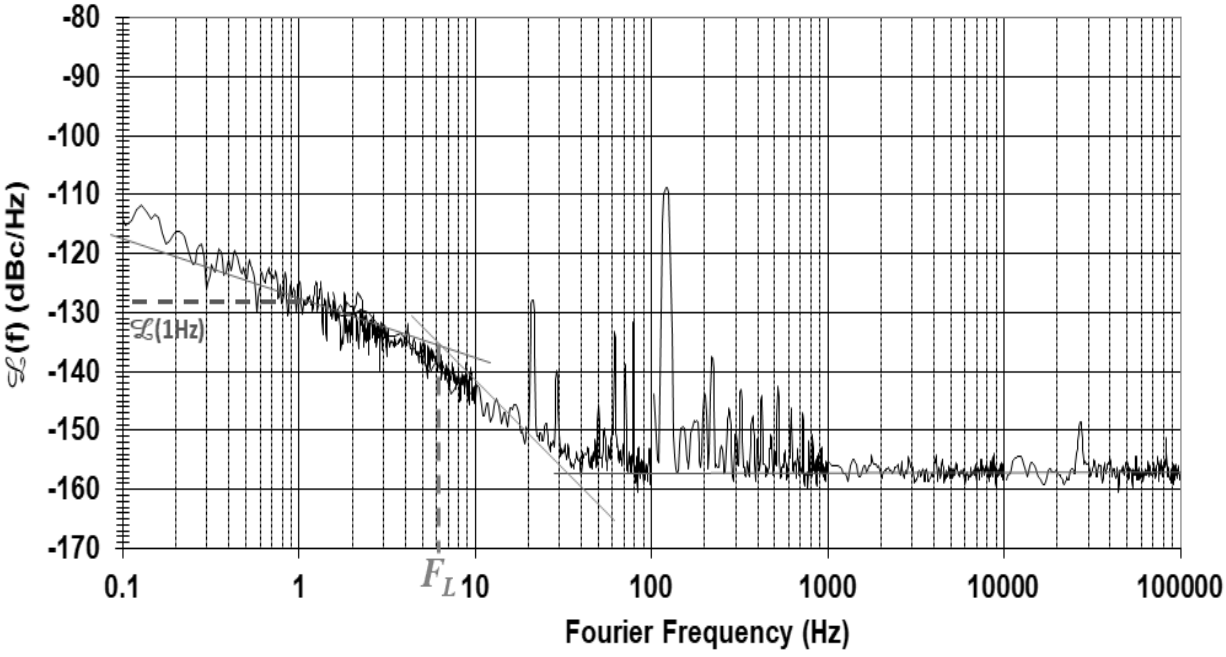


*Figure 2.23: Example of Phase noise of the resonator pair (a and b) with T1-16 transformer.*

## 2.6 Summary

This chapter presented the noise measurement technic using carrier suppression. We tried to explain it systematically right from the classical methodology of resonator mounting to measuring the phase noise on resonators. Apart from this, we also showed an alternative way of measuring phase noise in different kinds of piezoelectric resonators like those made from LGT material. For LGT resonators, because of its low intrinsic impedance around 10 Ω special transformers matching was necessary to improve the loaded quality factor $Q_L$ of the resonators. With this modified approach of conditioning, the phase noise raised above the noise floor of the measurement system. Measurements show that the RF transformers do not degrade the noise floor of the measuring bench. The $\mathcal{L}(f)$ of the LGT resonators at 1 Hz computed from the phase noise measurement is around $-128\, dBcHz^{-1}$ , which seems to be quite near to the phase noise in average high quality quartz crystal resonators having the noise value between $-130$ to $-140\, dBcHz^{-1}$ (more details in Chapter 3).

# Chapter 3 Noise measurement on quartz crystal resonators to explain $1/f$ noise

## 3.1 $1/f$ phase noise measurement in bulk acoustic wave resonators

Laws of electricity and laws of mechanics govern the propagation of wave in the piezoelectric material like quartz and langatate. This chapter is concerned with the governing equations of electricity and mechanics for the plano-convex shaped bulk acoustic resonators followed by the technical approach used to measure the $1/f$ phase noise in them. In acoustics, because of the plano-convex shape, quartz has the property of confining or trapping vibratory energy in the centre of the resonator. This phenomenon can be termed as "energy trapping" as mentioned in Chapter 1 of this work. This trapping principle limits the external influence in the structure maintaining the resonating cavity for an improved performance in acoustic resonance. The well-known energy trapping model by Stevens-Tiersten for Bulk Acoustic Wave resonators will be introduced and used to determine the resonant frequencies and the spatial distribution of different modes of vibration within an acoustic cavity and will be shown considering the plano-convex geometry. Therefore, we will conclude our work for this chapter with the experimental results and observations concerning the measurement of phase noise on resonators at different working temperatures for different modes and the comparison with Finite Element Analysis simulation.

## 3.2 Principle or energy trapping – Stevens and Tiersten model of infinite plate resonators

### 3.2.1 For an infinite plate

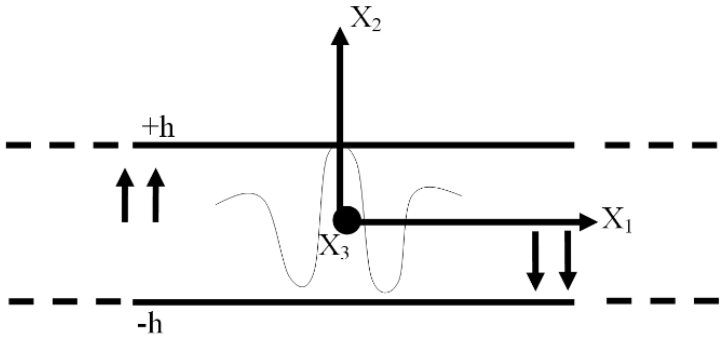


*Figure 3.1: Infinite plate thickness shear mode vibration.*

We consider the propagation of the bulk acoustic wave along the direction $x_2$ for the infinite plane of thickness $\pm h$ as in Figure 3.1. From this two-dimensional infinite plate, we will establish an expression for the plane wave for the displacement in the direction $x_2$ (see equation (1.29) of Chapter 1):

$$u_2(x_2,t) = u_2(x_1,x_3)e^{j(\omega t-\eta x_2)} \tag{3.1}$$

Where $\eta = \left\|\frac{\omega}{v}\overrightarrow{n_2}\right\|$ is the wave number and $\overrightarrow{n_2}$ the unit vector acting at $x_2$.

The linear piezoelectric constitutive relations involving the stress equations of motion and charge equation of electrostatics following (see equation (1.38) and (1.30) of Chapter 1) we have [98]:

$$T_{2j} = c^{E}_{2jk2} u_{k,2} + e_{22j} \phi_{,2} \tag{3.2}$$

$$D_2 = e_{2k2} u_{k,2} - \varepsilon^{S}_{22} \phi_{,2} \tag{3.3}$$

where $T_{2j}$ is the component of stress, $D_2$ is the electrical displacement component along $x_2$, $c^{E}_{2jk2}$ are the elastic stiffness tensor components measured at constant electric field $E$, $e_{22j}$ and $e_{2k2}$ are the elements of the piezoelectric stress tensor, $\varepsilon^{S}_{22}$ is the dielectric permittivity in the direction $x_2$ at a fixed strain $S$, $\phi_{,2}$ is the only component considered of electric potential obtained from quasi-static approximation of Maxwell's equation. At mechanical and electrical equilibrium, for an isolated body with electrodes we have:

$$T_{ij,j} = \rho \ddot{u}_i \tag{3.4}$$

$$D_{i,i} = 0 \tag{3.5}$$

Where, $\rho$ is the mass density of vibrating material. Now, the equation (3.2) in the case of equilibrium we have:

$$T_{2j,2} = c^{E}_{2jk2} u_{k,22} + e_{22j} \phi_{,22} = \rho \ddot{u}_j \tag{3.6}$$

$$D_{2,2} = e_{2k2} u_{k,22} - \varepsilon^{S}_{22} \phi_{,22} \tag{3.7}$$

The boundary conditions for electrical (electrical induction $D_2$) and mechanical (mechanical stress $T_{22}$) for an infinite plate without electrodes is given by:

$$T_{22} = 0 \text{ at } x_2 \pm \text{h} \tag{3.8}$$

$$D_{2,2} = 0 \text{ at } x_2 \pm \text{h} \tag{3.9}$$

From equation (3.3)(3.7) and (3.9) we have:

$$\phi_{,22} = \frac{e_{2j2}}{\varepsilon^{S}_{22}} u_{j,22} = 0 \text{ at } x_2 \pm \text{h} \tag{3.10}$$

Now, from equation (3.10) and (3.2):

$$T_{22} = c^{E}_{22k2} u_{k,2} - \frac{e^{2}_{2k2}}{\varepsilon^{S}_{22}} u_{k,2} = \bar{c}^{E}_{22k2} u_{k,2} \tag{3.11}$$

Where, $\bar{c}^{E}_{22k2}$ is the usual piezoelectric stiffened elastic constant.

In the case where we consider only a plane wave propagating in the direction $x_2$ normal to the plate, we consider only the derivatives with respect to $x_2$ are not zero. The solution of the propagating wave taken as :

$$\hat{u}_r = A_r e^{j(\omega t - \eta x_2)} \tag{3.12}$$

The equation (3.12) satisfies (3.6) provided we obtain in the form of eigen equations:

$$\left(\bar{c}^{E}_{2jk2} - \rho\frac{\omega^2}{\eta^2}\delta_{jk}\right)A_r = 0 \tag{3.13}$$

Where, the coefficients :

$$\bar{c}^{E}_{2jk2} = c^{E}_{2jk2} + \frac{e_{22j}e_{22k}}{\varepsilon_{22}} \tag{3.14}$$

are the stiffened coefficients and $\delta_{jk}$ is the Kronecker symbol. Hence, we obtain the speed $v = \frac{\omega}{\eta}$ (where $\eta$ is the wave number) and the polarization of the modes associated with the eigen values and vectors can be determined by cancelling the determinant of the amplitude $A_r$ as:

$$\left|\bar{c}^{E}_{2jk2} - \bar{c}\delta_{jk}\right| = 0 \tag{3.15}$$

Where, $\bar{c} = \rho\frac{\omega^2}{\eta^2}$ is the elastic constant associated to each mode.

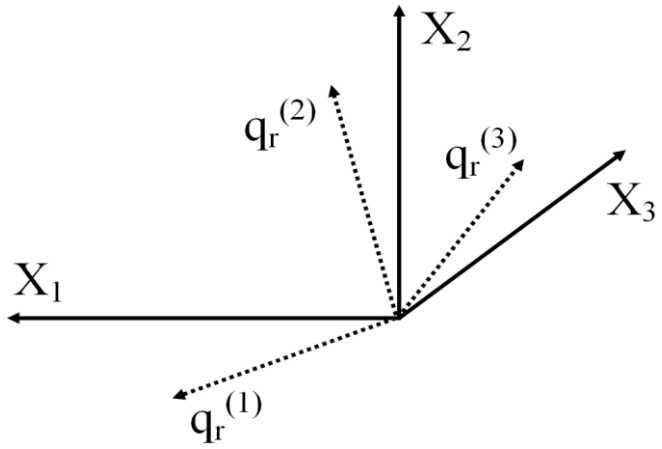


*Figure 3.2: Coordinate transformation schema for an infinite plate.*

Here, $\bar{c}^{E}_{2jk2}$ constitute a symmetric, positive definitive matrix. Then equation (3.15) yields three real positive roots $\bar{c}^{(i)}$, where $i = 1, 2, 3$ and these three eigen values or roots are associated with three mutually orthogonal eigenvectors $A_r^{(i)}$. These eigen vector when normalized gives (Figure 3.2):

$$q_r^{(i)} = \frac{A_r^i}{N_i} \tag{3.16}$$

Where, we substitute in equation (3.13) and may write as:

$$A_r^{(i)}A_r^{(j)} = N_{(i)}^2\delta_{ij} \tag{3.17}$$

Where, $N_i$ is the normalization factor. We can now transform the displacement component $u_r$ of the measurement coordinate system of the infinite plate to components in the eigen form by the transformation matrix:

$$Q_{ir} = q_r^{(i)} \text{ and } Q_{ir}Q_{jr} = \delta_{ij} \tag{3.18}$$

The transformation of the displacement vector $\hat{u}_r$ from the general coordinate system to components $u_i$ in the pure thickness eigenvector system given by:

$$\hat{u}_r = Q_{ir}u_i \text{ and } u_i = Q_{ir}\hat{u}_r \tag{3.19}$$

$$Q = \begin{bmatrix} Q_1^{(1)} & Q_2^{(1)} & Q_3^{(1)} \\ Q_1^{(2)} & Q_2^{(2)} & Q_3^{(2)} \\ Q_1^{(3)} & Q_2^{(3)} & Q_3^{(3)} \end{bmatrix} \tag{3.20}$$

In the asymptotic analysis presented by Stevens and Tiersten, the equations of motions transform using $Q_{ir}$ matrix. The elastic constants in equation (3.14) replaces by new constants :

$$c_{aij2} = Q_{jn}Q_{ir}\hat{c}_{arn2} \text{ and } c_{aijb} = Q_{jn}Q_{ir}\hat{c}_{arnb} \tag{3.21}$$

Where, index a, b = 1, 3, and do not take the value 2. The equation rewritten in the form in relation to the component of $u_i$ gives:

$$\bar{c}^{(j)}u_{j,22} + c_{aji2}u_{i,2a} + c_{aij2}u_{i,2a} + c_{ajib}u_{i,ab} = \rho\ddot{u}_j \tag{3.22}$$

Hence, the new effective elastic coefficients and new elastic constants are given as:

$$\bar{c}^{(j)}\delta_{ij} = \hat{\bar{c}}_{2nr2}Q_{ir}Q_{jn}, \tag{3.23}$$

$$c_{2jia} = Q_{jn}Q_{ir}\hat{c}_{2nra}, \tag{3.24}$$

$$c_{2ija} = Q_{ir}Q_{jn}\hat{c}_{2rna}, \tag{3.25}$$

$$\text{and } c_{ajib} = Q_{jn}Q_{ir}\hat{c}_{anrb}. \tag{3.26}$$

This work focuses specifically for calculating approximation for mode-*C* of the mechanical vibration. The slow shear thickness-shear or *C* mode of vibration is characterised by wave propagating along the $x_2$ direction with $u_1$ as the dominant polarization component and the detailed calculation regarding the equations is in [99]. We assume the three thickness modes to be apart so that they remain uncoupled. The compressed index notation is given in the Table 3.1 below:

| $ij$ or $kl$ | 11 | 22 | 33 | 23 | 31 | 12 | 32 | 13 | 21 |
|---|---|---|---|---|---|---|---|---|---|
| $p$ or $q$ | 1 | 2 | 3 | 4 | 5 | 6 | 7 | 8 | 9 |

*Table 3.1: Voigt's compressed index notation.*

Therefore from equations (3.6), (3.19) and (3.22) with $j = 1,2,3$ reduces to the forms:

$$\bar{c}^{(1)}u_{1,22} + 2c_{16}u_{1,12} + 2c_{56}u_{1,23} + 2c_{51}u_{1,13} + c_{58}u_{1,33} + (c_{12} + c_{66})u_{2,12} + (c_{52} + c_{76})u_{2,23} + (c_{17} + c_{86})u_{3,12} + (c_{36} + c_{57})u_{3,23} + c_{11}u_{1,11} = \rho\ddot{u}_1, \tag{3.27}$$

$$\bar{c}^{(2)}u_{2,22} + (c_{12} + c_{66})u_{1,12} + (c_{52} + c_{76})u_{1,23} + 2c_{29}u_{2,12} + 2c_{24}u_{2,32} = \rho\ddot{u}_2, \tag{3.28}$$

$$\bar{c}^{(3)}u_{3,22} + (c_{17} + c_{86})u_{1,12} + (c_{36} + c_{57})u_{1,23} + 2c_{45}u_{3,12} + 2c_{43}u_{3,32} = \rho\ddot{u}_3. \tag{3.29}$$

The all-possible solutions for displacements for the equations are:

$$u_1(x_2,t) = (A sin\eta x_2 + B cos\eta x_2)e^{-\xi x_1}e^{-\upsilon x_3}e^{j\omega t} \quad (3.30)$$

$$u_2(x_2,t) = (C sin\eta x_2 + D cos\eta x_2)e^{-\xi x_1}e^{-\upsilon x_3}e^{j\omega t} \quad (3.31)$$

$$u_3(x_2,t) = (E sin\eta x_2 + F cos\eta x_2)e^{-\xi x_1}e^{-\upsilon x_3}e^{j\omega t} \quad (3.32)$$

Where, $\eta$ is the thickness wavenumber, $\xi$ and $\nu$ are small lateral wave numbers along $x_1$ and $x_3$ directions, respectively and we intend to establish a dispersion relation for *C*-mode of vibration when $\xi$ and $\nu \rightarrow 0$. Following Tiersten's contribution, the characteristic equations involving the stress tensor and the dielectric displacement at equilibrium for thickness fluctuations and in the limit of $x_2 = \pm h$ the possible solution of displacement in equation (3.30) is as:

$$u_1(x_2,t) = (A sin\eta x_2^{+h} + B cos\eta x_2^{-h})e^{-\xi x_1}e^{-\upsilon x_3}e^{j\omega t} \quad (3.33)$$

Where, we have $\eta = \frac{n\pi}{h}$ and $n = 1, 3, 5 \ldots$ because of electrical boundary conditions in a quartz resonator only the odd modes are excited piezoelectrically and the velocity of propagation for shear waves is $\nu = \sqrt{\frac{\bar{c}}{\rho}}$ which satisfies the equilibrium condition for the limit $x_2 = \pm h$. Therefore, [100] gives the angular frequency $\omega_n$ as:

$$\omega_n = \frac{\pi n \nu}{2h} = \frac{n\pi}{2h}\sqrt{\frac{\bar{c}}{\rho}} \quad (3.34)$$

### 3.2.2 Energy trapping in electrodes

William Shockley et al. devised the phenomena of energy trapping in electrodes of defined thickness to obtain a strong resonance in 1963. They mathematically and experimentally explained energy trapping in terms of lateral standing-wave trapped-energy modes [100] and showed that trapping phenomenon relates to the notion of cut-off frequency. As indicated in Figure 3.3 if the cut-off frequency of the outer areas (non-grid part) is greater than the excitation frequency of the resonator, the energy essentially confines in the central zone (grid part). Therefore, it appears an exponential decay of the vibrational energy from the central point of the resonator.

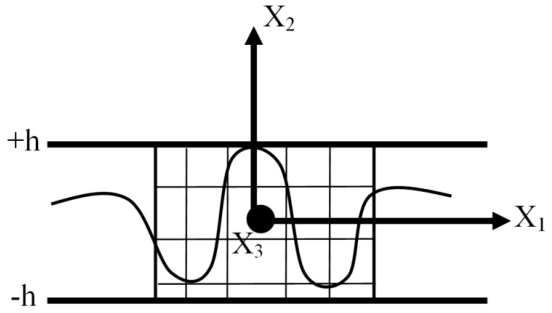


*Figure 3.3: Energy trapping zone defined by Shockley.*

The energy trapping is related to the resonant frequency of the infinite plate for the numerous lateral waves in the directions $x_1$ and $x_3$. There is a faint influence of the lateral wave numbers in comparison to the shear wave numbers in $x_2$ directions. The dispersion relation [98] connecting the resonance with a little or no influence in $x_1$ and $x_2$ direction is:

$$M_n\xi^2 + P_n\nu^2 + \rho\omega_n^2 = \rho\omega^2 \tag{3.35}$$

Where $\rho$ is the mass density, $\omega$ is the resonance pulse, $M_n$ and $P_n$ are the dispersion constants. Therefore, there are various configurations used to benefit from the energy-trapping phenomenon, but we will focus only on the energy trapping by the plano-convex geometrical structure proposed by Stevens and Tiersten.

### 3.2.3 Stevens – Tiersten plano-convex model

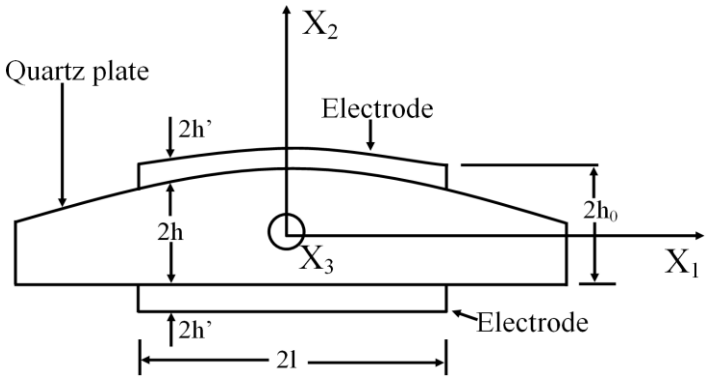


*Figure 3.4: Geometric definition of Plano-convex resonator.*

Stevens and Tiersten [98]-[101] gave the most well-known and detailed model including frequency-wavenumber dispersion relation in the doubly rotated SC-cut in quartz plates. They derived this relation just by using the equations of linear piezoelectricity within associated boundary conditions on the major vibrating surfaces. Their model comprises of all the principal modes of vibration that can be observed in a typical SC-cut quartz crystal with plano-convex geometry i.e. $A$, $B$ and $C$ modes along with their overtones and anharmonics. So, for the derivation of frequency-wavenumber dispersive relation for *C*-mode of vibration, we obtain after the appropriate boundary conditions at the major surfaces of the electroded plate in the limiting case of small lateral wave numbers in $x_1$ and $x_3$ directions. The form of the dispersion relation in equation (3.35) given as:

$$M_n^{(1)}\xi^2 + Q_n^{(1)}\xi\nu + P_n^{(1)}\nu^2 + \frac{n^2\pi^2\bar{c}^{(1)}}{4h^2} - \rho\omega^2 = 0 \tag{3.36}$$

Where the dispersion constants $M_n^{(1)}$, $P_n^{(1)}$, and $Q_n^{(1)}$ for mode *C* are given by:

$$\begin{aligned} M_n^{(1)} = c_{11} - \frac{c_{16}^2}{\bar{c}^{(1)}} + r_2(c_{12}+c_{66}) + r_5(c_{17}+c_{86}) \\ + \frac{4\left(r_2\bar{c}^{(1)} - c_{66}\right)\left(r_2\bar{c}^{(2)} + c_{12}\right)}{\bar{c}^{(2)}\kappa_2 n\pi}\cot\kappa_2\frac{n\pi}{2} \\ + \frac{4\left(r_5\bar{c}^{(1)} - c_{86}\right)\left(r_5\bar{c}^{(3)} + c_{17}\right)}{\bar{c}^{(3)}\kappa_3 n\pi}\cot\kappa_3\frac{n\pi}{2} \end{aligned} \tag{3.37}$$

$$Q_n^{(1)} = 2c_{51} - \frac{2c_{16}c_{56}}{\bar{c}^{(1)}} + r_2(c_{52} + c_{76}) + r_4(c_{12} + c_{66}) + r_3(c_{17} + c_{86}) + r_5(c_{36} + c_{57}) + \frac{4(r_2\bar{c}^{(1)} - c_{66})(r_4\bar{c}^{(2)} + c_{52}) + (r_2\bar{c}^{(2)} + c_{12})(r_4\bar{c}^{(1)} - c_{76})}{\bar{c}^{(2)}\kappa_2 n\pi} cot\,\kappa_2 \frac{n\pi}{2} + \frac{4(r_5\bar{c}^{(1)} - c_{86})(r_3\bar{c}^{(3)} + c_{57}) + (r_5\bar{c}^{(3)} + c_{17})(r_3\bar{c}^{(1)} - c_{36})}{\bar{c}^{(3)}\kappa_3 n\pi} cot\,\kappa_3 \frac{n\pi}{2} \quad (3.38)$$

$$P_n^{(1)} = c_{58} - \frac{c_{56}^2}{\bar{c}^{(1)}} + r_4(c_{52} + c_{76}) + r_3(c_{36} + c_{57}) + \frac{4(r_4\bar{c}^{(1)} - c_{76})(r_4\bar{c}^{(2)} + c_{52})}{\bar{c}^{(2)}\kappa_2 n\pi} cot\,\kappa_2 \frac{n\pi}{2} + \frac{4(r_3\bar{c}^{(1)} - c_{36})(r_3\bar{c}^{(3)} + c_{57})}{\bar{c}^{(3)}\kappa_3 n\pi} cot\,\kappa_3 \frac{n\pi}{2} \quad (3.39)$$

Where we have:

$r_2 = \frac{c_{12}+c_{66}}{\bar{c}^{(1)}-\bar{c}^{(2)}}$, $r_3 = \frac{c_{36}+c_{57}}{\bar{c}^{(1)}-\bar{c}^{(3)}}$, $r_4 = \frac{c_{52}+c_{76}}{\bar{c}^{(1)}-\bar{c}^{(2)}}$, $r_5 = \frac{c_{17}+c_{86}}{\bar{c}^{(1)}-\bar{c}^{(3)}}$, $\kappa_2 = \sqrt{\frac{\bar{c}^{(1)}}{\bar{c}^{(2)}}}$ and $\kappa_3 = \sqrt{\frac{\bar{c}^{(1)}}{\bar{c}^{(3)}}}$ [98] [100].

Here, considering displacement equations and boundary conditions for odd modes and for small lateral waves ξ and ν we have:

$$\left(M_n^{(1)}\xi^2 + Q_n^{(1)}\xi\nu + P_n^{(1)}\nu^2 + \frac{n^2\pi^2\bar{c}^{(1)}}{4h^2} - \rho\omega^2\right)u_1^n = 0 \quad (3.40)$$

Here, $M_n^{(j)}$, $P_n^{(j)}$and $Q_n^{(j)}$ are functions of the plate crystalline orientation, thickness mode given as $\hat{c}^{(j)} = \bar{c}^{(j)}\left(1 - \frac{8k_j^2}{n^2\pi^2} - 2\hat{R}\right)$(used in equations below), and $k_j^2 = \frac{e_{26}^2}{\bar{c}^{(1)}\varepsilon_{22}}$, $\hat{R} = 2h'\rho'/\rho h$ is the ratio of mass of electrodes and resonator, where $\rho'$ as the mass density of electrodes, the index $j = 1, 2, 3$ denote the *C*, *A* and *B* modes of vibration respectively. The asymptotic solution for the displacement $u_1$ for odd modes is given by:

$$u_1^n = 2\sin\left(\frac{n\pi x_2}{2h}\right)e^{-i\xi x_1}e^{-i\nu x_3}e^{i\omega t} \quad (3.41)$$

The form of the dispersion relation in equation (3.40) changes as a homogenous differential equation for $u_1^n$ -governing the mode shape along the surface of the electrodes is:

$$\left(M_n^{(1)}\frac{\partial^2 u_1^n}{\partial x_1^2} + Q_n^{(1)}\frac{\partial^2 u_1^n}{\partial x_1 \partial x_3} + P_n^{(1)}\frac{\partial^2 u_1^n}{\partial x_3^2} + \frac{n^2\pi^2\hat{c}^{(j)}}{4h^2}u_1^n\right) - \rho\ddot{u}_1^n = 0 \quad (3.42)$$

Likewise, the solution of the above homogenous equation (3.42) signify for the electroded region of the plate and further gets modified to the inhomogeneous form, hence, for three-odd modes we have as (further calculation details in [98]):

$$\sum_{n=1,3,5}^{\infty}\left(M_n^{(1)}\frac{\partial^2 u_1^n}{\partial x_1^2} + Q_n^{(1)}\frac{\partial^2 u_1^n}{\partial x_1 \partial x_3} + P_n^{(1)}\frac{\partial^2 u_1^n}{\partial x_3^2} - \frac{n^2\pi^2\hat{c}^{(j)}}{4h^2}u_1^n - \rho\ddot{u}_1^n\right) = \rho\omega^2(-1)^{(n-1)/2}\frac{e_{26}}{c^{(1)}}\frac{4Ve^{i\omega t}}{n^2\pi^2} \quad (3.43)$$

Where $Ve^{i\omega t}$ is the applied voltage, and the mixed derivative term in a second-order partial differential equation in (3.43) may be removed by an appropriate planar transformation of the independent coordinates $x_1$ and $x_3$. The transformation from [98] given as :

$$x_j = R_{ij}x_i' \text{ and } x_i' = R_{ij}x_j \tag{3.44}$$

$$R_{ij} = \begin{bmatrix} \cos\hat{\beta}_n & 0 & -\sin\hat{\beta}_n \\ 0 & 1 & 0 \\ \sin\hat{\beta}_n & 0 & \cos\hat{\beta}_n \end{bmatrix}$$

$$\hat{\beta}_n = \frac{1}{2}\tan^{-1}\left(\frac{-\mathrm{Q}_\mathrm{n}^{(1)}}{\mathrm{M}_\mathrm{n}^{(1)} - \mathrm{P}_\mathrm{n}^{(1)}}\right)$$

$R_{ij}$ , here represents the rotation about $x_2$ by the angle $\hat{\beta}_n$. The above transformation establishes the solution of the equation (3.43) and expressed in a separable form. The differential equation of the equivalent form for the $n^{\text{th}}$ harmonic family of an electrode, doubly rotated quartz plate is given by the form:

$$\left(M_n'^{(1)}\frac{\partial^2 u_1^n}{\partial x_1'^2} + P_n'^{(1)}\frac{\partial^2 u_1^n}{\partial x_3'^2} - \frac{n^2\pi^2\hat{\mathrm{c}}^{(1)}}{4h^2}u_1^n - \rho\ddot{u}_1^n\right) = \rho\omega^2(-1)^{(n-1)/2}\frac{e_{26}}{\mathrm{c}^{(1)}}\frac{4V\mathrm{e}^{\mathrm{i}\omega\mathrm{t}}}{n^2\pi^2} \tag{3.45}$$

Where $Ve^{i\omega t}$ is the applied voltage and the dispersion constants $M_n'^{(1)}$ and $P_n'^{(1)}$ are:

$$M_n'^{(1)} = M_n\cos^2\hat{\beta}_n - Q_n\ \sin\hat{\beta}_n\cos\hat{\beta}_n + P_n\ \sin^2\hat{\beta}_n \tag{3.46}$$

$$P_n'^{(1)} = M_n\sin^2\hat{\beta}_n + Q_n\ \sin\hat{\beta}_n\cos\hat{\beta}_n + P_n\ \cos^2\hat{\beta}_n \tag{3.47}$$

The equation (3.45) is the equation of motion defined for the plane of plate. We consider the plano-convex geometry for the design of the resonator. Equation (3.48) gives the gradual thickness variation of the radius of curvature of the convex part from where onwards we insert the values defined for the plano-convex design of the resonator.

## 3.3 Modelisation of SC- cut BAW quartz crystal resonator using Tiersten's model

### 3.3.1 Investigation of flicker noise of ultra-stable quartz crystal resonator

We measure phase noise in 5 MHz SC-cut BAW resonators. The typical 5 MHz SC-cut resonator that we discuss having the diameter of 14 mm and thickness of 1.09 mm [102]. A plano-convex shape allows the energy trapping for the 3rd overtone of the slowest thickness shear mode (*C*-mode). A radius of curvature of 130 mm chosen to optimize this energy trapping according to the Tiersten-Stevens [98] model and the diameters of electrodes are 8 mm. The plano-convex shape has sharper angle of propagation of acoustic waves as we move from the centre to the edges. The value of radius of curvature *R* was chosen by taking the distance from the ratio of vibration of amplitude from the centre to one of the edges of the plano-convex shape to be around $10^6$.

The Figure 3.4 is the well-known model by Steven and Tiersten. Because of the plano-convex shape, the thickness of the resonator $2h$ is:

$$2h \cong 2h_0\left[1-\frac{(x_1^2+x_3^2)}{4Rh_0}\right] \tag{3.48}$$

Where, we insert equation (3.48) in (3.45) for the plano-convex resonator we have:

$$M_n'^{(1)}\frac{\partial^2 u_1^n}{\partial x_1'^2}+P_n'^{(1)}\frac{\partial^2 u_1^n}{\partial x_3'^2}-\frac{n^2\pi^2\hat{c}^{(1)}}{4h_0^2}\left(1+\frac{(x_1^2+x_3^2)}{2Rh_0}\right)u_1^n+\rho\omega^2 u_1^n = \rho\omega^2(-1)^{(n-1)/2}\frac{e_{26}}{c^{(1)}}\frac{4V e^{i\omega t}}{n^2\pi^2} \tag{3.49}$$

For voltage, $V = 0$ the solution of amplitude of the mechanical displacement in the resonator given by the Hermite polynomials is as formulas (124) and (125) of [98]:

$$u_1^{(nmp)} = e^{-\alpha_n^{(1)}\left(\frac{x_1^2}{2}\right)}H_m\left(\sqrt{\alpha_n^{(1)}}\,x_1\right)e^{-\beta_n^{(1)}\left(\frac{x_3^2}{2}\right)}H_p\left(\sqrt{\beta_n^{(1)}}x_3\right)\cdot e^{j\omega_{nmp}t} \tag{3.50}$$

$$\text{With: } \alpha_n^{(1)2} = \frac{n^2\pi^2\hat{c}^{(1)}}{8Rh_0^3 M_n'^{(1)}} \text{ and } \beta_n^{(1)2} = \frac{n^2\pi^2\hat{c}^{(1)}}{8Rh_0^3 P_n'^{(1)}} \tag{3.51}$$

Where, the superscript (1) denotes the solution for acoustic vibration of mode-*C*, $n = 1,3,5,\ldots$ are the overtone numbers, and $m,p = 0,2,4\ \ldots$, represents the different mode shapes in the plane of the resonator or termed as the ranks of the anharmonic modes. $H_m$ and $H_p$ are Hermit polynomials. $R$ is the curvature radius. $2h_0$ is the thickness of the resonator centre, $M_n'^{(1)}$ and $P_n'^{(1)}$ are the dispersion constants, $\hat{c}^{(1)}$ corresponds with effective elastic constant associated to the propagation of $C$ mode of vibration including piezoelectricity and electrodes. Therefore, the resonant frequency of the mode is:

$$\omega_{nmp}^{(1)} = \sqrt{\frac{n^2\pi^2\hat{c}^{(1)}}{4h_0^2\rho}\left[1+\frac{1}{n\pi}\sqrt{\frac{2h_0}{R}}\left(\sqrt{\frac{M_n'^{(1)}}{\hat{c}^{(1)}}}(2m+1)+\sqrt{\frac{P_n'^{(1)}}{\hat{c}^{(1)}}}(2p+1)\right)\right]} \tag{3.52}$$

The motional capacitance for the Plano-convex shape further expressed as [103]:

$$C_{mot\_nmp}^{(1)} = \frac{64\hat{e}_{26}^{(1)2}\left(\int_0^{\frac{D}{2}} e^{-\alpha_n^{(1)}\frac{x_1^2}{2}}H_m(\sqrt{\alpha_n^{(1)}}x_1)dx_1\cdot\int_0^{\frac{D}{2}} e^{-\beta_n^{(1)}\frac{x_3^2}{2}}H_p(\sqrt{\beta_n^{(1)}}x_3)dx_3\right)^2\sqrt{\alpha_n{}^{(1)}}\sqrt{\beta_n^{(1)}}}{n^2\pi^3 2^m m!\,2^p p!\,h_0\hat{c}^{(1)}} \tag{3.53}$$

Where D is the electrode diameter, $\hat{e}_{26}^{(1)}$ the effective piezoelectric constant that considers the direction of the vibration of the mode. Resolution of the Christoffel equations [103] gives the complex Eigen value $\hat{c}^{(1)} + i\hat{\eta}^{(1)}$, where $\hat{\eta}^{(1)}$ is the viscosity matrix [104]. Then, we can obtain an order of magnitude of the $Q^{(1)}$ factor using the following equation:

$$Q^{(1)} = \frac{\hat{c}^{(1)}}{\hat{\eta}^{(1)}\cdot 2\pi f_{nmp}^{(1)}} \tag{3.54}$$

The energy trapping is quasi-independent of the electrode's dimensions in contoured resonators. It influences the motional resistance and the static capacitor. Consequently, we can compute the motional resistance $R_{mot}$ from the motional capacitance $C_{mot}$ using:

$$R_{mot\_nmp} = \frac{1}{Q^{(1)} C^{(1)}_{mot\_nmp} 2\pi f^{(1)}_{nmp}} = \frac{L^{(1)}_{mot\_nmp} 2\pi f^{(1)}_{nmp}}{Q^{(1)}} \tag{3.55}$$

The static capacitor $C_0$ has the following expression as:

$$C_0 = \frac{\pi D^2}{4}\left(1 + \frac{(D/2)^2}{8Rh_0}\right)\frac{\varepsilon_{22} + \frac{\hat{e}^{(1)2}_{26}}{\hat{c}^{(1)}}}{2h_0} \tag{3.56}$$

Where, $\varepsilon_{22} = 39.78 \cdot 10^{-12}\ F/m$ is the permittivity constant in SC-cut.

### 3.3.2 Instability in Quartz crystal resonator

Frequency control and stability of the quartz resonator at a given frequency is an important criteria in the design of resonators. The design carries out for ultra-stable quartz crystal resonator on different parameters, which needs to be counteracted. The parameter, which is of concern for frequency stability is frequency-temperature effect. Due to the material properties of quartz, resonators manufactured using quartz for high frequency applications i.e. greater than 1 MHz should be stable in the orders of parts per million. The frequency instabilities of resonators at higher frequencies and excitation levels may have their origin in nonlinear behaviour of quartz crystal resonators. This non-linearity has possible origins due to the omnipresence of defects in the quartz crystal during the fabrication process. These phenomena depend on the crystal anisotropy and geometry, and the wave structure of the propagating wave and possibly $1/f$ phase noise might be the result of these non-linearity possibly due to defects.

The crystal resonator plate is isolated using the special enclosure. The resonant frequency depends on the size, shape, elasticity, and the speed of the acoustic wave in the material. When we cut a crystal of quartz properly and mount it, its frequency dependence on temperature can be very low. However, the vibration modes of the quartz resonator depend on the temperature. The temperature variation causes the quartz to expand anisotropically by nature and the value of its elastic coefficients vary. This temperature variations causes shift in the resonant frequency of the resonator. To describe the frequency temperature effect, we take the expression of angular frequency for an infinite plate given by Shockley [100] in equation (3.34) as:

$$\omega_n = \frac{n\pi}{2h(T)}\sqrt{\frac{\bar{c}^{(j)}(\mathrm{T})}{\rho(T)}} \tag{3.57}$$

Where $\bar{c}^{(j)}(T)$ is the effective elastic coefficient and $j = 1, 2$ and 3 determine the acoustic modes-*C*, *A* and *B*, $h(T)$ is the thickness of the plate, $\rho(T)$ is the mass density. This formula generalizes using the Taylor series expansion as [105]:

$$G(T) = G(T_o)\left[1 + \sum T^{(s)} G(T - T_o)^s\right] \tag{3.58}$$

Where, $G$ is the dummy variable, which can be equal to either $h, \rho$ or $\bar{c}$ , $T_o$ is the reference temperature normally around 294 K and $s$ is the order of the thermal coefficient given in the form:

$$T^{(s)}G = \frac{1}{q!}\frac{1}{G(T_o)}\frac{d^s G}{dT^s} \tag{3.59}$$

Usually, the order is limited by $s = 3$ that makes the frequency-temperature curve to have a cubic shape along with third order thermal coefficients of the elastic constants. Following equation (3.59) the relation between frequency and temperature written as [106]-[108]:

$$\frac{\Delta f_n}{f_{no}} = T_f^{(1)}(T - T_o) + T_f^{(2)}(T - T_o)^2 + T_f^{(3)}(T - T_o)^3 \tag{3.60}$$

Where, $f_{no}$ is the initial frequency of resonance at $T_o$ and $T_f^{(1)}, T_f^{(2)}, T_f^{(3)}$ are the frequency coefficients of the temperatures respectively. In equation (3.60), we can see the relationship between the frequency and the temperature along with their coefficients is of the polynomial form, and the resonators fabricated, operates exactly at these points to nullify the frequency-temperature derivatives. On the contrary, the technical constraints don't allow to nullify all the frequency-temperature derivatives to zero and this is the reason why almost all the quartz resonators do not have exactly the same turn-over temperature and end having a turn-over point almost around (74-84° C) above the room temperature. The third order expressions [107] of equation (3.59) as:

$$T_{f_n}^{(1)} = -\frac{1}{2}T_\rho^{(1)} - T_h^{(1)} + \frac{1}{2}T_{\bar{c}}^{(1)} \tag{3.61}$$

$$T_{f_n}^{(2)} = -\frac{1}{4}\left[T_{\bar{c}}^{(1)}\right]^2 + \frac{1}{2}\left[T_{f_n}^{(1)}\right]^2 + \frac{1}{4}\left[T_\rho^{(1)}\right]^2 + \frac{1}{2}\left[T_h^{(1)}\right]^2 - \frac{1}{2}T_\rho^{(2)} - T_h^{(2)} + \frac{1}{2}T_{\bar{c}}^{(2)} \tag{3.62}$$

$$T_{f_n}^{(3)} = T_{f_n}^{(1)}T_{f_n}^{(2)} - \frac{2}{6}T_{f_n}^{(1)} - \frac{1}{6}\left[T_\rho^{(1)}\right]^3 + \frac{1}{6}\left[T_{\bar{c}}^{(1)}\right]^3 - \frac{2}{6}\left[T_h^{(1)}\right]^3 + \frac{1}{2}T_\rho^{(1)}T_\rho^{(2)} + T_h^{(1)} \cdot T_h^{(2)} - T_h^{(3)} - \tfrac{1}{2}T_{\bar{c}}^{(1)} \cdot T_{\bar{c}}^{(2)} - \tfrac{1}{2}T_\rho^{(3)} + \tfrac{1}{2}T_{\bar{c}}^{(3)} \tag{3.63}$$

The coefficients of temperature relative to the thickness $h$ are related to the linear coefficients of thermal expansions $\alpha_{11}$ and $\alpha_{33}$ in the direction X and Z respectively [105], the third order expressions are:

$$T_h^{(1)} = T_{\alpha_{11}}^{(1)} + T_{\alpha_{33}}^{(1)} \tag{3.64}$$

$$T_h^{(2)} = T_{\alpha_{11}}^{(2)} + T_{\alpha_{33}}^{(2)} \tag{3.65}$$

$$T_h^{(3)} = T_{\alpha_{11}}^{(3)} + T_{\alpha_{33}}^{(3)} \tag{3.66}$$

For the mass density $\rho$ the third order expressions are:

$$T_\rho^{(1)} = -\left(2T_{\alpha_{11}}^{(1)} + T_{\alpha_{33}}^{(1)}\right) \tag{3.67}$$

$$T_\rho^{(2)} = -\left(2T_{\alpha_{11}}^{(1)} + T_{\alpha_{33}}^{(2)} - 3\left(T_{\alpha_{11}}^{(1)}\right)^2 - \left(T_{\alpha_{33}}^{(1)}\right)^2 - 2T_{\alpha_{11}}^{(1)}T_{\alpha_{33}}^{(1)}\right) \tag{3.68}$$

$$T_{\rho}^{(3)} = -\left(2T_{\alpha_{11}}^{(3)} + T_{\alpha_{33}}^{(3)} - 2T_{\alpha_{11}}^{(1)}\left(3T_{\alpha_{11}}^{(2)} + T_{\alpha_{33}}^{(2)}\right) - 2T_{\alpha_{33}}^{(1)}\left(T_{\alpha_{11}}^{(2)} + T_{\alpha_{33}}^{(2)}\right) + 3\left(T_{\alpha_{11}}^{(1)}\right)^2 T_{\alpha_{33}}^{(1)} + 2T_{\alpha_{11}}^{(1)}\left(T_{\alpha_{33}}^{(1)}\right)^2 + 4\left(T_{\alpha_{11}}^{(1)}\right)^3 + \left(T_{\alpha_{33}}^{(1)}\right)^3\right) \quad (3.69)$$

The acoustic resonant frequency of a mechanical system is a function of its elastic coefficients of the material, which are temperature dependent. For quartz, in a plano-convex geometry with energy trapping we have the relation between stress-strain given by Cauchy as [106] [107]:

$$T_{ij} = c_{ijkl}\frac{\partial_{u_k}}{\partial_{x_l}} \quad (3.70)$$

Where, we have $c_{ijkl}$ is the tensor of elastic constants and $u_k$ the displacement vector. This realization when put in the equation (3.58) gives:

$$c_{ijkl}(T) = c_{ijkl}(T_o)\left[1 + \sum\nolimits_y T_{c_{ijkl}}^{s}(T - T_o)^s\right] \quad (3.71)$$

Where, $c_{ijkl}(T_o)$ is the elastic coefficients at the reference temperature $T_o$ and $T_{c_{ijkl}}^{s}$ of order $s$.

For the plano-convex shape resonator the resonant frequency in equation (3.52) can be re-written as:

$$f_{nmp}^2 = f_n^2\left[1 + \frac{1}{n\pi}\sqrt{\frac{2h}{R}}\left(\sqrt{\frac{M_n^{'}}{\hat{c}^{(1)}}}(2m+1) + \sqrt{\frac{P_n^{'}}{\hat{c}^{(1)}}}(2p+1)\right)\right] \quad (3.72)$$

Where, $f_n$ is the expression of frequency for the infinite plate resonator. By integrating, the fact that quartz is a piezoelectric material and considering the metallization of the exciting electrodes, the eigen frequency for the electroded plate is:

$$f_n^{(j)\ 2}(T) = \frac{n^2}{4h^2(T)}\frac{\bar{c}^j(T)}{\rho(T)}\left(1 - \frac{8k_\alpha^2}{n^2\pi^2} - \hat{R}\right) \quad (3.73)$$

where $\bar{c}^{(j)}$ is the effective elastic coefficient and $j$ determines the different modes of vibration, $k_\alpha^2$ electromechanical coupling coefficient, $h$ is half of the total thickness of the resonator because thickness of electrodes are very small around 200 nm, $\rho$ is the mass density of the quartz, $\hat{R}$ is the ratio of mass of the resonator and that of the electrodes. We neglect the terms $\hat{R}$ because it has no contribution to temperature, $k_\alpha^2$ because it has very low value around $10^{-4}$ and the term $n^2$ at the denominator of the equation (3.73) has almost negligible influence. Therefore, the frequency temperature curve follows the equation (3.57) of the given overtone and mode.

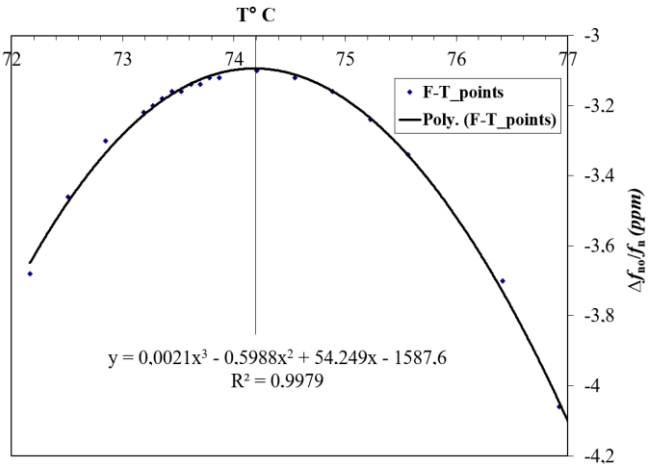


*Figure 3.5: Frequency-Temperature curve of 5 MHz SC-cut plano-convex shape resonator.*

The frequency-temperature curve for *C*- mode SC-cut quartz crystal resonator of 1.09 mm thickness and curvature radius of 130 mm, shown in Figure 3.5. The curve shows the turnover temperature to be around 74.1 °C. It has been observed that the value of the inversion point temperature of the quartz crystal resonators is never exactly same even been fabricated with same orientation, cut, thickness etc. This is the reason why the inversion point temperature has been represented in a range and raises a question whether any similarity exists or not for the same kinds of resonators in all aspects.

## 3.4 Experimental results on phase noise measurement in BAW resonators

The Figure 3.6 represents the noise floor of the interferometric bench at 5 MHz operating frequency at room temperature. The resulting flicker frequency floor is given in terms of Allan Deviation ( short- term stability $\sigma_{y\_floor}$).

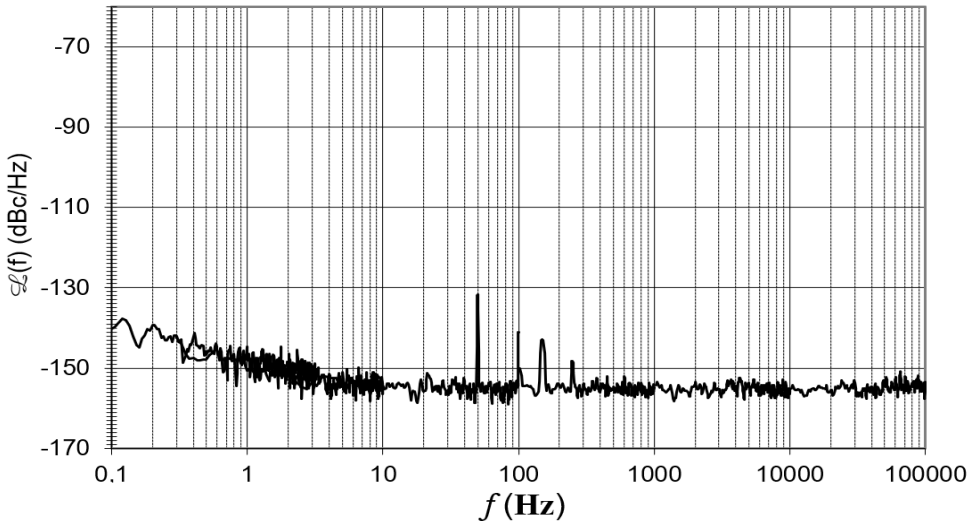


*Figure 3.6: Phase noise graph of the noise floor.*

Once the noise floor is realised, we put the 5 MHz SC-cut quartz crystal resonators as our measurement resonators. The resonators once connected to the arms of the bench remains for more than five hours in the oven to let it stabilize and adapt the bench for having the good value of noise keeping in mind that the room temperature is always around 21° C. Figure 3.7 typically shows the phase noise

measurement of the resonator pair. From the graph, we can observe that at 1 Hz, the value of the PSD of phase fluctuation is approximately around $-139\ dBcHz^{-1}$ , obtained by measuring the phase noise in a pair of resonators and, hence, for that value of PSD the leeson frequency $F_L$ is around 2 Hz. We did the same kind of phase noise measurements for the series of resonator pairs and categorised the resonators as Good-good, Good-average, and Good-bad resonator pairs. The notations good, average and bad resemble distinction of resonators based on PSD of phase fluctuation values as shown in Table 3.3 and Table 3.4. Likewise, on tables, we also report Q-factors for several overtones and anharmonic modes of the resonators, measured at 353K and at 4K as a function of short-term stability of the resonator measured on their metrological vibrating mode at 353K. Hence, the noise results of the resonators are compared according to the overtone behaviour on different vibrating modes (harmonics and anharmonics) to find a correlation with the intrinsic noise of the resonators.

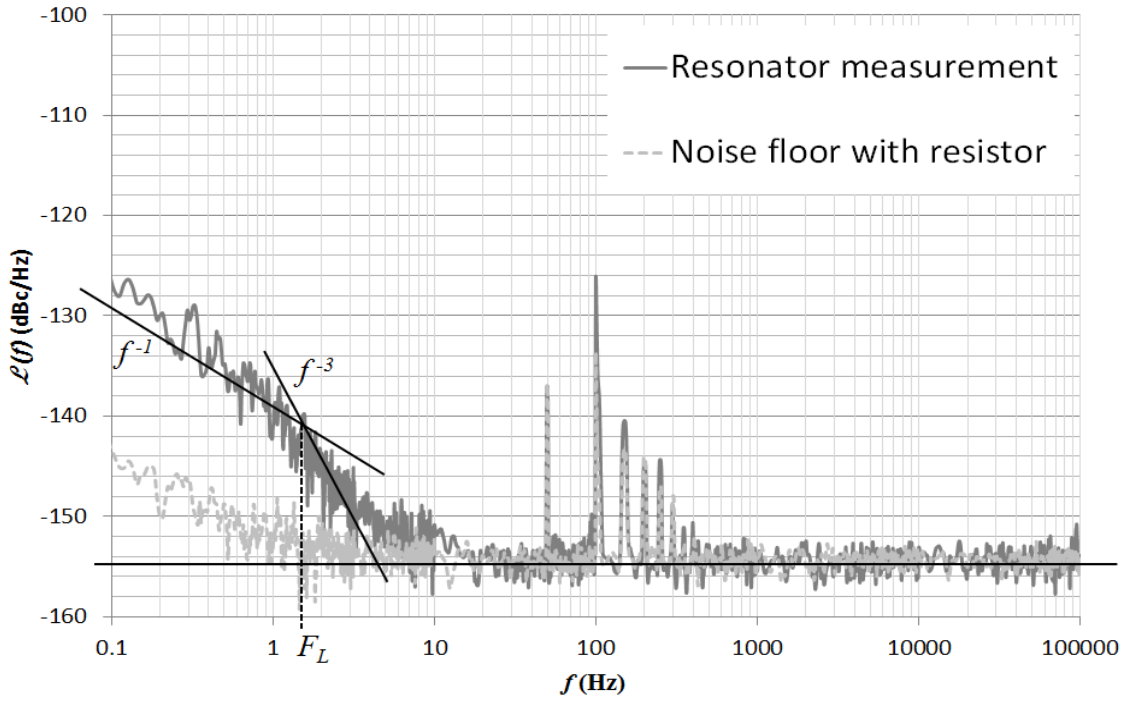


*Figure 3.7: Phase noise graph of 5 MHz SC-cut quartz resonator pair.*

We used around ten quartz crystal resonators fabricated from the same mother block to study $1/f$ noise [109]. The Table 3.2 mentions the theoretical resonant frequencies for each mode observed in the resonator computed from Tiersten's formulae [98]. Then, the experimental resonant frequencies are searched near these theoretical values (i.e. obtained using Tiersten's formula) using a network analyser. The observed modes are thickness shear and longitudinal modes (*A*: longitudinal, *B*: fast shear mode, *C*: slow shear mode). The representation of modes i.e. the first letter refers to the vibrating type, the first number is the overtone and the second and third numbers gives the rank of the anharmonic modes. The Q-factors of Mode-C at different overtones and ranks and anharmonic modes of C300 shown in Table 3.3 and Table 3.4. For the Modes *A* and *B*, only the overtones have been tested.

| | | | | | | | | |
|---|---|---|---|---|---|---|---|---|
| Mode B | **B300** | | | | | | | |
| F (MHz) | 5.487 | | | | | | | |
| Mode A | **A300** | | | | | | | |
| F (MHz) | 9.362 | | | | | | | |
| Mode C | **C300** | **C320** | **C302** | **C340** | **C322** | **C304** | **C500** | **C700** |
| F (MHz) | 5.000 | 5.119 | 5.131 | 5.237 | 5.248 | 5.259 | 8.299 | 11.594 |

*Table 3.2: Resonant frequencies of modes A, B and C (Overtones & anharmonics of mode C300 at 4 K) as computed using Tiersten's plano convex formula.*

The resonators are typically 5 MHz SC-cut quartz crystals (details already mentioned above in section 3.3). For simplicity and confidential issues, resonators are named alphabetically from *a* to *j* [109] in Table 3.3 and Table 3.4. The empty cells with a (-) represents the mode that have not been found or without Q-factor because of failure in calibrating the spectrum analyser. Those resonators, which are termed as good *(a, b, c* and *d)*, have $\sigma_{y\_floor} < 10^{-13}$, for average *(e, f* and *g)* $10^{-13} < \sigma_{y_floor} < 10^{-12}$and for bad *(h, i, j)*, it is around $\sigma_{y\_floor} > 10^{-12}$.

| **Q ($10^6$)** | **Resos.** | *a* | *b* | *c* | *d* | *e* | *f* | *g* | *h* | *i* | *j* |
|---|---|---|---|---|---|---|---|---|---|---|---|
| | $\sigma_{y_{floor}}$ | ***6.26 × $10^{-14}$*** | ***6.25 × $10^{-14}$*** | ***5.96 × $10^{-14}$*** | ***7.11 × $10^{-14}$*** | ***1.68 × $10^{-13}$*** | ***2.12 × $10^{-13}$*** | ***3.36 × $10^{-13}$*** | ***1.81 × $10^{-12}$*** | ***2.27 × $10^{-12}$*** | ***2.30 × $10^{-12}$*** |
| **353K** | **C300** | 2.04 | 2.35 | 2.59 | 2.62 | 2.54 | 2.25 | 2.32 | 2.16 | 1.12 | 2.66 |
| | **C320** | 1.29 | 1.58 | - | 1.75 | 1.23 | - | 0.829 | 1.32 | 2.23 | 1.81 |
| | **C302** | 1.169 | 1.49 | - | 0.476 | 1.435 | - | 1.432 | 1.94 | 0.719 | 0.8237 |
| | **C340** | 0.4564 | 0.225 | - | 0.379 | 0.649 | - | 0.5475 | 0.7078 | 0.377 | 0.524 |
| | **C322** | 0.3415 | 0.407 | - | 0.213 | 0.102 | - | 0.231 | - | 0.532 | 0.306 |
| | **C304** | 0.2733 | 0.243 | - | 1.14 | 0.391 | - | 1.24 | - | 0.21 | 0.306 |
| | **C500** | 1.412 | 1.548 | - | 1.576 | 1.45 | - | 1.446 | 1.414 | 1.22 | 1.59 |
| | **C700** | 0.985 | 1.040 | - | 1.055 | 1.09 | - | 1.103 | 1.100 | 1.003 | 1.161 |

*Table 3.3: Quality factor and short-term stability ($\sigma_{y\_floor}$) at 353 K for overtones and anharmonics.*

Following these notations, we then plot graphs considering for the quality factor versus noise measurements done at 353 K and 4K. Figure 3.8 shows the quality factors Q measured at turn over temperature according to the frequency of anharmonic modes of 3rd overtones. Red dots (star and triangle) represent the resonators that have a short-term stability up to $10^{-13}$. Green dots (square and circle) the resonators with short-term stability below $10^{-13}$. Amongst the worst resonators in terms of noise ($\sigma_{y_{floor}}$ around $2.3 \cdot 10^{-12}$), resonator *i* has the lowest Q-factor ($1.12 \cdot 10^6$) and *j* has the highest Q-factor ($2.66 \cdot 10^6$).The Q-factors of C300 mode at the turnover temperature (353K) is around $2.5 \cdot 10^6$ since it was the design requirement. The Figure 3.8 clearly shows the position of 3rd overtone along with its anharmonic modes of vibration with their Q-factors as a function of the short-term stability measured at C300 [102]. The graph does not seem to show any kind of correlation between the short-term stability and Q-factor of different modes. Similarly, Figure 3.9, (A), gives an example of resonators those are good and bad i.e. *b* and *i* respectively in noise performances. Resonators *b* and *i*

have short-term stability of $6.25 \cdot 10^{-14}$ and $2.27 \cdot 10^{-12}$ respectively. The Q-factor is represented according to the frequency differences with C300 mode. Overtones C500 ($5^{th}$) and C700 ($7^{th}$) are given for both resonators and no correlation could be seen at higher overtone modes for Q-factors as a function of short-term stability measured at C300 mode.

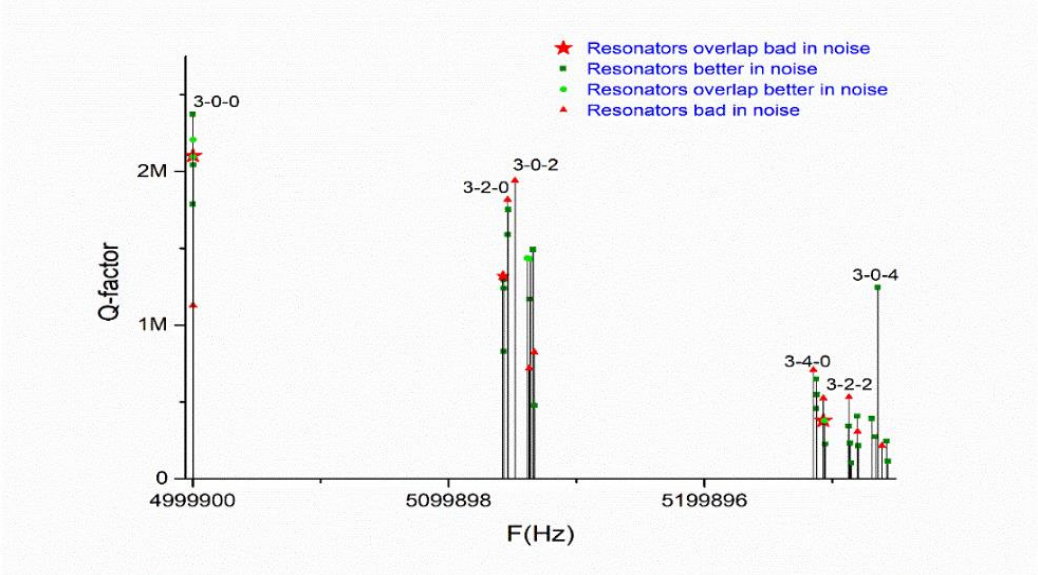


*Figure 3.8: Quality factor for anharmonics modes of vibrations at 353K.*

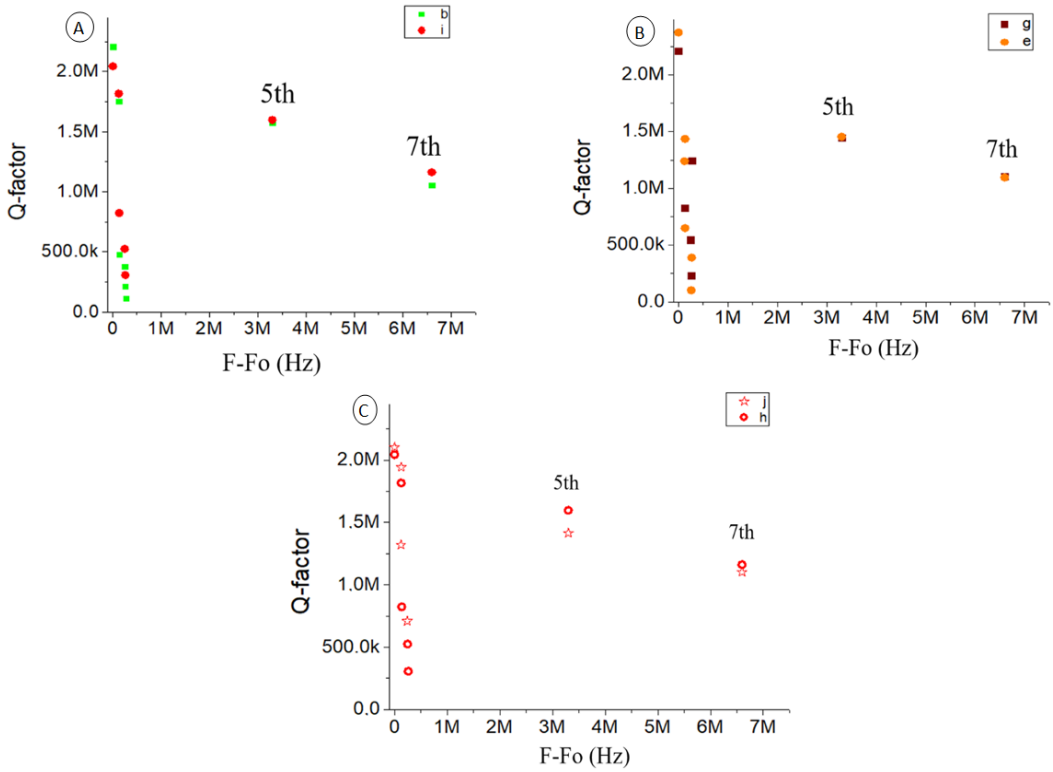


*Figure 3.9: Quality factors of resonators ( $b, i$ in(panel $A$), $g, e$ in (panel $B$) and $h, j$ in (panel $C$)) presented according to the shift of frequency measured at turnover temperature considering the short-term stability of C300 mode at 353K.*

Figure 3.9, (B), gives an example like (A) but with one average resonator and the other bad regarding performances in noise. Resonators $g$ (average) and $e$ (bad) have a short-term stability of

$3.36 \cdot 10^{-13}$ and $1.68 \cdot 10^{-13}$ respectively. Likewise, (C) is also an example of same kind of plot as in (A) and (B) but with both bad resonators showing bad performances in noise and no significant correlation could be seen in terms of Q-factor and short-term stability. Where, these resonators *j* (bad) and *h* (bad) have s short-term stability of $1.82 \cdot 10^{-12}$ and $2.30 \cdot 10^{-12}$ respectively.

| **Q** ($10^6$) | **Resos.** | *a* | *b* | *c* | *d* | *e* | *f* | *g* | *h* | *i* | *j* |
|---|---|---|---|---|---|---|---|---|---|---|---|
| | $\sigma_{y_{floor}}$ | ***6.26*** **$\times 10^{-14}$** | ***6.25*** **$\times 10^{-14}$** | ***5.96*** **$\times 10^{-14}$** | ***7.11*** **$\times 10^{-14}$** | ***1.68*** **$\times 10^{-13}$** | ***2.12*** **$\times 10^{-13}$** | ***3.36*** **$\times 10^{-13}$** | ***1.81*** **$\times 10^{-12}$** | ***2.27*** **$\times 10^{-12}$** | ***2.30*** **$\times 10^{-12}$** |
| **4K** | **C300** | 33.52 | 23.78 | 43.57 | 43.57 | 43.57 | 43.57 | 29.05 | 21.79 | 1.74 | 43.57 |
| | **C320** | 3.95 | 6.60 | 5.58 | 11.16 | 6.87 | 2.41 | 4.06 | 5.95 | 2.23 | 8.93 |
| | **C302** | 7.21 | 1.65 | 3.31 | 2.60 | 2.35 | 1.32 | 3.44 | 2.24 | 1.99 | 1.99 |
| | **C340** | - | 0.91 | - | 0.69 | 0.22 | - | - | 0.06 | - | 1.59 |
| | **C322** | 0.19 | 0.91 | - | 0.44 | 0.49 | 2.56 | 0.98 | - | - | 0.45 |
| | **C304** | 0.07 | - | 0.42 | - | 0.43 | 1.99 | - | - | - | 0.56 |
| | **C500** | 48.22 | 31.51 | 72.33 | 36.16 | 72.33 | 36.16 | 12.05 | 36.16 | 0.44 | 48.22 |
| | **C700** | - | 39.67 | 50.55 | 40.43 | 67.40 | 40.44 | 20.22 | - | 10.11 | - |
| | **B300** | 19.16 | 0.32 | | 31.92 | 31.93 | | 19.16 | 23.94 | 2.94 | 23.94 |
| | **A300** | 0.38 | 19.79 | | 5.45 | 1.95 | | 3.99 | 0.38 | 5.56 | 16.34 |

*Table 3.4: Quality factor at 4 K for overtones and anharmonics as function of short-term stability ($\sigma_{y\_floor}$) at 353K.*

Hence, continuing with the similar kind of work at 4K, Figure 3.10 shows the Q-factor of the different modes of resonators at 3rd overtones, measured at 4K and /or 353K, as a function of their $\sigma_{y\_floor}$ measured at 353K, which shows the non-existence of correlation between them for noise and quality factor measured at 4K.

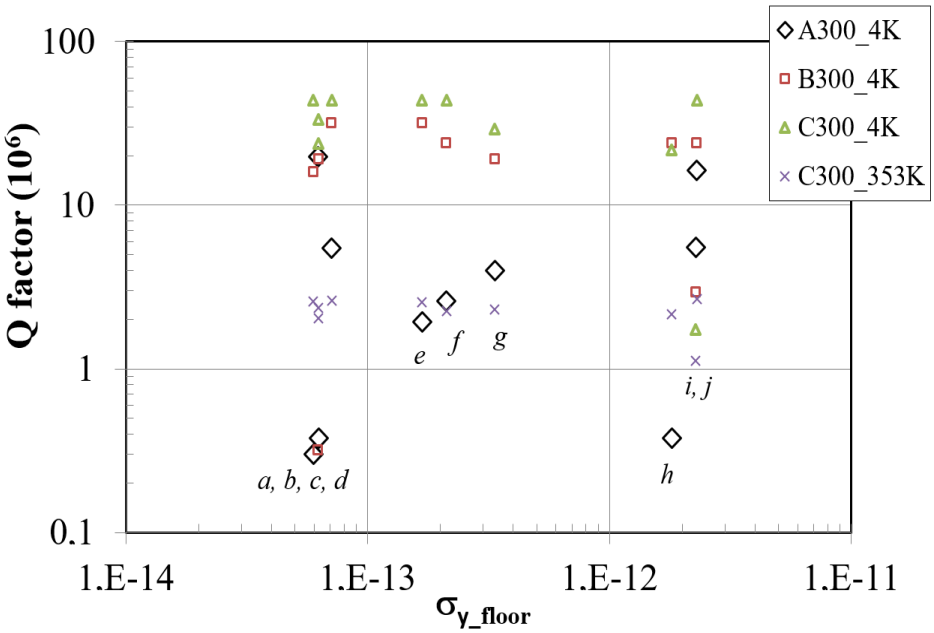


*Figure 3.10: Quality factor for different modes of vibrations (4K and/or 353K) as function of short-term stability ($\sigma_{y\_floor}$) at 353K.*

Following Table 3.4, quality factors of Mode-*C* at 4K seems to increase by a factor of 17 with respect to the results at 353 K for resonators *a*, *d*, *e*, *f* and *j*, whereas this factor is close to 10 for resonators *b*, *g* and *h* and only an order of 1.5 for resonator *i*. The results show the similarity in Q-factors from the best to the worst resonators i.e. from *a*-*j*. On the other hand, Q-factors of mode-*B* at 4K has the homogenous value (around $20 \cdot 10^6$, except for resonator *i* and *b*), and because of this, distinction between resonators were not possible.

Similarly, Figure 3.11 shows the Q-factors at 4K for anharmonic modes of C300 as a function of $\sigma_{y\_floor}$ measured for C300 mode at 353K. The anharmonic modes here are because of the energy trapping and the plano-convex shape of the resonators [98]. The Q-factors for the mode C320 and C302 have been measured for all the resonators. They are in the range of $10^6 - 10^7$, and do not show a clear correlation with the measured level of noise. For the other modes, due to the small signal and presence of parasitic capacitance, Q-factors could not be measured for some of the tested resonators (e.g. *c*, *h*, *f* and *i* for C322; *b*, *c*, *d*, *f*, *g*, *h* and *i* for 304; *a*, *c*, *f*, *g* and *i* for 340). The Q-factor values for the modes C322 and C304 are below $1 \cdot 10^6$ except for resonator *f* which has an intermediate noise level. The Q-factor for the C340 mode seems to decrease with noise level (*b*, *d*, *e* and *h*) but this tendency is contradicted by resonator *j*. We note that, for the same mode at 353 K the values are homogeneous for resonators regarding the Q-factor.

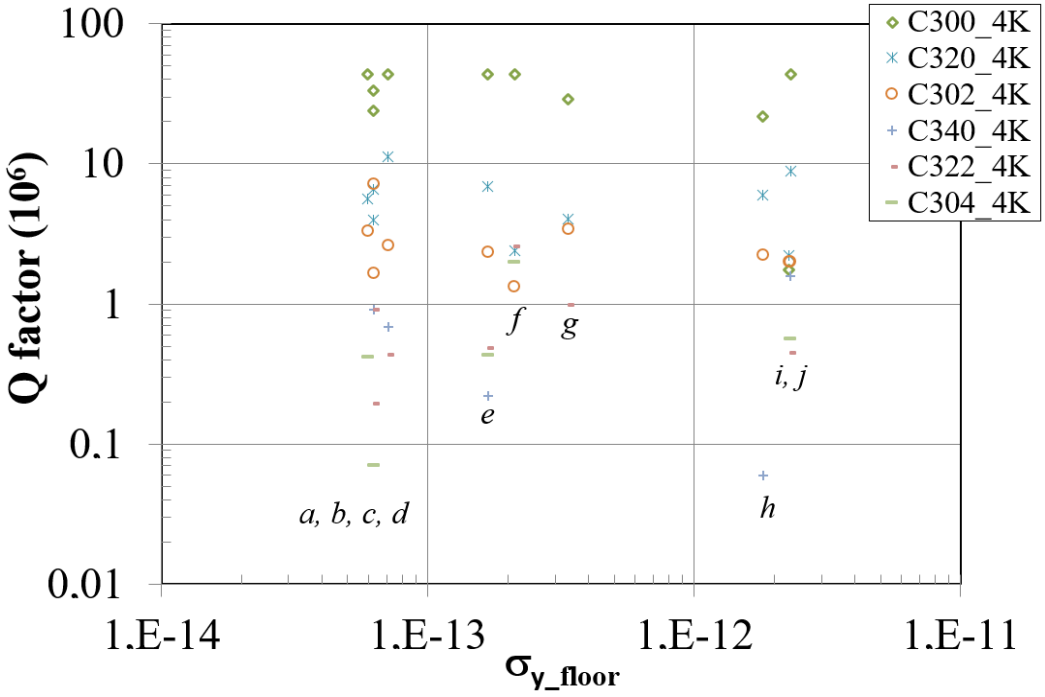


*Figure 3.11: Quality factor for anharmonic modes of C300 at 4K as a function of the short-term stability ($\sigma_{y\_floor}$) measured for C300 mode at 353K.*

Figure 3.12 shows the Q-factors for the overtones of C300 mode (i.e. C500 and C700) as a function of the noise level. The Q-factor of the C700 mode could not be measured for resonators *c*, *h* and *j*. The worst resonator in terms of noise also has the minimum value for C500.

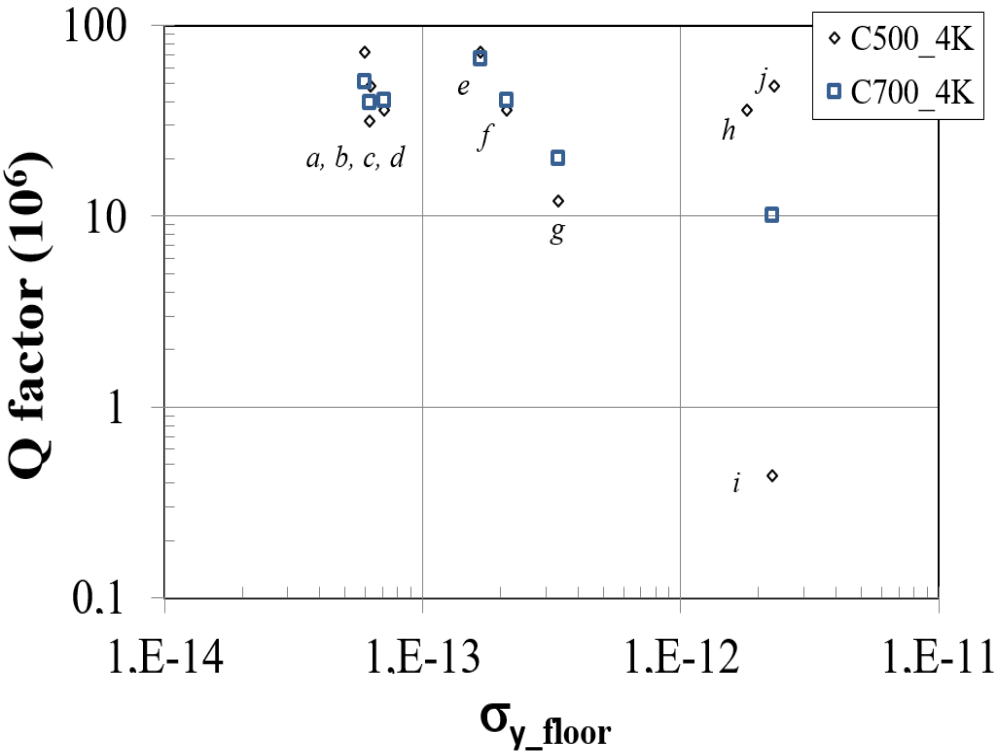


*Figure 3.12: Q-factor of overtone modes (at 4K) as function of short-term stability (measured for C300 mode at 353K).*

Likewise, in search for finding the resonant frequencies of harmonic and anharmonic modes of three different acoutic modes of vibration i.e. mode *A*, mode *B* and mode *C* at 353K we measured the transfer function of our BAW resonators and established a comparison between experimental values and Tiresten's value for resonant frequencies of different anharmonic modes. We observed that Tiersten's formula was not found exactly for determining the resonant frequencies which can be seen in Figure 3.13. For the fundamental mode-*C*, the value of resonant frequency experimentally measured and those calculated using Tiersten's formula had a difference up to 10 Hz which could be considered to some extent. But the difference in resonant frequencies for anharmonic modes and overtone modes were very high, some of them were even in orders of kHz which were beyond consideration.

As we measure phase noise in resonator pairs, this huge difference in resonant frequencies (for e.g around kHz and more) did not allow us to measure phase noise in anharmonic modes and overtone modes. We were not successful to even find a single resonator pair where the difference in their resonant frequencies were less than 5 Hz. Therefore, apparatus of our phase noise measuring bench is not compatible to adjust the difference in frequencies beyond 5 Hz and we failed to measure noise on anharmonic modes and overtones. For the anharmonic modes at 4K, the significant increase in the quality factor exists but the differences in overtones and anharmonics shows same nature as in 353K.

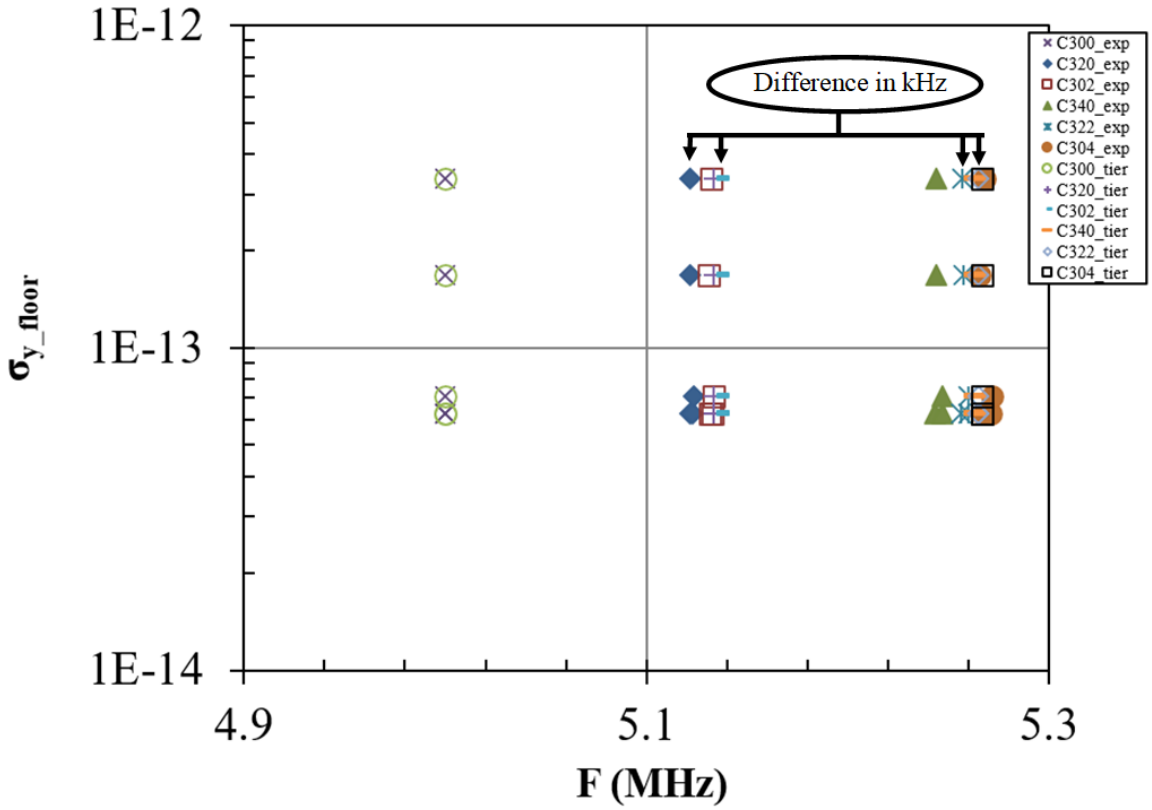


*Figure 3.13: Resonant frequencies of anharmonic modes of mode-C vs $\sigma_{y\_floor}$ at 353K.*

## 3.5 Finite Element Method (FEM) analysis

We used the COMSOL-*Multiphysics* software to analyse the Tiersten's plano-convex model which determines the frequencies of fundamental, overtones and anharmonic modes. This part of the work in finite element analysis particularly focuses on the software modelling of the 5 MHz SC-cut quartz crystal resonator with a number of elements that allows us to observe the resonant frequencies of different modes of acoustic vibration. As already mentioned, the 5 MHz SC-cut quartz crystal resonator has a diameter of 14 mm and thickness of 1.09 mm. The electrical contact is made through circular gold electrodes of 8 mm diameter with a thickness around 200 nm. The radius of curvature chosen is around 130 mm. The electrodes being much thinner than the quartz plate we decided not to physically model them but to simply draw their imprint on the upper and lower faces of the resonator and then apply a loading condition on these surfaces. The plate is also clamped on its four corners as to give the real fabricated environment to the resonator. This simplification of the modelling will make it possible to avoid a possible discontinuity of the mesh between these different elements designed and avoid errors in the result. The equation for mass-loading:

$$\sigma_i = \rho h \omega^2 u_i \tag{3.74}$$

Where, $\sigma_i$ is the surface loading, $\rho$ is the density of the material for electrodes, $\omega$ is the frequency and $u_i$ the displacement. This equation considers the charge effect of the electrodes on the system.

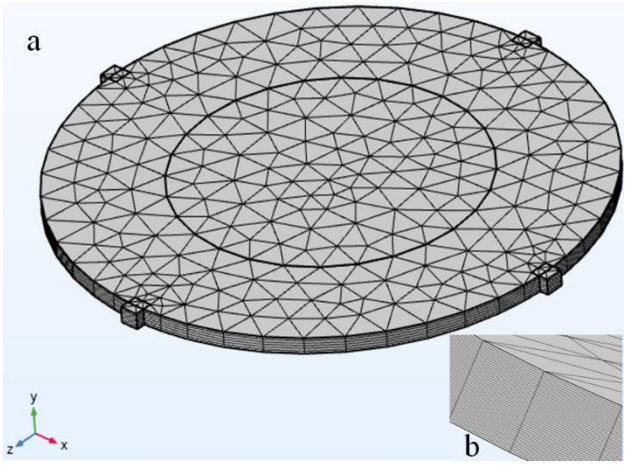


*Figure 3.14: a. Mesh resonator structure, b. Number of elements in thickness axis.*

The resonator in Figure 3.14 vibrates at third overtone of mode-*C* with resonant frequency at around 5 MHz. Following the Nyquist-Shannon [110][111], the mesh of this structure has 40 elements in the thickness axis and altogether has 51000 elements in three dimensions to resonate at 5 MHz. This structure is strictly based on Tiersten's plano-convex shape which is obtained by deforming the face of the disc using the equation below as:

$$x_2(x_1, x_3) = \left(h\left(1 - \frac{x_1^2 + x_3^2}{4 * R_c * h}\right)\right) - x_2' \tag{3.75}$$

Where, $x_2$ is the thickness axis of the blade after deformation in $x_1$ and $x_3$ axis, $h$ is the thickness of the resonator plate, $R_c$ is the curvature radius, $x_2'$ is the thickness of the plate before deformation with respect to the thickness of the plate at one of its edge.

Similarly, to be more precise and accurate obtaining the eigen frequencies (overtones and anharmonics) at and around 5 MHz for the model designed, we implemented Coefficient form PDE (Partial Differential Equation) [112] in COMSOL- *Multiphysics*. This is a kind of interface that allows to specify and solve PDEs in the coefficient form chosen from the PDE interfaces and helps to include the anisotropy of the material within the equation, shown as:

$$\lambda^2 e_a \frac{\partial^2 u}{\partial t^2} - \lambda d_a \frac{\partial u}{\partial t} + \nabla \cdot (-c\nabla u - \alpha u + \gamma) + \beta \cdot \nabla u + au = f \tag{3.76}$$

Where, $u$ is the unknown scalar to be solved, $t$ and $f$ are the time and source term, respectively. $\lambda$ is the eigen value and $e_a, d_a, c, \alpha, \gamma, \beta$ and $a$ are the coefficients defined by user and $c$ is a matrix because of the material anisotropy. For the 3D domain, $\nabla = \left[\frac{\partial}{\partial x}, \frac{\partial}{\partial y}, \frac{\partial}{\partial z}\right]$, the meshed 3D model is shown in Figure 3.14. For comparing with the coefficient form PDE, the equations of the plano-convex resonator taken from equation (3.49) and can be rewritten as:

$$(4\pi^2\rho)f^2u_1^n + M_n'^{(1)}\frac{\partial^2 u_1^n}{\partial x_1'^2} + P_n'^{(1)}\frac{\partial^2 u_1^n}{\partial x_3'^2} - \frac{n^2\pi^2\hat{c}^{(1)}}{4h_0^2}\left(1+\frac{(x_1^2+x_3^2)}{2Rh_0}\right)u_1^n = \rho\omega^2(-1)^{(n-1)/2}\frac{e_{26}}{c^{(1)}}\frac{4Ve^{i\omega t}}{n^2\pi^2} \quad (3.77)$$

Where, $f$ is the characteristic frequency. Comparing the equations, we have the values as:

$$e_a = \rho,\ c = \begin{bmatrix} -M_n' & 0 & 0 \\ 0 & 0 & 0 \\ 0 & 0 & -P_n' \end{bmatrix},\ a = -\rho\left[\frac{n^2\pi^2\hat{c}^{(1)}}{4h_0^2}\left(1+\frac{(x_1^2+x_3^2)}{2Rh_0}\right)\right],\ d_a = \beta = \gamma = 0$$

The software automatically initializes other parameters of the equation (3.76) with the appropriate values. Finally, we set the number of eigen values interested in a defined range.

## 3.6 Simulation results and comparison with Tiersten's model

The resonator has been modelled with an appropriate meshing i.e. 51000 elements [113] were required to have an accord with the Tiersten's theory. Initially, we started with 4 elements (for the first seven elements column in Table 3.5) on the thickness axis and later we ended using 40 elements (for the last two elements column Table 3.5) to be sure that all the modes of vibration will have sufficient number of elements to have the best results from simulation. The number of elements were chosen by varying the maximum and minimum values until the desired value of the motional resistance of vibrating plate would be attained and the processing limit allowed by COMSOL for the maximum number of elements for a given geometrical structure. The increase in number of elements on the other hand did not have any change on the modes of vibration except the increment in the size of the simulation file and hence we had to be limited with the maximum number of elements that allowed us to have good results in simulation. Some of the trials regarding the number of elements are shown in Figure 3.15 and their values in the Table 3.5 below:

| Elements | 6000 | 7000 | 8000 | 9000 | 10500 | 11000 | 12000 | 30000 | 51000 |
|---|---|---|---|---|---|---|---|---|---|
| R (Ω) | 114.7 | 84.24 | 89.78 | 105.35 | 81.85 | 82.45 | 105.35 | 82.61 | 84.24 |
| Q ($10^6$) | 0.588 | 2.42 | 0.49 | 0.155 | 0.606 | 1.73 | 0.519 | 2.55 | 2.49 |

*Table 3.5: Number of elements, motional resistance and quality factor of 5 MHz resonator.*

The eigen frequencies of different overtones and anharmonics were searched. There was a difference in resonant frequencies from simulation in comparison to those obtained by using Tiersten's plano-convex resonator formulae. The fundamental mode of vibration C300 is observed in the centre of the resonator plate in Figure 3.16 and Figure 3.17 with little or no distortion at around 5 MHz. Modes C320, C302 and C322 have less than 3% difference in their frequency of resonance between the simulation and theory.

| **Modes** | C300 | C320 | C302 | C322 | C700 | B300 |
|---|---|---|---|---|---|---|
| **Freq.Simul (MHz)** | 5 | 5.0308 | 5.1047 | 5.182 | 11.1 | 5.331 |
| **Freq. Tiersten (MHz)** | 5 | 5.119 | 5.131 | 5.248 | 11.594 | 5.487 |
| **Appx.Diff (in per)** | - | 2% | 0.5% | 1.5% | 5% | 3% |

*Table 3.6: Difference table of simulated and measured values of resonant frequencies.*

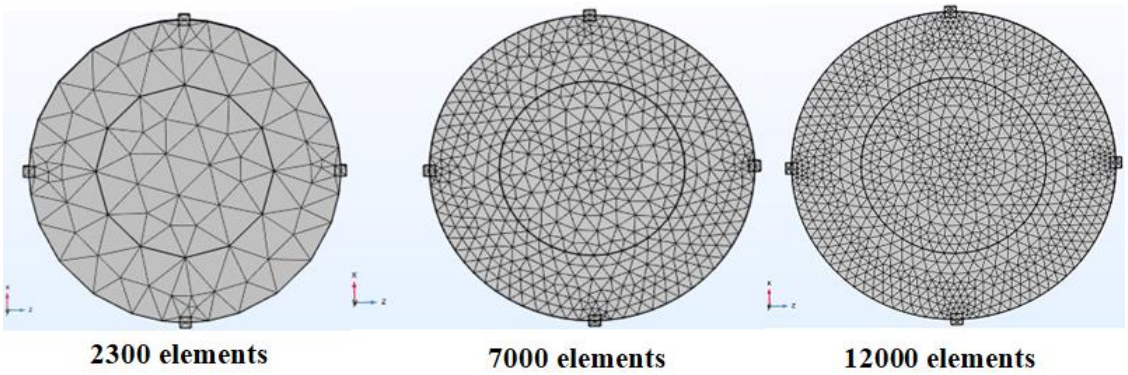


*Figure 3.15: Examples of resonator plate with varying meshed elements.*

Similarly, mode C700 has almost 5% difference in the frequency of resonance compared to that of the theory followed by B300 which has around 3% difference. This shows that the Tiersten's theory of plano-convex resonator seems to have a good agreement with the simulation results.

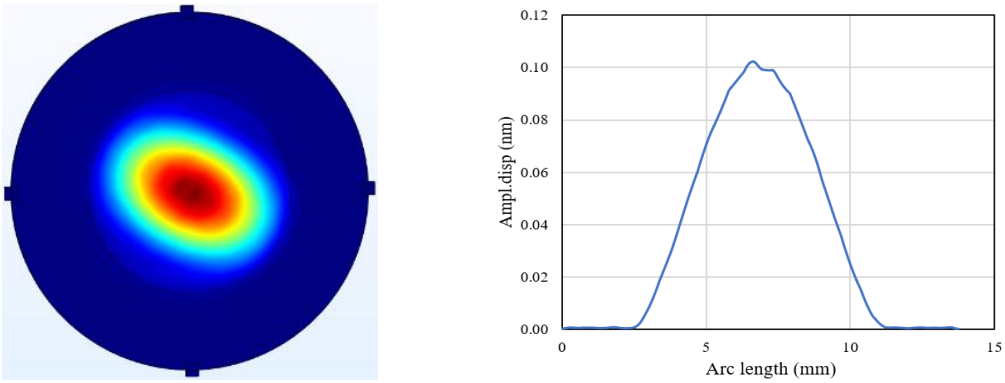


*Figure 3.16: Left: Vibration of 5 MHz resonator at mode C300*
*Right: Amplitude displacement mode C300 of the resonator plate in the thickness direction.*

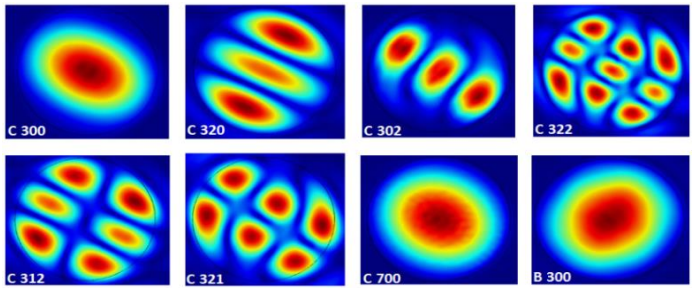


*Figure 3.17: Different modes of vibration observed in the resonator.*

Likewise, to have an idea of the influence of defects inside the quartz crystal to the main vibration mode i.e. C300 principally we carried out simulation in the resonator in Figure 3.18 where we can see the zoomed view of the mode of vibration. The defects were introduced in the resonator by making a small geometrical figure i.e. circular and rectangular. The circular defect is of radius around 50 µm made on the surface of the resonator. The rectangular defect has the size of 50 µm × 30 µm on the surface and depth of 2 µm towards the thickness of the resonator plate. The defects were made on

the right side of the plate near to the main center of vibration as shown in Figure 3.18 and Figure 3.19 These geometrical figures were specified by selecting different materials i.e. Aluminium (Al) and Iron (Fe) and non-material as empty or "air particles". There seems to be a significant difference with defects introduced in the simulation, and the rectangular and circular defects introduced using Fe as impurity caused 15% reduction shown in Table 3.7 in reference to the Q-factor obtained from simulation.

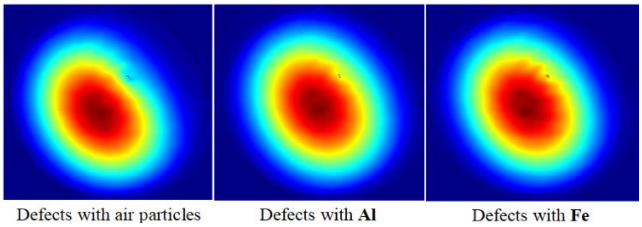


*Figure 3.18: C300 mode of vibration with circular shaped defects.*

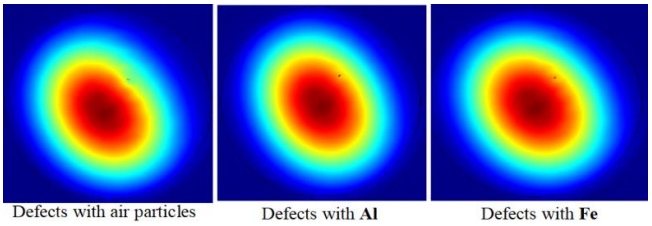


*Figure 3.19: C300 mode of vibration with rectangular shaped defects.*

| **Rectangular** | **Circular** |
|---|---|
| Q = 2.04 Million | Q = 2.08 Million |

*Table 3.7: Geometrical defects introduced using Fe as an impurity in the vibrating mode of the resonator.*

## 3.7 Summary

We realized the well-known plano-convex model by Tiersten to design the BAW resonators. Exploring the noise measurement results of Bulk Acoustic Wave (BAW), quartz crystal resonator using a passive measurement system based on carrier suppression technic was the heart of the work. We particularly focused for the phase noise measurement at 353 K and at 4 K and compared the results of Q-factor with the phase noise, but unfortunately could not find any significant correlation between the Q-factor and phase noise both at 353K and 4K for C300 mode along with its anharmonic and overtone modes. The significantly bigger difference in resonant frequencies obtained when comparing Tiersten's formula and the results from measurement seems to be an interesting matter of discussion regarding BAW quartz crystal resonators. Whereas in the contrary, the simulation results obtained from COMSOL- *Multiphysics* for the resonator shows a good accord with the results obtained using Tiersten's plano-convex formula regarding the resonant frequencies of different modes of acoustic vibrations. The defects were introduced with different geometrical structures and size on the resonator plate but not any significant correlation see between them.

# Chapter 4 Experimental attempts at checking a theoretical model for $1/f$ phase noise

## 4.1 Introduction

In the previous chapter, we showed measurements of $1/f$ noise using the carrier suppression technic in SC-cut Bulk Acoustic Wave (BAW) ultra-stable quartz crystal and Langatate resonators. We observed two different short-term stability values or fluctuations $(1/f)$ for quartz and LGT resonators, which allowed us to compare the two resonators in terms of fluctuations or $1/f$ noise. For this chapter, we will be more specific and report only about confrontation of some statistical models with results of repeated measurements of $1/f$ noise in pairs of quartz crystal resonators. Indeed, after a rapid introduction of our motivations to do repeated measurements of phase noise with 3 different pairs of resonators, we will review some considerations concerning stable distributions in statistics and power law intermittency models in physics as a preliminary to the discussion of a model proposed by Niemann et al. proposing power law intermittency[1] as a cause to $1/f$ noise in our experimental data.

While measuring thermal noise in vacuum tubes, J. B. Johnson found out that, at lower frequencies, the Power Spectral Density (PSD) of noise varied as $1/f$ (see) [17]. The result was intriguing to the scientific community all the more than a decade later the same phenomenon was observed in platinum films and granular graphite [114], which were completely different systems with respect to the vacuum tubes used by Johnson. Furthermore, the discovery of $1/f$ phase noise has not been limited to electronics, since considerable amount of discoveries have been done in other domains of science such as, cognitive psychology, hydrogeology and non-scientific domains like stock market fluctuations, economics and sociology [115]. More recent discoveries of $1/f$ phase noise were done in semiconductor nanocrystals [116], nano- electrodes [117], van der Waals materials [118] or carbon resistors [119]. In this very recent work [119], Mihaila et al. proposed a mechanism based on the non-linearity caused by electron-phonon coupling to explain the origin of $1/f$ noise in a carbon soot resistor, similarly to a previous work by Musha et al. [120] who showed that fluctuation in bulk and surface phonon numbers in quartz crystals could cause $1/f$ noise. However, despite all these efforts, and although general mathematical models for $1/f$ noise that could be valid in various contexts, have been found, so far, no definite, general and clear explanation is present regarding the microscopic origin of $1/f$ phase noise in ultra-stable oscillators. Hence, finding the origin of $1/f$ phase noise in these oscillators to optimize their fabrication process, is still an active research subject, after more than 8 decades since the discovery of $1/f$ noise!

[1] Here, "power law intermittency" means that waiting times in an unstable microstate of the system before transiting to a more stable microstate, would be distributed according to a power law.

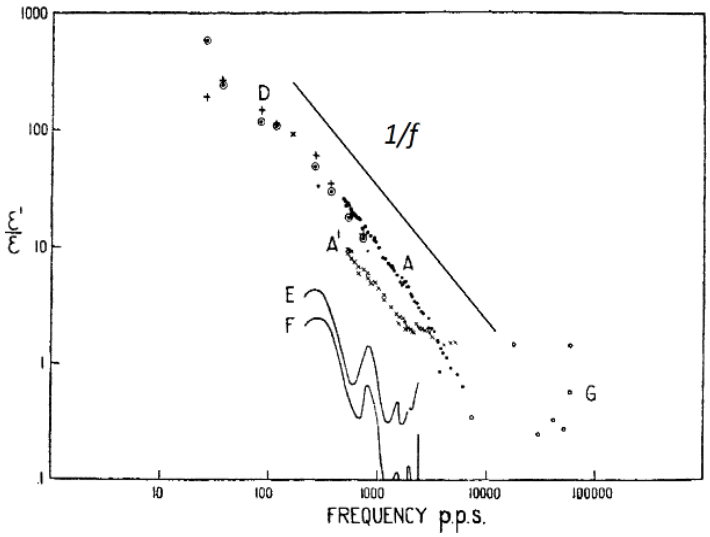


*Figure 4.1: Johnson's PSD observation [17], vertical: ratio of noise power density and shot noise power density, Horizontal: frequency in Hz.*

Furthermore, in the mid 70's, M. A. Caloyannides [121] performed tests on phase noise in operational amplifiers. His test was one of the longest measurements done in the early history of phase noise in terms of duration of measurement since he did the experiment for 3 weeks on many samples, extending the domain of Fourier frequency down to $10^{-6}$ Hz!. To his surprise and everyone's, despite that long measurement, the $1/f^{1.23}$ power spectrum he found had no cut-off frequency at lower frequencies (cf. Figure 4.2), whereas one would be needed for energy conservation reasons, since the power spectrum should be integrable which would not be possible it would keep its $1/f^{1.23}$ tendency down to zero frequency ($\int_0^\infty S(f)df \to \infty$ if $S(f) \sim 1/f^\gamma$ when $f \to 0$ and $\gamma \geq 1$).

Thus, we were very interested by the recent work of Markus Niemann et al. in which they show with numerical simulations for a general class of phenomena characterized by power law intermittency (sojourn times in microstates of the system have a power law statistics that is scale free [122]), that there does exist a cut-off frequency at lower frequencies, but that it is almost equal to the inverse of the measurement time, hence rarely measurable. Furthermore, this article introduces quantities that can be computed from experimental results to test the power law intermittency origin of the experimental noise. Since, it seemed to us, thanks to our understanding of the quantum noise model [12],[123], that the random and discrete (in time) nature of the events causing the frequency fluctuations may be a universal characteristic also found in quartz, we decided to do the required repeated experiments in order to test the existence of power law intermittency as a characteristic of the fluctuations giving rise to $1/f$ noise in our quartz resonators. This interest was further strengthened by the fact that we latter discovered that relaxation phenomena with power law tails were also suspected long ago to give rise to model fits much more in agreement with experimental data for permittivity measurements at low frequencies including the megahertz region and recalling that permittivity is central in the expression of the resonant frequency for a quartz resonator. More recently, statistical distributions like the one used

by Niemann et al. were also used in this permittivity context, so that we found useful to describe this context later in this chapter, before discussing our experimental results.

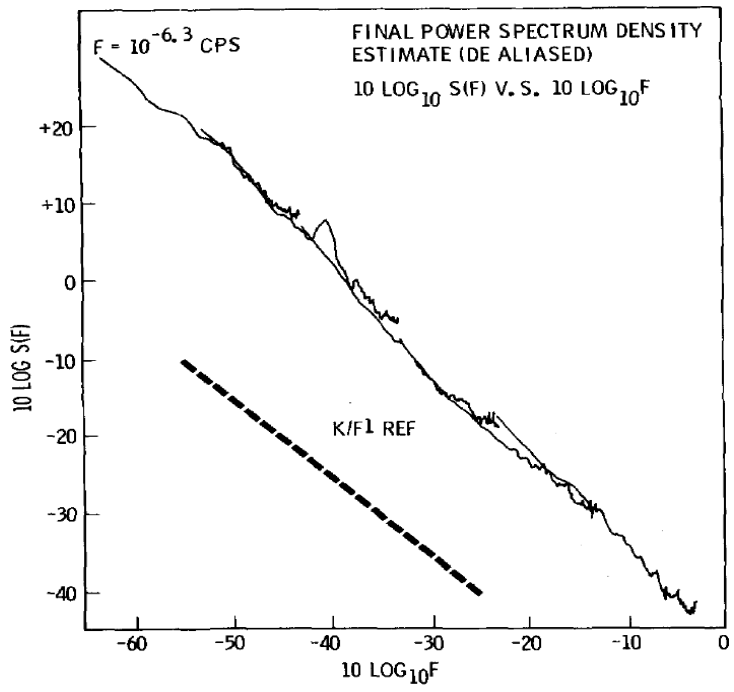


*Figure 4.2: PSD of noise in an array of operational amplifiers measured for 3 weeks by Caloyannides [121].*

## 4.2 Modelling background

We will begin this paragraph, by summarizing some statistical background that we think necessary to understand the main results of some general mathematical models of $1/f$ noise that we later present.

### 4.2.1 Stable distributions

Stable distributions constitute a class of probability distributions that allows skewness and heavy tails[2] and have many interesting mathematical properties. They could be very interesting for physicists since, as we will see below, their definition means that if we have plenty of independent sources of noise, all distributed according to a stable distribution, the total noise distribution (sum of all the noise sources) will also be that stable distribution (with different parameters). This therefore gives the possibility to generalize to the macroscopic scale the distribution that we could derive from a careful study of the microscopic origin for a single noise source or, inversely, to lead us to find a microscopic origin distributed in a way similar to our macroscopic noise measurements! These stable distributions

[2] Concerning heavy-tailed distribution, one can read with profit the relevant Wikipedia page:
https://en.wikipedia.org/wiki/Heavy-tailed_distribution or
https://reference.wolfram.com/language/guide/HeavyTailDistributions.html
Heavy tail means that there is a larger probability of getting very large values than with the Normal distribution. So heavy tail distributions typically represent wild as opposed to mild randomness.
The tails of the PDF of a stable distribution may be "fat" (i.e. the PDF decreases as $x^{-\alpha}$ for large x) or "thin" (i.e. the PDF decreases exponentially for large x), depending on the values of its parameters.

have been used in e.g. fluid mechanics, solid state physics, polymer chemistry, and mathematical finance and their derivation from models characteristic of these domains are given in [124]-[125], which is a pedagogical paper targeted for physicists as well as mathematicians.

Stable distributions were first studied by mathematician Paul Lévy in the mid-1920s [126]-[127], and can be introduced through a generalization of the Central Limit Theorem (CLT), as follows:

If a random variable $S_n$ is defined as the sum of $n$ independent and identically distributed random variables $X_1, X_2, X_3 \ldots, X_n$ with mean $\mu$ and finite non-zero standard deviation $\sigma$, then, for large enough $n$, the central limit theorem (CLT) states that $S_n$ is approximately normally distributed with parameters:

$$X_1 + X_2 + X_3 + \cdots + X_n = S_n \tag{4.1}$$

$$\mu_{S_n} = n\mu \text{ and } \sigma_{S_n} = \sqrt{n}\sigma \tag{4.2}$$

This can be restated as:

$$\frac{\bar{X}_n - \mu}{\sigma/\sqrt{n}} \underset{n\to\infty}{\rightarrow} N(0,1) \tag{4.3}$$

where $\bar{X}_n = \sum_{i=1}^{n} X_i/n$ and $N(0,1)$ is the normal distribution (Gaussian distribution with mean 0 and variance 1). This result holds regardless of the shape of the $X$ distribution (i.e. the $X_i$ do not have to be normally distributed), provided its variance is non-zero and finite! If the variance common to all the $X_i$ distribution is not finite, then a generalization of the CLT[3] states that the sum of several random variables with symmetric distributions having power-law tails decreasing as $1/|x|^{1+\alpha}$with $0 < \alpha \leq 2$ (and therefore having infinite variance), will tend to a symmetric distribution characterized by this $\alpha$ value (called stability index) and a scale parameter, as the number of summands grows[4]. Hence, these distributions are termed as *stable* and their sums are also a random variable of the same kind for every $n$. Hence, the following definition extracted from Cahoy's PhD thesis [128] which aimed at studying long memory processes through fractional Poisson process:

***Definition 1:*** *The common distribution $F_X$ of independent identically distributed random variables $X_1, X_2, \ldots, X_n$ belongs to the domain of attraction of the distribution $F$ if there exist normalizing sequences, $a_n, b_n > 0$, such that:*

$$\lim_{n\to\infty}\left[b_n^{-1}\left(\sum_{i=1}^{n} X_i - a_n\right)\right] = X \tag{4.4}$$

*in distribution.*

[3] Theorem 5 in Chapter 7, Section 35, page 181 of a book titled "Limit distributions for sums of independent random variables", by B.V. Gnedenko and A.N. Kolmogorov (Cambridge, Addison-Wesley 1954), according to https://en.wikipedia.org/wiki/Stable_distribution#cite_note-12.

[4] If $\alpha > 2$, then the sum converges to a symmetric stable distribution with stability parameter equal to 2, i.e. a Gaussian distribution.

The non-degenerate limit laws $X$ are called stable laws. The above definition can also be restated as follows: The probability distribution $F$ has a domain of attraction if and only if it is stable. This means that, if we consider a sequence of independent and identically distributed random variables $X_1, X_2, X_3, \ldots . X_i$ considering it without any presumption about the kind of distribution, in the presence of normalizing sequences $a_1, a_2, a_3, \ldots a_n$ and $b_1, b_2, b_3, \ldots b_n$, we have the expression of sums $Z_n$ as:

$$Z_n = \frac{\sum_{i=1}^{n} X_i - a_n}{b_n} \tag{4.5}$$

where $a_n$, $b_n > 0$, are chosen accordingly so that the distribution function of $Z_n$ weakly converges to some limit distribution function $G(x)$, as:

$$P\{Z_n < x\} \rightharpoonup G(x) \qquad n \to \infty \tag{4.6}$$

where, $\rightharpoonup$ denotes the weak convergence and $x$ is any continuity point of the function $G(x)$.

The class of distributions with the above property is named *stable distributions* [129]. If $\forall n, a_n = 0$, it is said to be strictly stable.

Since this definition is not computationally effective, another definition can be found e.g. in help pages of *Matlab*™ or *Mathematica*™. This consists in defining stable distributions through their characteristic functions:

***Definition 2:*** *A random variable X is said to have a stable distribution if there exist parameters $\alpha, \beta, \gamma, \delta$ with $0 < \alpha \leq 2$, $-1 \leq \beta \leq 1$, $\gamma > 0$, and $-\infty < \delta < +\infty$, such that the characteristic function has one of the following forms*[5]*:*

Type 0:

$$\phi(t) \equiv \mathbb{E}\left(e^{itX}\right) \begin{cases} exp\left[-\gamma^{\alpha}|t|^{\alpha}\left(1 + i\beta\, sign(t)\, tan(\pi\alpha/2)\left((\gamma|t|)^{1-\alpha} - 1\right)\right) + it\delta\right], & \alpha \neq 1 \\ exp[-\gamma|t|(1 + i\beta(2/\pi)\, sign(t)\, ln(\gamma|t|)) + it\delta], & \alpha = 1 \end{cases} \tag{4.7}$$

Type 1:

$$\phi(t) = \begin{cases} exp[-\gamma^{\alpha}|t|^{\alpha}(1 - i\beta\, sign(t)\, tan(\pi\alpha/2)) + it\delta], & \alpha \neq 1 \\ exp[-\gamma|t|(1 + i\beta(2/\pi)\, sign(t)\, ln(|t|)) + it\delta], & \alpha = 1 \end{cases} \tag{4.8}$$

In Definition 2, α is the index of stability. It determines the rate at which the tails decay. When $\alpha = 2$, the stable distribution is just a Gaussian distribution while, when $\alpha < 2$, it decays with a power law[6] and the only possible choice for the constants $b_n$ is $b_n = n^{1/\alpha}$. The skewness parameter $\beta$ along with the index of stability α determines the shape of the distribution. If $\beta > 0$ the distribution is skewed to

[5] Matlab(TM) uses the type 0 stable functions (cf. https://fr.mathworks.com/help/stats/stable-distribution.html) with same order of parameters $\alpha, \beta, \gamma, \delta$, while Cahoy uses type 1 in his PHD thesis with parameters $\alpha, \beta, \gamma, \eta$. As for Mathematica™, https://reference.wolfram.com/language/ref/StableDistribution.html in the "Details section" names the parameters $\alpha, \beta, \sigma, \mu$ and defines $S_t(\alpha, \beta, \mu, \sigma)$, hence an exchange of the last 2 parameters with respect to the definition adopted in our text (and in Matlab™).

[6] As an example, we have $Q_{\alpha}(x) \equiv S_1(\alpha, 0,1,0)(x) \sim \Gamma(1 + \alpha)\sin(\pi\alpha/2)/(\pi|x|^{1+\alpha})$ when $|x| \to \infty$.

the right and to the left if $\beta < 0$. The $\delta$ parameter shifts the distribution to the left or right on the x-axis, while γ is the scale parameter and:

$$sign(t) = \begin{cases} 1 & t > 0 \\ 0 & t = 0 \\ -1 & t < 0 \end{cases} \quad (4.9)$$

We then write $X \sim S_t(\alpha, \beta, \gamma, \delta)$ to say that $X$ has a stable distribution of type $t$ and parameters $\alpha, \beta, \gamma, \delta$ and note that an $\alpha$-stable random variable has finite absolute moments only for order(s) $n < \alpha$. Moments of order $n \geq \alpha$, such as the variance (related to the energy of the signal), are infinite!

Let us insist on the fact that type 0 distribution is continuous in $\alpha$, while type 1 is discontinuous at $\alpha = 1$ because of the $\tan(\pi\alpha/2)$ term that is not compensated by the $((\gamma|t|)^{1-\alpha} - 1)$ term. Furthermore, it is said in *MATLAB™* help page that accurate numerical calculations of the corresponding densities show that in this type 0 representation, α and β have a much clearer meaning as measures of the heaviness of the tails and skewness parameters.

If $\beta = 0$ and $\delta = 0$, then the distribution is symmetric, $S_0(\alpha, 0, \gamma, 0) = S_1(\alpha, 0, \gamma, 0)$, and its characteristic function is greatly simplified:

$$\phi(t) = \int_{-\infty}^{+\infty} e^{itx} S(\alpha, 0, \gamma, 0)(x) dx = exp[-\gamma^\alpha |t|^\alpha] \quad (4.10)$$

$$\Leftrightarrow S(\alpha, 0, \gamma, 0)(x) = \frac{1}{2\pi} \int_{-\infty}^{+\infty} exp[-itx - \gamma^\alpha |t|^\alpha] \, dx \quad (4.11)$$

This means that in a loglog vs. log coordinate plot, the characteristic function of an $\alpha$-stable density is a straight line with slope $\alpha$. This fact makes it possible to estimate the parameter $\alpha$ via a regression procedure.

On Figure 4.3, we illustrate the role of each of the 4 parameters on the shape of the distribution.

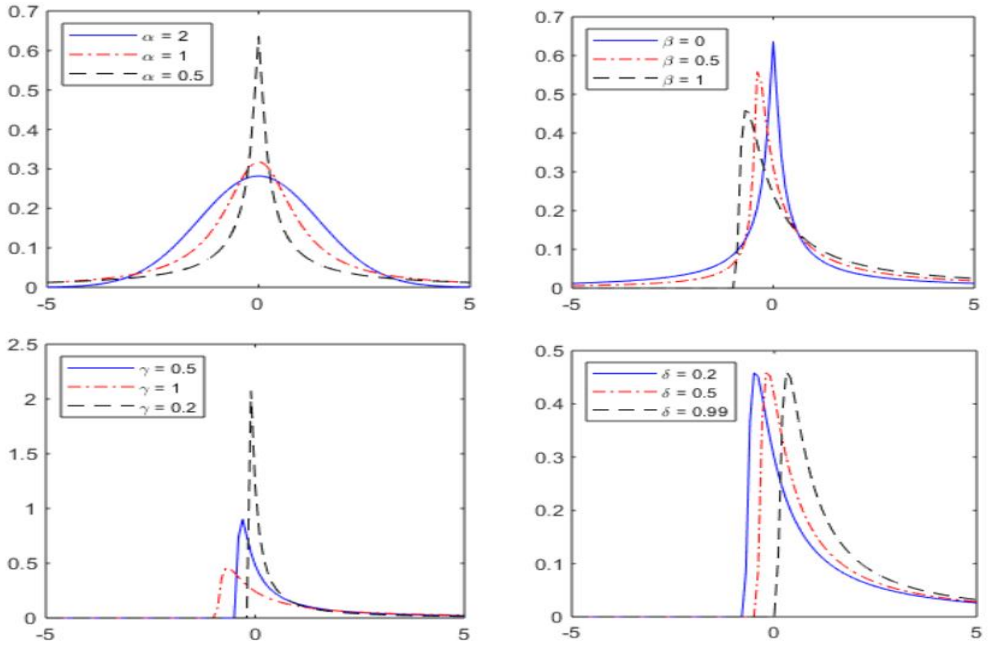


*Figure 4.3: Effect of different parameters on the general stable distribution* $S_0(\alpha,\beta,\gamma,\delta)$. *For the upper-left figure* $\beta = 0, \gamma = 1, \delta = 0$. *For the upper-right figure* $\alpha = 0.5, \gamma = 1, \delta = 0$. *For the lower-left figure* $\alpha = 0.5, \beta = 1, \delta = 0$. *For the lower-right figure* $\alpha = 0.5, \beta = 1, \gamma = 1$.

Another interesting property of stable distributions that allows to elucidate the connection between distributions of type 0 and distribution of type 1 is that, if we call $Z$ a random variable with a distribution function of type $S_1(\alpha,\beta,1,0)$, then a random variable $X$ distributed according to $S_0(\alpha,\beta,\gamma,\delta)$ can be written under the form[7]:

$$X = \begin{cases} \gamma\left(Z - \beta\ tan(\pi\alpha/2)\right) + \delta, & \alpha \neq 1 \\ \gamma Z + \delta, & \alpha = 1 \end{cases} \tag{4.12}$$

Furthermore, a random variable $X$ distributed according to $S_1(\alpha,\beta,\gamma,\delta)$ can be written under the form:

$$X = \begin{cases} \gamma Z + \delta, & \alpha \neq 1 \\ \gamma Z + (\delta + \beta(2/\pi)\gamma\ ln\,\gamma), & \alpha = 1 \end{cases} \tag{4.13}$$

Hence, if we call $\delta_0$ the location parameter of a distribution of type $S_0(\alpha,\beta,\gamma,\delta)$ and $\delta_1$ the location parameter of a distribution of type $S_1(\alpha,\beta,\gamma,\delta)$, then $\delta_0$ and $\delta_1$ are linked by:

$$\delta_0 = \begin{cases} \delta_1 + \beta\gamma\ tan(\pi\alpha/2), & \alpha \neq 1 \\ \delta_1 + \beta(2/\pi)\gamma\ ln\,\gamma, & \alpha = 1 \end{cases} \quad or \quad \delta_1 = \begin{cases} \delta_0 - \beta\gamma\ tan(\pi\alpha/2), & \alpha \neq 1 \\ \delta_0 - \beta(2/\pi)\gamma\ ln\,\gamma, & \alpha = 1 \end{cases} \tag{4.14}$$

so that $X \sim S_1(\alpha,\beta,\gamma,\delta) = S_0\left(\alpha,\beta,\gamma,\delta + \beta\gamma\tan(\pi\alpha/2)\right)$ if $\alpha \neq 1$ and $Z \sim S_1(1,\beta,\gamma,\delta) = S_0(1,\beta,\gamma,\delta + \beta(2/\pi)\gamma\ln\gamma)$. Furthermore, the support of $S_0(\alpha,\beta,\gamma,\delta)$ and $S_1(\alpha,\beta,\gamma,\delta)$ are respectively given by:

[7] See the first chapter of a book by J. P. Nolan titled "Stable Distributions, Models for Heavy Tailed Data", available at http://academic2.american.edu/~jpnolan/stable/chap1.pdf

$$\begin{cases} [\delta - \gamma\, tan(\pi\alpha/2), \infty[ & \alpha < 1\ and\ \beta = 1 \\ ]-\infty, \delta + \gamma\, tan(\pi\alpha/2)] & \alpha < 1\ and\ \beta = -1\ \ and \\ ]-\infty, \infty[ & otherwise \end{cases} \begin{cases} [\delta, \infty[ & \alpha < 1\ and\ \beta = 1 \\ ]-\infty, \delta] & \alpha < 1\ and\ \beta = -1 \\ ]-\infty, \infty[ & otherwise \end{cases} \quad (4.15)$$

We now turn to the asymptotic properties of stable distributions that are in fact our main point of interest. As stated in the generalized central limit theorem, these distributions are heavy tailed (moments of order greater than $\alpha$ are undefined). More precisely, if we define $c_\alpha = \sin(\pi\alpha/2)\ \Gamma(\alpha)/\pi$ and if $X \sim S_0(\alpha, \beta, \gamma, \delta)$, with $0 < \alpha < 2$ and $-1 < \beta \leq 1$, then as $x \to \infty$:

$$P(X > x) \sim \gamma^\alpha c_\alpha (1+\beta) x^{-\alpha}\ and\ \boxed{S_0(x|\alpha, \beta, \gamma, \delta) \sim \alpha \gamma^\alpha c_\alpha (1+\beta) x^{-(\alpha+1)}} \quad (4.16)$$

For the other tail, we have similarly, for $0 < \alpha < 2$ and $-1 \leq \beta < 1$, as $x \to \infty$:

$$P(X > -x) \sim \gamma^\alpha c_\alpha (1-\beta) x^{-\alpha} and\ \boxed{S_0(-x|\alpha, \beta, \gamma, \delta) \sim \alpha \gamma^\alpha c_\alpha (1-\beta) x^{-(\alpha+1)}} \quad (4.17)$$

Finally, we note that the lack of closed formulas for densities and distribution functions for all but a few stable distributions *(Gaussian[8], Cauchy[9] and Lévy[10])*, was a major drawback to the use of stable distributions by researchers. Nonetheless, predefined functions to generate, use and fit the parameters of these distributions are now widely available and we could use them through Matlab™ and Mathematica™ scripts.

*Remark: other types of parametrization can also be found[130].*

### 4.2.2 One sided α -stable distribution and Cahoy's formula

In this paragraph, we are interested only in the one-sided $\alpha$-stable distributions with location parameter $\delta$ equal to zero, scale parameter $\gamma$ equal to $[\cos(\pi\alpha/2)]^{1/\alpha}$, skewness parameter $\beta$ equal to one, and the stability index $0 < \alpha < 1$. We follow the notations in Appendix A of Cahoy at al. [131] and use the notation $\boxed{g^{(\alpha)}(x) \equiv S_1\left(x|\alpha, 1, [\cos(\pi\alpha/2)]^{1/\alpha}, 0\right)}$ for the probability density function of a member of this class of distributions, that are called $\alpha^+$-stable distribution or one-sided alpha-stable distribution. $g^{(\alpha)}(x)$ is determined by its Laplace transform as (from [132] and [127], as cited in [131]):

$$\left\{\mathrm{L}\, g^{(\alpha)}(x)\right\}(\lambda) = \tilde{g}^{(\alpha)}(\lambda) \equiv \int_0^\infty g^{(\alpha)}(x) e^{-\lambda x} dx = e^{-\lambda^\alpha} \quad (4.18)$$

We also have :

$$g^{(\alpha)}(x) = \frac{1}{2\pi} \int_{-\infty}^{+\infty} \exp[-itx - \cos(\pi\alpha/2)\, |t|^\alpha (1 - i\, \mathrm{sign}(t) \tan(\pi\alpha/2))]\, dt$$
$$= \frac{1}{2\pi} \int_{-\infty}^{0} \exp[-itx - |t|^\alpha / q]\, dt + \frac{1}{2\pi} \int_{0}^{+\infty} \exp[-itx - q|t|^\alpha]\, dt$$

with $q = \exp(-i\,\pi\alpha/2)$.

---

[8] $\mathcal{N}(\mu, \sigma) = \exp(-(x-\mu)^2/2\sigma^2)/\left(\sqrt{2\pi}\sigma\right) = S_0\left(2, \beta, \sigma/\sqrt{2}, \mu\right) = S_1\left(2, \beta, \sigma/\sqrt{2}, \mu\right)$

[9] $\mathcal{C}(\delta, \gamma) = 1/[\pi\gamma(1 + (x-\delta)^2/\gamma^2)] = S_0(1,0,\gamma,\delta) = S_1(1,0,\gamma,\delta)$ which describes the distribution of the ratio of two independent Gaussian random variables.

[10] $\mathcal{L}(\delta, \gamma) = \sqrt{\gamma/2\pi} \times \exp(-\gamma/[2(x-\delta)])/(x-\delta)^{3/2} = S_0(1/2\,, 1, \gamma, \gamma + \delta) = S_1(1/2\,, 1, \gamma, \delta)$ which can be related to the distribution of the inverse of the square of a Gaussian random variable.

$g^{(\alpha)}(x)$ is equal to 0 on the negative semi axis including the origin, positive on the positive semi axis and satisfies the normalization condition $\int_0^\infty g^{(\alpha)}(x)\,dx = 1$.

Since it can be easily checked with Eq. (4.18) that:

$$\tilde{g}^{(\alpha)}(\lambda)\tilde{g}^{(\alpha)}(\lambda) = \tilde{g}^{(\alpha)}\left(2^{1/\alpha}\lambda\right)) \tag{4.19}$$

the convolution of two $\alpha^+$-densities is again an $\alpha^+$- density given as:

$$\int_0^t g^{(\alpha)}(x-x')g^{(\alpha)}(x')dx' = 2^{-1/\alpha}g^{(\alpha)}(2^{-1/\alpha}x) \tag{4.20}$$

More generally, if $X_1$, $X_2$,…, $X_n$ are independent and identically distributed random variables distributed according to $g^{(\alpha)}(x)$, with $P\left(X_j > x\right) \sim ax^{-\alpha}, x \to \infty$, then the probability density of their sum is:

$$f_{\sum X_j}(x) \sim [a\,\Gamma(1-\alpha)]^{1/\alpha} g^{(\alpha)}\left([a\,\Gamma(1-\alpha)]^{1/\alpha}x\right)) \tag{4.21}$$

Properties of these densities include (Appendix A of Cahoy at al. [131]):

$(i)$ Special cases :

$$\text{When } \alpha \to 1, \quad g^{(\alpha)}(x) \to \delta(x-1) \tag{4.22}$$

$$g^{(1/2)}(x) = \frac{1}{2\sqrt{\pi}}t^{-3/2}\exp[-1/(4x)] = \mathcal{L}(0,1/2), \quad x > 0 \tag{4.23}$$

$(ii)$ Their moments can be explicitly computed via a Mellin transform:

$$\int_0^\infty g^{(\alpha)}(x)x^u dx = \begin{cases} \Gamma(1-u/\alpha)/\,\Gamma(1-u)\,, & -\infty < u < \alpha \\ \infty, & u \geq \alpha \end{cases} \tag{4.24}$$

$(iii)$ They can be represented in the form of a convergent series as $x \to 0$ as:

$$g^{(\alpha)}(x) = \sum_{n=1}^{\infty} \frac{(-1)^{n-1}\ n\alpha}{n!\,\Gamma(1-n\alpha)} x^{-n\alpha-1} \tag{4.25}$$

$(iv)$ For numerical calculations, the following integral formula may be more convenient[11]:

$$g^{(\alpha)}(x) = \frac{\alpha x^{1/(\alpha-1)}}{\pi(1-\alpha)} \int_{-\pi/2}^{\pi/2} \exp\left\{-x^{\alpha/(\alpha-1)}U(\phi;\alpha)\right\} U(\phi;\alpha)d\phi \tag{4.26}$$

Where we have:

$$U(\phi;\alpha) = \left[\frac{\sin\left(\alpha(\phi+\pi/2)\right)}{\cos\phi}\right]^{\alpha/(\alpha-1)} \frac{\cos\left((\alpha-1)\phi + \alpha\pi/2\right)}{\cos\phi} \tag{4.27}$$

$(v)$ The following asymptotic approximation obtained by saddle point method can be used for small values of $x$:

$$g^{(\alpha)}(x) \sim \frac{1}{\sqrt{2\pi(1-\alpha)\alpha}} (x/\alpha)^{(\alpha-2)/(2-2\alpha)} \exp\left[-(1-\alpha)(x/\alpha)^{-\alpha/(1-\alpha)}\right], \quad x \to 0 \tag{4.28}$$

[11] According to our tests with Mathematica™, the series representation seems to be better than the numerical integral, when compared to the Mathematica™ function. However, for a given number of terms in the summation, the relative difference is decreasing very rapidly when $x$ increases at constant $\alpha$, or when $\alpha$ decreases, at constant $x$, (seen with log scale) and only moderately (for $x < 1$) when the number of terms in the summation is doubled. Even with 20 terms, the relative difference can be of the order of 100% for $x < \alpha$.

Examples of these one-sided $\alpha^+$-stable distributions for various values of the parameter $\alpha$ are represented on Figure 4.4 using *Matlab*$^{TM}$ and approximation (4.28). We later found that we could compute their exact value using e.g. the StableDistribution function of *Mathematica*$^{TM}$. We compare the exact distribution and its approximation for $\alpha = 0.1$ and $\alpha = 0.9$ on Figure 4.5. The difference between the exact distributions and their approximation (4.28) is then represented on Figure 4.6. We note that for $\alpha = 1/2$, the asymptotic form is in fact exactly $g^{(1/2)}(t)$, but the approximation becomes less and less accurate when α is more and more different from $1/2$.

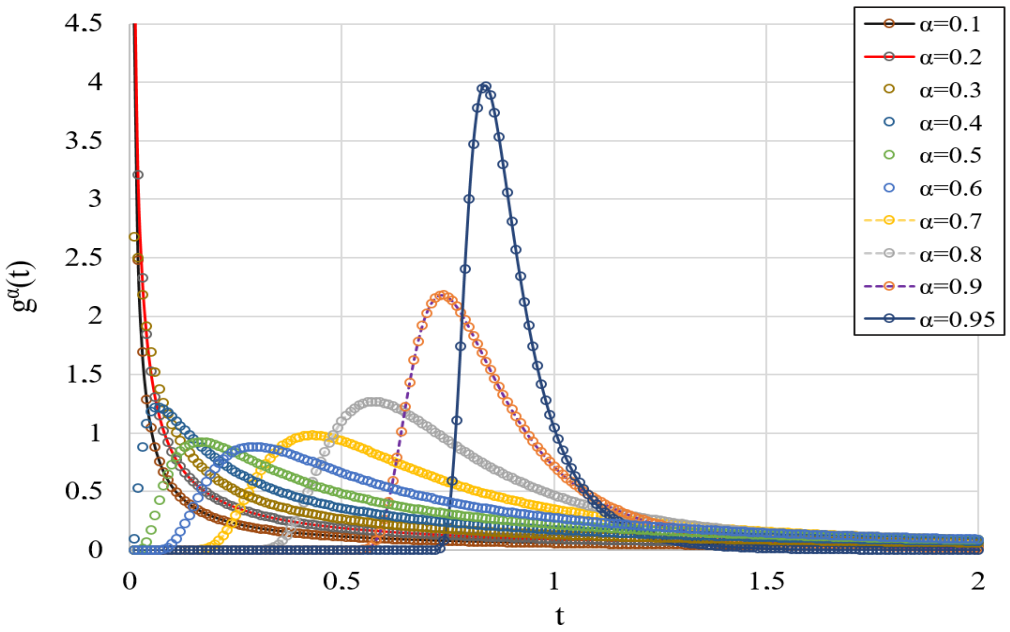


*Figure 4.4: Plot of the asymptotic approximation of one-sided Levy stable densities for different alpha values, obtained using equation (4.28) and Matlab™.*

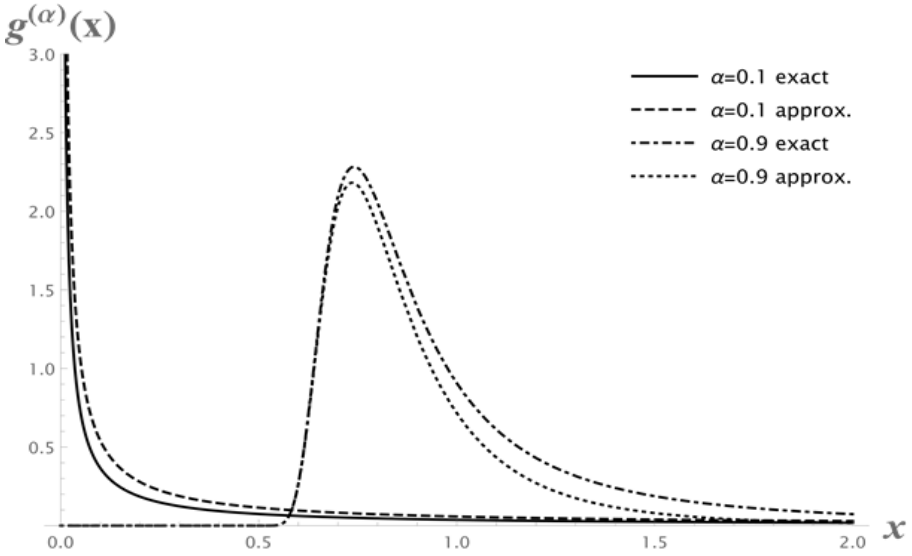


*Figure 4.5: Comparison between "exact" and approximative (using (4.28)) representations for one-sided Levy stable densities, with $\alpha = 0.1$ and $\alpha = 0.9$.*

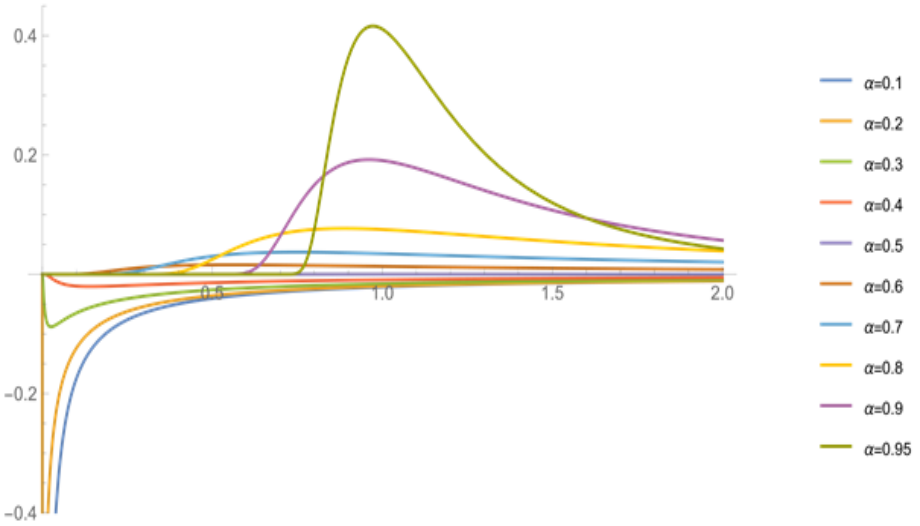


*Figure 4.6: Plot of the difference between the "exact" one-sided α-stable distribuions and their asymptotic approximations (4.28), for the same alpha values as in Figure 4.4.*

### 4.2.3 Mittag-Leffler functions and distributions

#### 4.2.3.1 Mittag-Leffler functions

Just as the Gamma function is a generalization of the factorial, the Mittag-Leffler function is a generalization of the exponential function. Indeed, since we have:

$$exp(x) = \sum_{n=0}^{\infty} \frac{x^n}{n!} = \sum_{n=0}^{\infty} \frac{x^n}{\Gamma(n+1)} \tag{4.29}$$

the Mittag-Leffler function can be defined as[12]:

$$E_{\alpha,\beta}(x) = \sum_{k=0}^{\infty} \frac{x^k}{\Gamma(\alpha k + \beta)} = \frac{1}{2\pi i} \oint \frac{t^{\alpha-\beta} e^t}{t^\alpha - z} dt \tag{4.30}$$

In this definition, $x$ is a real or complex variable, $\Gamma(\alpha n + \beta)$ is a Gamma function (equal to $n!$ if $\alpha = \beta = 1$) and the contour of the integral starts and ends at $-\infty$ and circles around the singularities and branch points of the integrand.

The function $E_\alpha = E_{\alpha,1}$ is increasing on the real line, for $x < 0$, and $E_\alpha(0) = 1$. Some values of $\alpha$ lead to a function $E_\alpha$ that can be written in closed form, e.g.[133]:

$$E_1(x) = exp(x) \tag{4.31}$$

$$E_2(x) = cosh\left(\sqrt{x}\right) \tag{4.32}$$

$$E_{1/2}(x) = exp(x^2)\, erfc\left(\sqrt{x}\right) \tag{4.33}$$

[12] The original Mittag-Leffler function, introduced by the Swedish mathematician Magnus Gustaf (Gösta) Mittag-Leffler (1846–1927) in 1903 (Mittag-Leffler, M.G.: "Sur la nouvelle fonction E(x)". C. R. Acad. Sci. Paris, **137**, 554–558 (1903)), had only one parameter: $E_\alpha(x) = E_{\alpha,1}(x)$.

The ordinary $(E_\alpha)$ and generalized $\left(E_{\alpha,\beta}\right)$ Mittag-Leffler function for $0 < \alpha < 1$ interpolates between the $x \mapsto \sum_{k=0}^{\infty} x^k = 1/(1-x)$ function and the exponential function, while $E_\alpha(-x^2)$ for $0 < \alpha < 1$ interpolates between Cauchy's distribution ($E_{0,1}(-x^2) = 1/(1+x^2)$ called Lorentzian distribution by physicists) and the Gaussian distribution ($E_{1,1}(-x^2) = \exp(-x^2)$). The Mittag-Leffler function is used in models of random walks, Lévy flights, so-called superdiffusive transport [133] and power-like behaviour of phenomena governed by ordinary kinetic equations and their fractional counterparts [134] since it arises naturally in the solution of fractional integral equations[13]. The problem is that several kinds of probability distribution have been derived from this function, which is a problem when comparing results of various authors.

Finally, we note that at https://fr.mathworks.com/matlabcentral/fileexchange/48154-the-mittag-leffler-function, one can find a Matlab implementation by Roberto Garappa [135], of a Generalized Mittag-Leffler function with up to three parameters, such that:

$$E_{\alpha,\beta,\gamma}(z) = \sum_{k=0}^{\infty} \Gamma(\gamma+k) z^k / [\Gamma(\gamma) k! \, \Gamma(\alpha k + \beta)] \tag{4.34}$$

#### 4.2.3.2 Mittag-Leffler distributions of the first kind.

Since the exponential function $\exp(-x)$ is positive over $[0, \infty]$ and integrates to 1, we can define a continuous probability distribution whose probability density function (PDF) is $f(x) = \exp(-x)$ and whose cumulative distribution function (CDF) is $F(x) = 1 - \exp(-x)$. Similarly, we can use the Mittag-Leffler function to define a continuous probability distribution $g(x)$ from its CDF $F_{ML}(x)$, given as:

$$F_{ML}(x) = 1 - E_\alpha(-x^\alpha) = 1 - \sum_{n=0}^{\infty} \frac{(-1)^n x^{\alpha n}}{\Gamma(\alpha n + 1)} \tag{4.35}$$

For $0 < \alpha < 1$, this defines a continuous Mittag-Leffler distribution of the first family[14] [136]. It is a generalization of the exponential distribution which reduces to the exponential distribution when $\alpha = 1$.

The relevant Wikipedia page [136] and [137] give its Laplace transform as:

$$\mathbb{E}(e^{-zX_\alpha}) = \int_{-\infty}^{\infty} e^{-zx} f_{ML}(x|\alpha) dx = 1/(1+z^\alpha) \tag{4.36}$$

[13] The solution of $(d^\mu/dx^\mu) f(x) = a f(x)$ is $f(x) = C^{te} x^{\mu-1} E_{\mu,\mu}(a x^\mu)$.

[14] This family was originally introduced in Pillai, R. N., "On Mittag-Leffler distribitions", Annals of the Institute of Statistical Mathematics, vol. 42, 157-161 (1990)

In order to include a scale parameter, we find in [138], the probability density function of the Mittag-Leffler distribution with index $\alpha$ and scale parameter $\gamma$ defined as[15,16]:

$$f_{ML}(x|\alpha,\gamma) = \frac{1}{x}\int_0^\infty e^{-\xi} g[x/(\gamma^\alpha \xi)]d\xi = \frac{x^{\alpha-1}}{\gamma^\alpha} E_{\alpha,\alpha}[-(x/\gamma)^\alpha] = \frac{x^{\alpha-1}}{\gamma^\alpha}\sum_{n=0}^{\infty}\frac{(-1)^n (x/\gamma)^{\alpha n}}{\Gamma(\alpha n+\alpha)} \quad (4.37)$$

with $g(t) = \sin(\alpha\pi)/[\pi(t^\alpha + t^{-\alpha} + 2\cos(\alpha\pi))]$

Its Laplace transform is then given as [138]:

$$\tilde{f}_{ML}(z|\alpha,\gamma) = \int_{-\infty}^{\infty} e^{-zx} f_{ML}(x|\alpha,\gamma)dx = 1/(1+(\gamma z)^\alpha) \quad (4.38)$$

These distributions are monotonically decreasing faster and faster as $\alpha$ goes from 1 to 0. They were not interesting for our purpose, since we wanted distributions with peaks at non-zero values.

#### 4.2.3.3 Mittag-Leffler distributions of the second kind

Another family of continuous MLD is defined in [136], thanks to their moment generating functions. For all $\alpha \in [0,1]$, a random variable $Y_\alpha$ is said to follow a Mittag-Leffler distribution of order $\alpha$ from that family, if for some constant $A > 0$ and $\alpha > 0$, we have for all z in the complex plane [136], [137]:

$$\mathbb{E}(e^{zY_\alpha}) = E_\alpha(Az) \quad (4.39)$$

More explicitly, this means:

$$\sum_{n=0}^{\infty}\frac{z^n m_n}{n!} = \mathbb{E}(e^{zY_\alpha}) = \int_{-\infty}^{\infty} e^{zy} f(y)dy = E_\alpha(Az) = \sum_{n=0}^{\infty}\frac{(Az)^n}{\Gamma(\alpha n+1)} \quad (4.40)$$

where, the convergence stands for all z in the complex plane if $\alpha \in ]0,1]$, and all z in a disc of radius $\frac{1}{A}$ if $\alpha = 0$. Hence, the moments of this distribution are:

$$m_n = A^n n!/\Gamma(\alpha n+1) \quad (4.41)$$

In this family, it is the MLD of order 0 which is an exponential distribution (and not the distribution of order 1 as in the previous family!). The MLD of order ½ is, here, the distribution of the absolute value of a normal distribution random variable and the MLD of order 1 is a degenerate distribution [136]. In opposition to the first family of Mittag-Leffler distribution, these distributions are not heavy-tailed!

---

[15] Our numerical tests indicate that for $\alpha = 0.6$ and $\gamma = 0.5$, when the sum is truncated to $10 \times y$ terms, it gives a good approximation of $f_{ML}(x|\alpha,\gamma)$ as computed with the integral, between 0 and approximately $y$, then diverges very rapidly. A Numerical evaluation (with Mathematica™ 12.1) of the integral seems better since $f_{ML}(x|\alpha,\gamma)$ decreases fast enough so that its numerical integral for $x \in [0,\infty[$ does give 1, which is not the case for the truncated series!

[16] $\frac{dF_{ML}(x|\alpha,\gamma)}{dx} = \frac{d}{dx}\left[1 - \sum_{n=0}^{\infty}\frac{(-1)^n (x/\gamma)^{\alpha n}}{\Gamma(\alpha n+1)}\right] = -\sum_{n=1}^{\infty}\frac{\alpha n}{\gamma}\frac{(-1)^n (x/\gamma)^{\alpha n-1}}{\Gamma(\alpha n+1)} = \frac{1}{\gamma}\sum_{n=1}^{\infty}\frac{(-1)^{n-1}(x/\gamma)^{\alpha(n-1)}(x/\gamma)^{\alpha-1}}{\Gamma(\alpha(n-1)+\alpha)} = \frac{x^{\alpha-1}}{\gamma^\alpha}\sum_{n=0}^{\infty}\frac{(-1)^n (x/\gamma)^{\alpha n}}{\Gamma(\alpha n+\alpha)} = f_{ML}(x|\alpha,\gamma)$, where we used the fact that $\Gamma(z+1) = z\Gamma(z)$.

One can see in the supplemental information of [122] that Niemann et al. have used this kind of MLD with $A = \Gamma(1+\alpha)$ since, in this supplemental information, the moments of the MLD are written as:

$$\langle Y_n^{\alpha} \rangle = n!\,[\Gamma(1+\alpha)]^n/\Gamma(1+n\alpha) \tag{4.42}$$

Since moments are defined at all orders, this kind of MLD has a short-tailed distribution and is in the domain of attraction of the stable laws [139]. It interpolates between the classic purely exponential function of phenomena governed by ordinary kinetic equations and the power-like behavior of phenomena governed by their fractional counterparts, just as the Mittag-Leffler function $E_{\alpha}(-x^2)$ interpolates between the Gaussian (for $\alpha = 1$) and Lorentzian (for $\alpha = 0$) functions.

In their contribution, He et al. [140] stated that those kinds of dimensionless Mittag-Leffler distributions of random variables can be computed by:

$$Y_{\alpha}(M) = \frac{\Gamma^{1/\alpha}(1+\alpha)}{\alpha M^{1+1/\alpha}}\, g^{(\alpha)}\left[\frac{\Gamma^{1/\alpha}(1+\alpha)}{M^{1/\alpha}}\right] \tag{4.43}$$

where $g^{(\alpha)}$ is the $\alpha^+$-stable distribution seen in the previous sub-section.

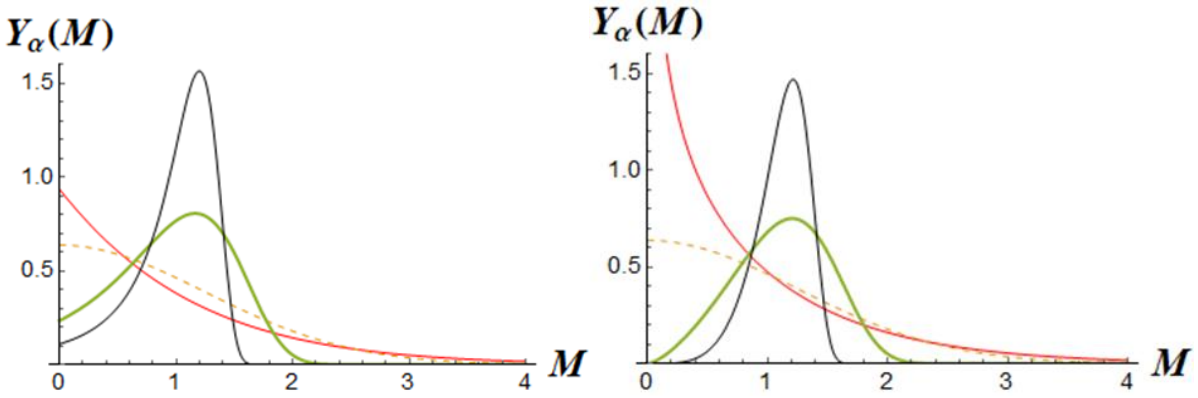


*Figure 4.7: Curves of Mittag-Leffler distributions as given in (4.43) for $\alpha = 0.2\ (red), 0.5\ (yellow\ dashed), 0.8$ (green) and 0.9 (black). The $\alpha^+$-stable distribution $g^{(\alpha)}$ is computed using Mathematica™ functions for stable distributions, while for the right picture it is computed with asymptotic approximation (4.28).*

The distributions on the left part of Figure 4.7 correspond to the distributions represented in Figure 2 of the paper by Niemann et al. to which we will refer for the interpretation of our repeated noise measurements described below. For small values of the abscissa, one can see important differences between the left figure (plotted using the Stable Distribution function of *Mathematica™* for $g^{(\alpha)}$) with the right figures (plotted using asymptotic approximation (4.28) for $g^{(\alpha)}$). This later form was nonetheless very useful for fast comparison of our data with (approximated) Mittag-Leffler distributions since its closed analytic form allowed us to use it easily in *Excel™*. Finally, we not that Mittag-Leffler distributions can be considered as a special case of geometric stable distributions[17].

[17] Geometric stable distributions have a property similar to that of stable distributions, as concerns their sums, but where the number of elements in the sum is a geometrically distributed random variable: If $X_1, X_2, \ldots$ are independent and identically distributed random variables taken from a geometric stable distribution, the limit of

### 4.2.4 Non-exponential relaxation

A real substance is always in contact with its surroundings. If it is composed of a small number of constituents, its behaviour will be deterministically determined by the way it is influenced by its surroundings. However, in a macroscopic system, there is an extremely large number of constituents interacting in a complicated way with or within the surroundings. Therefore, we must use thermodynamical statistics and describe its behaviour by certain probability laws.

In general, a macroscopic quantity (thermodynamic variable) of a system fluctuates with time. For example, the pressure in a perfect gas is due to the collision of molecules with the wall of the container, and so it always fluctuates because of irregular molecular motion. However, if we take an average of these fluctuations for real measurements, done over a very long time, we will have a result independent of the initial conditions. If we would do a measurement in a comparatively small interval of time and still get practically the same result as the long-time average, then the system would be in a state of equilibrium. When a system starts from a state out of equilibrium and is isolated, then it will approach a state of equilibrium with a time-dependency often characterized by a single characteristic time called the relaxation time.

Early work showed that a set of exactly equivalent, non-interacting, dipoles characterized by a single relaxation time (as in Debye theory of exponential relaxation) adequately explained the behaviour of weak dipolar solutions or dipolar molecules in the gas phase, but was insufficient to account for the broader frequency range over which dispersion was observed in solids and liquids in the frequency range below ~$10^{10}$ Hz. Indeed, in complex condensed matter systems, the non-exponential character of the relaxation of any fluctuating quantity as a function of time is a characteristic feature [141] indicating cooperative behaviour of the relaxing dipoles. Many experimental data, e.g. mechanical, dielectric, enthalpic, volumetric, and magnetic relaxation, or reaction kinetics dynamic light scattering and quasi-elastic neutron scattering, exhibit such a behaviour. Hence, we expect that there might be some universal relaxation law to define such a non-exponential behaviour in the dynamical systems. A way for a better understanding of the origin of the relaxation phenomenon and its independence with respect to a particular material property under consideration can be provided by probabilistic models [142]-[156]. Indeed, models such as continuous fractal time random walk, appear to give strict constraints on the mathematical form of the relaxation function [141], [142], [143], [146]. The drawback of using those kinds of probabilistic models is the inability to assign precise physical meaning to the random variables,

---

the sum $Y = a_{N_p}\left(X_1 + X_2 + \cdots + X_{N_p}\right) + b_{N_p}$ approaches the distribution of the $X_i$s for some coefficients $a_{N_p}$ and $b_{N_p}$ as p approaches 0, where $N_p$ is a random variable independent of the $X_i$s taken from a geometric distribution with parameter $p$. In other words: $Pr\left(N_p = n\right) = (1-p)^{n-1}p$. Furthermore, the distribution is said to be strictly geometric stable only if the sum $Y = a_{N_p}\left(X_1 + X_2 + \cdots + X_{N_p}\right)$ equals the distribution of the $X_i$s for some $a$. (cf. https://en.wikipedia.org/wiki/Geometric_stable_distribution)

which introduction is motivated only by general remarks on the expected properties. Hence, they usually give no clues of how to link their parameters to the microscopic details of the physical mechanism behind the relaxation. Nonetheless, the general constraints they give are very interesting.

Concerning the frequency dependent dielectric susceptibility (which is part of the formula used to compute the resonant frequencies or our resonators, hence interesting for us), some general characteristics have been experimentally established [141], [148]:

$$\begin{cases} \chi'(\omega) \propto \chi"(\omega) \propto (\omega/\omega_p)^{n-1} & \text{for } \omega > \omega_p \\ \chi'(0) - \chi'(\omega) \propto \chi"(\omega) \propto (\omega/\omega_p)^{m} & \text{for } \omega < \omega_p \end{cases}$$

where $n$ and $m$ are parameters ranging between 0 and 1, and $\omega_p$ is the loss peak frequency. Hence, we can see the power law relaxation that points towards the stable or geometric stable laws considered in the previous paragraph.

The Cole-Cole model [147] provides an example of power-law relaxation in dielectric medium for which the spectral function (frequency dependent dielectric permittivity) adjusts to the form:

$$\frac{\hat{\epsilon}(\omega) - \epsilon_\infty}{\epsilon - \epsilon_\infty} = [1 + (i\omega\tau_0)^\alpha]^{-1} \tag{4.44}$$

where, $\omega = 2\pi f$, $\tau_0$ is the relaxation time, $\alpha$ is the width parameter with interval $0 < \alpha < 1$, $\hat{\epsilon}(\omega)$ and $\epsilon$ are the frequency dependent and static dielectric permittivities. The relaxation phenomena relate to the time dependent function as $f(t/t_0)$ through Laplace transform as:

$$L[f(x); s] = \int_0^\infty e^{-px} f(x) dx \tag{4.45}$$

When we replace equation (4.44) by the Laplace transform, we have:

$$\frac{\hat{\epsilon}(\omega) - \epsilon_\infty}{\epsilon - \epsilon_\infty} = L[f(t - t_0), p = i\omega] = [1 + (pt_0)^\alpha]^{-1} \tag{4.46}$$

The inverse Laplace transform of equation above gives:

$$f\left(\frac{t}{t_0}\right) = \left(\frac{t}{t_0}\right)^{-1} \sum_{n=0}^{\infty} \frac{(-1)^n (t/t_0)^{\alpha n}}{\Gamma(\alpha n + 1)} = -\frac{d}{d(t/t_0)} E_\alpha[-(t/t_0)^\alpha] \tag{4.47}$$

Where, $E_\alpha(x)$ is the Mittag-Leffler function,

$$E_\alpha(x) = \sum_{n=0}^{\infty} \frac{x^n}{\Gamma(\alpha n + 1)} \tag{4.48}$$

The permittivity ratio can be related to the Mittag-Leffler distribution by:

$$\begin{aligned} f_{ML}(x|\alpha, \gamma) &= \frac{1}{x} \int_0^\infty e^{-\xi} g[x/(\gamma^\alpha \xi)] d\xi = \frac{x^{\alpha-1}}{\gamma^\alpha} E_{\alpha,\alpha}[-(x/\gamma)^\alpha] \\ &= \frac{x^{\alpha-1}}{\gamma^\alpha} \sum_{n=0}^{\infty} \frac{(-1)^n (x/\gamma)^{\alpha n}}{\Gamma(\alpha n + \alpha)} \end{aligned} \tag{4.49}$$

with $g(t) = \sin(\alpha\pi)/[\pi(t^{\alpha} + t^{-\alpha} + 2\cos(\alpha\pi))]$

Its Laplace transform is then given as [138]:

$$\tilde{f}_{ML}(z|\alpha,\gamma) = \int_{-\infty}^{\infty} e^{-zx} f_{ML}(x|\alpha,\gamma)dx = 1/(1+(\gamma z)^{\alpha}) \tag{4.50}$$

Later *K. Górska et al*. [149] in their work have mathematically started from an alternative method involving the analytical properties of phenomenologically determined spectral functions. This led them to use tools of theory of completely monotonic functions, to the time dependent relaxation functions uniquely determined as the weighted sums of elementary Debye relaxations where different Mittag-Leffler type functions appear to play a crucial role. Despite the limited applicability of the Cole-Cole model, they have however tried to use this model and modified it using an integral version and differential version. In the integral version, they have shown that the validity of Cole-Cole relaxation function holds for their experimental work. Whereas for the differential version, they have realised that the fractional Fokker-Planck equation is solvable in terms of Mittag-Leffler function. Elaborately, they have modelled a modified time independent relaxation model as a combination of integration and differentiation. This explicit form of the model equation provides the integro-differential relation governing the Cole-Cole relaxation. Next, they rewrote the equation as a fractional differential equation expected to be followed by a Mittag-Leffler function. Furthermore, the formal solutions of those equations are obtained using Laplace transforms giving Mittag-Leffler functions involving a one-sided Lévy stable distribution. Hence, we can say that stable distributions and Mittag-Leffler distributions have been used to model a relaxation equation that involves the relationship between the dielectric dispersion and frequency fluctuation.

### 4.2.5 Intermittency

Intermittency is the irregular alternation of phases in periodic dynamical systems with chaotic noise. *Yves et al.* [150] described routes to intermittency where a nearly periodic system shows irregularly spaced bursts or chaos as shown in Figure 4.8. In the apparently periodic phases, the behaviour is only nearly periodic, slowly drifting away from an unstable periodic point. The system eventually gets far away from the periodic point, affected by the chaotic dynamics, until it gets close to the point again and returns to the nearly periodic behaviour. Intermittency [151], has long been a subject of interest in theory and experimental studies. The recent measurements of blinking quantum dots [152]-[154], liquid crystals in the electro-hydrodynamic convection regime [155], bio-recognition [156], and nanoscale electrodes [117] shed new light on the nature of $1/f$ noise.

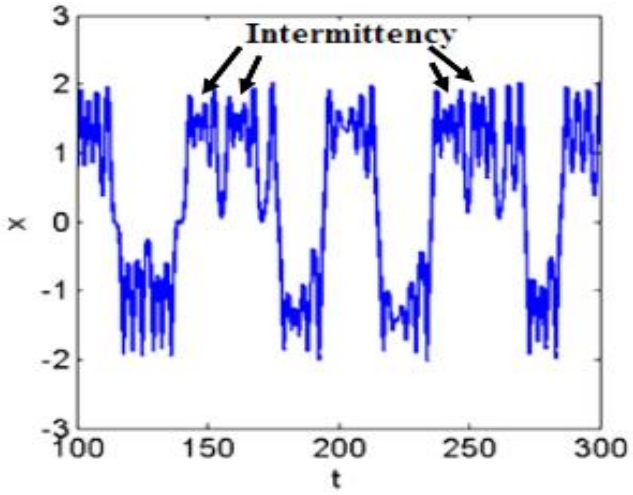


*Figure 4.8: Intermittent jumping in Duffing Oscillator [157].*

These systems, while very different in their nature, reveal a power law intermittency that routes to $1/f$ noise. This means that waiting times following power laws in a microstate of the system are responsible for the observed spectrum. The approach suggests a fundamental mechanism for $1/f$ noise in the context of intermittency chaos and turbulence. Indeed, in the work of Manneville [158], it is showed that a discrete dissipative dynamical system displays the intermittency phenomenon. Thanks to the fluctuation-dissipation theorem [159], [160], this suggests a possible connection between intermittency and $1/f$ noise. Manneville then proposed a model connecting intermittency, self-similarity and a $1/f$ spectrum, which works as a generator of random noise bursts and proves that there might be a hidden coherence in the distribution of the random noise bursts because of the peculiar properties of dynamical systems displaying intermittency. In addition to this, his contribution focuses on the fact that self-similarity at the intermittency threshold leads naturally to $Const/f^{\delta}$ power laws for the power spectrum of the noisy signal, so that instabilities with an intermittent behavior might provide an explanation to certain random noises. We note that this type of dynamics is scale free because the average sojourn times diverge, leading to weak ergodicity breaking.

Waiting time distribution with the form $\psi_t(t) \sim At^{-\alpha}$, have also been applied to deal with several problems in complex amorphous materials, intermittent currents in xenographic films [161], electron hole recombination reactions [162], $1/f$ noise [163], and dielectric relaxation as in Kohlrausch-Williams-Watts function [163]-[164]. In [162], Shlesinger showed that it is possible to use a stable distribution to describe the jumping of charges between traps, in order to explain fluctuations of electric currents in selenium. Following this contribution of Shlesinger, Montroll and Bendler [164] proposed that electron hole recombination is a "chemical reaction" between hopping charges and stationary charges, where the reaction rate is termed as the rate for a hopper to reach a trap. In single dimension, hopping of charges follows time distribution $\psi_t(t) \sim At^{-\alpha}$ and points towards the existence of a cross correlation between the survival probability of the charge carriers and the traps in a dynamical systems

that follows this type of power law. Therefore, in addition to Mittag-Leffler distributions, we also tried to fit stable distributions to our data of $1/f$ noise fluctuations in quartz crystal resonators.

## 4.3 Observation and test of Markus Niemann et al.'s model on $1/f$ fluctuations in quartz resonators

As seen in the previous paragraphs, some authors in their contributions have already implemented the possibility of representing relaxation as a non-exponential process, employing a stable law distribution [165]. On the contrary, many classical reviews concentrate only on the exponential relaxation laws or rather convolution of the exponential relaxation law with some distribution of decay rates or characteristic relaxation times [166]-[167]. However, to progress towards a better understanding of the physical origin of low frequency noise in 5 MHz SC-cut quartz resonators, we will follow the procedure proposed by *Markus Niemann et al.* to check the presence of power law intermittency (those characterised by Stable laws) as the source of $1/f$ noise in our resonators. Precisely, we will start with the introduction of their model and its relation to the Mittag-Leffler distribution. Finally, we will test whether their model applies to our work or not based on a test with experimental data that they suggest.

### 4.3.1 Definition of Niemann et al.'s model and notations

In their work [122], *Niemann et al.* considered a two-state model to show the existence of power law intermittency in the fluctuations of the power spectrum of a signal, at lower frequencies. The "up" corresponds to a signal value $I = I_0$ and the "down" state to $I = -I_0$, as shown in Figure 4.9. If we consider a given simulation, the simulation time is split into sequences during which a waiting time (denoted by $\tau_i$ for the i$^{th}$ sequence) is randomly chosen according to a probability density function (PDF) $\psi(\tau)$, with:

$$\psi_t(\tau) \propto \tau^{-(1+\alpha)} \qquad 0 < \alpha < 1 \tag{4.51}$$

in the (long) tails. Then another random choice between staying in the same state (denoted by $\chi_i$ for the i$^{th}$ sequence, with $\chi_i \equiv I(t') = \pm I_0$ for $t' \in \left[\sum_{n=1}^{i-1} \tau_n , \sum_{n=1}^{i} \tau_n\right[$) or transiting to the other state is done with equal probabilities. Then sequence $(i+1)$ starts and another waiting state $\tau_{i+1}$ is randomly chosen, and so on. The power spectrum for a given simulation during a time interval $[0, t]$ is computed by $S_t(\omega) = [\tilde{I}_t(\omega) I_t^*(\omega)]/t$, with $\tilde{I}_t(\omega) = \int_0^t I(t') \exp(-i\omega t') dt'$.

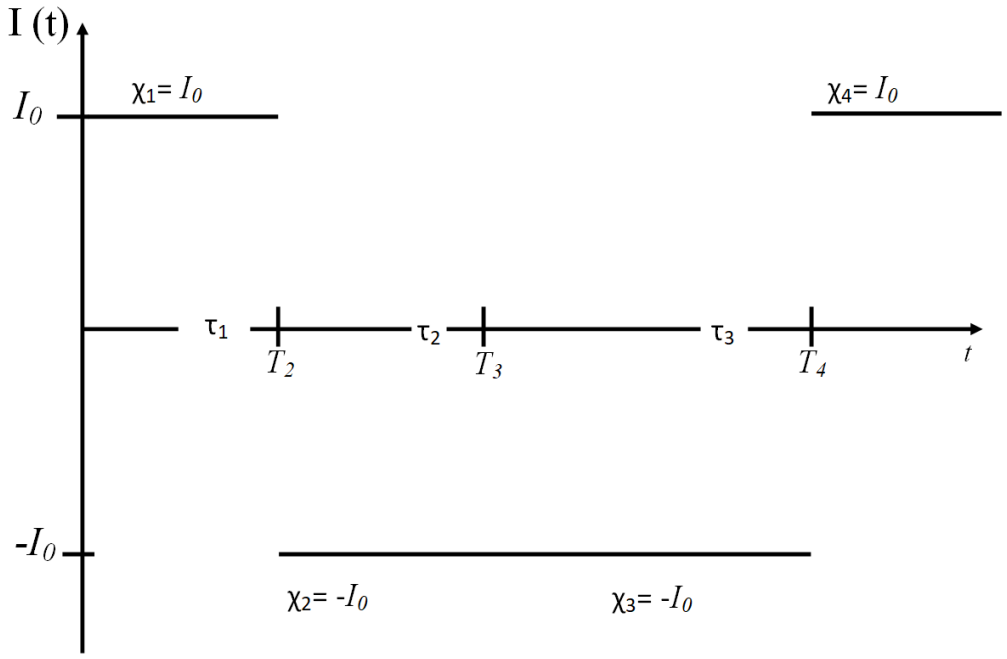


*Figure 4.9: Illustration of the notations used in the article by Niemann et al. (after Fig. S1 of the supplemental information to [122]).*

Numerically, for any given value of $\alpha$, the waiting times are generated as:

$$\tau = c_\alpha X^{-1/\alpha} \tag{4.52}$$

where, $X$ is a random variable uniformly distributed between 0 and 1 and $c_\alpha$ is chosen so that $\langle n(1) \rangle \approx 10\,000$, with $n(t)$ the number of completed waiting times up to time $t$ and $\langle \quad \rangle$ the ensemble average (i.e. $\langle X \rangle$ is the average of the values of a quantity $X$ computed for each of the repetitions of the simulation, for a given set of parameters). With reference to the two-state model mentioned above, if $\tau_i$ is taken as the $i^{th}$ waiting time and $\chi_i = \pm I_0$ is the value taken during this waiting time, times $T_j$, called end of epochs, are given by:

$$T_j = \sum_{i=1}^{j-1} \tau_i \tag{4.53}$$

With these notations, Niemann et al. find that:

$$\int_0^t d\tau \, exp(i\omega\tau) I(\tau) \backsimeq \sum_{j=1}^{n(t)} d_j(\omega) \tag{4.54}$$

Where, we have :

$$d_j(\omega) = i\chi_j \, exp\big(i\omega T_j\big) \frac{1 - exp\big(i\omega\tau_j\big)}{\omega} \tag{4.55}$$

From this approximation, Niemann et al. then obtained the expression of the ensemble averaged power spectrum as:

$$\boxed{\langle S_t(\omega) \rangle \backsimeq \frac{2I_0^2 \cos\left(\frac{\alpha\pi}{2}\right)}{\Gamma(1+\alpha)} \frac{t^{\alpha-1}}{|\omega|^{2-\alpha}} \qquad \omega \to 0} \tag{4.56}$$

In this equation one can recognize the presence of $1/f^{\delta}$ noise through the $1/|\omega|^{2-\alpha}$ factor, hence $\boxed{\delta = 2 - \alpha}$, but also a measurement time dependency through the $t^{\alpha-1}$ term! The full derivation of this expression and more details about its implications can be found in the supplementary material provided in [168].

Furthermore, they state that for a given set of $N$ non-zero measurement frequencies $\{\omega_i\}_{i=1,\cdots,N}$ the distribution of the normalized values of Power Spectral Densities (PSD) $S_t(\omega_i)/\langle S_t(\omega_i)\rangle$ should converge in distribution to the product of a random variable $Y_\alpha$ from a normalized *Mittag-Leffler distribution* (MLD) and an exponential random variable $\xi_i$, *with unit mean*, in the limit of large measurement time $t$:

$$\left(\frac{S_t(\omega_1)}{\langle S_t(\omega_1)\rangle}, \cdots, \frac{S_t(\omega_N)}{\langle S_t(\omega_N)\rangle}\right) \to Y_\alpha(\xi_1, \xi_2, \ldots\ldots \xi_N) \tag{4.57}$$

Since the respective distributions of the $\xi_i$ are supposed to be uncorrelated, they should average out in an average over the frequencies (for sufficiently large N), so that the random variable:

$$M = \frac{1}{N}\sum_{i=1}^{N} \frac{S_t(\omega_i)}{\langle S_t(\omega_i)\rangle} \tag{4.58}$$

should be distributed as the Mittag-Leffler distribution $Y_\alpha$. The verification of this fact is taken as "a strong fingerprint of power law intermittency" in $1/f$ noise by Niemann et al. and this is what we wanted to test to see whether power-law intermittency could be at the origin of $1/f$ noise in our resonators.

### 4.3.2 Experimental setup

In the remaining part of the chapter, we report $1/f$ noise measurements in 5 MHz doubly rotated SC-cut ultra-stable quartz crystal resonators, at 353 K, using a carrier suppression technic. For phase noise measurements, these resonators are temperature-controlled by ovens. The double oven heating technology allowed to have a stable slope for the power spectral density of frequency fluctuation almost up to 0.056 Hz of Fourier frequency for 1 hour and 30 minutes of measurement time. Because of the thermal drift in quartz as can be seen in Figure 4.10, a stable slope of power spectral density at the lower frequencies was not possible to obtain below this frequency. Hence, this limited the lower frequency shift that we could measure. We note in passing that for resonators fabricated in other materials, less sensitive than quartz to this thermal drift, we may possibly observe $1/f$ phase noise down to lower frequencies.

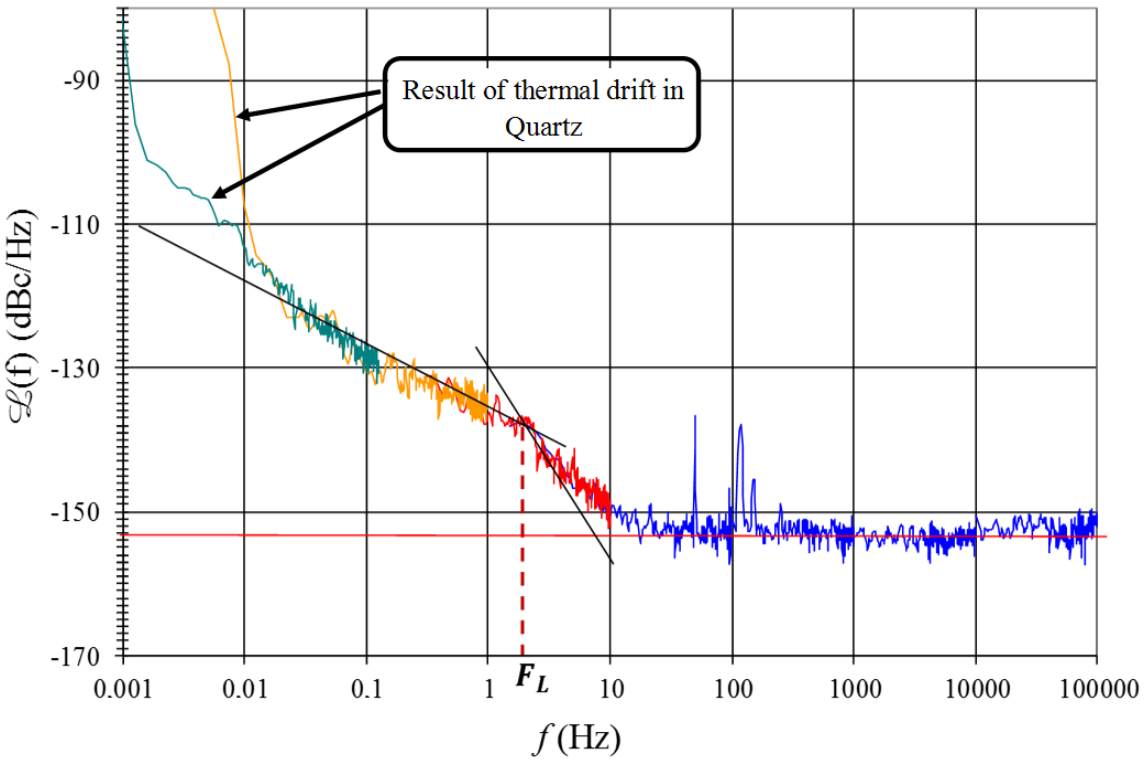


*Figure 4.10: Phase-noise graph of SC-cut 5 MHz resonator with effect of thermal drift.*

For each measurement, the power spectral density $S_y(f)$ is computed with the following relation:

$$S_y(f) = \left[\frac{F_L^2+f^2}{f_{res}^2}\right] \cdot [\mathscr{L}(f)] \tag{4.59}$$

where, $y = \Delta f_{res}/f_{res}$ with $f_{res}$ the resonant frequency, $F_L = \frac{f_{res}}{2Q_L}$ is Leeson frequency with $Q_L$ is the loaded quality factor, $\mathscr{L}(f) = S_\varphi(f)$ (identical resonators) is the single side band power spectral density of phase fluctuations, computed by using Fourier transform of the fluctuations of the signal during the measurement time $t$, Figure 4.10 shows the phase noise graph of a SC-cut quartz crystal resonators pair.

We did the same kind of phase noise measurements 101 times on three pairs of resonators. Resonator pairs are categorised according to their value of short-term stability as good-good, good-average, and good-bad pairs, the details of which one can find in the previous chapter. This allowed us to compute average values of frequency fluctuations $\langle S_y(f)\rangle$, where $\langle\ \ \rangle$, represents the statistical ensemble average, i.e. the average on our 101 measurements, for bandwidths smaller than 1 Hz. Using this average quantity, we could then compute values of $S_y(f_i)/\langle S_y(f_i)\rangle$ for a given measurement time $t$, and $N$ frequency shifts $f_i$ and finally compute 101 values of $M = \frac{1}{N}\sum_{i=1}^{N}\frac{S_t(\omega_i)}{\langle S_t(\omega_i)\rangle}$ that we have binned to represent their distribution as an histogram and be able to compare it with Mittag-Leffler distributions corresponding to various values of $\alpha$ the parameter.

### 4.3.3 Preliminary results for a series of 48 phase noise measurements for a good-average quartz crystal resonator pair

To assess the validity of the intermittency hypothesis for the origin of $1/f$ phase noise in 5 MHz SC-cut plano-convex quartz crystal resonators, we first measured $S_y(f)$ for $N$ frequency shifts $f_i$, $p$ = 48 times, for a good-average resonator pair. Figure 4.11 shows our results on $\langle S_y \rangle$ as a function of $f$ for the average computed over the 48 measurements [169] given from the formula as:

$$\langle S_y(f_i) \rangle = \frac{1}{p} \sum_{j=1}^{p} \left[ S_y(f_i) \right]_j \tag{4.60}$$

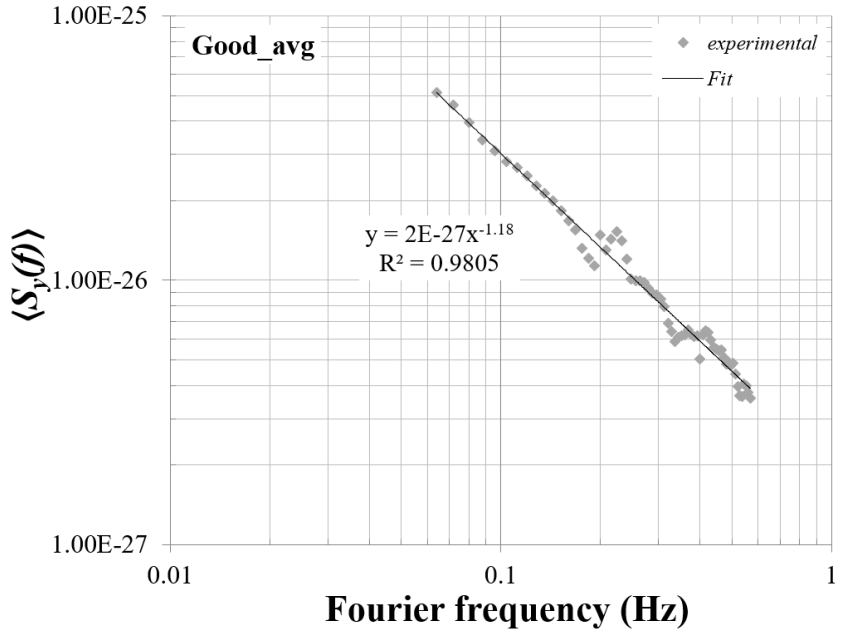


*Figure 4.11: $\langle S_y(f) \rangle$, as a function of $f$, averaged for 48 measurements.*

The fit clearly shows that the low frequency noise is of $1/f^{\delta}$ type, with a characteristic exponent $\delta = 1.180 \pm 0{,}050$[18], so that the characteristic exponent of the Mittag-Leffler distribution would be $\alpha = 2 - \delta = 0.82$ if the intermittency hypothesis developed in Niemann at al.[122] would be applicable for the kind of noise we have in our resonators (see the end of section 4.3.1).

In order to compare with the Mittag-Leffler distribution, we computed the distribution of the $p = 48$ values of the quantity $M$ defined by Niemann et al. as an average over $N$ frequencies $f_i$ of the normalized PSD values $S_y(f_i)/\langle S_y(f_i) \rangle$:

$$M = \frac{1}{N} \sum_{i=1}^{N} \frac{S_y(f_i)}{\langle S_y(f_i) \rangle} \tag{4.61}$$

[18] The uncertainty is computed thanks to the formula $\Delta\delta = \left|\hat{\delta}\right| \times t_{0{,}995,N-2} \sqrt{(1-R^2)/\left((N-2)R^2\right)}$ where $\hat{\delta}$ is the estimation of the slope, $t_{0{,}99,N-2}$ the Student coefficient corresponding to a unilateral probability of 99.5% and $N$ measurements. $R^2$ is the coefficient of determination given by EXCEL™ (0.9805 in *Figure 4.11*) for the linear fit of $\ln\left(S_y(f_i)\right)$ as a function of $\ln(f_i)$.

At first, we thought that results were very encouraging, as can be seen on Figure 4.12 and submitted these results to a conference[169].

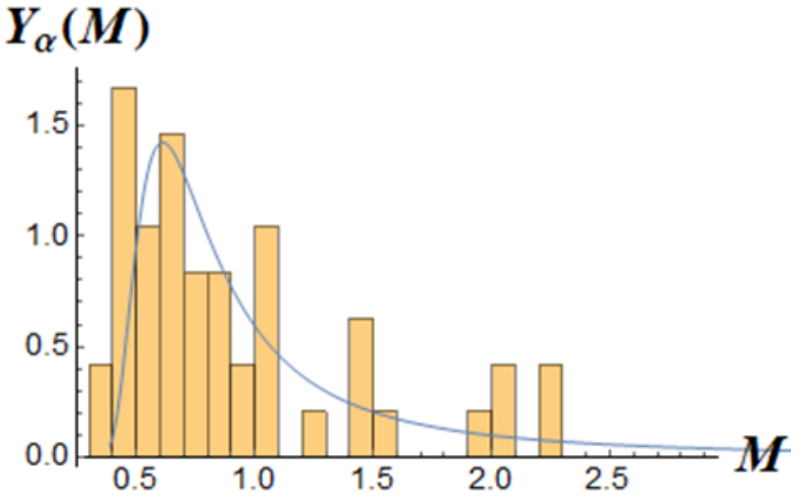


*Figure 4.12: Plot of the histogram of the probability density of M quantities for $p = 48$ measurements and the corresponding distribution for $\alpha = 2 - \delta = 0.82$.*

Hence, after the conference, we decided to make systematic studies of this kind for various pairs of resonators, as will be described in the next subsection. Unfortunately, we later discovered that we had not drawn the Mittag-Leffler distribution for $\alpha = 0.82$, but the one-sided $\alpha$-stable distributions for $\alpha = 0.82$! The result for the Mittag-Leffler function (Figure 4.13) is unfortunately much less encouraging.

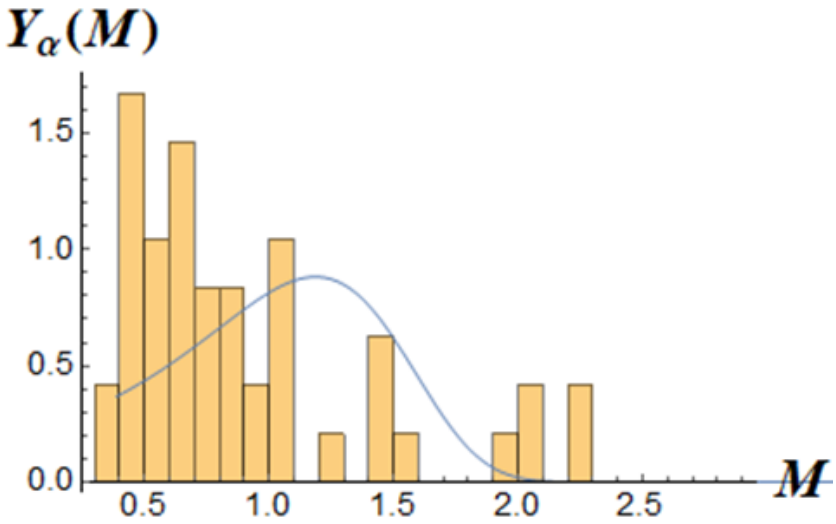


*Figure 4.13: Plot of the histogram of the probability density of M quantities for $p = 48$ measurements and the corresponding Mittag-Leffler distribution for $\alpha = 2 - \delta = 0.82$.*

### 4.3.4 Results for series of 101 phase noise measurements in various ultra-stable quartz crystal resonator pairs

After seeing the first results for our series of 48 measurements, we did similar phase noise measurements on the same good-average resonator pair and other pairs of resonators: a good-bad pair and a good-good pair. The plots in Figure 4.14 and Figure 4.15 are the ensemble averages of the PSD

for 101 measurements versus the frequency intervals of the resonator in logarithmic scale, for the good-average pair and the good-bad pair, respectively. Both graphs exhibit a power law scaling of $\langle S_y(f) \rangle$ versus $f$ in our measurements. The value of the power law exponent $\delta$ for the good-bad pair is $\delta = 1.231$ while it is $\delta = 0.694$ for the good-good resonator pair. The corresponding values of $\alpha = 2 - \delta$ are thus respectively $\alpha = 0.769$ and $\alpha = 1.306$, to be compared with the characteristic exponent of the Mittag-Leffler or one-sided alpha-stable distributions that would best fit our histograms of $M$ values.

Unfortunately, the value $\alpha > 1$ that we got from Figure 4.16*:* for the good-good resonator pair is a problem for the comparison with the statistical model, since for Mittag-Leffler distributions, we must have $0 < \alpha < 1$. Since in that case, the correlation coefficient was much worse than in the two previous cases, we decided to perform another series of measurements with another pair of good resonators. We can see in Figure 4.17*:* that this time the correlation coefficient is better (and the absolute values for the noise PSD lower) but we still get a slope $\delta = 0.944$ lower than 1 (but much nearer to 1) and we do not really have an explanation for the fact that, the fit for the two good-good pairs seem to be worse than for the good-bad or good-average pairs, since the methodology is the same for all these pairs. However, it was this event that triggered our reconsideration of our preliminary results and our finding that we had plotted a one-sided alpha-stable distribution and not a Mittag-Leffler distribution in our preliminary graph.

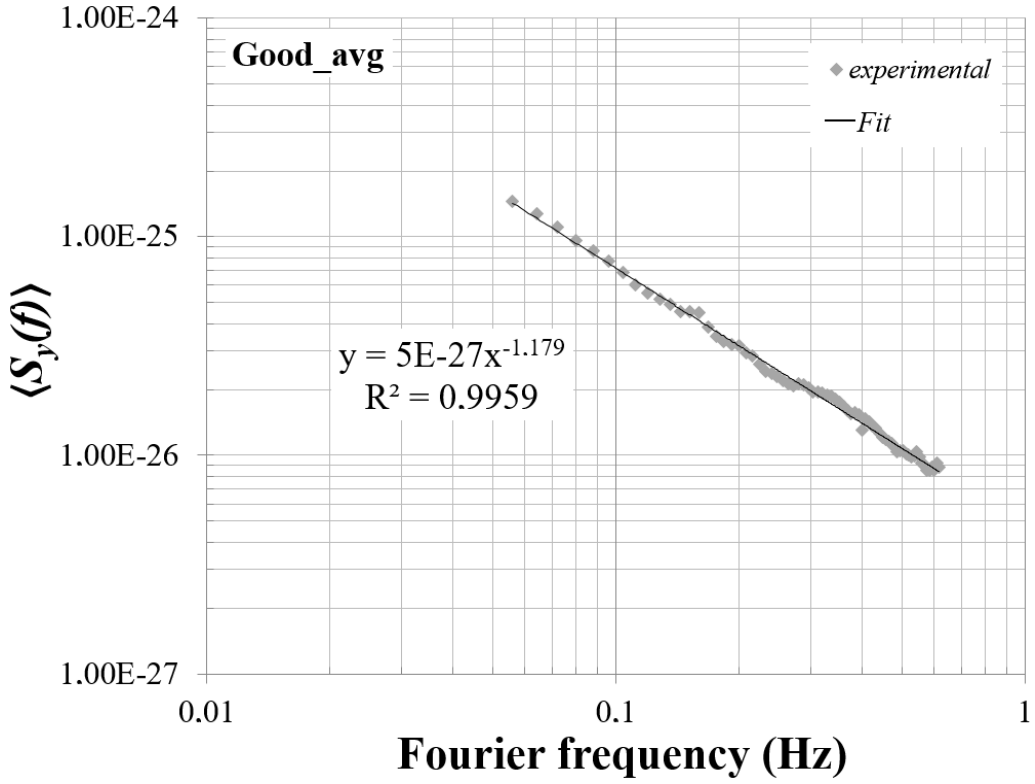


*Figure 4.14: $\langle S_y(f) \rangle$, as function of $f$, averaged over 101 measurements for the good-average resonator pair.*

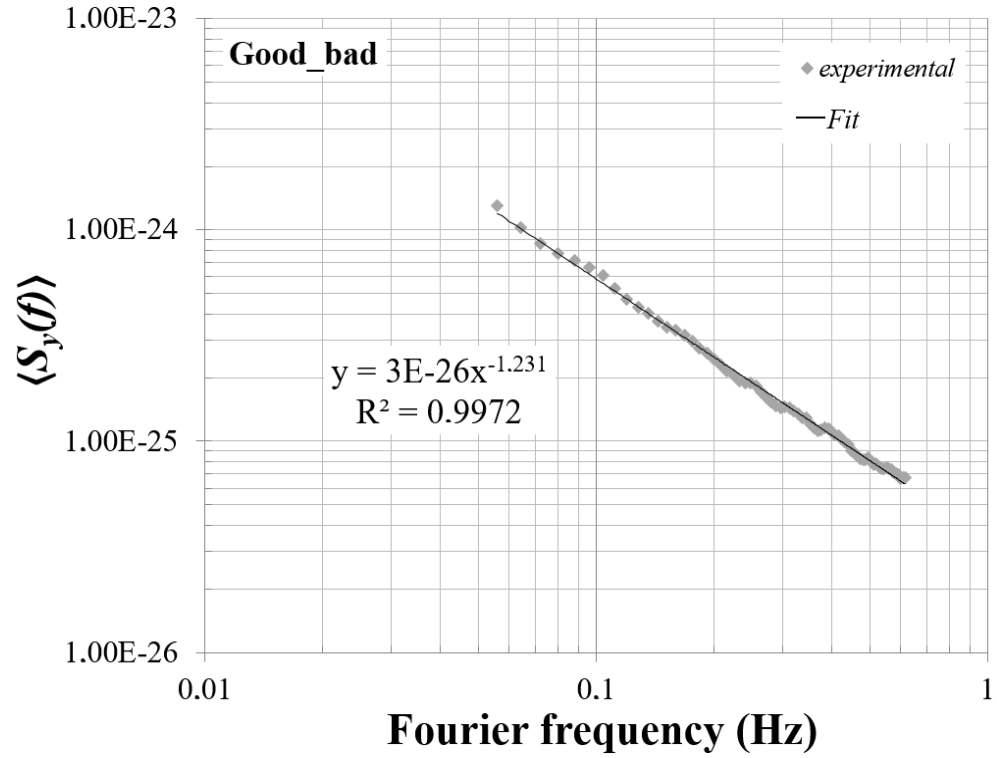


*Figure 4.15: $\langle S_y(f) \rangle$, as function of $f$, averaged over 101 measurements for the good-bad resonator pair.*

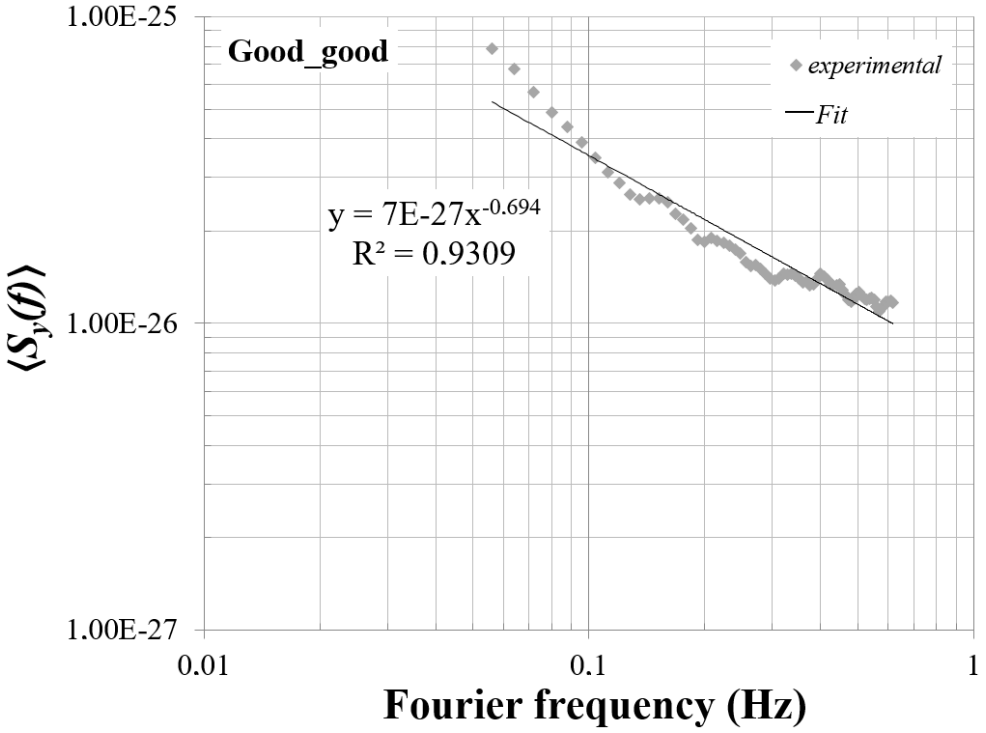


*Figure 4.16: $\langle S_y(f) \rangle$, as function of $f$, averaged over 101 measurements for the first good-good resonator pair.*

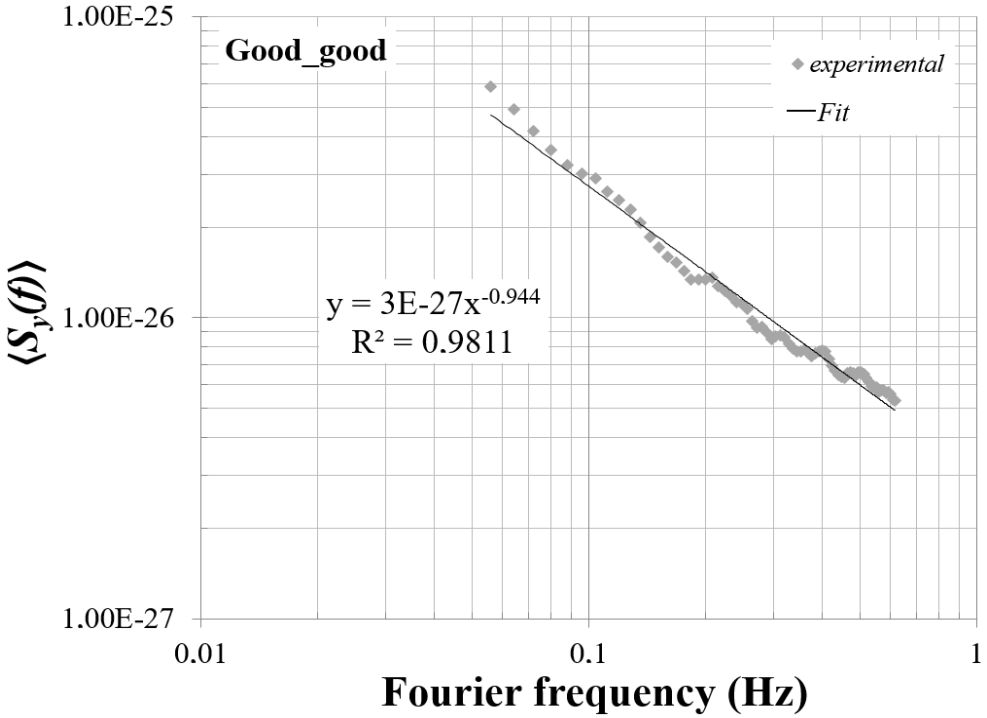


*Figure 4.17: $\langle S_y(f) \rangle$, as function of $f$, averaged over 101 measurements for the second good-good resonator pair.*

Next, we wondered what the spread of the individual measurements around these average delta values would be. We plot, in Figure 4.18, Figure 4.19, and Figure 4.20, the characteristic exponent $\delta$ and the amplitude $A$ of the fit to phase noise by $10^A/f^\delta$, for each of the 101 measurements done with the three different resonator pairs mentioned above (the second one in case of the good-good pair). $\delta$ and $A$ correspond respectively to the slope and the intercept of the straight line obtained in log scale. We can see that the correlation between these two quantities is at best weaker for the good-bad and the good-good resonator pairs and seemingly completely absent for the good-average resonator pair. Surprisingly for us, slope values ($\delta$) greater than 1 seem to be quite common in the individual measurements for all resonator pairs (but especially for the good-good resonator pair). By looking at some individual curves, we could see that this may be a consequence of some instabilities in the curves occurring at different frequencies near the upper limit of the frequency interval we selected for our study. Unfortunately, we have not been able to go further in the interpretation of these instabilities, but we note that the detailed aspect of those figures is dependent on the value of the limits that we use for the frequency interval used to draw them.

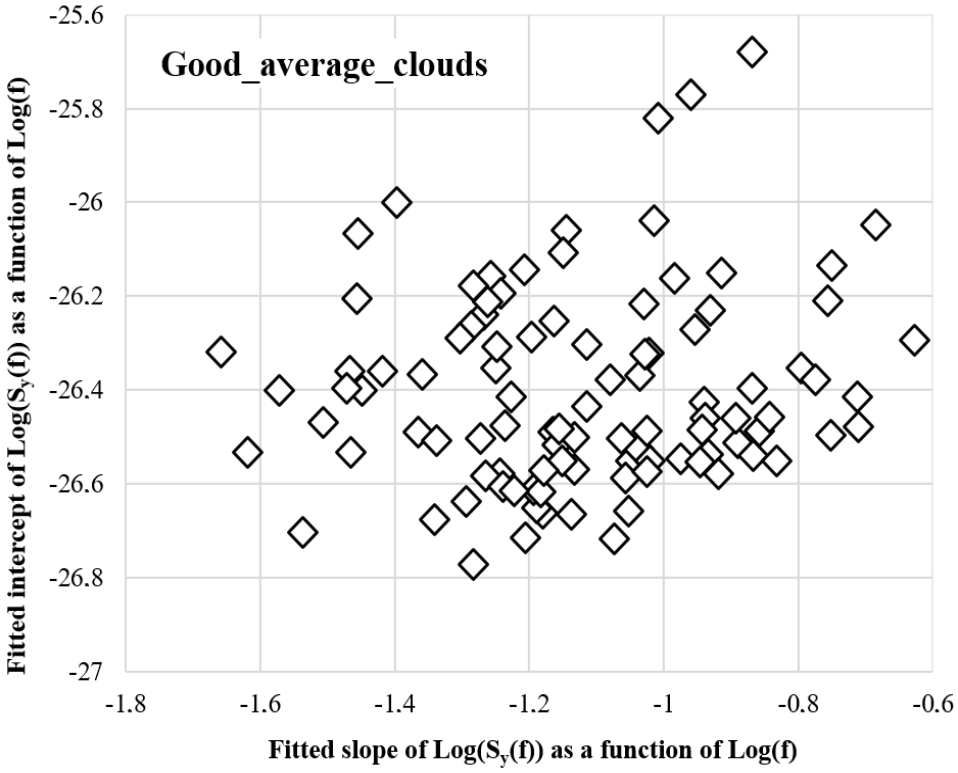


*Figure 4.18: Intercept versus slope of the fit of $log(S_y(f))$ as a function of $log(f)$ for each of the 101 measurements (Good-average resonator pair).*

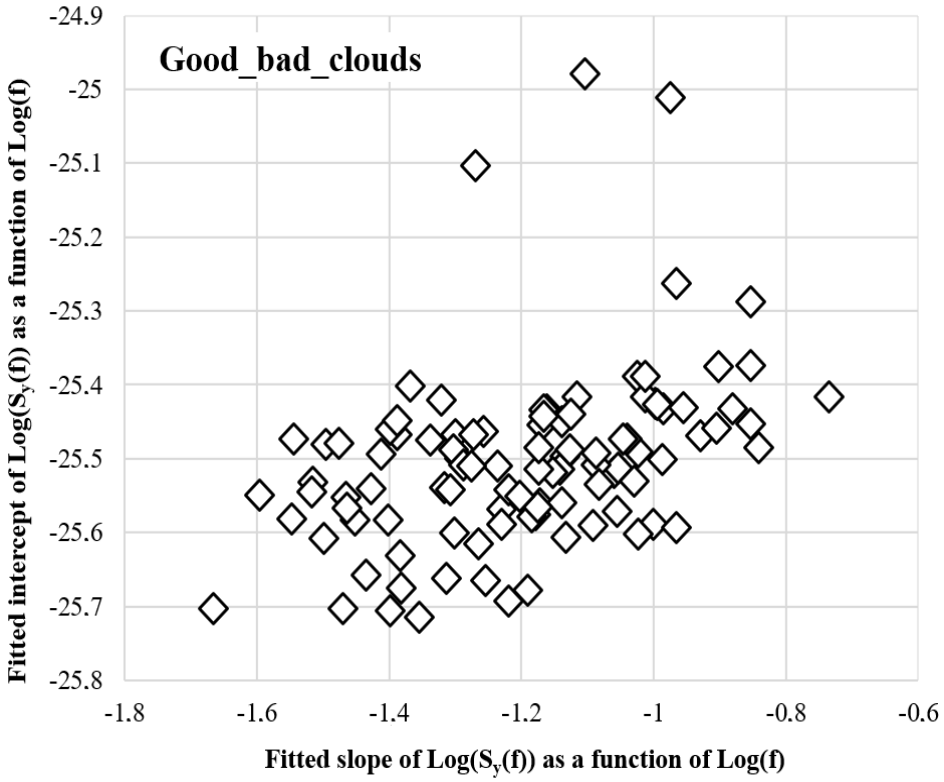


*Figure 4.19: Intercept versus slope of the fit of $log(S_y(f))$ as a function of $log(f)$ for each of the 101 measurements (Good-bad resonator pair).*

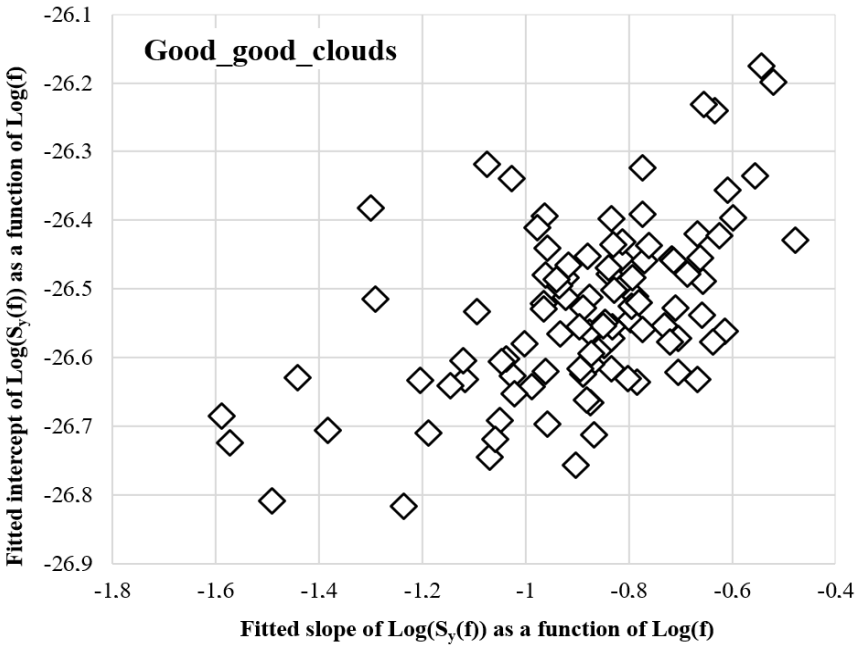


*Figure 4.20: Intercept versus slope of the fit of $log\left(S_y(f)\right)$ as a function of $log(f)$ for each of the 101 measurements (second good-good resonator pair).*

### 4.3.5 Tests on the possibility to model $1/f$ phase noise in the ultra-stable quartz crystal resonators using Mittag-Leffler or one sided α-stable distributions

We now turn to the comparison with Mittag-Leffler and other stable distributions, of the distribution of the $p = 101$ values of $M$ computed as an average over the $N$ frequencies of the $N$ $S_y(f_i)/\langle S_y(f_i)\rangle$ values, for each of the three pairs mentioned in the previous section:

$$M = \frac{1}{N}\sum_{i=1}^{N}\frac{S_y(f_i)}{\langle S_y(f_i)\rangle} \tag{4.62}$$

We recall, that according to the model of intermittency developed in the paper of Niemann at al., these 101 values of $M$ should be distributed according to a Mittag-Leffler distribution (MLD) of the second kind, with parameter alpha given by $\alpha = 2 - \delta$, where $\delta$ was determined from the slope of the straight line fit of $log\left(S_y(f)\right)$ as a function of $log(f)$, averaged over $p = 101$ measurements, for each of the three pairs. The values found in the previous paragraph are summarized in Table 4.1.

| Type of pair | Good-bad | Good-avg | Good-good |
|---|---|---|---|
| $\delta$ | $1.231 \pm 0.021$ | $1.179 \pm 0.024$ | $0.944 \pm 0.042$ |
| $\alpha = 2 - \delta$ | 0.769 | 0.821 | 1.056 |

*Table 4.1 : values of the slopes δ of the fits of $log\left(\langle S_y(f)\rangle\right)$ as a function of $log(f)$, for three resonator pairs and corresponding candidate $\alpha = 2 - \delta$ for the index of the Mittag-Leffler distribution supposed to fit the distribution of M values if the intermittency model of Niemann et al. would be applicable for our data.*

We first represent the histograms with a bin size of 0.1. We can see that all three histograms are skewed to the right, while we recall that Mittag-Leffler distributions for $\alpha > 0.5$ are skewed to the left!

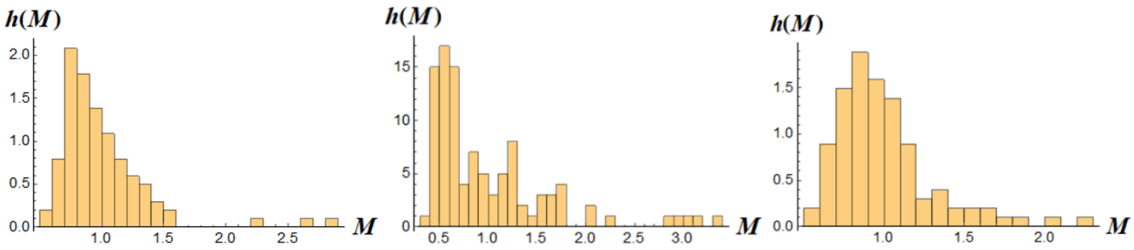


*Figure 4.21: Histograms of the 101 M values for the good-bad pair (left), the good-average pair (center) and the good-good pair (right).*

The figures above show that MLD distributions are not adequate to describe our data, hence probably rejecting the intermittency hypothesis developed in Niemann at al. [122] as the physical origin of $1/f$ noise in our quartz resonators.

Nonetheless, considering that our preliminary data was reasonably well fitted by a one-sided alpha stable distribution, we decided to fit the data of Figure 4.21 by stable distributions $S_1(x|\alpha,\beta,\gamma,\delta_1)$ using *Mathematica*$^{TM}$. The corresponding values of the parameters for the best fit are gathered in Table 4.2, while $p$-values for various statistical tests proposed by *Mathematica*$^{TM}$ are gathered in Table 4.3 and plots of the histograms and corresponding best fit functions are pictured in Figure 4.22 for the good-bad pair, Figure 4.23 for the good-average pair and Figure 4.24 for the second good-good pair.

| **Values of parameters** | **Good-bad** | **Good-Avg** | **Good-good** |
|---|---|---|---|
| $\alpha$ | 1.3733 | 0.8590 | 1.4543 |
| $\beta$ | 1. | 1. | 1. |
| $\gamma$ | 0.1351 | 0.1586 | 0.1443 |
| $\delta_1$ | 1.0707 | $-0.0851$ | 1.0535 |
| $[\cos(\pi\alpha/2)]^{1/\alpha}$ | $-0.43+0.49\,i$ | 0.1713 | $-0.42+0.62\,i$ |

*Table 4.2: values of the parameters of for the best fitting stable distributions $S_1(x|\alpha,\beta,\gamma,\delta)$.*

| | *p-values* | | |
|---|---|---|---|
| **Type of test** | **Good-bad** | **Good-Avg** | **Good-good** |
| *Anderson-Starling* | 0.9739 | 0.3450 | 0.9994 |
| *Cramér-von Mises* | 0.9458 | 0.3847 | 0.9990 |
| *Kolmogorov- Smirnov* | 0.9306 | 0.4262 | 0.9736 |
| *Kuiper* | 0.8683 | 0.1563 | 0.9861 |
| *Pearson* $\chi^2$ | 0.2160 | 0.1391 | 0.9964 |
| *Watson* $U^2$ | 0.8625 | 0.1019 | 0.9972 |

*Table 4.3: p-values for the best fitting stable distributions.*

We can see that the fit for the good-good pair is nearly perfect, while it is excellent for the good-bad pair and quite good for the good-average pair, but the most important point is that we do have, but unfortunately, only the good-average plot is fitted by a nearly one sided $\alpha$ stable function which $\alpha$ index is almost in the confidence interval for $2-\delta, \beta=1, \gamma\approx[\cos(\pi\alpha/2)]^{1/\alpha}$ and $\delta\approx 0$. For the two other distributions, $\alpha$ is neither given by $2-\delta$, nor by $\delta$, but $\beta$ is clearly one (entirely right skewed

distributions). To convince ourselves that these results were reproducible and not the result of the convergence towards a secondary minimum during the fit, we also fitted the same data with $S_0(x|\alpha,\beta,\gamma,\delta_0)$. We found the same values of $\alpha, \beta$ and $\gamma$ up to seven digits and the same for the relation $\delta_0 - \delta_1 = \beta\gamma \tan(\pi\alpha/2)$ for the good-good and the good-bad fits. For the good-average fit, it is slightly worse but still very good, since we have 4 identical digits for $\alpha$, 6 for $\gamma$ and 3 for the relation between $\delta_0$ and $\delta_1$ ($\beta = 1$. In both cases).

Looking at these quite good fits, we now think that it could be interesting to go back to the $\langle S_y(f)\rangle$ plots and study the influence of the choice of the limits of the frequency intervals chosen to draw these plots and compute the $\delta$ values and their confidence interval, or study in more details each of the $p = 101$ plots and in particular those corresponding to the outliers, to see whether there would be particular features in them. Unfortunately, first attempts at doing that do not exhibit anything special for the moment.

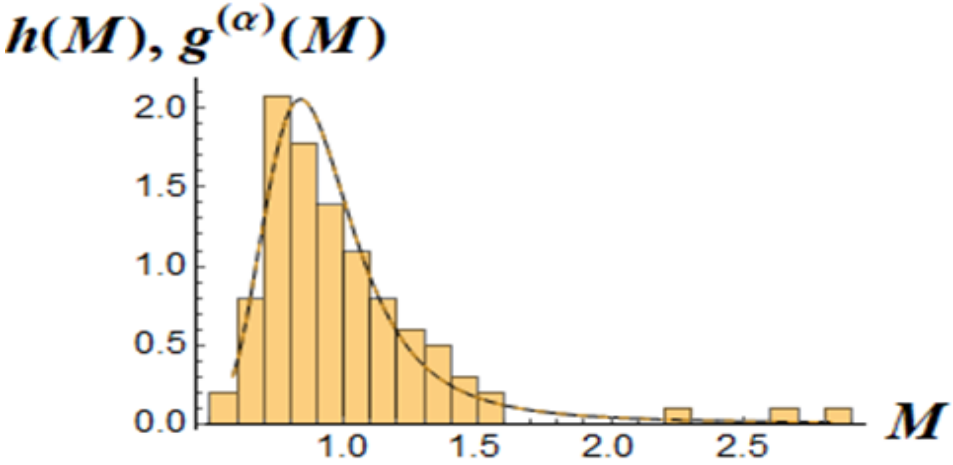


*Figure 4.22: Histogram of M values and corresponding best fit one sided α-stable distribution, for the good-bad resonator pair.*

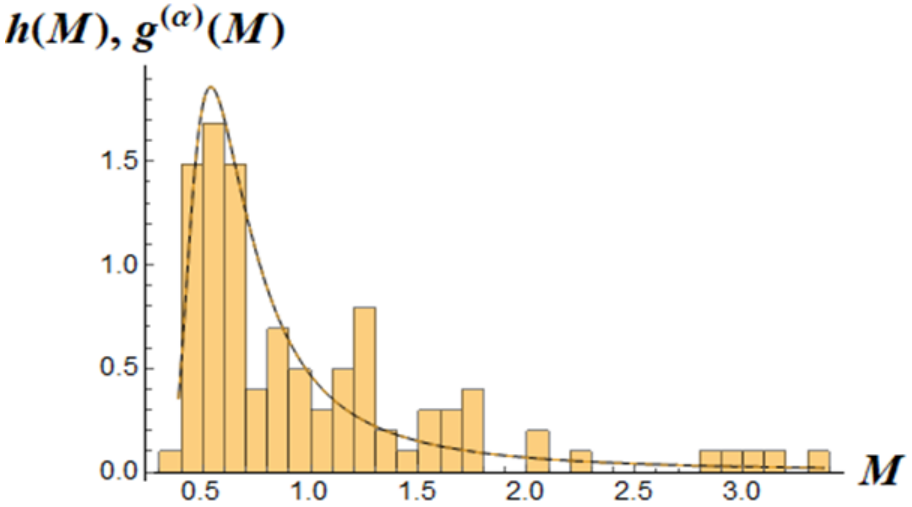


*Figure 4.23: Histogram of M values and corresponding best fit one sided α-stable distribution, for the good-average resonator pair.*

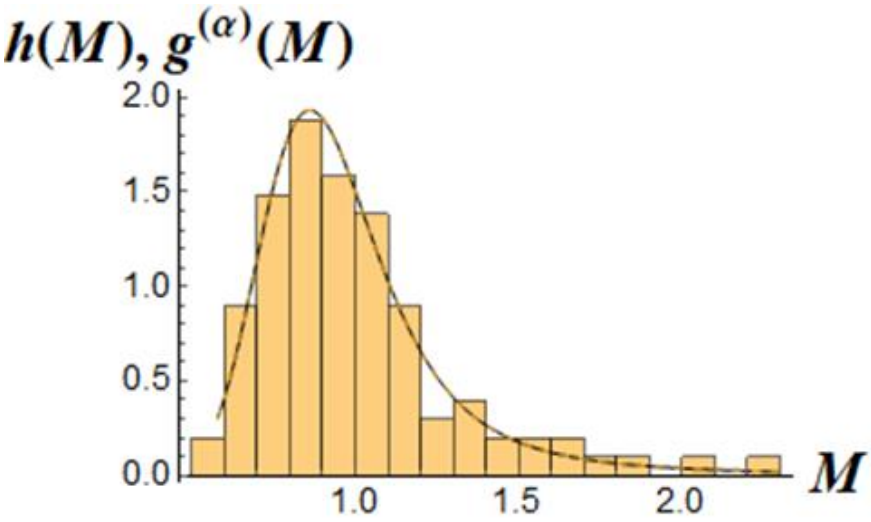


*Figure 4.24: Histogram of M values and corresponding best fit one sided α-stable distribution, for second good-good resonator pair.*

## 4.4 Summary

In this chapter, after some description of stable and Mittag-Leffler statistical distributions, we reported that many authors now point the deficiencies of the exponential law as the building block to study relaxation (that can be connected through the fluctuation-dissipation theorem to noise) and favor laws with an inverse power scaling at lower frequencies, especially for the study of the dielectric permittivity for frequencies of interest for us. We then described the intermittency model proposed by Markus Niemann and collaborators in [122] to first elucidate the puzzle of the absence of cut-off frequency for $1/f^{\delta}$ noise in most systems in which this type of noise is found and, second, to provide tests in order to evaluate the pertinence of a power-law scaling intermittency model for low frequency phase noise in our resonators. Unfortunately, our experimental data does not compare well with the Mittag-Leffler distributions that should have described it according to Niemann et al., if power-law intermittency would be the origin of noise in our ultra-stable quartz resonators. We also saw that right-skewed stable distributions could be a better (but not always excellent) fit, which is interesting considering the connection of stable distributions with fluctuations of a collection of random uncorrelated noise sources. Hence, we think that this connection with stable distributions should be pursued. The difficulty here is to understand the link between the statistical distribution and the behavior of the noise sources.

# Chapter 5 Quartz crystal resonator in reverse engineering

## 5.1 Analysis of the quartz crystal resonator by reverse engineering

This chapter deals with the dismantling part of the quartz crystal resonator fabricated by the European manufacturers for CNES (Centre Nationale d'Etudes Spatiale) as already mentioned in Chapter 1. The title "Reverse Engineering" is used to say that we dismantled and studied the parts of some resonators of various qualities. We have had already measured phase noise in quite several resonators provided to us by CNES. As in the previous chapters, the classification of resonators according to their short-term stability values may help or else might give an idea to the manufacturers to identify the resonators during production beforehand if we would be able to find a type of information on characteristic of the bad resonator . In this chapter, we show the few possible experimental methods we used in search for intrinsic information regarding the quartz material. X-rays and Laser scattering are possible methods to localize and quantify internal defects of the resonator material i.e. quartz in our case. Hence, in this work, we will start with dismantling of the resonator, study the possible residual defects of the quartz crystal material, influence of the chemical impurities present, and try to conclude our experimental data with possible scientific analysis.

Quartz is a material with a crystalline structure and is anisotropic in nature. The word "crystal" refers to a solid matter where the pattern of atom arranges singly and repeats throughout the mass. Atoms in the crystal appears in a tiny group, these groups are almost same in orientation and alignment along all three dimensions. Individually, the group seems to be as a parallelepiped and building blocks of the crystal material. The formation of the crystal is then by mounding together in all three dimensions the ditto of parallelepiped with no spaces among them. This kind of block is termed as a unit cell [170]. Since the choice of a set of atoms to form a unit cell is random, there exists a wide range of selections in the shapes and dimensions of the unit cell. Normally, the unit cell which is selected is related to the actual crystal faces and X-rays reflection and has the symmetry of the crystal itself. These data signifies, e.g. atomic cell dimensions and angles, interfacial angles, optical properties, and X-rays properties [171].

Quartz is dielectric material used for the realization of acoustic cavities because of its property of piezoelectricity. The quartz material being anisotropic, resonators are made from quartz plates of with orientation and follows a standard from *IEEE* (see Chapter 1 and Annex A). Quartz has been serving as a frequency component in piezoelectric application for almost 80 years. The synthesis work progressed slowly and little by little, synthetic quartz replaced natural quartz. As a result, it has occupied a huge space in the field of telecommunication applications.

Industrial productions these days, particularly those fabricating clocks and oscillators, have rapidly moved towards the use of synthetic quartz. Although quartz is abundantly present on Earth, in

its natural state quartz is faintly piezoelectric and has a large number of impurities i.e. for example atoms of Al, Li, B, Fe, Mg, Ca, Ti, Na [172].

## 5.2 Bulk acoustic wave cavity quartz crystal resonators at room temperature and constraints

Quartz resonators are one of the most used components in time measurements. Commonly, it has vital role as a local reference of frequency for wristwatches and as an integrated part in most of the time-keeping devices. The atomic clocks based on the transition of two energy levels of an atom of rubidium and caesium rely on the stability of a crystal resonator kept at the feedback of an oscillator. The resonant frequency in the case of a BAW resonator is that of specified mode of mechanical vibration and excited piezoelectrically for any dielectric material, which in our case is a quartz crystal resonator. Acoustic resonator made from quartz, can excite in three distinct modes of vibration *A*, *B* and *C* that are associated with quasi extension-compression mode-*A*, quasi-fast shear mode-*B* and quasi-slow shear mode-*C*. These modes have distinct properties, whatever the quartz cut is, mode A is highly damped, and temperature sensitive. Similarly, mode-*B* shows high sensitivity to temperature for SC-cuts, which is good for fabricating sensors using this mode. Whereas, for the realisation of oscillators with a very descent or the very good frequency stability up to $10^{-14}$ for few secs at room temperature, mode-*C*. Thus, it is one of the best modes and known as metrological mode. As we have mentioned in previous chapters, a mode-*C*, SC-cut quartz resonator, has a quality factor around 2.5 Million at 5 MHz, and it exhibits good performance at room temperature.

However, the work done for several years on acoustic quartz crystal resonators laid to improvements but a proper understanding and clear physical explanation for the origin of the intrinsic fluctuation that may have some possible relation to $1/f$ flicker noise in quartz crystal resonators still lacks. Viewing this, in this chapter we particularly focus on characterisation of defects in a quartz material through dismantling to explore the knowledge and idea in a search to trace a possible means to find out a relation leading to the cause for intrinsic fluctuation or noise because of intrinsic defects in quartz material.

## 5.3 Dismantling the quartz crystal resonator

We dismantled a pair of resonators one good in noise and the other bad. The dismantling carried out in a simple way uses a metal cutter shown in Figure 5.1. The resonator is hold gently in the cutting area of the cutter. The cutter is gently pressed, and the resonator made to rotate clockwise or anticlockwise within the cutting area according to the preference. It hardly takes 10 minutes per resonator and the resonator cut opens as can be seen in step 1 to 8 below. Once the resonators dismantled, we analysed them thoroughly using a digital microscope by Keyence capable of ×1000 times zoom. We took several images of the internal structure of the resonator plates mounted with gold electrodes. The Figure 5.2 (5,6) below shows the top and side view of the resonator plates with

electrodes. The thickness of gold electrodes mounted on the quartz crystal is around 200 nm. In between the gold and the quartz material, there is one nanometer thin chromium layer. This chromium layer helps to hold the gold electrodes with the quartz material.

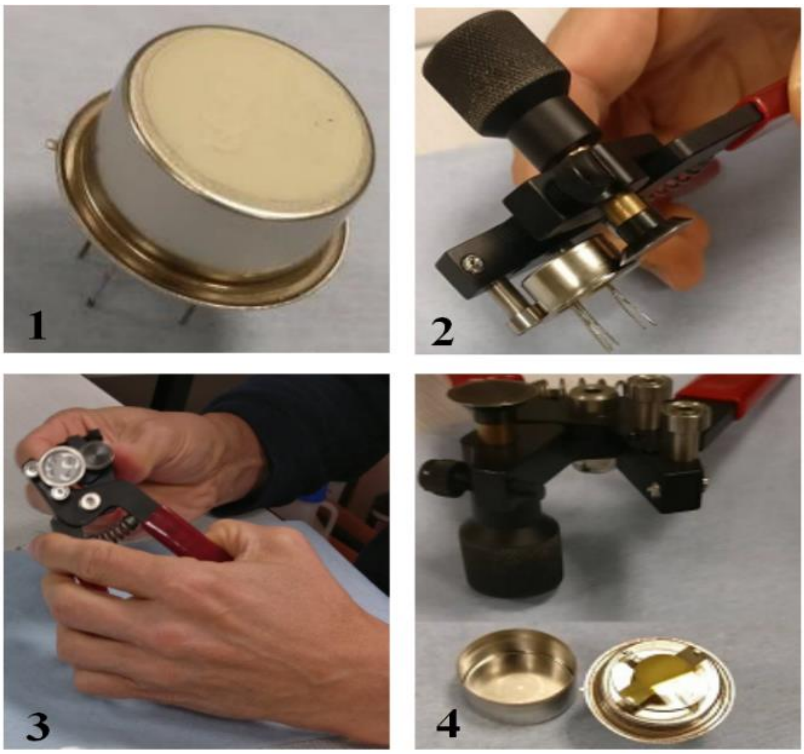


*Figure 5.1: Dismantling of the quartz crystal resonator.*

Similarly, enlarging images of the quartz plates Figure 5.3 (7,8) with electrodes, there are significant amount of scratches observed both in bad and good resonators. The central part of both the plates have dense scratches and resembled as if made by a sharp instrument. However, the number of scratches did not resemble any significant differences in terms of kind of (bad or good) resonators. In addition to this, we took images of all the glue points of both the resonator plates. Still, no significant differences found that could distinctly justify the bad and good resonators.

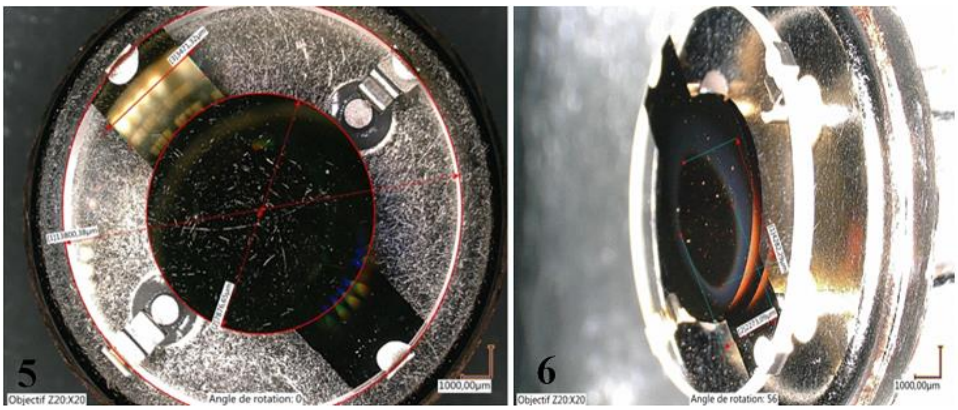


*Figure 5.2: From left: Top and side views of the electrode mounted plates.*

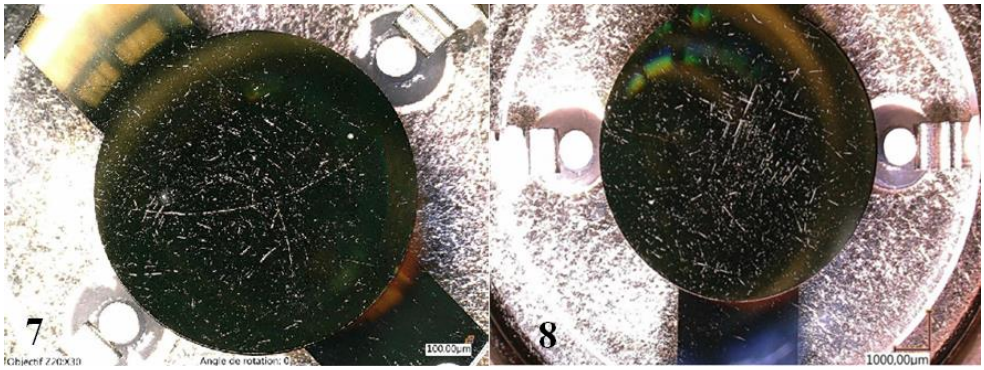


*Figure 5.3: From left: Bad and good resonator plates with electrodes.*

## 5.4 Defects in the quartz crystal material

The quartz crystal resonators that we use in our work are cuts from synthetic quartz bars. The synthetic quartz produced today is free from many natural quartz defects but not perfect [172]. The main objective of this work will be to list different kinds of defects that can be observed within the synthetic quartz crystals used for resonator fabrication. Therefore, in this chapter we will only discuss those kinds of probable quartz crystal defects in relation to our resonators.

Synthetic quartz is widely used in optical and electro-mechanical devices. Today, we can easily get clear blocks, free from twins, and possible infrared imperfections, that are also easy to cut to get synthetic quartz plates. Some of the specific structural defects of quartz are chemical impurities, inclusions, and dislocations, and below we present some brief explanation on some of these defects.

### 5.4.1 Chemical impurities

Chemical impurities refer to the atoms or molecules foreign to the crystal which are within the crystal piece possibly by substitution i.e. replacing another atom or molecule. Precisely, all the atoms outside the crystal lattice, other than silicon and oxygen. The most abundant defect is due to a hydrogen atom coming close to an oxygen atom and forming a hydroxide (OH) ion. These OH group link with the other atoms to establish an atomic neutrality, possibly forms Si-OHX groups, where X can be $Al^{3+}$, $Fe^{3+}$ and so on. Similarly, there are other alkalis like Sodium (Na), Lithium (Li), Potassium (K), or ions of Silver (Ag) or Copper (Cu) that can participate in the charge defect compensation by substituting the Silicon atom [172].

### 5.4.2 Inclusions

Inclusions are a common type of defect in synthetic quartz. These defects range from $\mu m$ to tens of $\mu m$ for any high-quality quartz and can be visible to naked eyes. Some examples of inclusions are in Figure 5.4. These inclusions are usually external materials trapped during the crystal formation. In the block of synthetic quartz, the solid inclusions as seen on figure above can be acmite since acmite, is present in the walls of the autoclave during the time of growth of the crystal. J.J. Boy [172] in his PhD thesis has also mentioned that, sometimes an internal fracture appears is caused by the high temperature

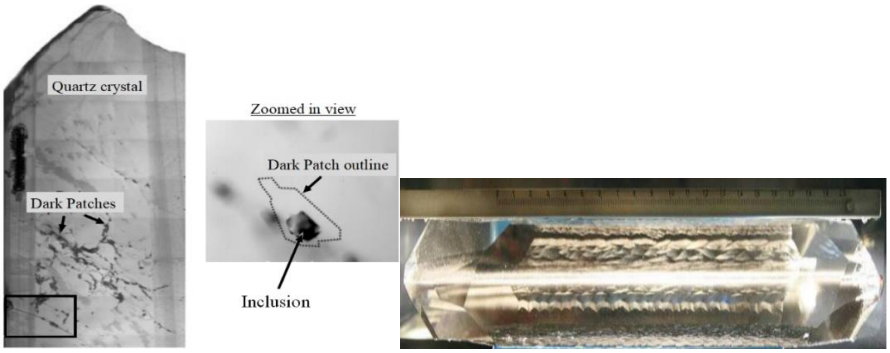


*Figure 5.4: Left: Inclusions in quartz crystal*
*right: Inclusion detection and seed localization [173].*

in the quartz sample. The presence of this kind of defect is possibly a crucial constraint influencing the quality of the resonator, for e.g. we can even anticipate that if these kinds of defects are present in the vibrating zone of the resonator they could possibly cause irregularities in the resonator.

### 5.4.3 Dislocations

Generally, dislocations are linear defects in any crystalline solids. They correspond to discontinuities in the organisation of the crystalline structures. Although of small atomic width, the dislocations can be very long. They generally propagate until meeting another defect or a surface. When the crystalline structure of the quartz crystal is disturbed, it might cause energy losses and diminish the Q-factor, which is one of the useful parameters for a resonator connected to the intrinsic resistance. As already mentioned in Chapter 1, Q-factor resembles the amount of attenuation, which includes the losses because of defects like inclusions, dislocations, or imperfections. Chirla and Illiescu [170], have classified dislocations based on their "Burger vector" which gives the direction of dislocations and the interatomic spacing in their direction. As in Figure 5.5, the Burger vector are denoted by $\vec{b}$; $\vec{l}$ is a dislocation line vector for a chosen line and orientation, $\vec{b}$ is invariant along the dislocation, it means the Burger vector is constant for dislocation, orientation, and line direction. If $\vec{b}$ is perpendicular to $\vec{l}$, the dislocations are edge type, if $\vec{b}$ is parallel the dislocation is of screw type. Edge dislocation outlines as an extra-plane of atoms and the screw dislocation appears as a spiral staircase effect.

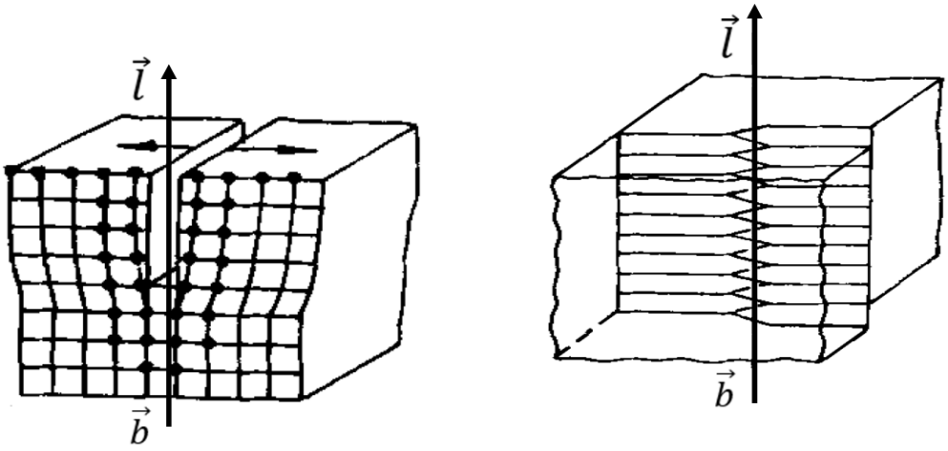


*Figure 5.5: Left: Edge type dislocation, right: Screw type dislocation [170].*

Johnson and Irvine [174] in their contribution have stated that the dominant source of dislocations in the synthetic crystal might be by the latent seed dislocations and the seed-crystal interface. Later the composition of the interface might consist of solid inclusions coexisting with a group of dislocations. Etch channels are possible to be formed by dislocations during the fabrication process of a resonator. They can create electrical faults when they encounter the electrodes, and possibly accumulating contamination responsible for quick aging. In addition to this, dislocations are impurity traps i.e. the foreign atoms come to lodge and diffuse in the spaces created by the dislocations. In synthetic quartz, dislocations often originate from an inclusion, so it will be relatively easy to locate one if the former gets already identified in the crystal. Therefore, to see the effects of dislocation there are technics like, *Etching*,
*X-rays diffraction topography*, *X-rays-topography using synchrotron radiation*, *X-rays tomography* and *Light scattering tomography*. Among these technics mentioned, for our quartz crystal we will use X-rays diffraction topography and tomography, the details of this process followed with the experimental results will be shown in this chapter.

## 5.5 X-rays diffraction Topography

X-rays topography method provides a picture of distribution of defects in a crystal [175]. Here, the topography we have used for research is that of diffracting planes in the crystal, not the topography of the exterior features. The contours of the crystal surfaces are important in determining the contrast on X-rays topography. When we use the technic to observe dislocations, we are trying to study the topography of the lattice planes around the defect. We do this by recording the intensity of the X-rays diffracted from the deformed planes, which differs from the intensity diffracted by the perfect crystal forming a localised image of the defect. Hence, we use the phenomena of diffraction to analyse the internal structure of the crystal.

**Bragg formulation of X-rays diffraction:**

A beam of X-rays incident on a crystal may be scattered coherently. This is also called as diffraction [176]. The condition for coherent scattering or diffraction (additive interferences of scattered waves) from a crystal is known as Bragg diffraction relation, which is written as:

$$n\lambda = 2 \cdot d_{hkl} \cdot \sin\theta_B \qquad \text{n = 1, 2, 3....} \tag{5.1}$$

Where, $\lambda$ is the wavelength of the X-rays, $d_{hkl}$ is the distance between planes of atom (hkl) in the crystal, $\theta_B$ the Bragg angle at which the diffraction occurs. The integer $n$ is called the order of refraction. The origin of Bragg relation can also be seen in Figure 5.6.

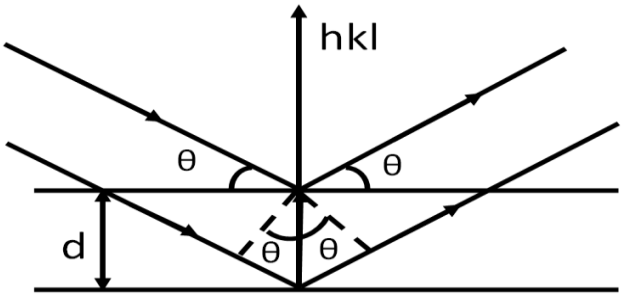


*Figure 5.6: The Bragg relation considering a crystal.*

### 5.5.1 Production of X-rays

Röntgen first discovered X-rays in 1895 and in 1913 Von Laue [177] suggested their essential wave nature with the realisation of the first diffraction experiments. Subsequently, the Nobel laureate Charles Glover Barkla showed the transversal character of these waves establishing that they were electromagnetic waves. The X-rays wavelength range is from 0.1 Å to 100 Å. In terms of energy, this corresponds to about 0.1- 100 eV. The energy in electron volt (eV) of a photon X of wavelength $\lambda(\text{Å})$ given by:

$$E = \frac{12400}{\lambda} \tag{5.2}$$

Where, we know universally that, $E = h \cdot \nu = h \cdot c/\lambda$ and 1eV= $1.6 \cdot 10^{-19}\, Joules$. In radio crystallography, those X-rays are used whose wavelength lies between 0.5-2.5 Å.

### 5.5.2 Principle of production of X-rays

One way of production of X-rays is during the impact of an electron, accelerated by an electric field, on the target anode or anticathode as known historically. The X-rays yield is given by:

$$\eta = \frac{photon\ energy}{energy\ of\ electrons} = 1.1 \cdot 10^{-9} \cdot Z \cdot V \tag{5.3}$$

Where, Z is the atomic number of the target, V is the potential in volts. For an anticathode of tungsten fed at 100 kV that gives a yield of 0.8%.

### 5.5.3 Anticathodes

The X-rays generating tubes has a steel body pierced with four windows closed by a thin beryllium plate as shown in the Figure 5.7. The metal pellet constituting the target is brazed on a copper block cooled by a water circuit. A molybdenum filament is heated by a variable current (so as to regulate the temperature which in turn regulates the emissive power and consequently, the current in the tube) and is maintained at a negative potential compared to that of the anticathode. A cup shaped focusing material as seen in the Figure 5.7 placed to focus the electron beam on a small rectangular area of the target. With the delimited collimators, we have beams of X-rays at the output. Similarly, the electric power dissipated in conventional cathode is in the range 1.5-2 kW. Almost all energy converts into heat, which imposes an energetic cooling of the anticathode. To improve the cooling the anode can be rotated.

The maximum power dissipation in the system with the rotating anode is of the order of 20 kW. This whole setup is enclosed in a glass tube and maintained in vacuum.

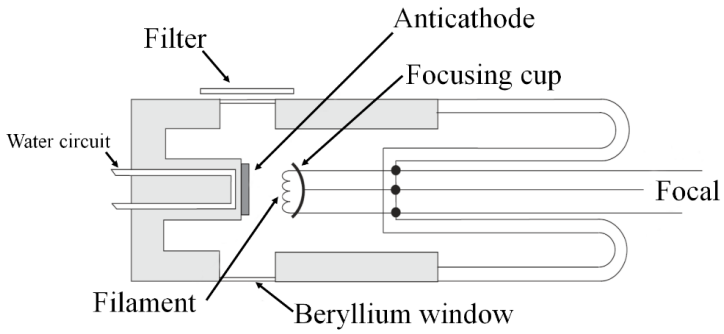


*Figure 5.7: Anticathode used for X-rays [177].*

### 5.5.4 X-rays generator

An adjustable DC voltage between 30- 100 kV powers the X-rays tube. The current flowing through the tube regulates from few mA to 60 mA. As a fact, the charge flow from the tube being the function of the current flowing through it, modern generators usually come voltage and current enslaved. Because of high voltage usage in the generator there is a need for using transformer and tough isolation cables for proper safety. However, modern-day generators have best switching power supplies, which make it possible to produce compact and reliable generators. In FEMTO-ST [173], we use X-rays vertical beam generator of 45 kV with the tube current of 25 mA. In some locations in the world, synchrotron radiation is in practice to produce very intense X-rays beam. Synchrotron radiation generates by the movements of electrons whose speed is close to that of light. The brightness of the beam is 105 times that of the conventional generator.

### 5.5.5 Absorption of X-rays

The total absorption of X-rays involves two phenomena i.e. diffusion and photoelectric effect. The first cause of absorption produces almost insignificant effects in relation to the second. It results from the coherent diffusion without the change in wavelength (Thompson diffusion) and incoherent diffusion with change in wavelength (Compton diffusion) [177].

### 5.5.6 Coefficient of absorption of X-rays

A monochromatic beam of unit section that passes through a homogenous screen, losses energy $dI$ proportional to the mass of the screen per unit area $dp$, the expression given as:

$$dI = -\mu \cdot I \cdot dp \tag{5.4}$$

Where, $\mu$ is the coefficient of mass absorption of the screen, if p can be considered independent of x then by integration of equation (5.4) we have for the screen thickness $x$ and density $\rho$:

$$\frac{I}{I_0} = e^{-\mu \cdot p} = e^{-\mu \cdot \rho \cdot x} \tag{5.5}$$

### 5.5.7 X-rays transmission technic used in FEMTO-ST

Among all the experimental methods of investigating piezoelectric crystals, the X-rays diffraction topography is a non-invasive method that provides qualitative and quantitative information, both on the surface and in the volume of the resonator. It is the periodic crystal structure which allows the diffraction of the electromagnetic waves according to Bragg's law of diffraction.

**Lang's technic**

This technic invented by Sir Lang is one of the most popular and widely used technic for X-rays transmission [175]. Its orientation sensitivity is about $5 \cdot 10^{-4}\, rad$ and is also considered one of the most precise methods of X-rays topography. In this technic the beam of X-rays are limited by a very small opening slit. After diffraction, the beam passes through to the exit slit which serves to stop the main beam and avoids veiling the film. The whole resonator and sensitive films are positioned on a small table which allows rotational movements (for initial diffraction adjustment) and back-to-back translation for scanning the entire surface of the resonator. This method allows resolutions of a few micrometres but has the disadvantage of large time exposure, especially when high resolution topography is required. Experimental mounting of Lang's technic is shown in Figure 5.8.

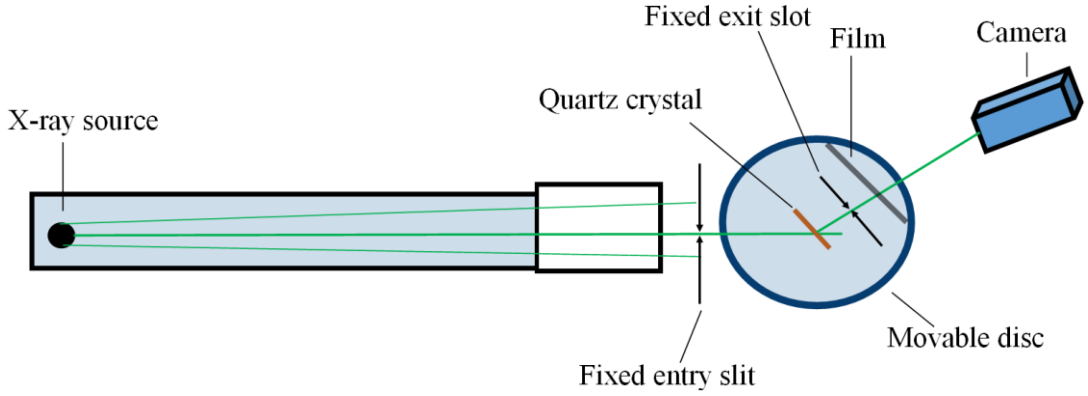


*Figure 5.8: Lang's transmission technic.*

As Lang's technic comprises of the source, sample (crystal blank), slits and photographic film, the arrangement of topography in the technic corresponds to the stationary situation, and the projection topographs are taken by scanning crystal and film across the beam. Slits are preferably double to reduce the scatter and manufactured from tantalum, which gives high X-rays absorption. Therefore, the image records information on the direction of the energy flow within the crystal. The effect is the increase in the intensity of X-rays transmitted through a crystal when it is being setup for Bragg diffraction.

**X-rays characterisation equipment for resonator used in FEMTO-ST**

The Lang method makes possible to perform high resolution topographies. The image below shows the installation from the team Acoustic-Electronic and Piezoelectricity of the Time and Frequency department of FEMTO-ST situated in ENSMM is used for the experiments performed in

this chapter [175]. The X-rays generator used has a nominal power of 2.5 kW and its anti-cathode is made of molybdenum. It emits the following wavelengths:

$\lambda_{K\alpha 2} = 0.7135$ Å , $\lambda_{K\alpha 1} = 0.7093$ Å , $\lambda_{K\beta 1} = 0.6323$ Å etc.

For our experimental purpose we use $\lambda_{K\alpha 1}$ as the wavelength because it offers a higher intensity than the other wavelengths.

The emission efficiency of this kind of generator is very low, which makes it to consume high power and need of water cooling. To have an extended life of the emission tube, we should not exceed the voltage beyond 50 kV and the current to 35 mA i.e. 1.65 kW which is near to its rated capacity limit.

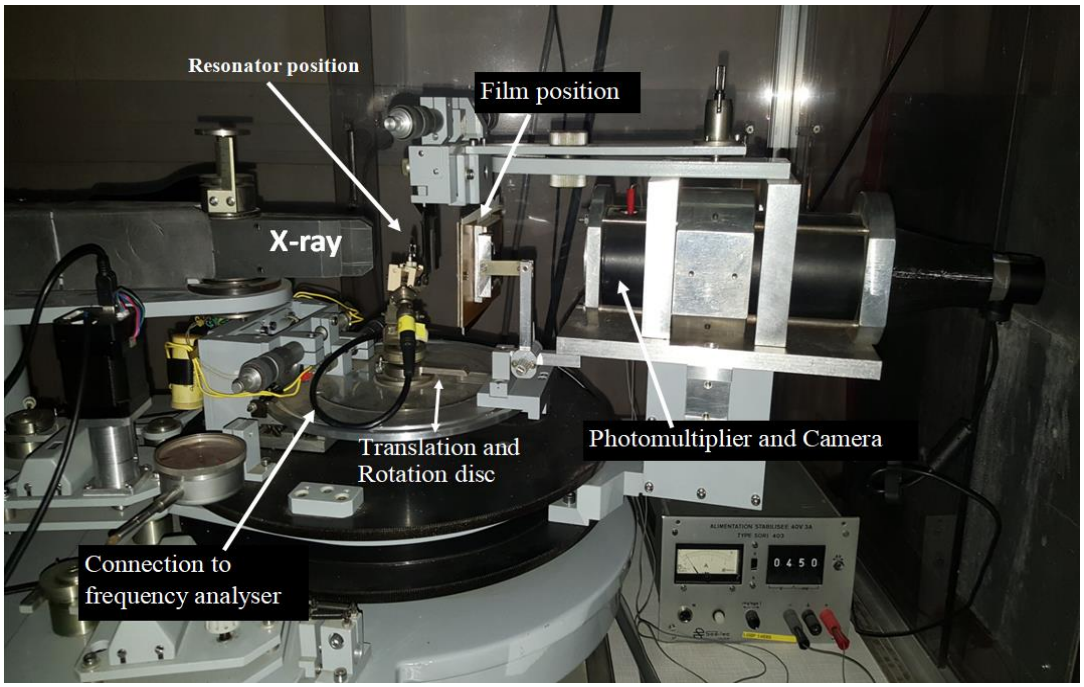


*Figure 5.9: Lang's topography experimental setup.*

Figure 5.9 shows the real view of the Lang's topography for X-rays diffraction. The height of the Lang chamber slot is approximately 25 mm, and the width is adjustable up to 0.01 mm. The resonator is mounted in a goniometric head as in Figure 5.10 which allows its orientation according to all degrees of freedom. The table (or disc) rotates around the vertical axis and the positioning accuracy is better than a minute of arc, which is necessary to settle the diffraction. The same table has a translational movement back and forth perpendicular to the X-rays beam. The translational speed is practically not critical but for reasons of exposure time, it is preferable to have a stroke little greater width than of the resonator, so that the diffraction pattern has a better view.

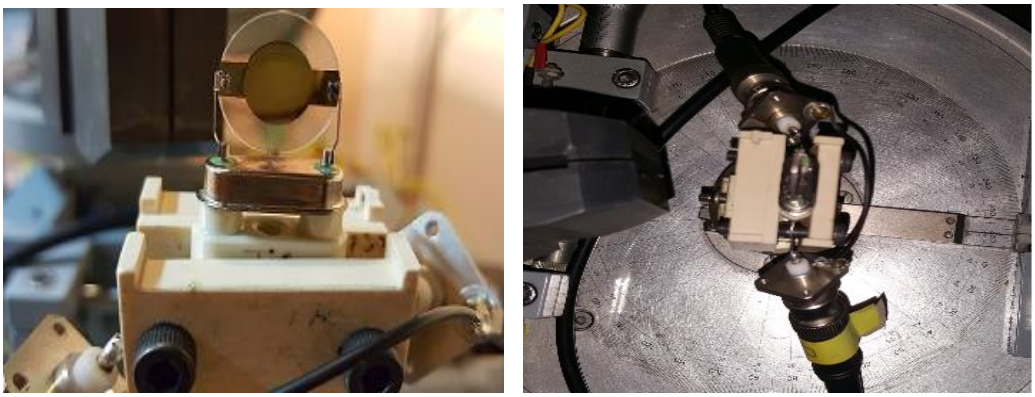

*Figure 5.10: Left: zoomed side view of resonator mounted, right: top view of the resonator mounted.*

Carestream Industrex AA400 photographic films are used. The revelation and fixation of the films are carried out by the conventional methods using chemicals. The image amplifying camera offers significantly lower resolution than the film but is very useful during the adjustment stage to obtain and adjust the diffraction.

The various stages of Lang's topography are mentioned stepwise below:

I. Place the resonator in a position as close as possible to that of the diffraction and put the camera at an angle prescribed by Bragg's law. Open the entry slot to the large width.

II. Slowly start the X-rays generator in voltage step of 10 kV and current at a step of 5 mA to the required limit keeping in mind the maximum limits allowed.

III. Maintain the sampling resonator to the resonant frequency using a synthesizer (in our case we maintained the resonant frequency of the resonator using LabVIEW programming).

IV. Open the X-rays generator window and allow it to pass through the sample resonator.

V. Search for the appropriate diffraction by rotating the resonator.

VI. If the diffraction does not appear, it means that the normal to the diffraction plane is not found in the generator-detector plane. In this case, we cut the X-rays generation and slightly rotate the generator around the horizontal axis of the support. Once done we repeat again from step IV.

VII. Once we obtain the diffraction, we check for the better view of diffraction by increasing and decreasing the voltage and current from the generator. Hence, we make the fine adjustment of the table so that the diffraction of the line $\lambda_{K\alpha 1}$ has the maximum intensity.

VIII. We can now set the photographic film between the resonators and the camera and let the film for getting exposed to the diffraction at least for 8 hours (can also be exposed for a longer period).

IX. After the exposure for a period, the film is developed. If the image is not well contrasting than we must adjust the excitement level of resonator and try adjusting the current of the X-rays generator and repeat the process from step VII.

## 5.6 Quartz crystal block and cutting

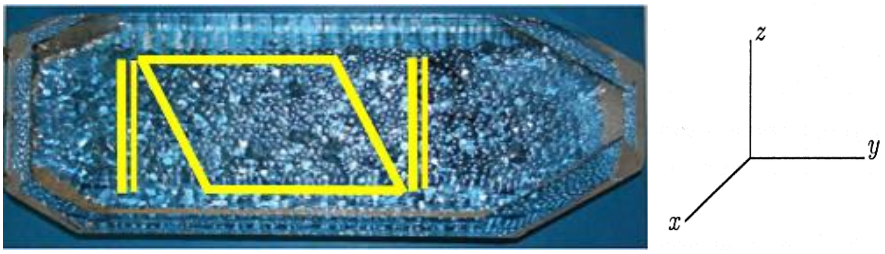


*Figure 5.11: Mother quartz crystal block.*

The mother quartz crystal block as shown in Figure 5.11 is the same block as mentioned in the earlier chapters, which has been grown using a natural seed in one of the CNES project [173]. The block is around 220 mm in length along the Y-axis, and 36 mm in the Z-axis and 110 mm along the X-axis. The two Y-cut slices are cut to achieve ten quartz bars (parallelogram mark). These Y-cut slices were used in the previous project work in X-rays analysis for evaluating dislocations in the quartz material.

In the search for observing the defects in the quartz plate, here in Figure 5.12 we present the distribution of stationary (a) and different modes of vibration (from b to d) of mode-*C* taken using X-rays diffraction using Lang's technic for one of the several bad resonators. The X-rays vertical beam was given by adjusting the generator at voltage 45 kV and current 25 mA for different exposure times. For e.g. in Figure 5.12 (a) exposed for 24H (b) exposed for 16H, (c) for 8H, (d) for 5H30 to have the best results for vibrating modes. The difference in the contrast of figures are mainly because of different exposure times for the modes. There seem to be few dislocations on the edge of vibrating zone under electrodes (in top right inside the smaller circle) in Figure 5.12 (a) for the resonator in stationary mode after 24 hours of exposure. This dislocation could explain the cause of phase noise in bad resonator. Whereas the long and few short dark rings in (c) is a minor photographic film error caused by chemicals.

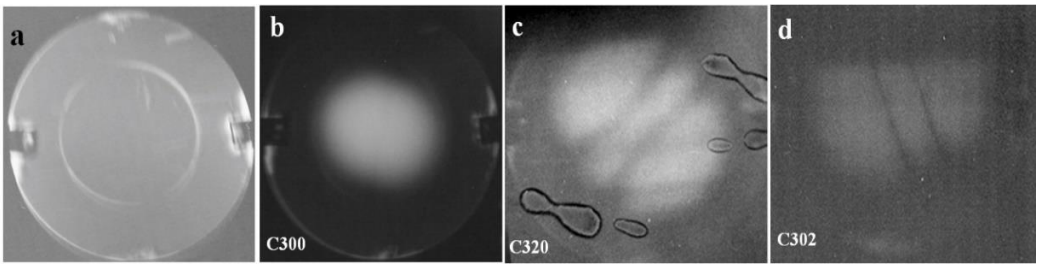


*Figure 5.12: X-rays topographic image of modes for a Plano-convex quartz resonator plate (bad).*

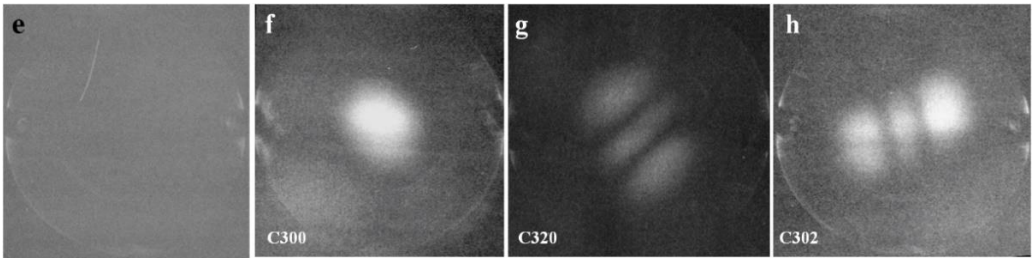


*Figure 5.13: X-rays topographic image of modes for a Plano-convex quartz resonator plate (good).*

Similarly, in Figure 5.13 (e) is the stationary and vibrating modes (from f to h) taken using X-rays for good resonator as mentioned above where, (f) is exposed for 56H, (g) exposed for 15H30 and (h) for 24H. There exists a visual deformation for the stationary mode of Figure 5.13 (e) which is a photographic film error (the scratch visible on the left top is on the film surface) and no visible dislocations were observed in the vibrating zone of quartz crystal plate of the good resonator. Hence, more resonators should be studied to see whether bad resonators usually have dislocations in the vibrating zone and no dislocations in the good ones. On the other hand, the figures show a satisfactory agreement with the simulation results obtained using FEM analysis in see Chapter 3 section 3.6 but the defects observed from X-rays cannot be compared to the defects in simulation because we have no idea about the size of defects observed using X-rays. Therefore, further study can be done to do a comparative study between defects from X-rays and simulation.

## 5.7 X-rays Tomography

This is a computerised technology [178] based on the ability of X-rays radiation to penetrate objects. The longer is the radiographic length of the object, the lesser the radiation escapes from the opposite side. The absorption is also dependent on the kind of material [179]. An X-rays sensor captures the escaping X-rays radiation as a two-dimensional radiographic image. With a detector of sizes approximately 50 mm to 400 mm, a large portion of the measured object captures in a single image.

To use computerized tomography (CT) on an object, several hundreds of two-dimensional radiographic images are made in a sequence, with the measured object in various rotated positions as shown in Figure 5.14. The object is located on a rotating table for this purpose, and gradually rotated stepwise. The three-dimensional information about the measured object contained in this series of images is extracted using a suitable mathematical process and is made available as a “voxel image” (volume pixel). Each voxel embodies the X-rays absorption by the measured object for a defined location in the measured volume.

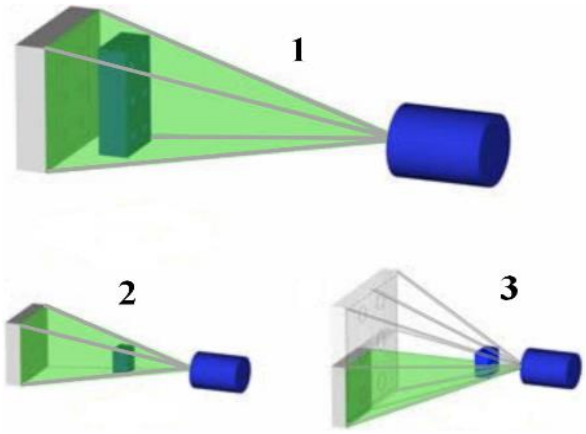


*Figure 5.14: X-rays Tomography.*

The modern sensors currently used are capable to capture up to 4 million image points. Typically, several hundred thousand and approximately few million-measurements point and derives in the

measured volume Figure 5.14 (1). These points distribute evenly across the surface of the measuring part. Hence, the interior of the measured object can be characterised.

The process of tomography is like image processing, where it is possible to change the magnification of the object as in Figure 5.14 (2) in order to capture smaller parts with higher magnification, or larger parts with lower magnification. For doing this, either the measured object positioned in the radiation path or the X-rays components (source and detector) can be moved in an axial direction relative to the measured object.

In some cases, the number of pixels available is not enough to meet the requirements for the measuring of the object. For such cases as in Figure 5.14 (3), several images stitches together by moving the rotary table with the measured object relative to the X-rays components.

**X-rays tomography in Femto-ST, Dept, MIFHySTO platform**

EasyTom CT (Computerised Tomography) are X-rays inspection machines allowing a collection of complex internal and external geometry. The EasyTom 3D CT scanners features high-resolution digital radioscopy, versatility for a wide variety of applications, 6 motion axis and large volume inspection.

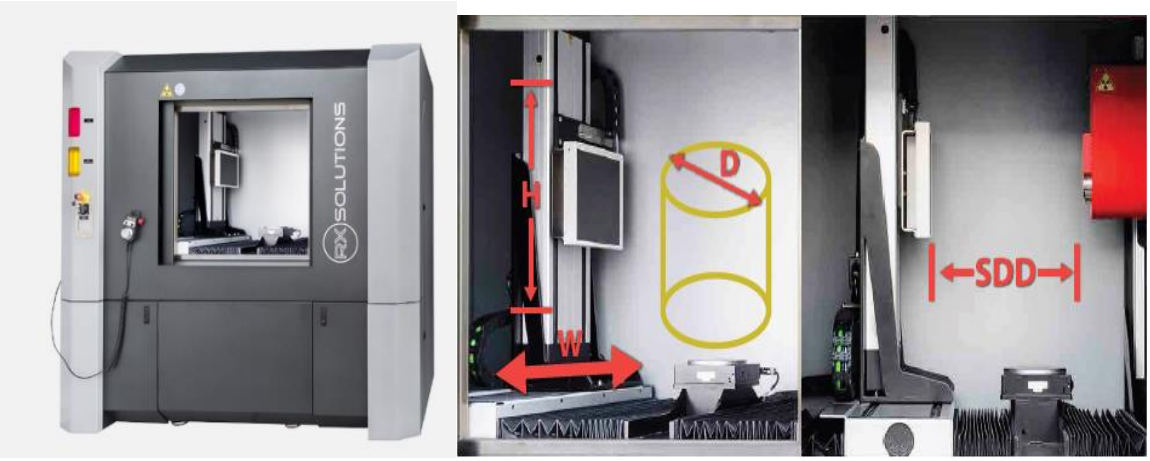


*Figure 5.15: Left: X-rays Tomograph, right: Internal structure of the Tomograph [180].*

The tomograph attains measurements in real time with high resolution digital radioscopy. It captures highly accurate measurements at ±11 µm accuracy with resolution to 1.5 µm and has a high motorised rotation with 3 Axis translations, Figure 5.15. Regarding the capability of the parts of the machine, the full scanning volume is of 320 mm and diameter 420 mm, an example of a sample with a holder can be seen in Figure 5.16. The maximum horizontal and vertical shift *W* and *H* respectively, are 410 mm, using the system in 3D CT and 2D Radio. *SDD*-the distance between the emitter and the detector is 900 mm which is the maximum space available for sampling.

*Figure 5.16: Holder with a quartz blade of 14 mm diameter.*

There are several options and combinations available in terms of X-rays generator in this machine. It has sealed or open type micro-focus tube. The open nano-focus tube (160 kV) but can be increased to (230 kV). An example of the lapped sampled blade with its voxel limit is shown in Figure 5.17.

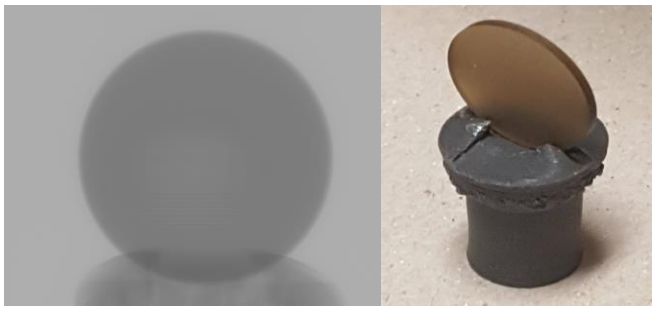

*Figure 5.17: Left: Voxel resolution of the sample, right: Sampled quartz blade of 14 mm diameter.*

Unfortunately, the result so far obtained for the sampled quartz blade does not show satisfactory result. The smoky colour of the quartz tested shows an irradiation at high energy which causes a redistribution of the electrons in the structure. The initially transparent colour became dark showing the presence of impurities in quartz used as a sample. In general, this colour corresponds to the presence of aluminium, with an added alkali like lithium or sodium and a little hydrogen [172]. Other investigations are necessary to make the method more reliable and avoid damaging quartz.

## 5.8 Laser scattering

It is an optical method using a laser beam to detect smaller inclusions as in Figure 5.18. The setup [181]-[182] is usually basic, a light beam, supplied by a laser, shines through the sample to be measured and behind it; the intensity distribution caused by the scattering is picked up with a detector. The measured intensity distribution shows numerous concentric rings, and hence, the spacing between these rings correlates with the particle size.

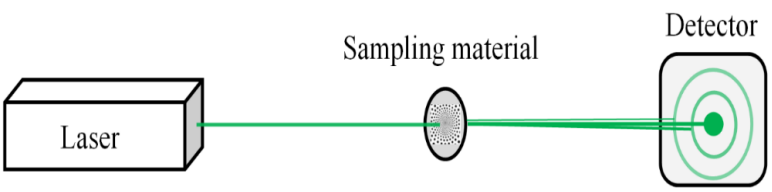


*Figure 5.18: Laser scattering setup.*

When a particle is illuminated by a light, different effects occur, together it leads to inertial transmission, absorption, and scattering. The sum of the last two is called extinction. In absorption, the part of the electromagnetic energy of the incident light absorbed by the particle changes into another form of energy, particularly into thermal energy. This energy is either through infrared radiance (thermal radiation) or through convection of the surrounding medium emitted, an effect, which is without significance for dynamic laser scattering. When absorption is sufficiently large, the radii of non-transparent particles are merely obtained from their geometric transverse shadow section. "Sufficiently large" means in this context, their diameter is clearly above the wavelength of the used light.

### 5.8.1 Scattering

There are many forms of scattering, but we focus on the two types i.e. coherent scattering and the incoherent scattering. For us, the later one is not of the point of interest, and the coherent scattering is our point of interest for discussion. Coherent scattering classifies everything deflecting the incident light from its original direction. It can be divided into three parts i.e. the reflection, refraction, and diffraction.

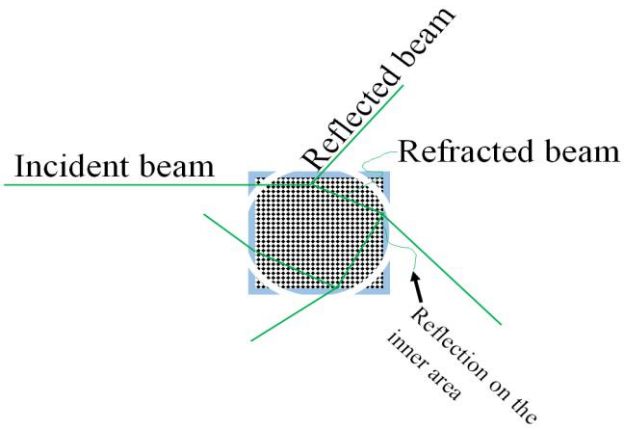


*Figure 5.19: Forms of laser scattering [181].*

### 5.8.2 Reflection

Reflection is a coherent scattering by large interface and occurs on the surface of the particles and it is described is according to the law "angle of incidence equals angle of reflection". When viewing the angle dependent complete course of an intensity distribution caused by scattering, the reflection on the surface of sphere provides a very smooth share. Reflection with transparent materials can also occur on inner boundary surface.

### 5.8.3 Diffraction

In diffraction, the light beam has a wide wave front, and hits a particle and partially encircles it, like a water wave, hitting a pole or even a larger obstacle. Through the superimposition of various parts of the broken wave front (interference) behind the particle, the characteristic diffraction patterns evolve and depends on the diameter of the particles.

## 5.9 Experimental laser setup in FEMTO-ST

The experimental laser setup is shown in the Figure 5.20 , He-Ne (Helium Neon) laser beam with a wavelength of around 632.8 nm and an output power of 35 mW has been used to detect the inclusion in the resonator plate [172]-[173]. When the laser illuminates an inclusion in Z-axis as in Figure 5.20, the light is scattered and an optical image (with camera) is taken to locate all the inclusions in the crystal as shown in Figure 5.21 .

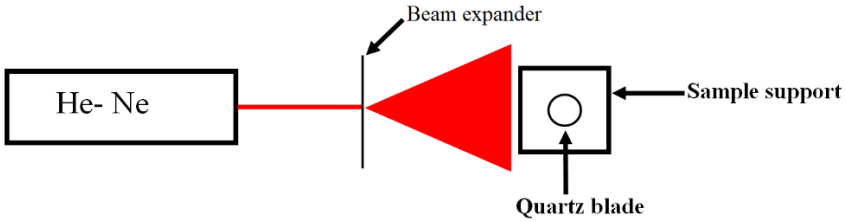


*Figure 5.20: Laser inclusion measurement technic.*

*Figure 5.21: Left: Instrument passing the beam, Right: Enlarged illuminated crystal blade.*

The illuminated blade in Figure 5.21 is lapped, polished and the outlines of the blades have been carefully chamfered for sampling. Some of the inclusions identified with a manual movement of the laser beam has been marked in small white circles.

## 5.10 Summary

We successfully dismantled the 5 MHz SC-cut quartz crystal resonators without any destruction to the quartz crystal. The X-rays diffraction technic using Lang's method allowed us to observe intrinsic defects in the quartz crystal and allowed us to see the shapes of different overtones and anharmonics of mode-*C* vibration. The X-rays result showed some dislocations in the quartz plate for the stationary mode, and it might be the possible cause of phase noise in bad resonators but the absence of dislocations in good resonators did not allow us to answer the presence of phase noise in good resonators. Computerised tomography revealed the impurities in the quartz sample. Similarly, we used laser scattering to see the presence of inclusion and managed to see a few already present in the material. The technics used in this work should be used on a larger scale with other available resonators to confirm the obtained results.

# Conclusion

Growing demand and technological advancement brings a need to keep improving operating devices in electronics. Losses are related to noise in devices and usually limit the performance of the system. The objective of this thesis is to perform an analysis by reverse engineering on ultra-stable piezoelectric resonators and provide an appropriate statistical modelling for the physical origin of phase noise. This thesis work is part of a longtime study conducted in FEMTO-ST, department of Time and Frequency, on 5 MHz BVA SC-cut quartz resonators. A major part of it covers the concepts and realization of measuring phase noise using carrier suppression technic which, concerning quartz resonators, is a peculiarity of FEMTO-ST at the world level. Noise measurements were performed at 353 K and 4K for around 100 BAW resonators manufactured by several European manufacturing partners and provided for this thesis work by CNES.

The first chapter of this thesis begins by a partial review of the general literature on flicker noise in resonators. Then it specializes to noise in BAW resonators and particularly on its influence on operation of a resonator. The differences of phase noise in resonators and oscillators which sometimes bring confusion to researchers in time and frequency domain, are graphically explained.

The technical part of this thesis is covered in chapter two, where the realization of phase noise measurement technic commonly known as carrier suppression technic has been developed. Almost all the details from pin identification of resonator to connecting it to the measurement bench has been provided with experimental precautions. The carrier suppression technic characterizes the inherent phase stability of ultra-stable resonators. This method, also called interferometric method, offers one of the highest sensitivities for the measurement of devices under test (DUT). In the case of carrier suppression, a substraction of the two signals at the output of each of the resonators is carried out (combined with 180° phase shift). The combined signal can thus be strongly amplified without adding the noise of the amplifier highlighting the noise of DUTs. The measurement floors are in the range of -160 dBc/Hz at 1 Hz carrier frequency. In all cases, the resonators must be conditioned in impedance (to obtain a loaded quality factor Q around 60% of the unloaded quality factor) and temperature controlled to limit thermal frequency drifts. Similarly, the same phase noise measurement technic was also used for measuring phase noise in LGT resonators. For measuring phase noise in LGT, a special impedance matching circuit was implemented because of its intrinsic impedance being low (< 10 ohms). The impedance matching circuit was fabricated using transformers which allowed us to attain the loaded quality factor condition (as mentioned above) which was not the case in the traditional bench. The short-term stability obtained for LGT resonators was of the order $10^{-13}$ which is almost as good as for quartz resonators, thus offering the possibility of an alternative material for resonator fabrication.

Chapter three is devoted to the study of governing equation for the propagation of a plane wave in a quartz crystal plate. We considered the rotation of the crystallographic axes to compute the tensor

components necessary for the calculation of natural resonance frequencies of an infinite plane piezoelectric plate. This serves as a theoretical basis for introducing the concept of energy trapping in a quartz crystal resonator. We further determined the frequencies of different overtones and anharmonic modes of a quartz blade with parallel faces of an infinite dimensions where the energy trapping was carried out in the presence of electrodes. This was extended to the case of a plano-convex acoustic cavity using Stevens and Tiersten's model which allowed us to find the natural frequencies of different overtones and anharmonics. Experimentally, the 5 MHz plano-convex SC-cut quartz crystal resonators were classified in terms of noise as good, average, and bad and in terms of quality factor on the metrological vibration mode 353K and 4K. Also, a certain number of harmonics and anharmonics mode were characterized parallelly at those temperatures to determine a correlation between the phase noise and quality of the crystal. Finally, to validate the Stevens-Tiersten's plano-convex model we simulated the resonator with a Finite Element method and computed the natural frequency of vibration of different overtones and anharmonic modes. Different kinds of defects in the simulation inside the resonator model have also been studied to see their influences on the main vibration mode.

Chapter four covers the theoretical part of modelling noise in our resonators. In previous chapters we measured noise in ultra-stable quartz crystal resonators using carrier suppression technic and classified the resonators in terms of noise as good, average, and bad. These resonators were taken in pairs and tested statistically (firstly 48 and later 101 measurements per pair) to investigate the possibility of any behavioral law governing these resonator pairs. Up to our knowledge, this is the first time that such a systematic study was carried out. We used the Mittag-Leffler distribution recently introduced in the $1/f$ noise domain and stable distribution to characterize our samples. Unfortunately, the experimental data processed using Mittag-Leffler distribution, as proposed by Niemann et al., did not show a good agreement to our experimental results thus allowing us to tentatively reject power law intermittency as a cause of phase noise in our resonators. However, we got quite good fits using fully right skewed stable distributions, which opens possibilities to relate the physical origin of noise in quartz to the same kind of processes that could be described using stable distributions in previous studies of the frequency dependence of the imaginary part of the dielectric susceptibility.

The final chapter is concerned with the reverse engineering work of this thesis. The sealed resonators were dismantled using a common metal cutter tool by a simple twist and turn without causing any mechanical damage to the resonator. Several photographs of the internal part of the resonator devices were taken from different angles to observe macroscopic defects on the mountings, electrodes and crystal. These defects were observed easily but to have a deeper understanding of the intrinsic defects, X-rays diffraction and laser scattering were used. X-rays diffraction was typically used to see the dislocations in the quartz material and laser scattering was used to see the inclusions in the resonator blade. Unfortunately, up to now, no correlation could be found between all these kinds of defects and

the quality of the short-term stability of the resonators except may be with the dislocations. Preliminary results on one good and one bad resonators should be confirmed by another tests in other resonators.

The results obtained in this thesis work prove that phase noise measurements using the carrier suppression technic can also be used for resonators with low intrinsic impedances, such as LGT resonators. We also think that we could use a transformer to replace the traditional impedance matching circuit for phase noise measurement and observe the differences. Experimental resonant frequencies were shown to be different to those obtained using Tiersten's formula for the 5 MHz SC-cut plano-convex quartz crystal resonators. Because of this difference, we could not measure phase noise for an anharmonic mode in a resonator pair as none of the resonator pairs showed a difference less than 5 Hz in their frequency of resonance for an anharmonic mode. The measurement of phase noise in anharmonic modes could be pursued which could open a different perspective in seeing phase noise in BAW resonators. We also note that the experimental phase noise results obtained for good-good pairs of resonators have shown an unusual feature, namely that the α exponent of the $1/f^{\alpha}$ asymptotic law for the PSD at small frequencies were quite often below 1 and on average below 1 for repeated measurements on two different resonator pairs, whereas it was below 1 only for some of the measurements done on the other resonator pairs used (good-bad and good-average). Statistical tests of fits with fully right-skewed stable distributions may be continued for phase noise results obtained from resonator fabricated with materials other than quartz or for resonators at different resonant frequencies. This can possibly help to understand the nature of intrinsic fluctuations from a different aspect linked to other phenomena having in common heavy tailed fluctuations in the dielectric susceptibilities.

Hence, the overall study of the BAW resonator has allowed me to gain a broad knowledge in resonators and acquire enough experimental skills to get convincing experimental results. But, on the other hand, not being able to answer all the questions aroused after analyzing the experimental results brings a feeling of frustration. Therefore, all my best regards to future researchers in this field and my wishes beforehand to be able to answer those questions that I could not.

# Annexes

## A. Piezoelectric effect in Quartz and IEEE norms

The excitation of any quartz resonator involves an inverse piezoelectric effect when a potential difference applied to the crystal material. Because of the potential difference applied, the crystalline structure modifies, and the deformation occurs in the crystal. This deformation hence causes dissymmetry of the electric charges, which directly relates to the intrinsic structure of the quartz material resulting into the formation of piezoelectricity phenomenon in the quartz resonator. The two possible piezoelectric effects are direct and inverse piezoelectric effect. In direct effect, the application of mechanical stress therefore causes a displacement of the positive and negative charges. This effect has the effect of creating a voltage proportional to the mechanical pressure.

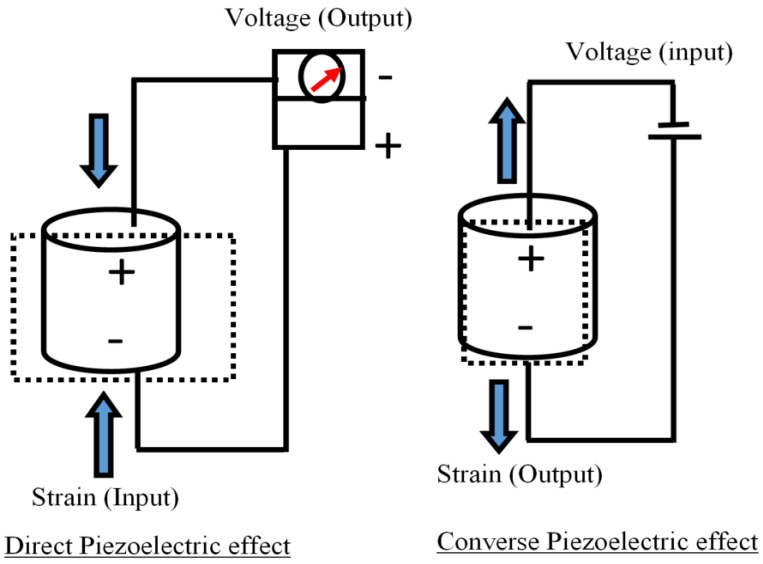


*Figure A.1:Direct and converse piezoelectric effect.*

Figure A.1 gives the summary of the actions and consequences of direct and inverse piezoelectric effects. Some of the well-known applications those based on piezoelectric effects are smoking lighters, quartz watches and clocks. Piezoelectric effects are also prevalent in other applications such as in the development of pressure sensors, scale, accelerometer, sonars, microphones, etc. Quartz being piezoelectric in nature, its anisotropic i.e. its physical and chemical properties differ depending on the direction considered. Similarly, Figure A.2 shows an example of the quartz crystal pointing the three orthogonal axes i.e. $X, Y$ and $Z$. The quartz plates can be cut into different well-known orientations and can have an arbitrary orientation relative to three orthogonal crystal axes. The rotational symbol provides one way in which the plate of the arbitrary orientation specifies. It uses a starting reference on one of these hypothetical plates with thickness along $X, Y$ or $Z$ and carries this plate through successive rotations about the coordinate axes, fixed in the reference plate, to reach the final orientation.

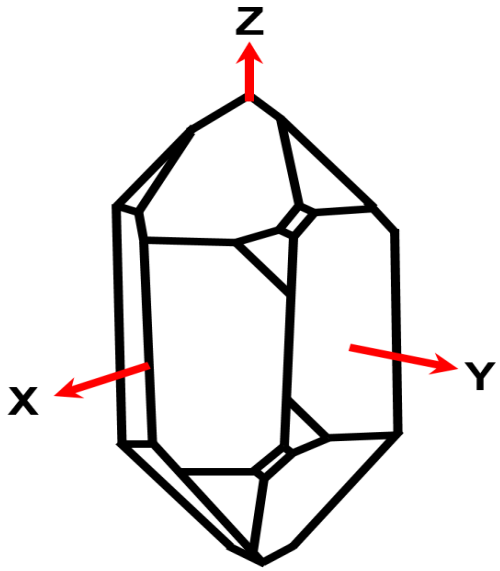


*Figure A.2: Crystallographic axes of quartz.*

The rectangular quartz plates are frequently used where the symbols $l, w, t$ denotes the length, width, and thickness of the plate as in Figure A.3. According to IEEE norms [9], they use the notation $l, w, t$ to denote the orthogonal coordinate axes fixed in the reference plate. The rotational symbol is defined by the convention that the first letter of the axes ($X, Y$ or $Z$) indicates the initial principal direction of the thickness of the hypothetical plate and the second letter ($X, Y$ or $Z$) indicates the direction of the length of the hypothetical plate. Thus, the third letter ($l, w$ or $t$) denotes which of the three orthogonal coordinate axes in the hypothetical plate is the axis. These orientations usually refer to as "Crystal cuts" and has a possibility to take maximum advantage of different physical and chemical properties, such as insensitivity to temperature or mechanical stress or on the contrary a great sensitivity to temperature. A quartz crystal cut is usually identified by three angles i.e. $\varphi, \theta, \psi$ and is defined in the crystallographic reference. An example of a doubly rotated cut given in Figure A.3 shows a typical SC-cut. In this case, the rotational symbol that specifies the cut is ($YXwl$) 22.4°/-33.88° according to IEEE standard. The SC-cut here actually represents a family (as shown in Table A.1) of cuts where the ranges in the angles $\varphi$ and $\theta$ are $\pm 2°$ and $\pm 1°$ respectively.

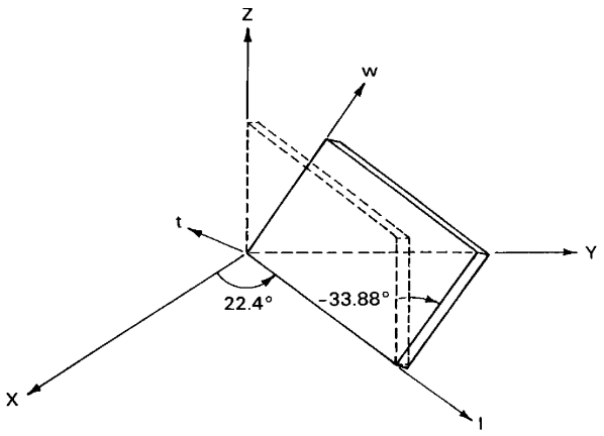


*Figure A.3: Doubly rotated SC-cut quartz plate.*

| Crystal cuts | $\varphi$ | $\theta$ | Specialities | Vibration mode |
|---|---|---|---|---|
| SC | 22.4° | 33.88° | Stress Compensated- weak force frequency effect. | Thickness shear |
| AT | 0° | 35° | Temperature compensated at room temperature. | Thickness shear |
| BT | 0° | -49° | Temperature compensated at room temperature. | Thickness shear |
| X | 5° | 30° | Temperature compensated at cryogenic temperature | Flexure |

*Table A.1: Some of the standard cuts defined by IEEE.*

## B. Numerical values of the components of material tensors for quartz

The different coefficients used for calculations are determined by Bechmann and collected by Ward [183]. The density of quartz is 2648 $kg/m^3$.

Elastic constants of quartz $c_{ij}$ [GPa]

$$c_{ij} = \begin{bmatrix} 86.74 & 7 & 11.91 & -17.91 & 0 & 0 \\ 7.00 & 86.74 & 11.91 & 17.91 & 0 & 0 \\ 11.91 & 11.91 & 107.2 & 0 & 0 & 0 \\ -17.91 & 17.91 & 0 & 57.94 & 0 & 0 \\ 0 & 0 & 0 & 0 & 57.94 & -17.94 \\ 0 & 0 & 0 & 0 & -17.91 & 39.88 \end{bmatrix}$$

Piezoelectric constants $e_{ij}[C/m^2]$

$$e_{ij} = \begin{bmatrix} 0.171 & -0.171 & 0 & -0.0406 & 0 & 0 \\ 0 & 0 & 0 & 0 & 0.0406 & -0.171 \\ 0 & 0 & 0 & 0 & 0 & 0 \end{bmatrix}$$

Viscoelastic constants $\eta_{ij}[mPa.s]$

$$\eta_{ij} = \begin{bmatrix} 1.37 & 0.73 & 0.71 & 0.01 & 0 & 0 \\ 0.73 & 1.37 & 0.71 & -0.01 & 0 & 0 \\ 0.71 & 0.71 & 0.96 & 0 & 0 & 0 \\ 0.01 & -0.01 & 0 & 0.36 & 0 & 0 \\ 0 & 0 & 0 & 0 & 0.36 & 0.01 \\ 0 & 0 & 0 & 0 & 0.01 & 0.32 \end{bmatrix}$$

Dielectric constant $\varepsilon_{ij}[\times 10^{-12}\ F/m\ ]$

$$\varepsilon_{ij} = \begin{bmatrix} 39.21 & 0 & 0 \\ 0 & 39.21 & 0 \\ 0 & 0 & 41.03 \end{bmatrix}$$

Third order temperature coefficients of elastic constant $Tc_{ij}$ at 300 $K$

| $T_f^{(1)}, 10^{-7}$ | $T_f^{(2)}, 10^{-8}$ | $T_f^{(3)}, 10^{-9}$ |
|---|---|---|
| 0.769 | 0.748 | 0.105 |
| -1.178 | -2.189 | -2.474 |
| -0.879 | -1.672 | -1.832 |
| -0.143 | -0.451 | -0.581 |
| 1.339 | 1.869 | 1.289 |
| -1.465 | -2.662 | -3.571 |

# References


[1] W. Heywang, K. Lubitz, W. Wersing, “Piezoelectricity, Evolution and Future of a Technology,” Springer Series in Material Science, vol. 114, 2008.

[2] Wikipedia contributors, “Crystal oscillator,” Wikipedia, the Free Encyclopedia. 30 Sep. 2019. Web. 25 Oct. 2019.

[3] K. S. Van Dyke, “The Piezo-Electric Resonator and Its Equivalent Network,” Proc. IRE, vol. 16, no 6, p. 742-764, June 1928.

[4] W. L. Everitt, G. E. Anner, “Communication Engineering,” Tokyo: McGraw-hill book company, inc, Third edition, Ch.4, pp. 131, 1956.

[5] F. Sthal, X. Vacheret, S. Galliou, P. Salzenstein, E. Rubiola, et G. Cibiel, “Advanced bridge instrument for the measurement of the phase noise and of the short-term frequency stability of ultra-stable quartz resonators,” in Proc. IEEE Joint meeting EFTF/IFCS, Geneva, Switzerland, 2007, p. 254-260.

[6] L. D. Landau, E. M. Lifshitz, J. B. Sykes, “Theory of Elasticity,” Course of theoretical physics. Pergamon Press, 1989.

[7] A. El Habti, F. Bastien, “Low temperature limitation on the quality factor of quartz resonators,” IEEE transactions on Ultrasonics, Ferroelectrics, and Frequency Control, vol.41, no°2, pp.250-255, 1994.

[8] Proc. of. IRE Standards on Piezoelectric Crystals, “Determination of the Elastic, Piezoelectric, and Dielectric Constants- The Electromechanical Coupling Factor,” April 1958, Coordinator, R.F. Shea.

[9] IEEE standard on piezoelectricity. ANSI/IEEE Std 176-1987, 1988.

[10] V.E. Bottom, “Introduction to quartz crystal unit design,” Van Reinhold Company, 1982.

[11] D. Royer, E. Dieulesaint, “Ondes élastiques dans les solides –Tome 1 Propagation libre et guidée, ” Enseignement de la Physique, Masson, Paris, 1996.

[12] F. Sthal, M. Devel, J. Imbaud, R. Bourquin, S. Ghosh, G. Cibiel, “Study on the origin of 1/f noise in quartz resonators,” J. Stat. Mech., n° 6, May, 054025, (2016).

[13] E. Rubiola, Phase Noise and Frequency Stability in Oscillators. Cambridge: Cambridge University Press, 2008.

[14] Saeed V. Vaseghi, “Advanced digital signal processing and noise reduction,” Second edition, John Wiley and Sons Ltd, 2000, ISBN: 0-470-84162-1.

[15] J. B. Johnson, “Thermal Agitation of Electricity in Conductors,” Phys. Rev., vol. 32, no 1, p. 97-109, July. 1928.

[16] H. Nyquist, “Thermal Agitation of Electric Charge in Conductors,” Phys. Rev., vol. 32, no 1, p. 110-113, July. 1928.

[17] J. B. Johnson, “The Schottky Effect in Low Frequency Circuits,” Phys. Rev., vol. 26, no 1, p. 71-85, July. 1925.

[18] IEEE, “IEEE Standard Definitions of Physical Quantities for Fundamental Frequency and Time Metrology -- Random Instabilities,” in IEEE STD 1139-2008: IEEE, 2008, pp. 135.

[19] D. B. Leeson, “Oscillator phase noise: A 50-year retrospective,” Presented in IEEE Joint meeting EFTF/IFCS, Denver, CO, USA, 2015, p. 332-337.

[20] J. Groslambert, V. Giordano, M. Brunet, et E. Rubiola, “Flicker noise measurement of HF quartz resonators,” IEEE transactions on Ultrasonics, Ferroelectrics and Frequency Control, vol. 47, p. 361-368, March 2000.

[21] E. Rubiola and V. Giordano, “Advanced interferometric phase and amplitude noise measurements,” *Rev. Sci. Instrum.*, vol. 73, nº 6, p. 2445-2457, June 2002.

[22] E. Rubiola, V. Giordano, et J. Groslambert, “Very high frequency and microwave interferometric phase and amplitude noise measurements,” *Rev. Sci. Instrum.*, vol. 70, nº 1, p. 220-225, Jan. 1999.

[23] F. Sthal, M. Mourey, F. Marionnet, W. F. Walls, “Phase Noise Measurements of 10 MHz BVA Quartz Crystal Resonators,” IEEE Transactions on Ultrasonics, Ferroelectrics and Frequency Control, vol. 47, no. 2, March, pp. 369-373, (2000).

[24] Agilent Technologies. (May 2003), Agilent 4395A Network/Spectrum/Impedance Analyzer: *Operation Manual*, Agilent Part No. 04395-90040: Printed in JAPAN.

[25] Keysight Technologies [formerly Agilent] (Oct 2017), Keysight 16092A Test Fixture: *Operation and Service Manual*, Manual Part No. 16092-90010: Printed in JAPAN.

[26] E. Belokoneva, M. Simonov, A. Butashin, B. Mill, and N. Belov, “Crystal structure of calcium gallogermanate $Ca_3Ga_2Ge_4O_{14}=Ca_3Ge(Ga_2Ge)Ge_2O_{14}$ and its analog $Ba_3Fe_2Ge_4O_{14}=Ba_3Fe(FeGe_2)Ge_2O_{14}$,” Soviet Physics - Doklady, vol. 25, no. 12, pp. 954-957, 1980.

[27] B. V. Mill and Y. V. Pisarevsky, “Langasite-type materials: from discovery to present state,” in Proc. of the IEEE International Frequency Control Symposium, 2000, pp. 133–144.

[28] I. A. Andreev, “Two decades following the discovery of thermally stable elastic properties of $La_3Ga_5SiO_{14}$ crystal and coining of the term ‘langasite’ (a review),” Technical Physics, vol. 49, no. 9, pp. 1101-1103, 2004.

[29] I. Andreev, “Single crystals of the langasite family: an intriguing combination of properties promising for acousto-electronics,” Technical Physics, vol. 51, no. 6, pp. 758-764, 2006.

[30] I. Andreev and M. Dubovik, “A new piezoelectric material, langasite ($La_3Ga_5SiO_{14}$), with a zero-temperature coefficient of the elastic vibration frequency,” Soviet Technical Physics Letters, vol. 10, no. 4, pp. 205-207, 1984.

[31] B. Mill, A. Butashin, G. Khodzhabagyan, E. Belokoneva, and N. Belov, “Modified rare-earth gallates with a $Ca_3Ga_2Ge_4O_{14}$ structure,” Soviet Physics -Doklady, vol. 27, no. 6, pp. 434-437, 1982, originally in Russian in Doklady Akademii Nauk SSSR, Vol. 264, N. 6, pp. 1385-1389.

[32] A. Kaminskii, B. Mill, I. Silvestrova, and G. Khodzhabagyan, “The nonlinear active material $(La_{1-x}Ndx)_3Ga_3SiO_{14}$,” Bulletin of the Academy of Sciences of the USSR, Physical Series, vol. 47, no. 10, pp. 25-31, 1983.

[33] A. Kaminskii, B. Mill, G. Khodzhabagyan, A. F. Konstantinova, A. I. Okorochkov, and I. Silvestrova, "Investigation of trigonal $(La_1\text{-}xNdx)_3Ga_3SiO_{14}$: Part 1. Growth and optical properties," Physica Status Solidi (a), vol. 80, pp. 387-398, 1983.

[34] A. Kaminskii, I. Silvestrova, S. E. Sarkison, and G. A. Denisenko, "Investigation of trigonal $(La_1\text{-}xNdx)_3Ga_3SiO_{14}$: Part 2. Spectral laser and electromechanical properties," Physica Status Solidi (a), vol. 80, pp. 607-620, 1983.

[35] V. B. Grouzinenko and V. V. Bezdelkin, "Piezoelectric resonators based on single crystals of strong piezoelectrics," in Proc. of the IEEE International Frequency Control Symposium, 1991, pp. 212-216.

[36] S. A. Sakharov, I. M. Larinov, and V. A. Issaev, "Monolithic filters using strong piezoelectrics," in Proc. of the IEEE International Frequency Control Symposium, 1991, pp. 181-183.

[37] H. Takeda, K. Sugiyama, K. Inaba, K. Shimamura, and T. Fukuda, "Crystal growth and structural characterization of new piezoelectric material $La_3Ta_{0.5}Ga_{5.5}O_{14}$," Japanese Journal of Applied Physics, Part 2, vol. 36, no. 7B, pp. L919-L921, 1997.

[38] T. Fukuda, P. Takeda, K. Shimamura, H. Kawanaka, M. Kumatoriya, S. Murakami, J. Sato, and M. Sato, "Growth of new langasite single crystals for piezoelectric applications," in Proc. of the IEEE International Symposium on Applications of Ferroelectrics, 1998, pp. 315-319.

[39] B. Chai, H. Qiu, Y. Y. Ji, and J. L. Lefaucheur, "Growth of high qualitysingle domain crystals of langasite family compounds," in Proc. of the IEEE International Frequency Control Symposium, 1999, pp. 821-828.

[40] J. Bohm, R. Heimann, M. Hengst, R. Roewer, and J. Schindler, "Czochralski growth and characterization of piezoelectric single crystals with langasite structure: $La_3Ga_5SiO_{14}$ (LGS), $La_3Ga_{5.5}Nb_{0.5}O_{14}$ (LGN) and $La_3Ga_{5.5}Ta_{0.5}O_{14}$ (LGT). Part I." Journal of Crystal Growth, vol. 204, no. 1-2, pp. 128-136, 1999.

[41] R. C. Smythe, R. C. Helmbold, I. Hague, G. E., and K. A. Snow, "Langasite, langanite, and langatate bulk-wave Y-cut resonators," IEEE Transactions on Ultrasonics, Ferroelectrics, and Frequency Control, vol. 47, no. 2, pp. 355-360, 2000.

[42] B. H. T. Chai, A. N. P. Bustamante, and M. C. Chou, "A new class of ordered langasite structure compounds," in Proc. of the IEEE International Frequency Control Symposium, 2000, pp. 163–168.

[43] R. C. Smythe, R. C. Helmbold, G. E. Hague, and K. A. Snow, "Langasite, langanite, and langatate resonators: recent results," in Proc. IEEE International Frequency Control Symposium, 1999, pp. 816–820.

[44] B. Mill, Y. Pisarevsky, and E. Belokoneva, "Synthesis, growth and some properties of single crystals with the $Ca_3Ga_2Ge_4O_{14}$ structure," in Proceedings of the IEEE International Frequency Control Symposium, 1999, pp. 829-834.

[45] B. Chai, J. L. Lefaucheur, Y. Y. Ji, and H. Qiu, "Growth and evaluation of large size LGS ($La_3Ga_5SiO_{14}$) LGN ($La_3Ga_{5.5}Nb_{0.5}O_{14}$) and LGT ($La_3Ga_{5.5}Ta_{0.5}O_{14}$) single crystals," in Proc. of the IEEE International Frequency Control Symposium, 1998, pp. 748-760.

[46] M. M. C. Chou, "Investigation of piezoelectric crystals, $La_3Ga_{5.5}Ta_{0.5}O_{14}$ (LGT), $La_3Ga_{5.5}Nb_{0.5}O_{14}$ (LGN), $La_3Ga_5SiO_{14}$ (LGS)," Ph.D. dissertation, University of Central Florida, 2000.

[47] H. Kimura, S. Uda, O. Buzanov, X. Huang, and S. Koh, “The effect of growth atmosphere and Ir contamination on electric properties of $La_3Ta_{0.5}Ga_{5.5}O_{14}$ single crystal grown by the floating zone and Czochralski method,” Journal of Electroceramics, vol. 20, no. 2, pp. 73-80, 2008.

[48] T. Taishi, N. Bamba, K. Hoshikawa, and I. Yonenaga, “Single crystal growth of langataite ($La_3Ta_{0.5}Ga_{5.5}O_{14}$) by vertical bridgman (VB) method along $[2\bar{1}\bar{1}0]$ in air and in an Ar atmosphere,” Journal of Crystal Growth, vol. 311, no. 1, pp. 205-209, 2008.

[49] R. Fachberger, T. Holzheu, E. Riha, E. Born, P. Pongratz, and H. Cerva, “Langasite and langatate nonuniform material properties correlated to the performance of SAW devices,” in Proc. of the IEEE International Frequency Control Symposium, 2001, pp. 235-239.

[50] R. Fachberger, E. Riha, E. Born, and P. Pongratz, “Homogeneity of langasite and langatate wafers for acoustic wave applications,” in Proc. of the IEEE International Ultrasonics Symposium, 2003, pp. 100–109.

[51] J. Bohm, E. Chilla, C. Flannery, H.-J. Frohlich, T. Hauke, R. Heimann, M. Hengst, and U. Straube, “Czochralski growth and characterization of piezoelectric single crystals with langasite structure: $La_3Ga_5SiO_{14}$ (LGS), $La_3Ga_{5.5}Nb_{0.5}O_{14}$ (LGN) and $La_3Ga_{5.5}Ta_{0.5}O_{14}$ (LGT). II. Piezoelectric and elastic properties,” Journal of Crystal Growth, vol. 216, no. 1-4, pp. 293-298,2000.

[52] E. Chilla, C. M. Flannery, H.-J. Frohlich, and U. Straube, “Elastic properties of langasite-type crystals determined by bulk and surface acoustic waves,” Journal of Applied Physics, vol. 90, no. 12, pp. 6084-6091, 2001.

[53] Y. V. Pisarevsky, P. A. Senyushenkov, B. V. Mill, and N. A. Moiseeva, “Elastic, piezoelectric, dielectric properties of $La_3Ga_{5.5}Ta_{0.5}O_{14}$ single crystals,” in Proc. IEEE International Frequency Control Symposium, 1998, pp. 742-747.

[54] T. Fukuda, P. Takeda, K. Shimamura, H. Kawanaka, M. Kumatoriya, S. Murakami, J. Sato, and M. Sato, “Growth of new langasite single crystals for piezoelectric applications,” in Proc. of the IEEE International Symposium on Applications of Ferroelectrics, 1998, pp. 315-319.

[55] J. Schreuer, “Elastic and piezoelectric properties of $La_3Ga_5SiO_{14}$ and $La_3Ga_{5.5}Ta_{0.5}O_{14}$: an application of resonant ultrasound spectroscopy,” IEEE Transactions on Ultrasonics, Ferroelectrics, and Frequency Control, vol. 49, no. 11, pp. 1474-1479, 2002.

[56] J. Stade, L. Bohaty, M. Hengst, and R. Heimann, “Electro-optic, piezoelectric and dielectric properties of langasite ($La_3Ga_5SiO_{14}$), langanite ($La_3Ga_{5.5}Nb_{0.5}O_{14}$) and langataite ($La_3Ga_{5.5}Ta_{0.5}O_{14}$),” Crystal Research and Technology, vol. 37, no. 10, pp. 1113-1120, 2002.

[57] C. Hubert, M. Gauthier, F. Decremps, G. Syfosse, P. Munsch, A. Polian, B. E.,and J. J. Boy, “Evaluation of non-linear elastic and piezoelectric propertiesof $La_3Ta_{0.5}Ga_{5.5}O_{14}$ single crystals under hydrostatic pressure,” in 5th World Congress on Ultrasonics Proceedings, Sept 2003, pp. 1253-1256.

[58] U. Straube, H. Beige, J. Bohm, R. B. Heimann, T. Hauke, and M. Hengst, “Elastic, dielectric and piezoelectric coefficients of langasite-type crystals,” in Technol. Health Care, ser. Abstracts of ESEM 2003, vol. 12, no. 2, 2004, pp.164-167.

[59] B. Sturtevant, P. Davulis, and M. Pereira da Cunha, “Pulse echo and combined resonance techniques: a full set of LGT acoustic wave constants and temperature coefficients,” IEEE Transactions on Ultrasonics, Ferroelectrics, and Frequency Control, vol. 56, no. 4, pp. 788-797, 2009.

[60] B. T. Sturtevant, “Ultrasonic characterization of single crystal langatate,” Ph.D. dissertation, University of Maine, 2009.

[61] D. C. Malocha, M. Pereira da Cunha, E. Adler, R. C. Smythe, S. Frederick, M. Chou, R. Helmbold, and Y. S. Zhou, “Recent measurements of material constants versus temperature for langatate, langanite and langasite,” in Proc. IEEE International Frequency Control Symposium, 2000, pp. 200–205.

[62] M. Pereira da Cunha, D. C. Malocha, E. L. Adler, and K. J. Casey, “Surface and pseudo surface acoustic waves in langatate: predictions and measurements,” IEEE Transactions on Ultrasonics, Ferroelectrics, and Frequency Control, vol. 49, no. 9, pp. 1291-1299, 2002.

[63] A. Pokharel, F. Sthal, E. Vaillant, J. Imbaud, J.J. Boy, F. X. Esnault, G. Cibiel, “Study of the phase noise of Langatate crystal resonators,” Proc. European Frequency and Time Forum, Torino, Italy, 9-12 April, pp. 37-40, 2018.

[64] R. Turner, P. Fuierer, R. Newnham, and T. Shrout, “Materials for high temperature acoustic and vibration sensors: a review,” Applied Acoustics, vol. 41, no. 4, pp. 299-324, 1994.

[65] C. Krause, “Myth: Wireless technologies are inherently unreliable,” Oak Ridge National Laboratory Review, vol. 41, no. 3, pp. 22-23, 2008.

[66] M. N. Hamidon, V. Skarda, N. M. White, F. Krispel, P. Krempl, M. Binhack, and W. Buff, “High-temperature 434 MHz surface acoustic wave devices based on $GaPO_4$,” IEEE Transactions on Ultrasonics, Ferroelectrics, and Frequency Control, vol. 53, no. 12, pp. 2465-2470, 2006.

[67] J. Thiele and M. Pereira da Cunha, “High temperature LGS SAW gas sensor,” Sensors and Actuators, B: Chemical, vol. 113, no. 2, pp. 816-822, 2006.

[68] P. L. Dreike, D. M. Fleetwood, D. B. King, D. C. Sprauer, and T. E. Zipperian, “An overview of high-temperature electronic device technologies and potential applications,” IEEE Transactions on Components, Packaging, and Manufacturing Technology, Part A, vol. 17, no. 4, pp. 594-609, Dec. 1994.

[69] A. McNad, K. J. Kirk, and A. Cochran, “Ultrasonic transducers for high temperature applications,” IEE Proc.- Sci. Meas. Tech., vol. 145, no. 5, pp. 229-236, 1998.

[70] W. Cullinane and R. Strange, “Gas turbine engine validation instrumentation: measurements, sensors, and needs,” in Proceedings of the SPIE- The International Society for Optical Engineering, vol. 3852, 1999, pp. 2-13.

[71] B. Chorpening, D. Tucker, and S. Maley, “Sensors applications in 21st century fossil-fuel based power generation,” in Proc. of IEEE Sensors, vol. 3, 2004, pp. 1153-1156.

[72] P. Neudeck, R. Okojie, and L.-Y. Chen, “High-temperature electronics - a role for wide bandgap semiconductors?” Proceedings of the IEEE, vol. 90, no. 6, pp. 1065-1076, Jun 2002.

[73] J. F. Rosenbaum, “Bulk Acoustic Wave Theory and Devices,”. Boston: Artech House, 1988.

[74] D. P. Morgan, “Surface-Wave Devices for Signal Processing,”. New York: Elsevier, 1991.

[75] E. Benes, M. Groschl, F. Seifert, and A. Pohl, “Comparison between BAW and SAW sensor principles,” IEEE Transactions on Ultrasonics, Ferroelectrics and Frequency Control, vol. 45, no. 5, pp. 1314 –1330, Sept. 1998.

[76] L. Reindl, G. Scholl, T. Ostertag, H. Scherr, U. Wolff, and F. Schmidt, “Theory and application of passive SAW radio transponders as sensors,” IEEE Transactions on Ultrasonics, Ferroelectrics and Frequency Control, vol. 45, no. 5, pp. 1281-1292, 1998.

[77] L. Reindl, “Wireless passive SAW identification marks and sensors,” in 2nd Int. Symp. Acoustic. Wave Devices for Future Mobile Communications, Chiba Univ., March 2004, paper ID 1B3.

[78] K. Lakin, “Thin film resonator technology,” IEEE Transactions on Ultrasonics, Ferroelectrics and Frequency Control, vol. 52, no. 5, pp. 707-716, 2005.

[79] J.H. Lin and Y.H. Kao, “Wireless temperature sensing using a passive RFID tag with film bulk acoustic resonator,” in Proc. of the IEEE International Ultrasonics Symposium, Nov. 2008, pp. 2209-2212.

[80] P. Krempl, G. Schleinzer, and W. Wallnofer, “Gallium phosphate, $GaPO_4$: A new piezoelectric crystal material for high-temperature sensorics,” Sensors and Actuators, A: Physical, vol. 61, no. 1-3, pp. 361-363, 1997.

[81] R. Fachberger, G. Bruckner, G. Knoll, R. Hauser, J. Biniasch, and L. Reindl, “Applicability of $LiNbO_3$, langasite and $GaPO_4$ in high temperature SAW sensors operating at radio frequencies,” IEEE Transactions on Ultrasonics, Ferroelectrics, and Frequency Control, vol. 51, no. 11, pp. 1427-1431, Nov.2004.

[82] J. A. Thiele, “High temperature LGX acoustic wave devices and applications for gas sensors,” Master’s thesis, University of Maine, 2005.

[83] J. A. Kosinski, “New piezoelectric substrates for SAW devices,” International Journal of High-Speed Electronics and Systems, vol. 10, no. 4, pp. 1017-1068, 2000.

[84] J. A. Thiele and M. Pereira da Cunha, “High temperature surface acoustic wave devices: fabrication and characterization,” Electronics Letters, vol. 39, no. 10, pp. 818-819, 2003.

[85] M. Pereira da Cunha and S. de Azevedo Fagundes, “Investigation on recent quartz-like materials for SAWapplications,” IEEE Transactions on Ultrasonics, Ferroelectrics, and Frequency Control, vol. 46, no. 6, pp. 1583–1590, 1999.

[86] B. V. Mill and Y. V. Pisarevsky, “Langasite-type materials: from discovery to present state,” in Proc. of the IEEE International Frequency Control Symposium, 2000, pp. 133-144.

[87] I. A. Andreev, “Two decades following the discovery of thermally stable elastic properties of $La_3Ga_5SiO_{14}$ crystal and coining of the term ‘langasite’ (a review).” Technical Physics, vol. 49, no. 9, pp. 1101-1103, 2004.

[88] I. Andreev, “Single crystals of the langasite family: an intriguing combination of properties promising for acousto-electronics,” Technical Physics, vol. 51, no. 6, pp. 758-64, 2006.

[89] B. Chai, J. L. Lefaucheur, Y. Y. Ji, and H. Qiu, “Growth and evaluation of large size LGS ($La_3Ga_5SiO_{14}$) LGN ($La_3Ga_{5.5}Nb_{0.5}O_{14}$) and LGT ($La_3Ga_{5.5}Ta_{0.5}O_{14}$) single crystals,” in Proc. of the IEEE International Frequency Control Symposium, 1998, pp. 748-760.

[90] B. Chai, H. Qiu, Y. Y. Ji, and J. L. Lefaucheur, “Growth of high-quality single domain crystals of langasite family compounds,” in Proc. of the IEEE International Frequency Control Symposium, 1999, pp. 821-828.

[91] J. Bohm, E. Chilla, C. Flannery, H.-J. Frohlich, T. Hauke, R. Heimann, M. Hengst, and U. Straube, "Czochralski growth and characterization of piezoelectric single crystals with langasite structure: $La_3Ga_5SiO_{14}$ (LGS), $La_3Ga_{5.5}Nb_{0.5}O_{14}$ (LGN) and $La_3Ga_{5.5}Ta_{0.5}O_{14}$ (LGT). II. Piezoelectric and elastic properties," Journal of Crystal Growth, vol. 216, no. 1-4, pp. 293-298, 2000.

[92] J. Bohm, R. Heimann, M. Hengst, R. Roewer, and J. Schindler, "Czochralski growth and characterization of piezoelectric single crystals with langasite structure: $La_3Ga_5SiO_{14}$ (LGS), $La_3Ga_{5.5}Nb_{0.5}O_{14}$ (LGN) and $La_3Ga_{5.5}Ta_{0.5}O_{14}$ (LGT). Part I." Journal of Crystal Growth, vol. 204, no. 1-2, pp. 128-136, 1999.

[93] R. Fachberger, T. Holzheu, E. Riha, E. Born, P. Pongratz, and H. Cerva, "Langasite and langatate nonuniform material properties correlated to theperformance of SAW devices," in Proc. of the IEEE International Frequency Control Symposium, 2001, pp. 235-239.

[94] J. Imbaud, S. Galliou, J.P. Romand, P. Abbe, R. Bourquin, "Development of a 10 MHz oscillator working with an LGT crystal resonator: Preliminary results," IEEE Trans. Ultrason. Ferroelec. Freq. Contr., vol. 55, Issue 9, pp. 1913-1920, September 2008.

[95] J. Imbaud, J. J. Boy, F. Sthal, "LGT alternative quartz materials for Ultra-stable Oscillators," Proc.IEEE Int. Freq. Contr. Symp., DOI 10.1109/FCS.2014.6859848, 2014.

[96] Y. Kim, "Amplitude-Frequency Effect of Y-cut Langanite and Langatate," IEEE Trans. on Ultrason., Ferroelect. and Freq. Contr., vol. 50, pp. 1683-1688, Dec. 2003.

[97] F. Sthal, M. Devel, S. Ghosh, J. Imbaud, G. Cibiel, R. Bourquin, "Volume dependence in Handel's model of quartz crystal resonator noise," IEEE Transactions on Ultrasonics, Ferroelectrics and Frequency Control, vol. 60, no. 9, November, pp. 1971-1977, 2013.

[98] D.S Stevens and H.F. Tiersten, "An analysis of doubly rotated quartz resonators utilizing essentially thickness modes with transverse variation," The Journal of the Acoustical Society America, Vol. 79, No.6, pp 1811-1826, June 1986.

[99] E.P. Eernisse, "Analysis of thickness modes of contoured, doubly rotated, quartz resonators," IEEE Transactions on Ultrasonics, Ferroelectrics, and Frequency Control, Vol. 48, n°: 5, pp 1351-1361, Sept 2001.

[100] W. Shockley, D.R Curran and D.J Koneval, "Trapped-Energy Modes in Quartz Filter Crystals," The Journal of the Acoustical Society America, Vol. 41, No.4, pp 981-993,1967.

[101] B. K. Sinha, "Doubly rotated contoured quartz resonators," IEEE Transactions on Ultrasonics, Ferroelectrics, and Frequency Control, Vol. 48, No. 5, pp 1162-1180, Sept 2001.

[102] A. Pokharel, F. Sthal, J. Imbaud,.X. Esnault, G. Cibiel, "Investigation on Flicker noise of overtones and anharmonic modes of ultra-stable quartz crystal resonators," IEEE Joint Conf. EFTF/IFCS, DOI: 10.1109/FCS.2017.8088838, 9-13 July, pp. 176-178, 2017.

[103] R. Bourquin, B. Dulmet, J. J. Boy, "SC-cut resonator operating in anharmonic modes with B-mode reduction," Proc. European Frequency and Time Forum, Brighton, United Kingdom, March 1996, pp. 239-243.

[104] J. Lamb, J. Richter, "Anisotropic acoustic attenuation with new measurements for quartz at room temperature," Proceedings R.Soc. Lond., Vol 293, No. 1435, pp 479-492, August 1966.

[105] Ballato A., "Basic Material Quartz and Related Innovations. In: Piezoelectricity. Springer Series in Materials Science," Vol 114. Springer, Berlin, Heidelberg, 2008.

[106] R.Bechmann, A.D. Ballato, T.J. Lukaszek,"Frequency-Temperature behaviour of Thickness Modes of Double-Rotated Quartz plates," 15th Annual Frequency Control Symposium, IEEE Xplore, pp 22-48, June 1961, Atlantic City, NJ, USA.

[107] A. Ballato, T. Lukaszek, "Higher-Order Temperature Coefficients of Frequency of Mass-loaded Piezoelectric Crystal plates," 29th Annual Frequency Control Symposium, IEEE Xplore, pp 10-25, May 1975, Atlantic City, NJ, USA.

[108] J. Vig, "Quartz crystal oscillators," 2018. Turtorial of International Frequency Control Symposium (IFCS 2018).

[109] A. Pokharel, F. Sthal, J. Imbaud, S. Ghosh, F.X. Esnault, G. Cibiel, "Flicker noise in Quartz Crystal Resonators at 353K as a function of Q-factor of overtones and Anharmonic Modes at 4 K," Fluctuation and Noise Letters, vol. 17, n° 2, April, 1871002, 2018.

[110] H. Nyquist, "Certain topics in telegraph transmission theory," Proceedings of the IEEE, Vol. 90 pp-280-305, 2002.

[111] C.E. Shannon, "Communication in the presence of noise," Proceedings of IEEE, Vol. 86, pp-447-457, 1998.

[112] B. Wang, X. Dai, X. Zhao, Z. Qian, "A semi-analytical solution for the thickness-vibration of centrally partially-electroded circular AT-cut quartz resonators," MDPI-Sensors (Basel), Vol. 17, pp: 1-13, August 2017.

[113] A. Clairet, "Modélisation et analyse numérique de résonateurs à quartz à ondes de volume," Thèse de doctorat, Université de Franche-Comté, 2014.

[114] C. J. Christensen & G. L. Pearson, "Spontaneous resistance fluctuations in carbon microphones and other granular resistances," Bell Sys. Tech. J., vol. 15, 197-223, and references therein (1936).

[115] E.-J. Wagenmakers, S. Farrell & R. Ratcliff, "Estimation and interpretation of $1/f^{\alpha}$ noise in human cognition," Psychonomic Bulletin & Review, vol.11, n°:4, pp.579-615, 2004.

[116] M. Pelton, D.G. Grier, P.-G Sionnest, "Characterizing quantum-dot blinking using noise power spectra," Appl. Phys. Letters, vol.85, n°5, pp.819-821, 2004.

[117] D. Krapf, "Nonergodicity in nanoscale electrodes," Phys. Chem. Chem. Phys., vol. 15, no. 2, 459-465, 2013.

[118] P. Karnatak, T. Paul, S. Islam, A. Ghosh, "Noise in van der Waals materials and hybrids," Adv. Phys.: X 2:2, pp. 428-449 (2017).

[119] M. Mihaila, D. Ursutiu, l. Sandu, "Electron-Phonon Coupling as the Source of Noise in Carbon Soot," Nature Scientific Reports, vol.9, 947, 2019.

[120] T. Musha, G. Borbely & M. Shoji, "1/$f$ phonon-number fluctuations in quartz observed by laser light scattering," Phys. Rev. Lett., vol. 64, pp.2394-2397, 1990.

[121] M. A. Caloyannides, "Microcycle spectral estimates of 1/$f$ noise in semiconductors," J. Appl. Phys., vol. 45, 307-316 (1974).

[122] M. Niemann, H. Kantz, and E. Barkai, "Fluctuations of $1/f$ noise and the low-frequency cutoff paradox," Phys. Rev. Lett., vol. 110, no. 14, pp. 140603, 5 pages, 2013.

[123] P. H. Handel, A. Tournier, and B. Henning, "Quantum $1/f$ effect in resonant biochemical piezoelectric and MEMS sensors," IEEE Trans. Ultrason. Ferroelectr. and Freq. Control, vol. 52, no. 9, pp. 1461-1467, 2005.

[124] W.A. Woyczyński, "Lévy Processes in the Physical Sciences," In: Barndorff-Nielsen O.E., Resnick S.I., Mikosch T. (eds) Lévy Processes. Birkhäuser, Boston, MA, 2001.

[125] E. W. Montroll and B. J. West, "Fluctuation Phenomena," North-Holland, Amsterdam, Chap. 2, 1979.

[126] P. Lévy, "Théorie de l'addition des variables aléatoires," Gauthier-Villars, vol.1, pp. XVII-328, 1937.

[127] V. V. Uchaikin and V. M. Zolotarev, "Chance and Stability: Stable Distributions and their Applications," Utrecht, The Netherlands: VSP, 1999.

[128] D. O. Cahoy, "Fractional Poisson Process in terms of alpha stable densities," PHD thesis, Case Western reserve University, August 2007.

[129] E. F. Fama, "Mandelbrot and the stable paretian hypothesis," The Journal of Business, vol. 36, n° 4, pp. 420-429, October 1963.

[130] V. M. Zolotarev, "One-dimensional Stable Distributions: Translations of Mathematical Monographs," vol.65. American Mathematics Society, United States of America, 1986.

[131] D. O. Cahoy, V. V. Uchaikin, W. A. Woyczynski, "Parameter estimation for fractional Poisson Processes," Journal of Statistical Planning and Inference, vol. 140, pp. 3106-3120, 2010.

[132] G. Samorodnitsky, and M. S. Taqqu, "Stable Non-Gaussian Random Processes: Stochastic Models with Infinite Variance," Chapman & Hall, 1994.

[133] E. W. Weisstein, "Mittag-Leffler Function," from MathWorld--A Wolfram Web Resource. http://mathworld.wolfram.com/Mittag-LefflerFunction.html, accessed several times in 2019 and 2020.

[134] R.K. Saxena, A.M. Mathai, H.J. Haubold, "On fractional Kinetic Equations," Astrophysics and Space science, vol. 282, pp.281-287, 2002.

[135] R. Garrappa, "Numerical evaluation of two and three parameter Mittag-Leffler functions," SIAM Journal of Numerical Analysis, vol. 53(3), 1350-1369, 2015.

[136] https://en.wikipedia.org/wiki/Mittag-Leffler_distribution

[137] Gwo Dong Lin, "On the Mittag–Leffler distributions," Journal of Statistical Planning and Inference, vol. 74, pp. 1-9, 1998.

[138] D. O. Cahoy, "Estimation of Mittag-Leffler Parameters," Communications in Statistics–Simulation and Computation, vol. 42, 303-315, 2013.

[139] W. Feller, "An Introduction to Probability Theory and Its Applications," Wiley, New-York, vol. 2, 1966.

[140] Y. He, S. Burov, R. Metzler, E. Barkai, “Random Time-Scale Invariant Diffusion and Transport Coefficients,” Phys. Rev. Lett., vol.101, pp. 058101(1)- 058101(4), 2008.

[141] K. Weron, M. Kotulski, “On the Cole-Cole relaxation function and related Mittag-Leffler distribution,” Phys. Lett. A, vol.232, pp. 180-188, 1996.

[142] G. Harth, D.L Clemens, M.A. Horwitz, “Glutamine synthetase of Microbacterium tuberculosis: extracellular release and characterization of its enzymatic activity,” Proc. Natl. Acad. Sci, vol 91, n° 20, pp. 9342-9346, 1994.

[143] K. Weron, A. Jurlewicz, “Two forms of self-similarity as a fundamental feature of the power-law dielectric response,” J. Phys. A, vol 26, pp.395-410.

[144] A. Jurlewicz, K. Weron, “A Relationship between Asymmetric Lévy-Stable Distributions and Dielectric Susceptibility,” J. Stat. Phys., vol. 73, n° 1/2, 1993

[145] A. Weron, K. Weron, W.A. Woyczynski, “Relaxation Functions in Dipolar Materials,” Journal of Statistical Physics, vol. 78, n° 3/4, 1995.

[146] I. Koponen, “Random transition rate model of streched exponential relaxation,” Journal of Non-Crystalline Solids, vol 189, pp. 154-160, 1995.

[147] K. S. Cole, R. H. Cole, “Dispersion and Absorption in Dielectrics I. Alternating Current Characteristics,” J. Chem. Phys., vol. 9, pp. 341-351, April 1941.

[148] R.M. Hill, “Characterisation of dielectric loss in solids and liquids,” Nature, vol. 275, 96-99 1978; R.M. Hill, “Characterisation of dielectric materials,” J. Mater. Sci., vol. 16, 118-124, 1981.

[149] K. Gorska, A. Horzela, A. Lattanzi, “Composition law for the Cole-Cole relaxation and ensuing evolution equations,” Phys. Lett. A, vol .254, pp. 1-6, 2019.

[150] Y. Pomeau, P. Manneville, “Intermittent Transition to Turbulence in Dissipative Dynamical Systems,” Commun. Math. Phys, vol. 74, pp. 189-197, 1980.

[151] Y. Pomeau, P. Manneville, “Intrinsic Stochasticity in Plasmas,” Ed. De Physique, p 239, Orsay 1979.

[152] M. Pelton, D. G. Grier, P. Guyot- Sionnest, “Characterizing quantum-dot blinking using noise power spectra,” vol. 85, n° 5, pp.819-821, 2004.

[153] M. Pelton, G. Smith, N. F. Scherer, R. A. Marcus, “Evidence for a diffusion-controlled mechanism for fluorescence blinking of colloidal quantum dots,” PNAS, vol.104, n°36, pp. 14249-14254, 2007.

[154] G. Ctistis, E. Papaioannou, P. Patoka, J. Gutek, P. Fumagalli, M. Giersig, “Optical and Magnetic Properties of Hexagonal Arrays of Subwavelength Holes in Optically Thin Cobalt Films,” J. Am. Chem. Soc., vol.9, n°1, January 2009.

[155] L. Silvestri, L. Fronzoni, P. Grigolini, P. Allegrini, “Event-Driven Power-Law Relaxation in Weak Turbulence,” Phys. Rev. Lett., vol. 102, 014502(1)-014502(4), January 2009.

[156] A. R. Bizzarri, S. Cannistrato, “$1/f^{\alpha}$ Noise in the Dynamic Force Spectroscopy Curves Signals the Occurrence of Biorecognition,” Phys. Rev. Lett., vol.110, pp. 048104(1)-048101(4), January 2013.

[157] Wikipedia contributors. (2020, May 16). Intermittency. In Wikipedia, The Free Encyclopedia. https://en.wikipedia.org/w/index.php?title=Intermittency&oldid=957053439.

[158] P. Manneville, "Intermittency, self-similarity and 1/f spectrum in dissipative dynamical systems," Journal of Physics, vol.41, pp. 1235-1243, November 1980.

[159] Mazonka, Oleg, "Easy as Pi: The Fluctuation-Dissipation Relation," retrieved from https://www.researchgate.net/publication/303859894_Easy_As_Pi_The_Fluctuation-Dissipation_Relation, (2016).

[160] P. R. Saulson, "Thermal noise in mechanical experiments," Phys. Rev. D, vol. 42, no. 8, pp. 2437-2445, 1990.

[161] H. Scher and E. W. Montroll, "Anomalous transit-time dispersion in amorphous solids," Phys. Rev. B., vol. 12, n° 6, pp. 2455-2477, Sep 1975.

[162] M. F. Shlesinger, "Electron scavenging in glasses," J. Chem. Phys. vol. 70, n° 11, pp. 4813-4818, 1979.

[163] E. W. Montroll and M. F. Shlesinger, "On $1/f$ noise and other distributions with long tails," Proc. Natl. Acad. Sci. vol. 79, n° 10, pp. 3380-3383, May 1982.

[164] E. W. Montroll and J. T. Bendler, "On Lévy (or stable) distributions and the Williams-Watts model of dielectric relaxation," J. Stat. Phys. vol. 34, n° 1-2, pp. 129-162, Jan 1984.

[165] E. W. Montroll and B. J. West, "Fluctuation Phenomena," North-Holland, Amsterdam, Chap. 2, 1979.

[166] B. Mandelbrot, "Some noises with spectrum, a bridge between direct current and white noise," IEEE Trans. Inform. Theory, vol. 13, p. 289, 1967.

[167] P. Dutta and P. M. Horn, "Low-frequency fluctuations in solids: $1/f$ noise," Rev. Mod. Phys., vol. 53, no. 3, 1981.

[168] Supplemental Material for Ref. [15], which can be found at: http://link.aps.org/supplemental/10.1103/PhysRevLett.110.140603.

[169] A. Pokharel, M. Devel, J. Imbaud, F. X. Esnault, G. Cibiel, F. Sthal, "Modeling of 1/f Phase noise on ultra-stable quartz crystal resonators using Mittag-Leffler distribution," Proc. Joint Meeting IEEE Int. Freq. Cont. Symp. and European Frequency and Time Forum, Orlando, FL, USA, 14-18 April, 0152_FI.pdf, 2019.

[170] R. Chirla, B. Iliescu, "Dislocations in synthetic crystals," Cryst. Res. Technol., vol 29, no°2, pp.159-169, 1994.

[171] Proc. of. IRE Standards on Piezoelectric Crystals, "Standards on Piezoelectric crystals," 1949, Chairman, J.G. Brainerd, and Vice-chairs A.G. Jensen, L.G. Cumming.

[172] J.J. Boy, PhD thesis, Université de Franche-Comté, n: 426, 1994.

[173] J. Imbaud, J.J. Boy, J.P. Romand, J. Frayret, D. Picchedda, G. Cibiel and F.Sthal, "Analyses of very high-Q quartz crystal aimed to high quality 5 MHz resonators achievement," 24th European Frequency and Time Forum (EFTF), 13-16 April 2010, Noordwijk, Netherlands.

[174] G. R. Johnson, R. A. Irvine, “Etch channels in single crystal cultured quartz,” 41st Annual Frequency Control Symposium, pp. 175-182, 1987.

[175] I.A Ivan, “Utilisation des résonateurs piézoélectriques fonctionnant en mode d’épaisseur pour la réalisation de capteurs,” Thèse de doctorat, Université de Franche-Comté, SPIM, n° : 1180, 2006.

[176] V.E. Bottom, “Introduction to quartz crystal unit design,” Van Nostrand Reinhold Ltd., 135 West 50th street, NY, 10020, USA, 1982.

[177] J.J. Rousseau, A. Gibaud, “Cristallographie géométrique et radiocristallographie,” 3rd Edition, DUNOD, Paris, 2000 and 2007.

[178] Computer Tomography- Principle of X-rays tomography, Werth Inc.- West Coast Office, 16060 Caputo Drive, Suite 120, Morgan Hill, CA 95037, https://werthinc.com/computer-tomography-principle-x-rays-tomography/

[179] E. Maire, P.J. Withers, “Quantitative X-rays tomography,” Int. Materials Reviews, vol 59, no°1, pp.1-43, 2014.

[180] “EasyTom CT scanner 3D Micro Computed Tomography and Digital Radioscopy System,” Cyberoptics LTD, 15a Hornbeam Park Oval, Hornbeam Park, Harrogate HG2 8RB, England, UK, https://www.rxsolutions.fr/easytom-rx-solutions-1191.

[181] Laser scattering basics, Fritsch GmbH, Milling and Sizing, Industriestrasse 8, 55743, Idat-oberstein, Germany, https://www.fritsch-international.com/fileadmin/Redakteur/Downloads/Reports_sizing/Introduction_Laser_Scattering/Laser_Scattering-introduction.pdf

[182] B. Chu, “Laser Light Scattering: Basic Principles and Practice,” Second Edition, Dover Publications Inc., Mineola, New York, 2007.

[183] R.W. Ward, “The constants of alpha quartz,” 38th Annual Symposium on Frequency Control, pp 22-31, USA, June 1984.

# List of figures

# List of tables

**Titre : Analyse par des méthodes de "reverse engineering" de résonateurs piézoélectriques hautes performances et modélisation du bruit**.

**Mots clés :** Résonateur à quartz ; résonateur BAW, résonateur coupe-SC ; métrologie ; bruit de phase ; suppression de porteuse ; bruit en 1/f ; résonateur LGT ; distributions stables et de Mittag-Leffler ; intermittence de la loi de puissance ; reverse engineering ; rayon-X ; diffusion du laser.

**Résumé :** Les résonateurs à ondes acoustiques de volume (BAW) ont été étudiés dans le domaine temps-fréquence à FEMTO-ST depuis longtemps et ont montré un rôle essentiel dans de nombreuses applications métrologiques telles que dans les dispositifs de positionnement comme GPS, Glonass, Galileo, etc. Ce travail de thèse présente la technique passive utilisée pour des mesures du bruit de phase dans les résonateurs BAW à quartz. Les résonateurs BAW de hautes performances ont été fabriqués par plusieurs fabricants européens et fournis par le CNES pour une étude de "reverse engineering" durant cette thèse.

Le manuscrit commence par rappeler les bases de cristallographie du quartz, de piézoélectricité et de caractérisation du bruit dans les résonateurs ultra-stables.

La deuxième partie du travail donne des détails sur la mesure de bruit dans les résonateurs par une technique de suppression de porteuse et sur une adaptation pour les résonateurs LGT d'impédance très faible (< 10 ohms).

La troisième partie concerne l'interprétation avec le modèle de Steven-Tiersten des résultats de mesures du bruit de phase à différentes températures et leur classification en fonction du bruit. Une simulation par méthode d'éléments finis (FEM) permet de comparer ces résultats avec la théorie de Steven-Tiersten.

La quatrième partie, présente un test de modélisation du bruit de phase à l'aide d'un modèle d'intermittence. Des comparaisons de nos résultats avec la distribution de Mittag-Leffler ainsi que des distributions stables semblent indiquer un rejet du modèle d'intermittence en loi de puissance, dans notre cas.

Enfin, le travail de "reverse engineering" est réalisé en démontant les résonateurs pour l'analyse des défauts par diffraction des rayons X et diffusion laser. Le démontage du résonateur a révélé des imperfections macroscopiques.

Les résultats préliminaires de diffraction des rayons X montrent la présence de dislocations qui pourraient être une cause de bruit de phase dans les résonateurs. Ceci devra être confirmé sur d'autres résonateurs.

**Title: Analysis by "reverse engineering" methods of ultra-stable piezoelectric resonators and noise modelling.**

**Keywords:** Quartz resonators; BAW; SC-cut resonator; metrology; phase noise; carrier suppression; 1/f noise; LGT resonators; stable and Mittag-Leffler distributions; power law intermittency; reverse engineering; X-ray; laser scattering.

**Abstract:** Bulk Acoustic Wave Resonators (BAW) have been studied in Time and Frequency domain for a long time, particularly at FEMTO-ST. They have an essential role in many metrological applications such as in positioning devices like GPS, Glonass, Galileo, etc. This thesis work presents the passive technic used for phase noise measurement in high-performance BAW resonators. These resonators were fabricated by several European manufacturers and provided for the thesis work by CNES for reverse engineering investigations.

The work begins with recalling the basics of piezoelectricity in quartz and noise in ultra-stable resonators.

The second part of the work gives details on noise measurement by carrier suppression technic with an alternative technic for low impedance resonators (< 10 ohms).

The third part is about the comparison of Steven-Tiersten's model with our phase noise measurement results at different temperatures and classification of resonators according to their short-term stability. A finite element simulation is used to compare the theory and experimental results.

The fourth part presents tests using Mittag-Leffler distribution and stable distributions of a model of phase noise due to power law intermittency.

Finally, the "reverse engineering" work is carried out by dismantling some resonators for defects analysis using X-rays diffraction and laser scattering. This revealed macroscopic imperfections and a few dislocations which could be a possible cause for phase noise in the resonators. This will have to be confirmed and quantified with other resonators.

Université Bourgogne Franche-Comté
32, avenue de l'Observatoire
25000 Besançon